

Characterization, Modeling and Prediction of Fretting Wear of Aeroengine Combustor Components

Ahmed Korashy Elsayed

Department of Mechanical Engineering

McGill University

Montreal, Quebec

October 2015

A thesis submitted to McGill University in partial fulfillment of the requirements of
the degree of Doctor of Philosophy

Copyright © Ahmed Korashy Elsayed 2015

All Rights Reserved

Abstract

The need for understanding and predicting the fretting wear failure of aeroengine combustor components is driven by the concern of proper design and reliable operation of aeroengines, which is of major economic and safety concern. The objectives of this research are to assess the tribological behaviour of some combustor component candidate contact pairs (CP1: Cobalt Alloy 2 / Cobalt Alloy 1, CP2: Cobalt Alloy 1 / Nickel Alloy 1 and CP3: Cobalt Alloy 2 / Nickel Alloy 1) at different loading conditions and temperature levels. It is required also to produce useful material selection maps that can be used by engine designers, and to provide, through fundamental understanding, some predictive models tools which can be reliably employed in the forecast of fretting wear failure.

The experimental investigation was carried out using a specially designed tribometer. Results showed that, for all tested contact pairs, the increase in the temperature from 350°C to 550°C was associated with a decrease in the coefficient of friction (COF). Results also showed that the least wear coefficient (wear damage) was exhibited by CP1 at 550°C, and by CP2 at 350°C. This was attributed to the formation of a protective layer of compacted oxides, which contributes to load bearing, precludes the metal-metal contact, and reduces the friction and wear damage. Although a decrease in friction was associated with a decrease in the wear coefficient for CP1, it was associated with an increase in the wear coefficient for CP2 and CP3.

Using a finite element thermomechanical model, it was found that the frictional heat causes a reduction in the depth at which subsurface cracks initiate, but once initiated, they propagate faster. A thermal model based on the surface topographies of the real surfaces was developed to predict the contact temperature. Compared to the model based on the uniformly-distributed equal-sized micro contact areas (MCAs), this model showed better ability to capture the contact temperature and its gradient in the subsurface layer. Results also showed that, unlike machined surfaces, fretted surfaces form agglomerated MCAs, which raise the surface temperature. In addition, the friction thermal effect was found to be pronounced for materials having high hardness and low thermal conductivity.

Résumé

La nécessité de comprendre et de prédire l'usure par fretting des pièces de chambre de combustion de moteurs d'avions est entraînée par le souci de conception et fonctionnement fiable de moteurs aéronautiques. Ceci représente une préoccupation majeure économique et sécuritaire. Les objectifs de cette recherche sont d'évaluer le comportement tribologique de certaines paires de contact candidates des pièces de chambre de combustion (PC1: Alliage de Cobalt 2 / Alliage de Cobalt 1, PC2: Alliage de Cobalt 1/ Alliage de Nickel 1 et PC3: Alliage de Cobalt 2 / Alliage de Nickel 1) à différentes conditions de chargement et niveaux de température. Il est également nécessaire de fournir des cartes de sélection des matériaux utiles qui peuvent être utilisées par les concepteurs de moteurs, et de fournir, grâce à une compréhension fondamentale, certains outils prédictifs de modélisation qui peuvent être utilisés de façon fiable dans les prévisions de ce type de défaillance.

L'étude expérimentale a été réalisée en utilisant un tribomètre spécialement conçu. Les résultats ont montré que l'augmentation de la température de 350°C à 550°C était accompagnée par une diminution du coefficient de frottement pour toutes les paires de contact. Les résultats ont montré également que le coefficient d'usure le plus bas s'est manifesté par PC1 à 550°C, et par PC2 à 350°C. Cela a été attribué à la formation d'une couche d'oxydes protectrice et compactées, appelée 'Glaze', ce qui contribue à supporter la charge, empêche le contact métal-métal, et réduit le frottement et l'endommagement par usure. Malgré une diminution du frottement accompagnée par une diminution du coefficient d'usure pour PC1, cette diminution du frottement a été accompagnée par une augmentation du coefficient d'usure pour PC2 et PC3.

En utilisant un modèle thermomécanique de calculs par éléments finis, on a constaté que la chaleur de frottement provoque une réduction de la profondeur à laquelle les fissures sous-surface sont amorcées, mais une fois amorcées, la chaleur de frottement cause une propagation rapide. Un modèle thermique fondé sur les topographies de surfaces réelles a été développé pour prédire la température de contact. Les résultats ont montré que, par

rapport au modèle fondé sur les micro-aires de contact (MAC) uniformément distribués et de taille égale, ce modèle était capable de mieux capturer le gradient de température. Les résultats ont également montré que les surfaces frettées forment des MAC agglomérées qui regroupent les générateurs de chaleur et augmente la température de surface. En outre, l'effet thermique de frottement est plus évident dans les matériaux ayant une dureté élevée et une faible conductivité thermique.

Acknowledgments

The author would like to express his sincere appreciation to his supervisors Dr. Helmi Attia and Dr. Vince Thomson, who were extremely helpful during the course of this research work.

The author would like to specifically express gratitude to his supervisor Dr. Helmi Attia, who immensely supported him and guided this work with puissance and patience. The author has benefited considerably by working under his supervision and feels fortunate to have been given this opportunity.

The financial support from Pratt and Whitney Canada (PWC) and the Consortium de Recherche et d'Innovation en Aérospatiale au Québec (CRIAQ) is gratefully acknowledged.

The partial financial support of the Natural Sciences and Engineering Research Council of Canada (NSERC) is also acknowledged.

The technical support from PWC is highly appreciated. The author would like to thank Mr. Saeid Oskooei, from the Hot Section Durability in PWC for his follow-up and constructive collaboration throughout the research work.

The author would also like to thank his friend Ahmad Sadek for his support.

Last but not least, the author would like to thank his spouse, Hebatalla Elkaraksi, for her patience and encouragement through the long working nights and weekends.

The author would like to dedicate this thesis to his parents.

Contribution to Knowledge

1. The high temperature fretting wear behaviour of cobalt and nickel superalloys, used in aeroengine combustor components, was characterized at high temperature, using a specially designed tribometer. These results which are not readily available in the open literature, provide aeroengine designers with the database for design optimization.
2. The effect of temperature and loading conditions on the surface oxide structure and composition has been revealed. Their tribological beneficial or detrimental role was established.
3. A thermal model that predicts the interface contact temperature during fretting wear, considering the anisotropic nature of the real fretted surfaces, was developed. This model takes into account the random spatial distribution of micro-contact areas, the existence of surface oxides at the contact interface and the temperature dependence of the thermal and mechanical material properties.
4. A three-dimensional Finite Element model was developed to establish the effect of frictional heat on the sub-surface crack initiation and propagation processes, which are required for modeling the wear debris formation by delamination. This model relates the global elastic behaviour of the contact asperities to the local elastoplastic behaviour of a single asperity-substrate contact. This aspect has never been investigated before.

Table of Contents

Abstract	ii
Résumé	iii
Acknowledgments	v
Contribution to Knowledge	vi
List of Figures	xi
List of Tables	xix
Nomenclature	xxi
Chapter 1 Introduction	1
1.1. Significance of the fretting wear prediction in aeroengine components	1
1.2. Research Objectives	3
1.3. Research Outline	4
Chapter 2 Literature Review	6
2.1. Introduction	6
2.2. Sliding wear of superalloys at elevated temperatures	7
2.3. Fretting wear of superalloys at elevated temperatures	9
2.4. Significance of frictional heat during fretting wear	10
2.5. Effect of the frictional heat on microstructure	11
2.6. Effect of contact temperature on oxidation kinetics	12
2.7. Effect of frictional heat on wear debris formation	14
2.7.1. Criteria for crack initiation	16
2.7.2. Criteria for crack propagation	17
2.8. Contact temperature prediction	20
2.8.1. Contact temperature prediction during sliding wear	21

2.8.2.	Contact temperature prediction during fretting wear	21
2.9.	Conclusions from the literature review	24
Chapter 3	Experimental Setup.....	26
3.1.	Introduction.....	26
3.2.	Setup components and acquisition system	27
3.3.	Setup dynamics	30
3.4.	Setup modifications for high temperature experiments.....	31
3.5.	Finite element thermal design for the experimental setup.....	32
3.6.	Interface temperature prediction and model validation	34
3.7.	Workpiece materials and geometries.....	36
3.8.	Samples alignment.....	37
3.9.	Surface scanning and 3-D map	38
3.10.	Parameters for the evaluation of the tribological properties	40
3.10.1.	Wear coefficient and maximum wear depth.....	40
3.10.2.	Coefficient of Friction	40
3.11.	Experimental parameters and test matrix	41
Chapter 4	Experimental Results: Comparison between Different Contact Pairs	45
4.1.	Introduction.....	45
4.2.	Comparison methodology and notes on the reported results	45
4.3.	Normalization procedure	45
4.4.	Evaluation of the material wear coefficient	46
4.5.	Evaluation of the maximum wear depth	51
4.6.	Evaluation of friction properties	56
4.7.	Evaluation of contact pressure.....	64

Chapter 5 Experimental Results: In-depth Investigation for Some Selected Cases.. 67

5.1. Introduction.....	67
5.2. Effect of loading conditions on friction and wear resistance	67
5.3. Effect of temperature on friction and wear resistance	70
5.4. Effect of temperature on oxide film composition and thickness	72
5.5. Oxide film composition and contact temperature	76
5.6. Further investigation of some selected ring samples.....	79

Chapter 6 Contact Temperature Prediction during Fretting Wear:

Significance of the Frictional Heat and Model Description 85

6.1. Introduction.....	85
6.2. Nature of engineering surfaces, frictional heat and constriction effect	85
6.3. Effect of frictional heat on fretting wear by delamination	87
6.3.1. Selected criteria for crack initiation and crack propagation.....	88
6.3.2. Finite element crack initiation and propagation model.....	89
6.3.3. Effect of frictional heat on crack initiation.....	96
6.3.4. Effect of frictional heat on crack propagation.....	101
6.3.5. Conclusion from the crack initiation – crack propagation model	103
6.4. Thermal model for contact temperature prediction	104
6.4.1. Overview of the model	104
6.4.2. Surface characterization.....	106
6.4.3. Material properties.....	108
6.4.4. Contact model used in the determination of Micro-Contact Areas (MCAs)	110
6.4.5. Finite element thermal model.....	112
6.5. Verification of model assumptions.....	115

6.5.1. Moving heat flux vs. stationary time-dependent heat flux.....	115
6.5.2. Number of cycles required to reach steady state	116
6.5.3. Analysis of heat partitioning.....	117
Chapter 7 Contact Temperature Prediction during Fretting Wear:	
Model Validation and Sensitivity Analyses.....	121
7.1. Introduction.....	121
7.2. Model validation	121
7.3. Real surface vs uniform idealized surface	122
7.4. Effect of fretting operation conditions on the maximum temperature rise	123
7.5. Effect of surface condition	124
7.6. Effect of oxide thickness	131
7.7. Effect of material properties and normal load	132
Chapter 8 Conclusions and Future Work Recommendations	139
8.1. Conclusions.....	139
8.2. Future Work Recommendations	141
References.....	143
Appendix A: Cylinder sample 3D surface scans and optical images	150
Appendix B: Energy ratio for the conducted tests	164

List of Figures

Figure 1-1: System approach for the fretting wear and the nonlinear nature of the process.	2
Figure 3-1: Schematic of the experimental setup showing its main components.	28
Figure 3-2: Image of the experimental setup for high temperature fretting wear, showing the displacement and force sensors, and their typical measurements for the friction force, the displacement measured by the proximity probe and the accelerometer.	29
Figure 3-3: (a) Static calibration of the proximity probe and (b) relative displacement read by the proximity probe compared to the absolute displacement read by the accelerometer. The close agreement confirms the setup rigidity.	29
Figure 3-4: Dynamic calibration of friction force transducer (a) and FFT analysis and response force spectrum of the frictional force assembly (b) showing the absence of undesired disturbances between 0 and 250 Hz.	30
Figure 3-5: Concept of local heating of the samples (left) and cross sectional view of the assembly (right).	31
Figure 3-6: Setup high temperature components (a) high density heaters (1000 W/in^2), (b) upper cylinder assembly, (b) lower ring assembly and (d) assembly showing the heaters and the cooling system at the critical points.	32
Figure 3-7: 3-D model of the fretting wear setup.	33
Figure 3-8: FE thermal model for the setup (Temperature in $^{\circ}\text{C}$).	33
Figure 3-9: Cross section of the fretting wear setup thermal model showing the thermocouple suggested points (above) and their correlation to the interface temperature (below).	34
Figure 3-10: Fretting samples (a) upper stationary cylinder sample G1 (provided by PWC), (b) upper stationary cylinder sample G2,	36
Figure 3-11: Working drawings of the fretting specimens (a) upper fixed cylinder sample (G1), (b) upper fixed cylinder sample (G2) and (C) lower oscillatory ring sample.	37
Figure 3-12: The 3D surface scanner Taylor Hobson Talysurf 120 with a close up on the scanning process.	39

Figure 3-13: Illustration of the wear volume, wear depth, and contact area calculation (a) optical image observed under the microscope, (b) 3D map of the fretted surface, (c) the contour defining the damaged area, and (d) the reference plane P plane.....	39
Figure 3-14: Calculation of the coefficient of friction.	40
Figure 3-15: Characterization of the fretting cycle under gross slip conditions.....	41
Figure 4-1: Effect of temperature on the wear coefficient when plotted against the work rate for CP1 (Cobalt Alloy 2 cylinder / Cobalt Alloy 1 ring).....	47
Figure 4-2: Effect of temperature on the wear coefficient when plotted against the work rate for CP2 (Cobalt Alloy 1 cylinder / Nickel Alloy 1 ring).	48
Figure 4-3: Effect of temperature on the wear coefficient when plotted against the work rate for CP3 (Cobalt Alloy 2 cylinder / Nickel Alloy 1 ring).	49
Figure 4-4: Effect of work rate on the wear coefficient for G1_CP0 at RT (Cobalt Alloy 1 cylinder / Cobalt Alloy 1 ring).	49
<i>Figure 4-5: Wear coefficient vs. work rate for different contact pairs at 350°C.</i>	<i>50</i>
Figure 4-6: Wear coefficient vs. work rate for different contact pairs at 550°C.....	51
Figure 4-7: Wear resistance material selection map (based on the wear coefficient).	51
Figure 4-8: Effect of temperature on the maximum wear depth when plotted against the work rate for CP1 (Cobalt Alloy 2 cylinder / Cobalt Alloy 1 ring).	52
Figure 4-9: Effect of temperature on the maximum wear depth when plotted against the work rate for CP2 (Cobalt Alloy 1 cylinder / Nickel Alloy 1 ring).	53
Figure 4-10: Effect of temperature on the maximum wear depth when plotted against the work rate for CP3 (Cobalt Alloy 2 cylinder / Nickel Alloy 1 ring).	53
Figure 4-11: Effect of the work rate on the maximum wear depth for G1_CP0 at RT (Cobalt Alloy 1 cylinder / Cobalt Alloy 1 ring).	54
Figure 4-12: Maximum wear depth vs. work rate for different contact pairs at 350°C.	55
Figure 4-13: Maximum wear depth vs. work rate for different contact pairs at 550°C.	55
Figure 4-14: Wear resistance material selection map (based on the maximum wear depth).	56
Figure 4-15: Effect of temperature on the coefficient of friction when plotted against the work rate for CP1 (Cobalt Alloy 2 cylinder / Cobalt Alloy 1 ring).	56

Figure 4-16: Typical fretting loop for CP1 (a) low load ($F_n = 10$ N) - high amplitude ($A = \pm 15$ μm) case at 550°C, with ER = 0.53 and (b) high load ($F_n = 30$ N) - low amplitude ($A = \pm 10$ μm) case at 550°C, with ER = 0.3.	57
Figure 4-17: Effect of temperature on the coefficient of friction when plotted against the work rate for CP2 (Cobalt Alloy 1 cylinder / Nickel Alloy 1 ring).	58
Figure 4-18: Effect of temperature on the coefficient of friction when plotted against the work rate for CP3 (Cobalt Alloy 2 cylinder / Nickel Alloy 1 ring).	58
Figure 4-19: Effect of the work rate on coefficient of friction for G1_CP0 at RT (Cobalt Alloy 1 cylinder / Cobalt Alloy 1 ring).....	59
Figure 4-20: Coefficient of friction vs. work rate for different contact pairs at 350°C.	59
Figure 4-21: Coefficient of friction vs. work rate for different contact pairs at 550°C.	60
Figure 4-22: Material selection map (based on the coefficient of friction).....	60
Figure 4-23: COF vs number of fretting cycles for CP0 at RT.	61
Figure 4-24: COF vs number of fretting cycles for CP1 at RT.	61
Figure 4-25: COF vs number of fretting cycles for CP1 at 350°C.....	62
Figure 4-26: COF vs number of fretting cycles for CP2 at 350°C.....	62
Figure 4-27: COF vs number of fretting cycles for CP3 at 350°C.....	63
Figure 4-28: COF vs number of fretting cycles for CP1 at 550°C.....	63
Figure 4-29: COF vs number of fretting cycles for CP2 at 550°C.....	64
Figure 4-30: COF vs number of fretting cycles for CP3 at 550°C.....	64
Figure 4-31: Contact pressure vs. work rate for different contact pairs at 350°C.....	65
Figure 4-32: Contact pressure vs. work rate for different contact pairs at 550°C.....	66
Figure 5-1: Wear rates and adhesion rates vs. the work rate for the Cobalt Alloy 2 specimen fretted at 550°C.....	68
Figure 5-2: Effect of temperature on the wear coefficient for the Cobalt Alloy 2 stationary specimen and the adhesion coefficient of the Cobalt Alloy 1 oscillating specimen at $W = 350$ mJ/s ($A = \pm 15$ μm , $F_n = 30$ N).	71
Figure 5-3: (a) Evolution of the coefficient of friction with time during the test and (b) steady state coefficient of friction at different temperatures.....	72

Figure 5-4: Evolution of the oxide layer on the surface of the Cobalt Alloy 2 cylinder with temperature at a work rate of 350 mJ/s (a) RT, (b) 200°C, (c) 350°C, and (d) 550°C.	73
Figure 5-5: 3-Dimensional topography of the extent of the fretted area at 2×10^6 cycles for the Cobalt Alloy 2 cylinder at a work rate of 350 mJ/s, (a) specimen fretted at 200°C and (b) specimen fretted at 550°C.	73
Figure 5-6: SEM photomicrographs and EDX chemical analysis of the Cobalt Alloy 2 cylindrical specimens cross sections.....	75
Figure 5-7: Raman spectroscopy for the Cobalt Alloy 2 specimen fretted at 200°C and 550°C and the corresponding optical images (a within the fretted area at 550°C, (b) outside the fretted area at 550°C, (c) within the fretted area at 200°C, and (d) outside the fretted area at 200°C.....	76
Figure 5-8: SEM photomicrographs and EDX chemical analysis of the Cobalt Alloy 2 cylindrical specimens cross sections (a) cross section of the specimen fretted at 200°C, (b) scattered thin oxide zones at 200°C, (c) EDX chemical analysis of the specimen fretted at 200°C, (d) cross section of the specimen fretted at 550°C, (e) thicker oxide layer at 550°C, (f) delaminated oxide broken into smaller debris and (g) EDX chemical analysis of the specimen fretted at 550°C.	77
Figure 5-9: Typical cross section of a metallic surface during high temperature oxidative wear, showing the oxide thickness within and outside the fretted area. Image adopted from [103]......	79
Figure 5-10: SEM photomicrographs of the cross section for the analysed ring samples, (a) and (b) the CP1 Cobalt Alloy 1 ring sample fretted at 550°C, (c) and (d) the CP3 Nickel Alloy 1 ring sample fretted at 550°C, and (e) and (f) CP3 Nickel Alloy 1 ring sample fretted at 350°C.....	81
Figure 5-11: EDX chemical analysis of the analysed ring samples, (a) CP1 Cobalt Alloy 1 ring sample fretted at 550°C, (b) CP3 Nickel Alloy 1 ring sample fretted at 550°C, and (c) CP3 Nickel Alloy 1 ring sample fretted at 350°C. The spectra show high tungsten content in the oxide transferred from the Cobalt Alloy 2 cylinder sample.	82

Figure 5-12: Raman spectroscopy for the CP1 Cobalt Alloy 1 ring sample fretted at 550°C, Nickel Alloy 1 ring sample fretted at 550°C, and Nickel Alloy 1 ring sample fretted at 350°C	83
Figure 6-1: Apparent area, contour areas, micro-contact areas and the spreading of heat flow lines to the two bodies	86
Figure 6-2: Wear debris formation by delamination as a result of subsurface crack initiation and propagation.	88
Figure 6-3: Rough surfaces replaced by an equivalent rough surface and a smooth surface (a) schematic of the 3D equivalent surface and (b) the standard deviation of the asperity heights σ , and the absolute mean slope of the equivalent surface m	90
Figure 6-4: FE thermal model used to predict the contact temperature for crack initiation and propagation (a) model overview showing the 3 x 3 array of asperities and the surrounding, (b) a cross section showing the central and the neighbouring asperities.....	91
Figure 6-5: Graph used in the estimation of the micro-contact parameters	92
Figure 6-6: Global thermoelastic model and the boundary conditions conveyed to the local thermoplastic submodel.....	94
Figure 6-7: Variation of the resultant displacement on the HFC boundaries with time during the loading cycle.....	95
Figure 6-8: (a) Mesh details of the thermoplastic submodel and (b) assumed material model, where E is the modulus of elasticity, E_t is the tangent modulus.....	95
Figure 6-9: Effect of the frictional heat on the elastic behaviour of the global model showing the resultant displacement mechanical loading (left) vs the thermomechanical loading (right) with the temperature field at the asperity contact ($\mu = 0.8$ and the asperity is at position 2 in Figure 6-8 (a))......	96
Figure 6-10: Resultant displacement (a) mechanical loading, (b) thermo-mechanical loading, (c) development of plastic deformation (quantified by the equivalent plastic strain) at the contact zone for the mechanical loading and (d) thermo-mechanical loading ($\mu = 0.8$ and the asperity is at position 2 in Figure 6-8 (a))......	98

Figure 6-11: Contour plot of the σ_{rr} / k_s , where the probable sites of crack initiation are the regions where $\sigma_{rr}/k_s \geq 1$ (a) mechanical loading and (b) thermomechanical loading ($\mu = 0.8$ and the asperity is at position 2 in Figure 6-8 (a)).	99
Figure 6-12: Effect of the frictional heat and the coefficient of friction on the probable sites of crack initiation (asperity is at position 2 in Figure 6-8 (a)).	99
Figure 6-13: Effect of the frictional heat on the tensile hydrostatic stress for the (a) mechanical loading and	100
Figure 6-14: Finite element model of crack propagation with a crack inserted at the probable site of initiation showing the mesh and crack details	101
Figure 6-15: In-plane shear stress at the crack tips ($l = 12 \mu\text{m}$)	103
Figure 6-16: Flowchart of the Contact-based Model used to estimate the contact temperature during fretting wear.	105
<i>Figure 6-17: Exporting the scanned fretted surface and determination of the apparent contact area (a) contact pair surface when exported as (x, y, z) points and (b) measurement of the apparent area of contact.</i>	107
Figure 6-18: Cobalt Alloy 2cylinder sample used for the macrohardness test and the recorded hardness values in R_c	108
Figure 6-19: Cross section of the Cobalt Alloy 2cylinder sample used for the nanoindentation test, the indentation point	109
Figure 6-20: Contact establishment, (a) surfaces imported with no load application, (b) load is applied by reducing the separation, (c) the upper surface converted to white and the lower surface is converted to black, (d) contact converted into a binary B&W image (e) colors histogram showing the black (contact) pixels peak and the white (non-contact) pixels.	111
Figure 6-21: Finite element model (a) alloy substrate covered by a thin layer of oxide and (b) the SOLID70-3-DThermal Brick Element used in the analysis.	113
Figure 6-22: Example of a contact pattern automatically conveyed from (a) the contact model to (b) the FE model.	114
Figure 6-23: The generated heat flux at the contact interface (Material Cobalt Alloy 2, $p_m = 2177 \text{ MPa}$, $F_n = 30 \text{ N}$, $A = \pm 15 \mu\text{m}$, $f = 200 \text{ Hz}$, $\mu = 0.33$).	114

Figure 6-24: the moving heat flux vs. the stationary sinusoidal time-varying heat flux at the maximum temperature point (Cobalt Alloy 2/Cobalt Alloy 1, $F_n = 30$ N, $A = \pm 15$ μm , $f = 200$ Hz, $T_b = 550^\circ\text{C}$ $\delta = 10$ μm , $\mu = 1$).....	115
Figure 6-25: Nodal temperature at the point experiencing the maximum temperature rise when plotted against time (Cobalt Alloy 2/Cobalt Alloy 1, $F_n = 30$ N, $A = \pm 15$ μm , $f = 200$ Hz, $T_b = 550^\circ\text{C}$ $\delta = 10$ μm , $\mu = 0.33$).....	117
Figure 6-26: Heat partitioning analysis showing the thermal impedance of the Cobalt Alloy 2 / Cobalt Alloy 1 pair as the slopes of the blue and red lines, respectively (Cobalt Alloy 2/Cobalt Alloy 1, $F_n = 30$ N, $A = \pm 10$ and 15 μm , $f = 100$ and 200 Hz, $T_b = 550^\circ\text{C}$ $\delta = 10$ μm , $\mu = 0.33$ and 0.71).....	119
Figure 6-27: Heat partitioning analysis for the Cobalt Alloy 2 and / AISI 1095 steel pair..	120
Figure 7-1: Uniformly distributed equal-sized MCAs model (a) model overview showing the 3×3 array of asperities, the surrounding and the oxide layer, (b) a cross section showing the central and the neighbouring asperities, and (c) the thermal field along the depth in the contact region (T in $^\circ\text{C}$), and (d) comparison of the temperature profile along the depth between the real contact-based model and the uniformly distributed equal-sized MCAs model (Cobalt Alloy 2/Cobalt Alloy 1, $F_n = 30$ N, $A = \pm 15$ μm , $f = 200$ Hz, $T_b = 550^\circ\text{C}$ $\delta = 10$ μm , $\mu = 0.33$).....	123
Figure 7-2: Effect of the fretting operation conditions process parameters on the maximum temperature rise.....	124
Figure 7-3: Contacting surfaces, contact pattern and cross section of (a) the unfretted sample and (b) the fretted sample ($F_n = 30$ N, $\varepsilon^2 = 1.26$ %, $T_b = 550^\circ\text{C}$, $A = \pm 15$ μm , $f = 200$ Hz, $A_a = 1$ mm^2).....	125
Figure 7-4: Effect of the surface condition on the maximum temperature rise for both pairs; Cobalt Alloy 2 / Cobalt Alloy 1 and Ti-6Al-4V / Ti-6Al-4V	127
Figure 7-5: Contact pattern of (a) the fresh samples and (b) the fretted samples for the Ti-5Al-2.5Sn / Ti-5Al-2.5Sn simulation ($F_n = 60$ N, $\varepsilon^2 = 4$ %, $T_b = 550^\circ\text{C}$, $A = \pm 15$ μm , $f = 200$ Hz, $A_a = 1$ mm^2 , $\delta = 0$ μm).....	128

Figure 7-6: Effect of surface topography on the contact temperature rise in the absence of the oxide layer. Temperature field for the (a) fresh sample and (b) fretted sample for the Ti-5Al-2.5Sn / Ti-5Al-2.5Sn simulation ($F_n = 60$ N, $\varepsilon^2 = 4$ %, $T_b = 550^\circ\text{C}$, $A = \pm 15$ μm , $f = 200$ Hz, $A_a = 1$ mm^2 , $\delta = 0$ μm).....	129
Figure 7-7: Effect of surface topography on the contact temperature rise in the absence of the oxide layer, (a) fresh sample and (b) fretted sample for the Ti-5Al-2.5Sn / Ti-5Al-2.5Sn simulation ($F_n = 60$ N, $\varepsilon^2 = 4$ %, $T_b = 550^\circ\text{C}$, $A = \pm 15$ μm , $f = 200$ Hz, $A_a = 1$ mm^2 , $\delta = 0$ μm).	129
Figure 7-8: Real surfaces (above) and autocorrelation functions (below) of the (a) machined surface and (b) fretted surface	130
Figure 7-9: Maximum temperature rise at different oxide thickness values ($q = 1.4$ $\text{e}7$ W/ m^2 , $F_n = 30$ N, $A = \pm 15$ μm , $f = 200$ Hz, $\mu = 0.33$, $T_{\text{bulk}} = 550^\circ\text{C}$).....	132
Figure 7-10: Maximum temperature rise vs oxide thickness ($q = 1.4$ $\text{e}7$ W/ m^2 , $F_n = 30$ N, $A = \pm 15$ μm , $f = 200$ Hz, $\mu = 0.33$, $T_{\text{bulk}} = 550^\circ\text{C}$).....	132
Figure 7-11: Effect of the material properties and applied load (pressure) on the maximum temperature rise ($A = \pm 15$ μm , $f = 200$ Hz, $\mu = 0.33$, $T_{\text{bulk}} = 25^\circ\text{C}$, $\xi = 0.5$, $A_a = 1$ mm^2).....	134
Figure 7-12: Effect of load on the maximum temperature rise – maximum heat flux relationship (Cobalt Alloy 2 / Cobalt Alloy 2, $A = \pm 15$ and ± 25 μm , $f = 100$ and 200 Hz, $\mu = 0.33$ and 0.71 , $T_{\text{bulk}} = 550^\circ\text{C}$).....	135
Figure 7-13: Contour plot of the temperature field at the top surface of the central area and the temperature plot along the depth at the point experiencing the maximum temperature rise (a) $F_n = 30$ N ($\varepsilon^2 = 1.26$) and (b) $F_n = 60$ N ($\varepsilon^2 = 2.61$) (Cobalt Alloy 2 / Cobalt Alloy 2, $A = \pm 25$ μm , $f = 200$ Hz, $\mu = 0.71$, $T_{\text{bulk}} = 550^\circ\text{C}$).....	137
Figure 7-14: Extent of the points having a contact temperature $> 700^\circ\text{C}$, shown as red zones, while the gray areas represent the zones having a temperature value between 550°C and 700°C (Cobalt Alloy 2 / Cobalt Alloy 2, $A = \pm 25$ μm , $f = 200$ Hz, $\mu = 0.71$, $T_{\text{bulk}} = 550^\circ\text{C}$)	137

List of Tables

Table 3-1: Maximum rated operating temperature for the different sensors, and the measured operation temperature.....	35
Table 3-2: Experimental parameters, variables and the fixed conditions.....	42
Table 3-3: Contact pairs used in the experiments [85], [86] and [87].....	42
Table 3-4: Full project test matrix.....	43
Table 5-1: 3Dtopography and evolution of the COF with the number of cycles at different work rates when the temperature was fixed to 550°C.....	69
Table 5-2: Series of oxides existing on the surfaces of the specimens fretted at 200°C and 550°C.....	77
Table 5-3: Series of oxides existing on the surfaces of the samples fretted at 200°C and 550°C.....	83
Table 5-4: Chromium oxide Cr_2O_3 peaks and the corresponding wear depth.....	84
Table 6-1: Parameters used in the FE model.....	93
Table 6-2: Effect of the frictional heat on the CTSD recorded after one loading cycle for the simulated crack lengths.....	102
Table 6-3: Hertzian contact calculations of the reference case.....	107
Table 6-4: Recorded nanohardness values in GPa.....	109
Table 6-5: Yield values for the solution treated Cobalt Alloy 2bar and its oxide.....	110
Table 6-6: Maximum temperature rise for the different conditions assuming 100% of the heat flows to each body separately.....	118
Table 7-1: Reference case conditions and the predicted maximum temperature rise.....	122
Table 7-2: Fixed conditions of the simulation conducted to study the effect of the surface condition.....	126
Table 7-3: Material properties and maximum temperature rise values when the surface condition changed from the unfretted to the fretted state.....	126
Table 7-4: Simulation conditions used in the study of the effect of surface condition in the absence of an oxide layer.....	128
Table 7-5: Simulation parameters for the investigation of the oxide thickness effect.....	131

Table 7-6: Simulation fixed conditions used to study the effect of material and normal load on the contact temperature prediction	133
Table 7-7: Material properties and maximum temperature rise for different materials and constriction ratio values.....	133
Table 7-8: Simulation conditions used to study the effect of normal load on the contact temperature prediction.....	135

Nomenclature

Symbols

A	Amplitude of slip (μm)
$A_{Arrhenius}$	Pre-exponential factor of the Arrhenius
a, b	Dimensions of the apparent contact area (mm)
Aa	Apparent contact area (mm^2)
A_{hole}	Hole area resulting from wear (mm^2)
A_{peak}	Peak area resulting from adhesion (mm^2)
A_r	Real contact area (mm^2)
A_{os}	Oxide-substrate interface area (mm^2)
C_p	Specific heat (kJ/kg.K)
E	Modulus of elasticity (GPa)
Ea	Activation energy for the oxidation process (kJ/mole)
E_d	Dissipated energy during the fretting cycle (N.m)
E_t	Total energy during the fretting cycle (N.m)
E_{tan}	Tangent modulus (GPa)
f	Frequency of oscillation (Hz)
F_n	Normal force (N)
F_t	Friction force (N)
Fo	Fourier modulus
h_{cr}	Thickness of the wear debris (μm)
h_{max}	Maximum wear depth(μm)
$k_{oxidation}$	Oxidation rate constant
k_s	Shear yield strength (MPa)
k	Thermal conductivity (W/m.K)
k_o, k_1, k_2	Constants that depend on the temperature and material
l	Crack lengths (μm)
L	Characteristic length of an asperity MCA (μm)

m	Mean absolute slope of the contacting asperities
M	Number of micro-contacts over the apparent area A_a
N	Number of test cycles
p_a	Applied contact pressure (MPa)
p_{avg}	Average Hertzian contact pressure (MPa)
Pe	Peclet number
p_m	Flow stress (MPa)
p_{max}	Maximum Hertzian contact pressure (MPa)
Q	Heat flow (W)
q	Heat flux (W/m ²)
q_{max}	Maximum heat flux occurring at the maximum velocity (W/m ²)
r	Micro-contact radius (μm)
R	Universal gas constant
R_{th}	Thermal resistance (K/W)
R_c	Thermal constriction resistance (K/W)
T	Temperature (°C)
ΔT_{max}	Maximum temperature rise at the contact interface (°C or °K)
t	Time (sec)
V	Wear volume (μm ³)
\dot{V}	Wear rate(μm ³ /s)
v	Sliding velocity (m/s)
\dot{W}	Work rate (mJ/s)
x, y, z	Cartesian coordinate system
X	Single parameter uniquely defined by the constriction ratio
Y	Separation (distance between the medians of the two surfaces)(μm)
Z_{th}	Thermal impedance (K/W)
α	Thermal diffusivity (m ² /s)
δ	Oxide film thickness (μm)
δ_{ol}	Oxide film thickness outside the fretted area (μm)

δ_{02}	Oxide film thickness inside the fretted area (μm)
ε^2	Constriction ratio
μ	Coefficient of friction
ρ	Density (kg/m^3)
σ	Standard deviation of the asperity heights (μm)
σ_h	Hydrostatic stress (MPa)
σ_{rr}	Interfacial normal stress (MPa)
σ_y	Yield strength (MPa)
τ_{max}	Maximum applied shear stress (MPa)
τ_r	Residual shear stress (MPa)
ξ	Heat partitioning factor
γ	Density of the MCAs (asperities/ mm^2)
ψ	Thermal constriction parameter
$\psi_{fretting}$	Thermal constriction parameter during fretting
$\psi_{stationary}$	Thermal constriction parameter at static contacts
ω	Angular frequency (rad/s)

Abbreviations

ACF	Autocorrelation Functions
COF	Coefficient of Friction
CP	Contact Pair
CTSD	Crack Tip Sliding Displacement
ER	Energy Ratio
FFT	Fast Fourier Transform
G	Geometry
HFC	Heat Flow Channel
MCA	Micro Contact Area
RT	Room Temperature
SIF	Stress Intensity Factor

Chapter 1 Introduction

With an increasing competition in the dynamic aerospace industry, the evolution of aeroengine designs and materials has a steep gradient. In a jet engine, the most effective way of increasing the specific thrust (thrust/weight) is to increase the engine operating temperature [1]. This could be made true through the use of superalloys, which since their introduction in the 1940s, made much of these very-high-temperature applications possible due to the fact that they can be utilized to a high fraction of their melting points [2]. Cobalt and nickel-based superalloys for instance are extensively used in aeroengine combustor components due to their high strength, corrosion and wear resistance at elevated temperatures.

1.1. Significance of the fretting wear prediction in aeroengine components

Fretting wear is encountered when structural components are subjected to relative displacement of small amplitudes (typically below 100 μm) in the presence of normal load coming from contact. The nature of cyclic loading in the aeroengine combustor leads to fretting wear of the combustor cylindrical parts having a clearance fit. The configuration studied in this investigation represents the positioning pin and bush used to support the combustor liner (Figure 1-1). During real operation, the loading reaches its peak during take-off and landing periods. Normally aeroengines experience regular maintenance every 5000 flight hours, and during that maintenance process, the fretted components are inspected and replaced when needed. Pratt and Whitney Canada's concern of proper design and reliable operation of its engines drives the need for accurate prediction of fretting wear failure criteria and makes the understanding, forecast and prevention of this tribological failure indispensable.

Fretting wear failure can be quantified by some criteria, among which are the volumetric wear losses, the maximum wear depth, and the dynamic friction. The fretting wear process is further complicated by some non-linear aspects. As Figure 1-1 shows, the forcing function that affects the contact interface, such as the contact stress, the frequency of oscillation, the amplitude of slip and the bulk temperature causes damage in the form of

volumetric wear losses, wear depth and dynamic friction. However, any damage changes the geometry of the mating components, and produces frictional heat that has a crucial effect on the oxidation process, mechanical and physical properties, material microstructure and subsurface deformation, making the process nonlinear by nature.

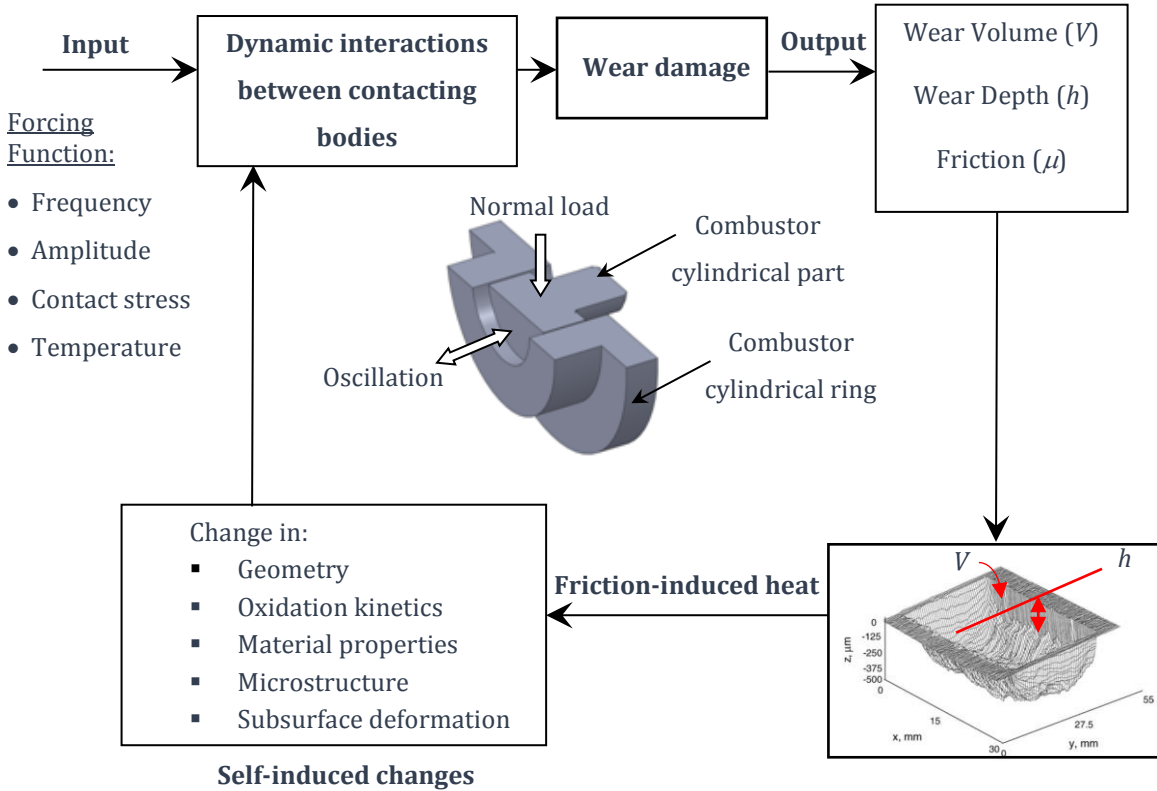


Figure 1-1: System approach for the fretting wear and the nonlinear nature of the process.

In order to simulate the tribological characteristics of the real system and to respect a number of similarity laws, typical engine operating conditions need to be duplicated as close as possible, e.g., components geometries, contact stress, amplitude of slip, frequency of oscillation and ambient temperature. This helps avoiding unreliable extrapolations, but on the other hand, gives rise to many of the inherent challenges, namely, heating the test specimens without causing excessive heat dissipation into the setup to avoid unwanted thermal deformation, cooling the measurement instrumentations to secure the reliability of the readings, and ensuring that the operating frequency does not coincide with any of the setup natural frequencies. As a consequence, researchers have always had difficulties with

high temperature experiments, and when they are conducted, the credibility of the setup as well as the reliability of the measurements remain questionable.

1.2. Research Objectives

Based on the discussion in the previous section, the present research aims at addressing the following two main objectives:

The first objective is to characterize the fretting wear of different combustor components material and geometries by carrying out fretting wear experiments at room and high temperature (up to 550°C). These experiments will be used in evaluating the wear characteristics of the selected superalloys pairs by unveiling the effect of surface oxides formed during the fretting process on the wear damage criteria (wear volume, wear depth and dynamic friction). The purpose of this study is to provide engine designers with the best choice of contact pair(s) at the specified operating conditions. In addition, the experiments should support the development of a fretting wear thermal model that can be used in the prediction of the contact temperature as an important step towards the understanding and prediction of fretting wear. To meet the above objectives, an existing setup designed for room temperature, sliding fretting wear was modified for high temperature testing up to 600°C.

The second objective is to develop a reliable thermal model capable of estimating the interface contact temperature in fretting wear. The model should have the following characteristics:

1. Import the real surface topography to the FE model in order to capture the maximum amount of information and avoid omitting surface important details.
2. The model has to be feasible from the computational time and effort point of view.
3. In order for the model to be reliable, it has to be properly validated with experimental results.
4. This model should represent the tool to link the friction-induced heat to the evolution the oxide film thickness, composition and oxidation kinetics.

5. The model will serve in the future as a nucleus for the development of a generalized thermo-mechanical model which can simulate the wear debris formation at a single contact asperity level, and then, generalize it over the whole contact surface to correlate the input work to the output wear.

1.3. Research Outline

The following outline depicts how the thesis will progress in order to achieve the aforementioned objectives:

- Chapter 1 presents the significance of the fretting wear problem of aeroengine combustor components, its non-linear nature, the scope of work and the approach followed.
- Chapter 2 looks at the state-of-the-art literature review on the tribological properties, the oxidation and the fretting wear of superalloys at high temperature. Furthermore, the significance of the frictional heat on the microstructure, the oxidation kinetics and the wear mechanism is reviewed. Finally, the models used to estimate the contact temperature either in unidirectional sliding or in fretting are covered. The chapter ends up with the missing link or the gap to be filled in order to solve the problem in a fundamental way.
- Chapter 3 describes the experimental setup used to carry out high temperature fretting wear tests. It describes the force, displacement and temperature measurement systems and the methods of process characterization and quantification of damage criteria. The chapter shows the systematic approach followed to modify the experimental setup in order to accommodate high temperature testing including the design concepts of local heating, local cooling and optimal thermal insulation. It illustrates the developed finite element model for the setup and its validation. Finally, the chapter shows the full experimental test matrix.
- Chapter 4 shows the experimental results, and specifically the evolution of wear damage criteria (wear volume, maximum wear depth and dynamic friction) with work rate and temperature for the different contact pairs. The chapter ends up with

the material selection map that shows the recommended contact pair(s) suitable for the different working conditions and temperatures.

- Chapter 5 provides in-depth explanation of the results shown in chapter 4. It includes a detailed analysis (cross sectioning, scanning electron microscopy (SEM), energy dispersive X-ray analysis (EDX) and Raman spectroscopy for oxide analysis) for the best contact pair, in addition to a detailed analysis for some special cases.
- Chapter 6 discusses the significance of the frictional heat on the mechanism of wear debris formation by delamination during fretting wear process by showing its effect on subsurface crack initiation and propagation processes. The chapter then discusses the proposed contact-based thermal model used for the temperature prediction.
- Chapter 7 discusses the model validation and some performed sensitivity analyses. The model is employed in the study of the effect of fretting parameters, material properties and surface condition on the surface temperature prediction.
- In chapter 8, the main findings and conclusions of the entire research are summarised as well as recommendations for future work.

Chapter 2 Literature Review

2.1. Introduction

Fretting wear is a hybrid wear mechanism characterized by the localization of frictional heat and the entrapment of wear debris, which leads to surface and debris oxidation, from which originates the historical name “fretting corrosion”. When this process takes place at high temperature, the damage becomes a combined effect of wear and corrosion. The mechanical damage is caused by the abrasive rupture of the oxide films existing on the surface together with the dislodgment of the metallic particles, which further increases wear. The corrosive or chemical part comes from the oxidation of wear debris or metallic surface, which either accelerates the damage or restrains it, depending on the oxide composition and structure.

With the ever increasing demand for power and reliability of aero-engines, the need for increase in the material strength and wear resistance at elevated temperatures becomes crucial. Accordingly, cobalt and nickel-based superalloys are used in aero-engine combustor components for their high strength and wear resistance at elevated temperatures. In order to properly design aero-engines, fretting wear of these superalloys needs to be well investigated.

In the following critical literature review, the sliding and fretting wear of superalloys at high temperature is covered. The fact that the temperature at the interface is the superposition of the bulk (environmental) temperature and the temperature coming from the frictional heat, has led to conduct a survey on the significance of the frictional heat on the microstructure, oxidation kinetics, and wear debris formation. Since the contact temperature cannot be directly measured, the survey also covered the methods used to estimate the contact temperature in sliding wear, as well as, in fretting wear.

2.2. Sliding wear of superalloys at elevated temperatures

Attempts to investigate the tribological behaviour of superalloys in sliding wear have focused on investigating the role of oxide films formed on the surface. The following review aims at collecting the most significant findings in this field with an attempt to focus on cobalt and nickel based superalloys.

Stott et al. [3] did a pioneering work in investigating the sliding wear of nickel alloys (Nimonic 75, Nimonic C263, Nimonic 108 and Incoloy 901) at high temperatures and studied in details the change in the wear scar and friction associated with the development of a compacted oxide layer termed “glaze”. This layer develops a load bearing action, reducing the metal-to-metal contact, and therefore, the wear damage. Once this layer is formed, two competing mechanisms take place; a mechanism of oxide layer fracture and breakdown leading to debris formation and a mechanism of consolidation, compaction, and sintering of oxidized debris to repair the damage and form new oxide layers [4]. Stott also indicated that in the absence of heat as a driving force (either frictional heating or the temperature of the environment), the oxide particles cannot sinter together to form a protective layer. Stott [5] differentiated between the oxidation occurring at high speed unidirectional sliding and the one occurring at low speed reciprocating sliding. At the first mode, the frictional heat is high, but the debris is not retained; therefore, the oxide melts and severe oxidational wear takes place. In the second mode, the frictional heat is relatively low, but debris can be retained, which leads to an increase in wear protection.

Laskowski et al. [6] investigated the friction and wear characteristics of superalloys employed in foil bearing, namely, Inconel X-750 (Ni 70 - Cr 15 - Fe 7), Incoloy 909 (Fe 42 - Ni 38 - Co 13), MA956 (Fe 75 - Cr 20 - Al 4.5), Rene 41 (Ni 55 - Cr 19 - Co 11) and Inconel 713 (Ni 70 - Cr 13 - Al 6). They found that at high temperatures (500°C and 800°C), these alloys form surface oxides, and that the properties of these oxides determine the degree to which they reduce friction and wear. They concluded also that comparable hardness and dissimilar material compositions are required for good tribological performance.

Dellacorte et al. [7] investigated the static and dynamic friction of high temperature airframe seal materials. They found that when Haynes 188 (Co 37 - Ni 22 - Cr 22) was sliding against Pt coated MoRe at 843°C in air, there was a substantial reduction in friction due to the formation of lubricious oxide on the Haynes 188 (Co 37 - Ni 22 - Cr 22) at temperatures above 550°C. Xue and Lu [2] studied the effect of temperature on the friction coefficient of Hastelloy C (N- 57 - Cr 16 Mo 16) pin against a cerium fluoride (CeF₃) disk. They showed that the CeO₂ oxide layer formed at the interface had a detrimental effect between 500°C and 700°C, while above 700°C it had good friction-reducing effect due to the softening and the film-forming properties of the CeO₂. Coskun et al. [8] studied the high temperature friction and wear characteristics of cobalt-nickel superalloys, namely, Haynes 25 (Co 50 - Cr 20.5 - W 15.5 - Ni 10), Haynes 188 (Co 37 - Ni 22 - Cr 22), and Haynes 214 (Ni 75 - Cr 16 - Al 4 - Fe 3) sheets when rubbed against Hastelloy X (Ni 47 - Cr 22 - Fe 18 - Mo 9) pins at room and high temperature for turbomachinery applications. They discovered that protective cobalt oxide layers were formed on the Haynes 25 and Haynes 188 at 540°C, in addition to nickel, chromium and tungsten oxides.

Wood et al. [9] studied the wear of Stellite 6 (Co 60 - Cr 30) collars against a sleeve made of the same material at 600°C. Based on experimental investigation, they suggested that the process of glaze formation and spallation passes through the following stages:

1. Formation of the load bearing glaze layer.
2. Cobalt and chromium diffusion to the glaze.
3. Oxygen diffusion into the glaze resulting in a chromium-rich oxide layer at the base of the glaze-substrate interface.
4. Mechanically Induced Chemical Failure (MICF) takes place at the base of the glaze leading to spallation.
5. Reformation of the load bearing oxide followed by elemental diffusion, suggesting that the above cycle repeats itself.

Inman et al. [10, 11] studied the sliding wear of Nimonic 80A (Ni 70 - Cr 20 - Fe 3 - Co 2) and Incoloy MA956 (Fe 75 - Cr 20 - Al 4.5) against Stellite 6 (Co 60 - Cr 30) and found that the rapid formation of a glaze layer, consisting mainly of cobalt and chromium debris, kept

the wear of the two mating materials at low levels. They argued that the improvement in the oxide layer wear resistance could be attributed to the absence of Hall-Petch (or grain size) softening and to the enhanced fracture toughness of the surface. They also found that the high oxide level generation, when combined with lack of debris residency or retention leads to debris mobility and poor sintering characteristics which can produce loose abrasive wear debris and further increase wear.

2.3. Fretting wear of superalloys at elevated temperatures

When looking at the high temperature fretting wear of superalloys, the available information in the literature is much less compared to that available for unidirectional sliding. Bill [12, 13] concluded that the formation of oxide is not always associated with a decrease in wear, as he proposed different types of fretting behaviour classified according to the oxidation role, a non-protective role, a behaviour of stripping the thin oxide layer at each fretting cycle, a surface fatigue-based behaviour, and finally a protective behaviour in which fretting is inhibited through the development of a continuous oxide film. His investigation showed that for Ni-Cr-Al alloys, the wear at 540°C was about an order of magnitude less than that at room temperature.

Hamdy and Waterhouse [14] found that the glaze formed on the surface of Ti-6Al-4V at 200°C, became well developed at 400°C, and then broke down at 600°C. For Inconel 718, on the other hand, (Ni 54- Fe 18.5 - Cr 16.5), the glaze is formed at 280°C only above an amplitude of 20 µm, while at 540°C it is formed at all amplitudes. This glaze has a wear reducing effect due to the formation of lubricious Ni-oxide.

Miyoshi et al. [15] carried out fretting experiments of Ti-Al alloys against nickel-based superalloys for aero-engine fan and compressor blade-disk contacts at temperatures up to 550°C. They found that the transfer of material was from the Ti-Al alloy to the Ni superalloy, causing scuffing or galling. They also found that the wear loss of the Ti-Al alloy decreased with the increase in the temperature from room temperature to 200°C, then increased above that level up to 550°C. This was attributed to oxide film disruption associated with crack generation, loose wear debris and pitting.

Lavella et al. [16] analyzed the fretting wear of CMSX 4 Ni superalloys (Ni 70 - Co 9 - Cr 7 - Ta 7 - Al 5), with and without T-800 (Co - Cr - Mo) spray coating, at high temperature used in turbomachinery. They found that at 800°C, when the coating was applied, the friction coefficient was reduced compared to the uncoated alloy, but did not change significantly with wear cycles. They also reported that uncoated surface showed a layer of oxides that was formed and broken continuously during the wear process. Balic et al. [17] in their investigation of the tribological behaviour of Rene 41 (Ni 55 - Cr 19 - Co 11) against plasma- and HVOF-sprayed PS304 coated stainless steel foil bearings pointed out the advantages of the Cr-oxides, namely, the resistance to wear at high temperatures and the resistance to further oxidation at 800°C. The latter advantage helped the oxide not to swell and preserved its bearing capabilities.

From the above literature review, it can be seen that there is no data available in the open literature about the fretting wear of the superalloys proposed by PWC. More specifically, there is no information about Cobalt Alloy 1 when fretted against Cobalt Alloy 2 or when any of them is fretted against Nickel Alloy 1 at high temperature. Furthermore, the effect of structure and composition of the oxide, on either accelerating or restraining wear damage, was never addressed.

2.4. Significance of frictional heat during fretting wear

The temperature at the contact interface is the superposition of the bulk (environmental) temperature and the temperature resulting from the frictional heat. It is important to investigate two things; first, the significance of the frictional heat in fretting wear, and second, how to estimate the contact temperature which cannot be directly measured.

In sliding wear, it is well established that frictional-induced heat has a significant and decisive effect on the oxidation process, mechanical and physical properties, material microstructure and subsurface deformation. The existence of transition temperature(s) at which the wear rate changes significantly for numerous alloys makes the identification of contact temperature an essential tool in the understanding of wear [18]. However,

contradicting conclusions have been made regarding the effect of frictional-induced heat during fretting.

On one side, some researches assume that during low-speed sliding (e.g. fretting), the thermal effects are not significant. Support for this opinion comes from the work done by Sproles and Duquette [19] who found that, during the fretting of 4130 carbon steel, the maximum temperature rise at the interface did not exceed 18°K. Weick et al. [20], in an attempt to measure the contact temperature at low sliding velocities in the fretting of ceramic materials, reported a low temperature increase explained by the relatively low rate of frictional heat generation. The previous observations could be true for some loading conditions and some materials; however, experimental observations show, with clear evidences, that frictional heat during fretting wear is significant.

2.5. Effect of the frictional heat on microstructure during fretting wear

Microstructural examination shows with no doubt that contact temperature rise coming from the frictional-induced heat during fretting can attain high values for some conditions. The use of metallographic technique to estimate the temperature has been reported by many authors. Dobromirski [21] demonstrated that the presence of martensitic caverns during the fretting fatigue of 1040 steel was evidence that the local temperature could reach at least 850°C on the fretted surface. The X-ray diffraction pattern of the fretting fatigue of drawn mild steel showed that the temperature had a considerable effect promoting surface oxidation [22]. Podgornik et al. [23] discovered a large difference in microstructure between adjacent layers during the fretting wear of steels, which was evidence of a great temperature gradient. The absence of secondary carbide particles from the austenite matrix indicated that the temperature rose above 1000°C. Their results showed also that white layers started to form under the contact spots, and then, coalesced to form a single larger area due to high local flash temperature. Kalin et al. [24] investigated the fretting wear of silicon nitride against bearing steel. At lubricated conditions, they discovered the formation of a low-viscosity protective layer due to the high contact temperatures. In the unlubricated condition, the absence of Si_3N_4 from the surface layer

unveiled by TEM analysis confirmed the intensive oxidative tribochemical reaction in this layer.

2.6. Effect of contact temperature on oxidation kinetics

From another angle, the contact temperature directly affects the oxide formation kinetics, which can be experimentally observed. It is well established in literature that the oxide film growth on metals and alloys follows one of the following rate laws [25]:

1. Logarithmic rate law: usually applies at low temperature for thin films, where the oxidation rate is controlled by transfer of electrons from metal to reaction product film when the film is charged throughout its volume, which can be described by the following equation:

$$d\delta/dt = k_{log}/t \text{ or } \delta = k_{log} \ln\left(\frac{t}{const} + 1\right) \quad (2-1)$$

where δ is the oxide thickness, k_{log} is the logarithmic oxidation constant and t is the time.

2. Parabolic and cubic rate laws: in these mechanisms, ionic dissolution and diffusion of ions through the scale is controlling the process. For a parabolic law, the oxidation rate is inversely proportional to the thickness of the oxide film, which can be described by the following equation:

$$d\delta/dt = k_{parab}/\delta \text{ or } \delta^2 = 2k_{parab}t + const \quad (2-2)$$

Oxide film growth is proportional to the exposure time to the 1/2 power (for the parabolic) and 1/3 power (for the cubic). This equation applies to protective scales in the oxidation of many metals at elevated temperatures like copper, nickel, iron, chromium and cobalt.

3. Linear rate law: this oxidation law takes place at higher temperatures when the environment reaches the oxide-metal interface through cracks and pores resulting in defect coalescence at the interface and oxide film debonding. Here, the reaction rate is constant, as shown in equation (2-3):

$$d\delta/dt = k_{lin} \text{ or } \delta = k_{lin}t + \text{const} \quad (2-3)$$

The temperature dependence of oxidation reaction rates is governed by the Arrhenius equation which has the exponential following form:

$$k_{oxidation} = A_{Arrhenius} e^{\frac{-E_a}{RT}} \quad (2-4)$$

where $k_{oxidation}$ is the oxidation rate constant, $A_{Arrhenius}$ is the pre-exponential factor, E_a is the activation energy for the oxidation process, R is the universal gas constant and T is the absolute temperature. For most metals and alloys, the oxidation rate is slow at low temperature and high at high temperature. Therefore, the knowledge of the contact temperature is imperative in the determination of the proper oxidation growth law.

For example, carbon steel has negligible oxidation in air up to 250-300°C, after which it obeys a slow logarithmic rate until 450°C, and then a faster linear rate at around 600°C and above [26]. Copper undergoes a change in the oxidation mechanism from a logarithmic rate at about 100°C to a parabolic rate above 200°C. Ti alloys undergo a transition from slow logarithmic oxidation to a faster parabolic oxidation at 540°C [12, 27].

For nickel-based and cobalt-based superalloys, which are the points of investigation in this study, the chemical nature of the oxide films vary with temperature and chromium content. Normally chromium oxide (Cr_2O_3), nickel oxide (NiO) and cobalt oxide (CoO) are the main stable oxides found in the scale.

Extensive information was reported by Lund and Wagner [28] on the effect of temperature on the oxidation of cobalt-based and nickel-based superalloys. For example, in Ni-based alloys, typically 80Ni-20Cr, it has been reported that NiO is the oxide that forms initially at around 400°C, while at temperatures between 500°C and 700°C, Cr_2O_3 was observed to be formed. At around 900-950°C, complex double oxides, called spinels, like NiO- Cr_2O_3 and NiO- Cr_2O_4 , are formed. In these cases, the Cr_2O_3 is closer to the oxide-substrate interface, whereas the spinels are closer the surface. In addition, spinels start to decompose at temperatures between 1110°C and 1200°C, allowing the CrO to vaporize from the surface, increasing the diffusion of the chromium through the oxide and resulting in more oxidation. In the presence of aluminum as an alloying element in these superalloys, the

metastability of $\gamma\text{-Al}_2\text{O}_3$ causes ineffectiveness in preventing the oxidation. This permits the Ni, Co, and Fe to become oxidized, forming NiO , Co_3O_4 , and Fe_3O_4 . Between 900°C and 1100°C , $\gamma\text{-Al}_2\text{O}_3$ transforms to $\alpha\text{-Al}_2\text{O}_3$, which hinders iron oxidation [29].

The evolution of oxidation kinetics has also been reported by many authors. Wlodek [30] reported that the oxidation kinetics of René 41 and Udimet 700 change from linear to parabolic rates as the temperature increases from 850°C to 1100°C . The same author reported that the oxidation of Hastelloy X at a temperature of 850°C remained linear for 2000 minutes and before transforming to parabolic. At 1000°C , the same behaviour was repeated, but the linear oxidation persisted for only 200 minutes. At a range of $1100\text{--}1200^\circ\text{C}$, the oxidation was fully parabolic over the time period.

For the oxidation of cobalt alloys like Haynes 25, at the range of $850\text{--}950^\circ\text{C}$, the alloy showed a change from an erratic behaviour to parabolic oxidation after 1000 minutes, whereas at higher temperatures this erratic behaviour persisted for only 10 to 100 minutes before quickly stabilizing to a parabolic oxidation rate law. On the oxide composition side, the oxides found in the range of $850\text{--}1200^\circ\text{C}$ were mainly spinel of the form CoCr_2O_4 , and during the parabolic oxidation, the Cr_2O_3 and the CoO were found. When the temperature rose to 1200°C , a catastrophic attack took place associated with the formation of low-melting scale of CoW_4 , Co_3O_4 , CoO , and CoCr_2O_4 . It is worth mentioning that a similar oxidation behaviour was also reported for the X40 alloy [28].

2.7. Effect of frictional heat on wear debris formation

In the early seventies, Suh [31, 32] introduced the delamination theory of wear as an explanation of the low wear rate in reciprocating, fretting and fatigue wear. The theory postulates that during repetitive sliding, sub-surface void or micro-crack nucleation takes place around a hard inclusion or a second phase particle in the plastically deformed zone only below a certain depth from the surface (owing to the large hydrostatic pressure near the asperity contact) and only above some other depth (owing to the decrease in stress and plastic deformation when moving away from the contact). The initiated crack propagates

parallel to the surface until a certain critical length at which it changes direction towards the surface, forming plate like wear debris.

The experimental findings of Waterhouse [33] concluded that, after the early fretting stages, removal of material occurs by delamination. Therefore, undertaking analyses based on the delamination theory of wear to model the fretting wear process has proven to be efficient [34]. It has been established that the emergence of frictional heat into the picture changes the mechanism of subsurface crack initiation and propagation needed for delamination wear; however, no studies in the available literature addressed the thermomechanical effects of the theory from a comprehensive point of view.

From the crack initiation point of view, Gong et al. [35] showed that frictional heat caused an increase in thermoelastic distortion, development of thermal stresses, increase of plastic deformation and reduction in the likelihood of surface cracking. Sofuoglu and Ozer [36] showed that, for a fractal surface, frictional heating increased the contact area and brought more asperities into contact, which decreased the load carried by each asperity. This reduced the intensity of surface and subsurface stress distributions preventing the propensity of the cracks. Attia [37] showed that thermal stresses during fretting could be as high as the isothermal stresses produced by mechanical loading, leading to residual stresses in the contact region which affect the fatigue behaviour of the material. Kulkarni et al. [38] developed a transient thermomechanical model to analyse the two-dimensional frictional rolling-sliding contact by including a translating heat source on an elastoplastic half-space. He concluded that the effect of the contact mechanical load depends on the solution of the thermal problem. He observed the development of residual stresses as a result of the compressive thermal stresses due to the steep temperature gradient followed by the non-uniform thermal contraction due to cooling. He also concluded that the residual tension and the alternating or transient tension coming from the translation of thermo-mechanical loads, suggest a possible mechanism for thermal cracking.

From the crack propagation point of view, there is less available work on the effect of frictional heat. Cho et al. [39] showed that the frictional heat during sliding wear increased the rate of subsurface crack growth and reduced the critical crack length at the onset of

kinking. They also showed that the frictional heat during sliding wear increased the maximum shear stress intensity factor (SIF), and therefore, increased the in-plane crack growth rate at both tips. Wang et al. [40] constructed a finite element model to study the mutual interaction of two oblique cracks at the wheel-rail contact under the effect of frictional load. Their results showed that the shearing mode crack growth for the thermomechanical case was more likely to occur and that the maximum crack tip opening displacement (CTOD) increased when increasing the wheel rail friction coefficient and the crack angle. In addition, they found that the decrease in the coefficient of friction at the wheel-rail contact delayed the rail surface crack growth.

In order to understand the effect of the frictional heat on wear by delamination, it is important to explore the different criteria for crack initiation and crack propagation suitable to model the fretting wear by delamination.

2.7.1. Criteria for crack initiation

Crack initiation can be predicted using a number of criteria like the local elastic strain energy density criterion [41] and the local stress criterion [32, 42]. In the local elastic strain energy density criterion, Gurland and Plateau [41] proposed that void nucleates from elastic spherical inclusions in an elastic matrix if the locally concentrated elastic energy in the inclusion, released upon void formation, becomes equal or greater than the work of adhesion of the particle-matrix interface.

In the local stress criterion, a void can form at some point around the particle-matrix interface when the tensile stress at that point exceeds the cohesive strength of the interface. The latter is defined as the bonding force between the inclusion and the surrounding matrix per unit area of contact, which is the shear yield strength of the matrix material. Mathematically, this criterion can be expressed as:

$$\sigma_{rr} = \sqrt{3}\tau_r + \sqrt{3}\tau_{max} + \sigma_h \geq 2k_s \quad (2-5)$$

where σ_{rr} is the radial tensile stress, τ_r is the residual shear stress, τ_{max} is the maximum applied shear stress, σ_h is the hydrostatic stress, and k_s is the material shear yield strength. Tanaka et al. [43] and Argon et al. [44] found that inclusions with diameters $> 0.025 \mu\text{m}$

require that the tensile radial stresses criterion be met beside the critical local elastic energy criterion.

Salehizadeh and Saka [45] studied the mechanics of crack initiation at hard particles in rolling line contacts using the local elastic strain energy density criterion and the local stress criterion. They concluded that the elastic stress fields around hard particles are compressive and that void nucleation cannot occur when deformation is purely elastic. In addition, he concluded that tensile residual stresses, which are set around the inclusion at sufficiently large applied Hertz pressure, lead to debonding and void formation during unloading.

Zhang et al. [46] used the average maximum shear plastic strain amplitude and the Fatemi-Socie (FS) parameter to model the subsurface fatigue crack nucleation at primary inclusions in carburized and shot-peened martensitic steel. They concluded that the residual stress state is less influenced by the subsurface inclusion shape as compared to the high influence inclusion arrangement and inclusion-matrix interface conditions (e.g. pre-existing cracks).

Rice and Tracey [47] developed a relationship to evaluate the subsurface void growth rate. They considered an elastically rigid and incompressible plastic material (either perfectly plastic, or strain hardening) and applied a Rayleigh–Ritz procedure to the enlargement of an isolated spherical void subjected to a triaxial stress and strain rate fields. They considered the growth rate of a void during shear to be depending on the ratio of hydrostatic stress to the flow stress, the radius of the void and the strain rate. They used that maximum growth rate to define the position of subsurface crack initiation.

2.7.2. Criteria for crack propagation

Techniques for modeling crack growth can be grouped into techniques where the crack driving forces are required to predict the crack propagation rate and direction and techniques where the crack driving forces are not required to predict the crack propagation rate and direction. Examples of the first type are the stress intensity factors (SIF), crack tip opening displacements (CTOD), crack tip sliding displacements (CTSD),

crack tip opening angles (CTOA), energy release rates, and elastic and elastoplastic crack front integrals.

In the second type of technique, the crack driving forces are not required to predict crack propagation rate and direction. The later family of techniques can be grouped into two broad categories, geometrical representation techniques and non-geometrical representation techniques. In the geometrical representation technique, the crack is a geometric entity; the geometry and the discretization model are updated with the crack growth. Examples of this technique are the prescribed methods, analytical geometry methods, known solution methods, mesh free methods and adaptive FEM/BEM methods. In the non-geometrical representation techniques, geometry does not contain the crack, and neither it nor the discretization model, if needed, changes during crack growth. The crack is rather represented either in the material constitutive model or in a kinematic model as an intense localization of strain. Examples of this technique are the element extinction method, the extended finite element method (XFEM) and the general finite element method (GFEM) [48].

Since the methods involving the computation of the crack driving forces are those widely used in the modeling of subsurface cracks in wear, the review is focused on them. Linear elastic fracture mechanics LEFM analysis of crack propagation are usually based on relating the propagation rate to the stress intensity factors (SIF) at the crack tip. In their pioneering work on crack initiation and propagation in sliding contacts, Jahanmir and Suh [32] used LEFM to calculate mode I and mode II stress intensity factors for a long subsurface crack subjected to normal and tangential surface tractions. The same technique was employed by Komvopoulos et al. [49] to analyze the subsurface crack propagation in a half-space due to a moving asperity contact, and also, by Ye and Komvopoulos [50] in studying the subsurface crack mechanisms under indentation load. The application of LEFM is challenged by a number of obstacles, e.g., locating the exact point where the crack goes from compression to tension, and not accounting for residual stresses. Generally, when the extent of plastic zone around of the crack tip becomes compared in size to the crack length,

the use of LEFM becomes tenuous. The LEFM has given unrealistic predictions of the radius of the asperity contact area and the depth of crack nucleation zone [34].

The use of the J-integral method suits both linear elastic fracture mechanics LEFM and elastic plastic fracture mechanics EPFM. However, due to the fact that the J-integral method is built on the deformation theory of plasticity, which is suitable for loading trajectories only, the method cannot be employed in the modeling of fretting wear because of its cyclic nature [51].

Sin and Suh [52] used the crack tip sliding displacement (CTSD), which is the difference between the displacement of the upper and lower crack surfaces, to study the subsurface crack propagation due to surface traction on sliding wear. They showed that crack propagation in delamination wear cannot be explained by the LEFM because of the large plastic zone at the crack tip. Salehizadeh and Saka [45] studied the crack propagation in rolling line contacts. They concluded that for the cases of short cracks on heavily loaded bearings, the CTSD is more suitable than the LEFM.

Gessesse et al. [34] successfully employed the CTSD in the prediction of crack propagation in elastoplastic materials during impact fretting wear. They concluded that the coefficient of friction at the crack surfaces is more significant for the determination of the crack propagation rate than the coefficient of friction at the asperity-substrate contact interface.

The crack propagation direction can be determined according to a number of criteria. The maximum stress intensity factor did not agree with the experimental results in wear, possibly due to the presence of compressive stresses in the neighbourhood of the crack. Under such conditions, the crack propagates along the direction of the maximum average shear stress in such a way that the average tensile stress perpendicular to that direction becomes minimum [34].

In the maximum principal stress criterion, the crack is assumed to take the direction normal to the direction of the principal stress [45]. However, this criterion is restricted to the case where the crack is subjected to compressive and shear loading only.

Gessese [34] concluded that a mode I crack propagates in the direction of the maximum effective stress when a high level of tensile stress exists under mixed loading conditions [53].

2.8. Contact temperature prediction

Numerous attempts in the open literature have been made to predict the contact temperature. These models use simplified assumptions that do not generally reflect the physics of the real application. The prediction of the contact temperature at rough surfaces encompasses two main components; mechanical (contact) and thermal. In the mechanical part, it is required to define the real area of contact (contact size and pattern) which represents the key element in the estimation of contact temperature. In the thermal part, the thermal resistance or contact temperature are required to be estimated based on the thermal load applied at the contact area.

Modeling the contact, or specifically the prediction of contact area may be achieved by several techniques that can be grouped into four main categories [54]: statistical [55], fractal [56], deterministic [57] and multiscale models [58]. Statistical models based on the well-known Greenwood and Willamson model [55] have been the subject of criticism since they showed dependency on surface profilometry resolution; however, they are still widely used. The extensive work done by Hisakado [59-62] in determining the number of micro-contacts, the average radius of micro-contacts and the distribution of the radii of micro-contacts, in addition to the detailed work done by Tsukada and Anno [63-64] to determine the mean interval between the contact points and the distribution of the distance between the contact asperities, represent an important base of many statistical contact models used in the prediction of thermal and electrical contact resistance. However, these contact models are based on the assumptions that the asperity heights follow a normal distribution curve and that asperities have a conical or pyramidal shape whose slope depends on the surface roughness.

Fractal methods [56], which assume that the surface has patterns repeated on each scale of roughness, have been also employed to model the contact of rough surfaces in static and

sliding wear. However, the surface self-affinity concept, on which fractal analysis is based, is questionable. Deterministic methods [57], which are based on conveying surface details for contact, require proper mesh density to ensure the reliability of solution but are computationally demanding. Recently, multiscale models were developed to relax the self-affinity assumption in the fractal analyses and to improve the mechanics of contact [54, 58]. The following review should cover the notable work done for contact temperature prediction with emphasis on fretting wear.

2.8.1. Contact temperature prediction during sliding wear

Early trials in this field started with the pioneering work of Blok [66] who introduced the concept of flash temperature for gear teeth applications. This opened the door to Jaeger [67] who developed an exhaustive analytical model to predict the contact temperature resulting from a moving heat source. Holm [68] used Jaeger's results to develop an analytical model of a circular heat source heating a semi-infinite body at a constant rate for both stationary and sliding contacts. Archard [69] developed a much simpler analytical model based on a single protuberance sliding against a surface plane. Ashby et al. [70] considered asperity contacts to be circular and clustered together in regions called junctions. They presented their results in the form of surface-temperature maps showing how the bulk and flash temperatures change with both sliding velocity and contact pressure for different contact pairs.

2.8.2. Contact temperature prediction during fretting wear

The calculation of the contact temperature during fretting wear went through different physical, mathematical and geometrical assumptions. Greenwood and Greiner [74] developed a simple model for circular contact during the study of diesel lubricants. They divided the heat input into a steady and a periodic component using Fourier analysis, and applied it to a square heat source and to a Hertzian contact. They found that at low amplitude, the temperature quickly reaches the steady state situation at which there is a periodic variation about a value equal to the mean heat input rate coming from steady state

heating. In addition, they found that for low frequencies, the maximum temperature rise is equal to that of the unidirectional sliding at the maximum speed of the fretting contact.

Tian and Kennedy [75] considered a concentrated heat source reciprocating on the surface of a semi-infinite medium and predicted the maximum contact temperature. They found that during oscillatory sliding the repetitive sliding movement of the heat source induced an additional surface temperature rise compared to unidirectional sliding. Pezdirnik et al. [76] developed a simple mathematical model and considered the contact spot to be circular, but producing an oblong sliding surface on the counterpart due to oscillation. They discussed the parameters and conditions affecting the temperature rise at a micro-contact interface, namely, the asperity slope, the amplitude of slip and the thermal conductivities.

In order to generalize the solution over the whole contact by considering the contribution from the different asperity contacts, Attia and Yovanovich [71] predicted the rise in the contact temperature in fretting considering the thermal constriction phenomenon following the method of infinite images developed by Beck [72] for static contacts. They proposed that the frictional induced heat developed at a micro-contact asperity point is the superposition of the heat generated at that asperity contact (named the starting heat source), the contribution from the neighbouring asperity contacts (named the image heat source in the near region), and the contribution of all other asperity contacts in the contour area, outside the near region (named the far region). Attia and Dsilva [73] investigated the effect of the mode of motion and process parameters, material properties, work hardening, oxide film and surface roughness on the temperature prediction during fretting wear. Fridrici et al. [65] developed a finite element model to study the effect of the spatial random distribution of the contact asperities on the thermal constriction parameter, and consequently, on the temperature rise during fretting.

Wen and Khonsary [77] developed an analytical approach to predict the temperature rise in fretting contacts. In their model, they considered a transient thermal analysis of a heat source having different shapes (circular, rectangular and elliptical). They concluded that the temperature distribution was affected by the distribution of the heat source, but not by its shape. They also concluded that the number of cycles to reach steady-state was affected

more by the frequency rather than the amplitude, and that at high frequency values, the oscillation of the temperature becomes unimportant.

The aforementioned models used for contact temperature prediction in both unidirectional sliding and in fretting wear, either used a single asperity contact model to treat the problem on a fundamental scale or a multiple asperity contact model using statistical surface information (probability distributions) or fractals to estimate the size and shape of the real contact area. This means that they ignored the surface details to simplify the geometrical modeling in order to make use of the available computational means, which justifies the dominance of the approach based on uniformly distributed equal-sized micro-contact areas. In addition to the previous geometrical assumptions, these models were mostly analytical and could not flexibly address the issues of surface oxides, multi-layered coatings, and properties of the material existing at the interface. With the improvement of computational capability, deterministic techniques came into the picture. With proper scanning and mesh sizing, it became possible to model rough surfaces for contact and thermal calculations.

Thompson et al. [57, 78] incorporated the real surface topography in a finite element analysis to predict the thermal contact resistance (TCR), and hence, the contact temperature. Liu et al. [79] imported surface topography measured by an atomic force microscope (AFM) to the finite element analysis and generated the contact using a 3D mesh. They investigated the effect of surface roughness on the force-displacement, force-contact area and force-electrical contact resistance (ECR) relationships in ohmic microswitches. They found that the number of contacts becomes constant at a certain load limit and that the harder material makes a smaller number of spots with smaller radii. The same authors [80] developed a multi-physics FE model to investigate the mechanical, thermal and electrical behaviour of electric contact in micro-switches. Due to the nature of their static contact, they found that the temperature distribution is almost uniform at the contact interface. They also found that the maximum temperature is at the asperities that experienced the highest deformation.

The above mentioned deterministic models were limited to static contacts. For dynamic contacts, e.g., fretting, the thermomechanical loading time variation plays a role in the temperature prediction. In addition, none of these models addressed the issue of surface topography evolution on thermal predictions, which means they used typically manufactured surfaces in their analyses. It is believed that with the improvement of computational capabilities, incorporating the real surface details in the contact and thermal simulation, along with available experimental information, provide a reasonable solution.

2.9. Conclusions from the literature review

1. The literature review shows that there is no data available in the open literature about fretting wear behaviour of the superalloys proposed by PWC. More specifically, Cobalt Alloy 1 and Cobalt Alloy 2 when fretted against each other or against the Nickel Alloy 1 at high temperature.
2. In the available literature on the wear of superalloys, the role played by the oxide composition and structure in accelerating or restraining damage was not thoroughly investigated.
3. Many authors pointed out the importance of the frictional heat, its effect on the oxide layer formation, and consequently, the wear process; however, no quantitative studies have been reported to link the friction-induced heat in fretting to the evolution of oxide film thickness, composition and oxidation kinetics.
4. Although there were attempts to address the effect of frictional heat on the crack initiation and propagation processes, each separately, no available three-dimensional models could combine both and handle the delamination theory of wear from a comprehensive thermomechanical point of view.
5. Most of the available single-asperity contact models employed in the analysis of crack initiation/propagation ignore the effect of neighbouring asperities to simplify calculations. In reality, the elastic behaviour of the global structure, encompassing the neighbouring asperities, needs to be considered in order to link the deformation of adjacent asperities.

6. Most of the available models used in the prediction of contact temperature, either during sliding wear or during fretting, ignored surface details to simplify the geometrical modeling. There is an obvious lack of reliable models used for the prediction of contact temperature during fretting which can bring the real surface topography to the prediction of the contact temperature, while also being capable of flexibly handling the existence of oxides and multi-layers at the interface.
7. There are no thermal models that can incorporate the effect of the estimated contact temperature on oxidation kinetics, and therefore, on oxide thickness and properties. This could help in understanding the role of oxide for preventing or accelerating damage.

Chapter 3 Experimental Setup

3.1. Introduction

In order to simulate the tribological characteristics of areal system and to respect a number of similarity laws, typical engine operating conditions need to be duplicated as close as possible. The experimental setup used in this study was designed to meet difficult requirements before being employed for testing, among which are the following.

Rigidity requirements:

The setup must be rigid enough in order to control the small relative displacement of fretting wear between the moving part and the stationary part. A lack of rigidity leads to erroneous relative displacements.

Geometrical requirements:

The setup must be geometrically perfected to ensure the reliability of measurements. The position of the samples and their contact must be aligned with the axis of motion of the driving engine. The location of measurement sensors must be adjusted in such a way that the frictional and normal force are measured along their axes of action, without including any unwanted moments that affect the readings of the forces.

Dynamic requirements:

The setup must be dynamically tested in order to make sure that the operating conditions are not coinciding with any of its natural frequencies.

Thermal and thermo-mechanical requirements:

In order to reach the desired operating bulk temperature, the setup must provide adequate heating to the test samples without transferring excessive heat to the setup or the measuring instrumentation. Excessive heat supplied to the setup leads to unnecessary thermal deformations, whereas excessive heat supplied to the instrumentation leads to erroneous measurements or in the worst case, damage of the measurement sensors.

A previously existing room temperature setup designed by Attia [81] was modified to accommodate high temperature experiments. Both setup and modifications meet the abovementioned requirements. They are detailed in this chapter.

3.2. Setup components and acquisition system

In the setup shown in Figure 3-1 and Figure 3-2, the oscillatory motion is generated by an electromagnetic shaker (Brüel & Kjaer model 1050), which incorporates a feedback control system. The latter is used to keep the oscillation amplitude and the frequency constant during the test. The design ensures the measurement of the frictional force in a direction that is co-planer with the fretting interface to eliminate the inclusion of any undesired bending moments. This plane is defined by the frictional force horizontal axis shown in red in Figure 3-1. The dynamic friction force F_t is monitored with time (fretting cycles) using a piezoelectric force transducer (Brüel & Kjaer, model 8200). Although a dead weight was used to apply the normal force F_n , a piezoelectric force transducer (Brüel & Kjaer, model 8200) was utilized to monitor the cyclic time variation.

Measurement of the relative displacement between contacting specimens was done using two independent methods. In the first method, the displacement was measured through a proximity sensor (Bently, model 3300) attached to the upper stationary specimen to monitor the linear movement of a target attached to the lower moving specimen. This method provided a direct measurement of the amplitude and frequency of the relative oscillatory movement between the two specimens. A static calibration of the contactless proximity probe against its target was carried out against a standard micrometer with an increment of 5 μm over a range of 100 μm , as shown in Figure 3-3 (a). The second method of measurement is the reading coming from a piezoelectric accelerometer (Brüel & Kjaer, model 4381) mounted on the lower fixture to measure its absolute displacement. Through a signal-conditioning unit (Brüel & Kjaer, model 2635), the acceleration signal was double integrated to determine the amplitude and frequency of the absolute oscillatory movement of the moving specimen. For each test, measurements of a 0.05 second-period were taken each 90 seconds with an acquisition rate of 6 KHz.

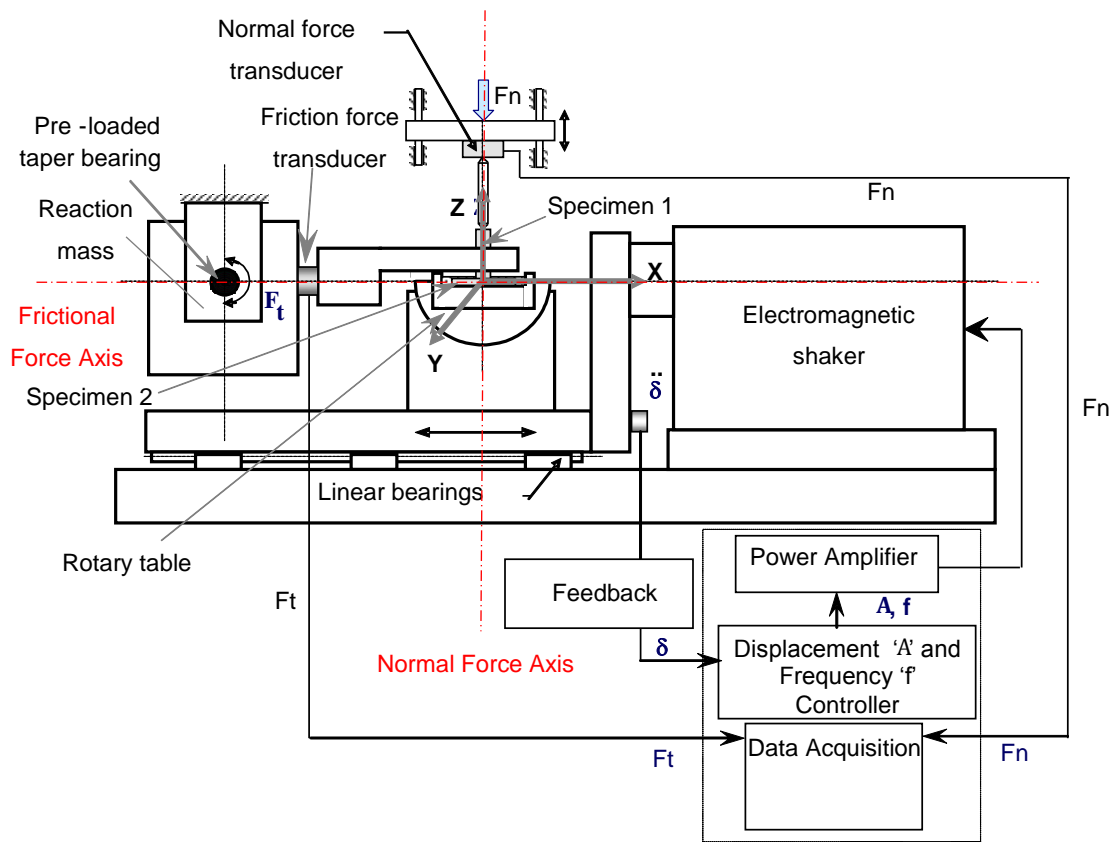


Figure 3-1: Schematic of the experimental setup showing its main components.

A comparison between the two methods of displacement measurement showed excellent agreement, and confirmed the rigidity of the stationary upper specimen holder and its pre-loaded linear bearing. The deviation between the two methods of measurement was estimated to be $<1 \mu\text{m}$ over a full range of $\pm 10 \mu\text{m}$, as shown in Figure 3-3 (b).

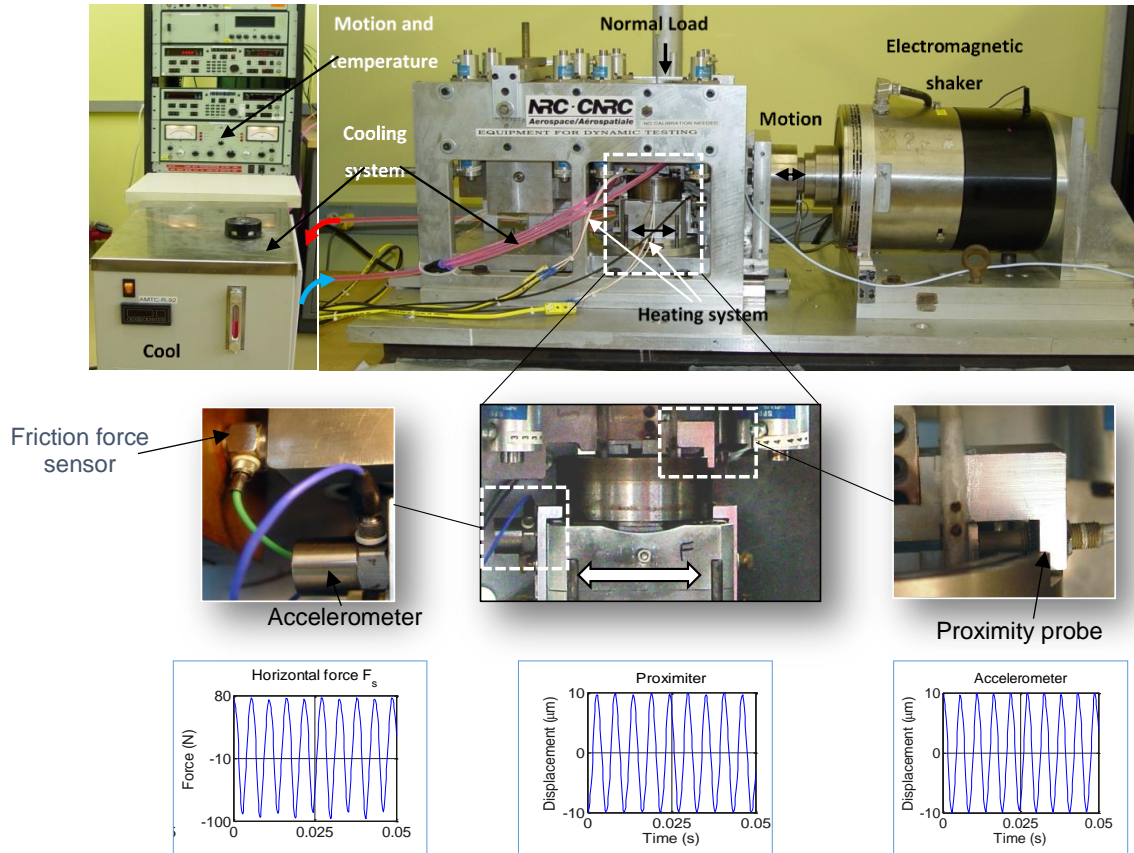


Figure 3-2: Image of the experimental setup for high temperature fretting wear, showing the displacement and force sensors, and their typical measurements for the friction force, the displacement measured by the proximity probe and the accelerometer.

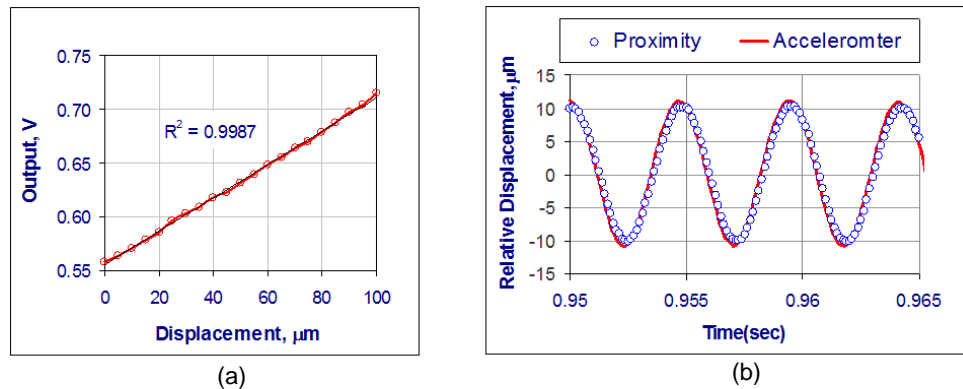


Figure 3-3: (a) Static calibration of the proximity probe and (b) relative displacement read by the proximity probe compared to the absolute displacement read by the accelerometer. The close agreement confirms the setup rigidity.

3.3. Setup dynamics

The setup dynamic behaviour was tested in order to ensure that the operation frequency did not coincide with any of the natural frequencies of the system. The dynamics of the friction force assembly, which connects the stationary specimen to the reaction mass (Figure 3-1), was examined by impact excitation. Using a standard hanging mass and standard accelerometer, the impact hammer (Brüel & Kjær model 8202) was first calibrated. Then, the friction force sensor was calibrated using a hanging dead weight that was suddenly released by burning the hanging thread.

Figure 3-4 (a) shows that the traces of the force signals from the impact hammer and the friction force transducer are nearly identical. Through Fast Fourier Transform (FFT) analysis, the response force spectrum indicated that the natural frequencies of the assembly did not introduce undesired disturbances in the frequency range $0 < f < 250$ Hz, as shown in Figure 3-4 (b).

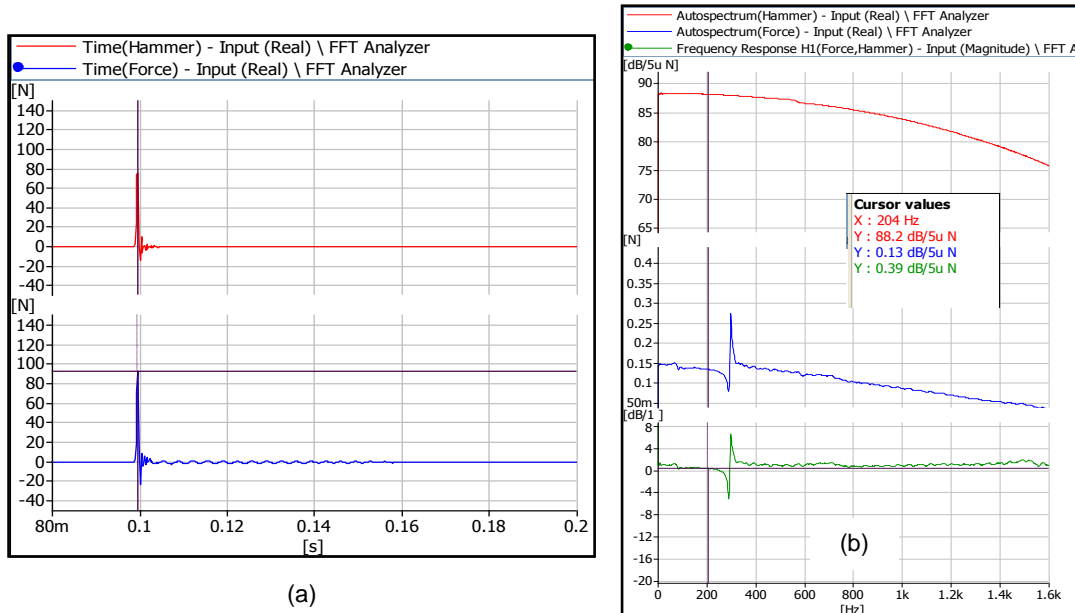


Figure 3-4: Dynamic calibration of friction force transducer (a) and FFT analysis and response force spectrum of the frictional force assembly (b) showing the absence of undesired disturbances between 0 and 250 Hz.

3.4. Setup modifications for high temperature experiments

The setup shown in Figure 3-2 was modified to allow high temperature experiments up to 600°C. The adopted design approach is based on local heating of the specimens, with optimal thermal insulation and local cooling at some critical points, as shown in Figure 3-5.

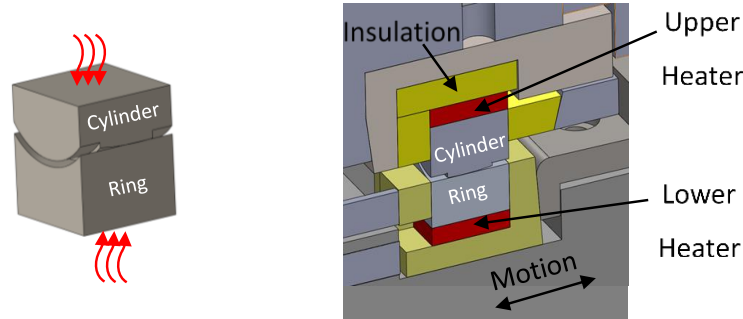


Figure 3-5: Concept of local heating of the samples (left) and cross sectional view of the assembly (right).

Local heating was achieved by using high density Ultramic 600 (1000 W/in²) ceramic heaters to heat both samples by conduction as shown in Figure 3-6 (a). Machinable ceramic with low thermal conductivity (1.5 W/m.K) was used for thermal insulation to ensure efficient heating of the samples and to prevent the heat from dissipating to the setup, and consequently, causing unnecessary thermal deformation. The rigidity of the ceramic insulation was employed to hold the samples firmly without enabling any play, as shown in Figure 3-6 (b) and (c). A cooling system (Turmoil model OC-50 R) was used to cool some critical areas of the test rig in order to protect the displacement probe, the accelerometers and the force sensors as shown in Figure 3-6 (d).

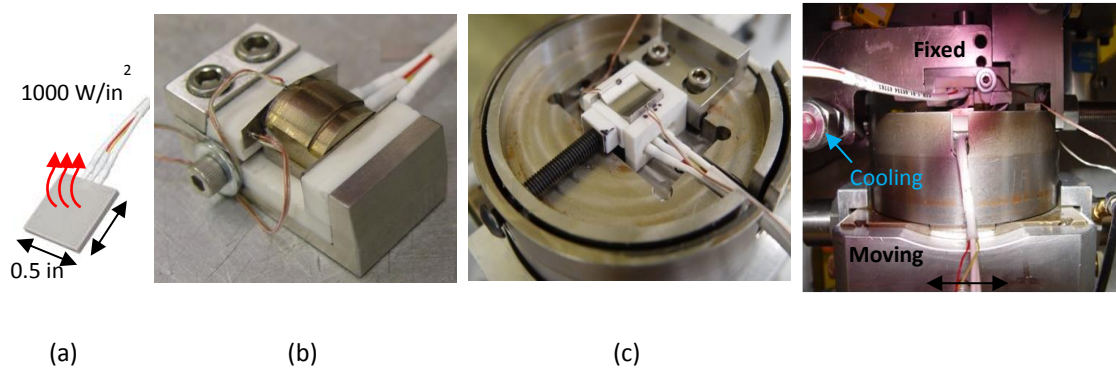


Figure 3-6: Setup high temperature components (a) high density heaters (1000 W/in^2), (b) upper cylinder assembly, (b) lower ring assembly and (d) assembly showing the heaters and the cooling system at the critical points.

3.5. Finite element thermal design for the experimental setup

In order to design the setup modifications for high temperature experimentation, a detailed finite element thermal analysis was conducted for the whole setup assembly. This model served the following purposes:

- Define the required heaters input wattage.
- Define the thermal insulation material and size.
- Determine the optimal cooling points.
- Correlate the interface contact temperature, which cannot be measured directly, to the heaters input.
- Optimize the setup design through multiple iterations.

Figure 3-7 shows the full model of the fretting wear setup, where the dimensions of the different setup components were carefully conveyed to the CAD model. Figure 3-8 shows the temperature field when the heaters are set to their maximum operating temperature (600°C). It also shows the locations at which the cooling fluid flows inside the setup.

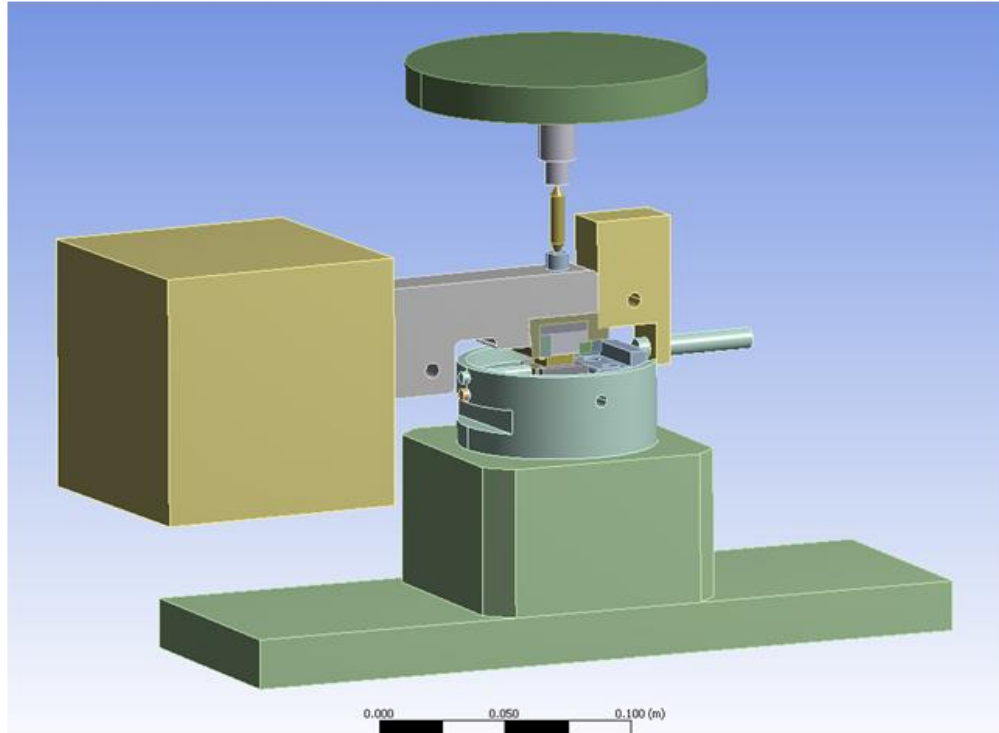


Figure 3-7: 3-D model of the fretting wear setup.

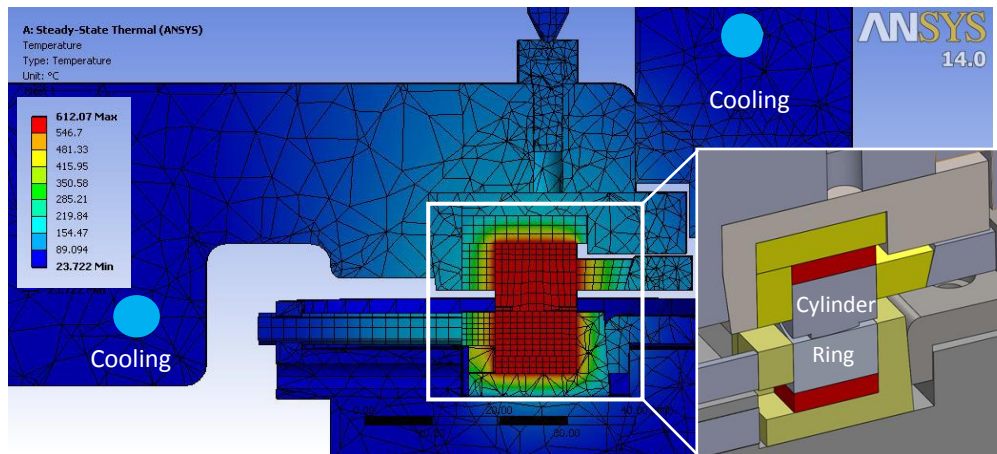


Figure 3-8: FE thermal model for the setup (Temperature in °C).

3.6. Interface temperature prediction and model validation

The FE model was used to correlate the heaters input to the fretting interface contact temperature, which cannot be measured directly. Therefore, a total number of 12 points were initially suggested as candidate locations for thermocouples. Figure 3-9 shows the cross section of the setup thermal model, where the suggested locations are shown as white dots. When the interface temperature was plotted against the temperatures of the suggested points, it was found that some locations were more sensitive to the interface temperature variation. These points were given propriety when selecting the thermocouple welding locations.

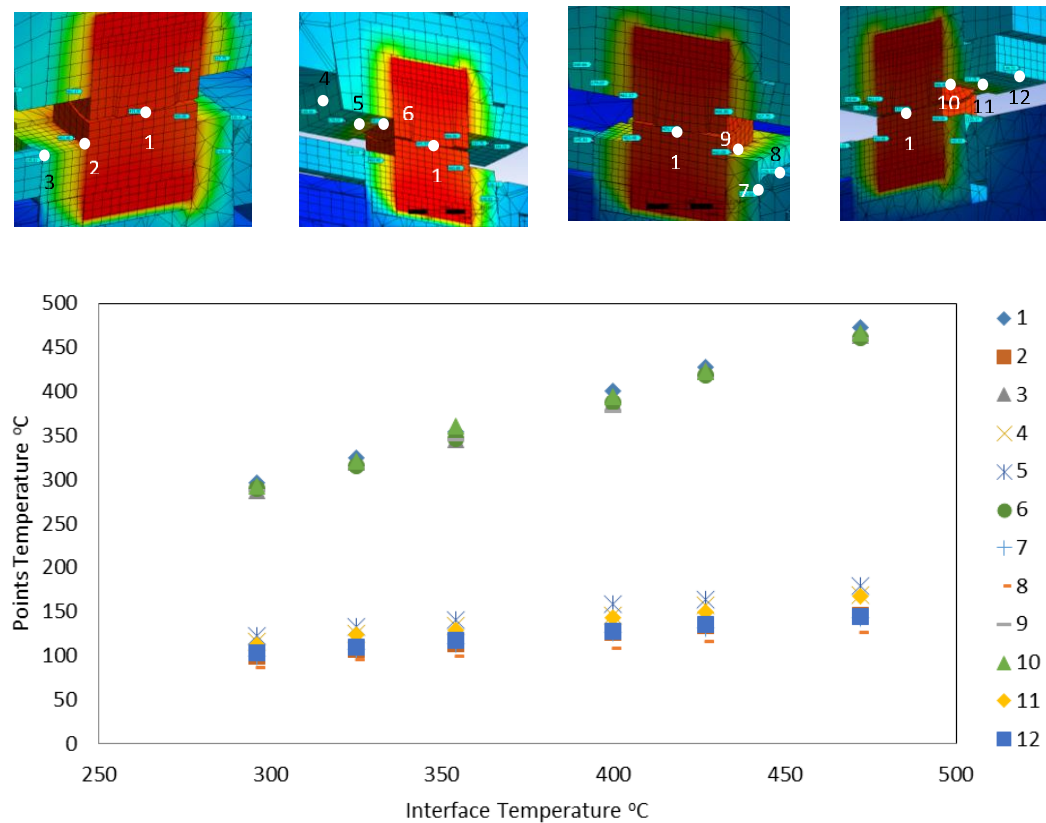


Figure 3-9: Cross section of the fretting wear setup thermal model showing the thermocouple suggested points (above) and their correlation to the interface temperature (below).

The model was first calibrated by welding thermocouples (type K) to the sensitive points. The heat transfer coefficients used in the FE model were adjusted in such a way that the predicted temperatures match the experimentally measured ones. When the model was validated, the total number of thermocouples was reduced to 5 for practical reasons. Two of these thermocouples were imbedded inside the heaters, another two were welded to each sample near the interface and the last one was welded to the proximity probe since it was the sensor experiencing the highest temperature rise and had the lowest rated maximum operating temperature. These thermocouples and temperature measurements ensured that the interface temperature was reached and allowed continuous monitoring the setup thermal behaviour. In addition, they ensured that the operating temperature of the measurement sensors were far below their maximum allowable temperatures, as shown in Table 3-1.

Table 3-1: Maximum rated operating temperature for the different sensors, and the measured operation temperature.

Sensor	Maximum rated operating temperature (°C)	Approximate actual operating temperature (°C)
Proximity probe (Bently, model 3300)	177	50
Accelerometer (Brüel & Kjaer, model 4381)	250	40
Normal force transducer (Brüel & Kjaer, model 8200)	200	35
Tangential force transducer (Brüel & Kjaer, model 8200)	200	30

3.7. Workpiece materials and geometries

The raw material was supplied by PWC in the form of bars. Samples geometries were designed and manufactured carefully to meet the following requirements:

- The contact surfaces of the samples must have the same geometry and surface finish as the real combustor parts.
- The same fits and tolerances specified by PWC were preserved to maintain the same contact conditions.
- The samples size must fit the fixture of the setup.
- The samples contact area must be aligned with the setup normal force axis.
- The samples contact interface must be aligned with the frictional force axis.
- The samples footprint must be equal to the heaters surface area in order to optimize the heat transfer and reduce the risk of the heaters cracking upon high load application.

Figure 3-10 shows the geometry of the fretting pairs and Figure 3-11 shows their detailed working drawings.

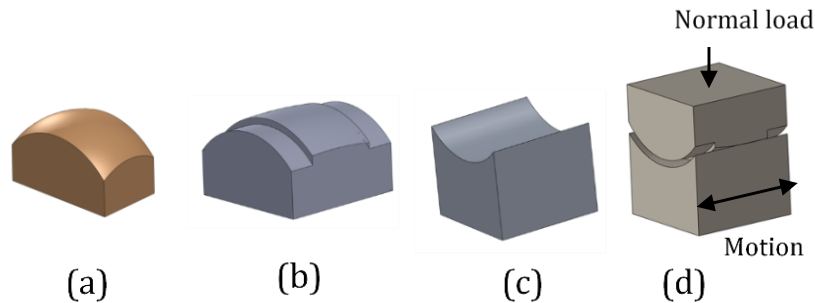


Figure 3-10: Fretting samples (a) upper stationary pin sample G1, (b) upper stationary pin sample G2, (c) lower oscillatory ring sample, and (d) the pair in contact when G2 is tested.

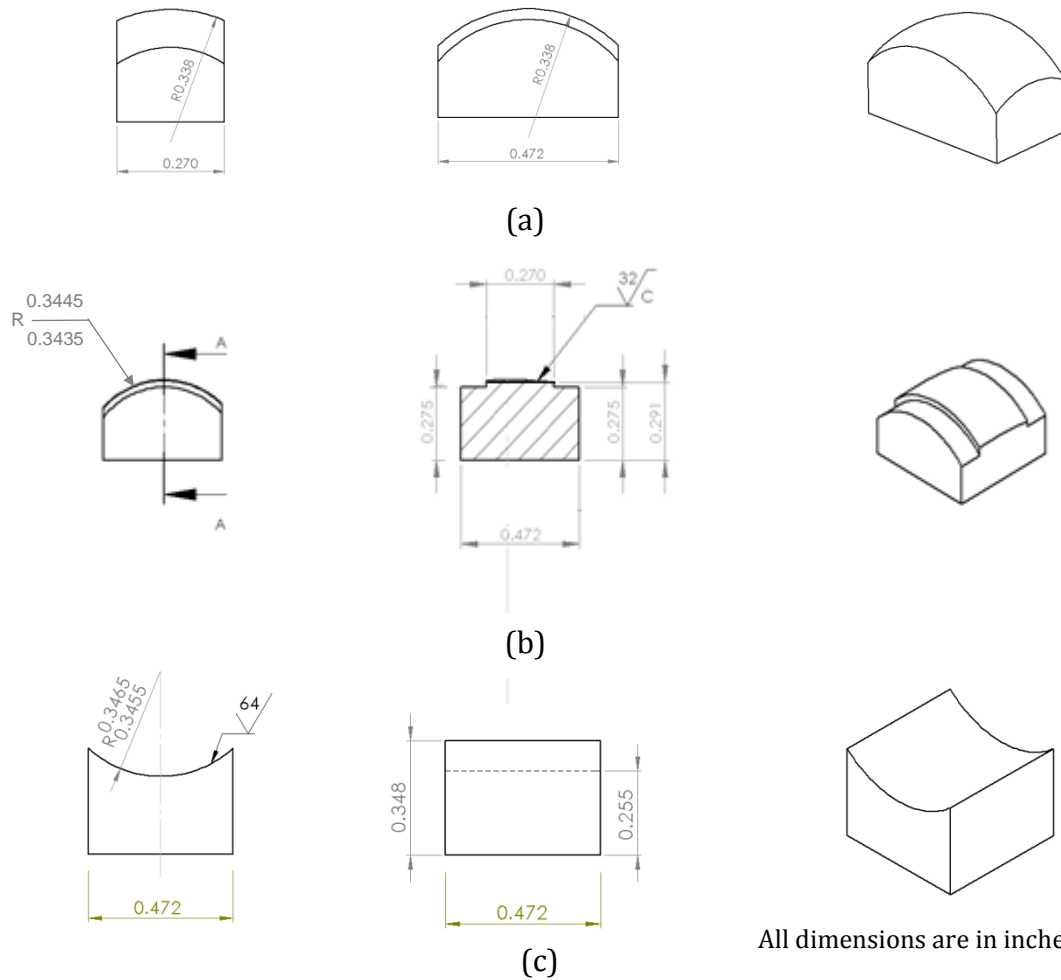


Figure 3-11: Working drawings of the fretting specimens (a) upper fixed cylinder sample (G1), (b) upper fixed cylinder sample (G2) and (c) lower oscillatory ring sample.

3.8. Samples alignment

The design of the tribometer provides the required degrees of freedom to ensure the alignment of the contacting surfaces along the X, Y and Z axes (Figure 3-1). Before the beginning of the test, special pressure sensitive paper was used to ensure a uniform contact between the upper and the lower specimens. To ensure the satisfaction of the pre-set test requirements, a test was not accepted unless the required alignment was achieved. Failure to meet the alignment requirement led to scraping the sample.

3.9. Surface scanning and 3-D map

The topography of the contacting surfaces was measured after each fretting wear test using a 3D surface scanner (Taylor Hobson, model Form Talysurf 120 mm), whose resolution is $0.25\text{ }\mu\text{m}$ in the z direction and $1\text{ }\mu\text{m}$ in the x direction, as shown in Figure 3-12 and 3-13. The images of the fretted surfaces were also captured using an optical microscope. The fretting wear scar was identified by comparing the damaged surface optical image observed under the microscope with the wear 3D map of the worn surface provided by the surface scanning machine.

In order to calculate the worn volume, the wear depth and the real area of contact, the fretting wear scar was identified by comparing the damaged surface optical image Figure 3-13 (a)) with the wear 3D map provided by the surface scanning machine (Figure 3-13 (b)). Using the 3D surface analysis software, a contour was carefully drawn around the damaged area (Figure 3-13 (c)), and a reference plane (called the P plane) was created. This P plane represented the least squares plane of all the points outside of the defined contour of the contact area (Figure 3-13 (d)). The reference P plane divided the wear scar into two portions: a negative portion existing below the plane, termed hole, which represented the volumetric wear losses, and a positive portion existing above the plane, termed peak, which represented the material transferred from the mating body by adhesion. The distance between the P plane and the lowest point in the hole represented the maximum wear depth. The average contact pressure was calculated by dividing the normal load by the actual contact area. The latter was the summation of the two areas: the hole area and the peak area (Figure 3-13 (c)). This calculation corresponds to the final stage of the fretting wear process, where the damage is already developed. This gives a lower value of the contact pressure, compared to that at the beginning of the process, since the contact area increases with the evolution of damage.



Figure 3-12: The 3D surface scanner Taylor Hobson Talysurf 120 with a close up on the scanning process.

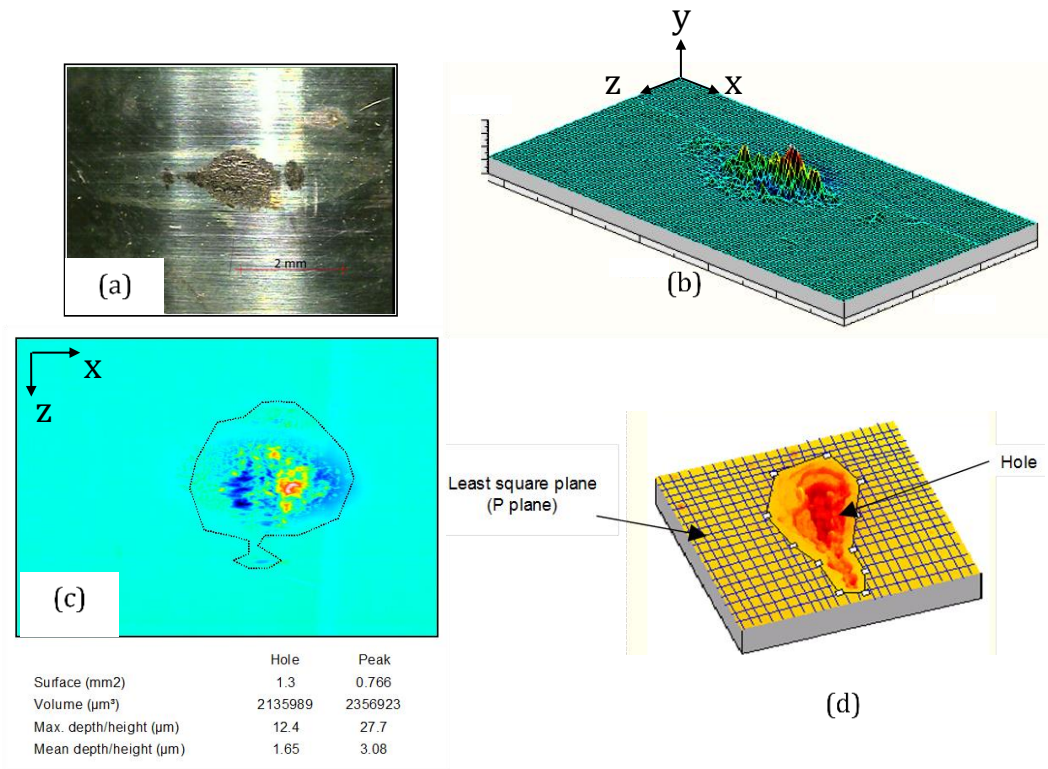


Figure 3-13: Illustration of the wear volume, wear depth, and contact area calculation (a) optical image observed under the microscope, (b) 3D map of the fretted surface, (c) the contour defining the damaged area, and (d) the reference plane P plane.

3.10. Parameters for the evaluation of the tribological properties

3.10.1. Wear coefficient and maximum wear depth

The wear resistance of the surface was determined based on the calculation of the specific wear coefficient K , defined as the volumetric wear rate \dot{V} (representing the output as damage) per work rate \dot{W} (representing the input as energy supplied to the system in the form of load and displacement combinations). A higher wear coefficient means higher damage and lower wear resistance. The wear rate is the wear volume divided by the total test duration. The wear volume V of the fretted surface was measured, after each test, using the surface scanner. The work rate is defined as:

$$\dot{W} = 4 f \cdot A \cdot F_n \quad (3-1)$$

where A and f are the amplitude and the frequency of oscillation, respectively, and F_n is the average normal force measured throughout the test. The other quantification of the wear damage is the absolute maximum wear depth, which is a useful measure of the removed material.

3.10.2. Coefficient of Friction

The friction coefficient μ is defined as:

$$\mu = \frac{\max(F_t) - \min(F_t)}{2F_n} \quad (3-2)$$

where F_t is the instantaneous friction force. The normal force F_n is based on the average of the measured normal force during 0.05 seconds, as shown in Figure 3-14.

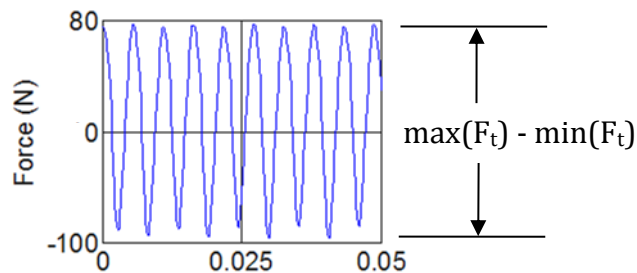


Figure 3-14: Calculation of the coefficient of friction.

Equation (3-2) is valid if the tests are conducted in the gross slip regime, which can be quantified by the energy ratio ER [82]:

$$ER = E_d/E_t \quad (3-3)$$

where E_d is the dissipated energy during the cycle (the area enclosed by the frictional force displacement loop) and E_t is the total energy defined as $2 \times ((F_t)_{\max} - (F_t)_{\min}) \times A$, where F_t is the frictional (or tangential) force and A is the amplitude of slip, as illustrated in Figure 3-15. If $ER > 0.2$, gross slip takes place, otherwise partial slip is expected [82]. This ratio is independent of the contact geometry and the material properties [82-84]. As will be seen in Chapter 4, all tests conducted in this study are in the gross slip regime ($ER > 0.2$).

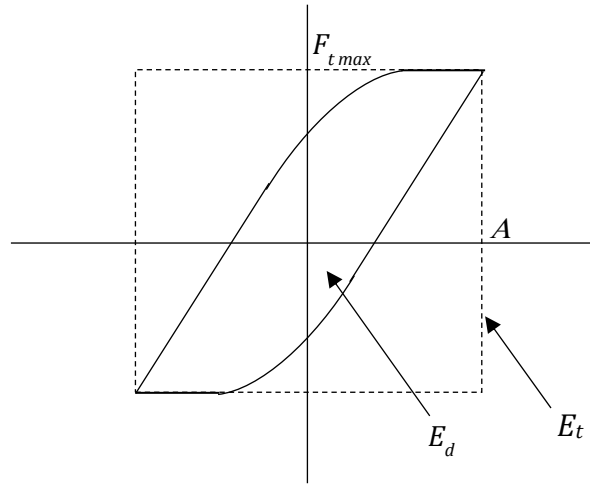


Figure 3-15: Characterization of the fretting cycle under gross slip conditions.

3.11. Experimental parameters and test matrix

The fretting wear experiments were conducted using different cylinder materials/geometries against different ring materials at room and high temperatures. A full factorial design was implemented in the design of experiments. Table 3-2 shows the experimental parameters and Table 3-3 shows the contact pairs. To ensure the reliability of the experiments, some selected tests were repeated, which bear the letter R in their numbering.

Table 3-4 shows the test matrix used in the present investigation. A color coding scheme was used to distinguish between the temperature levels, e.g., blue for room temperature (RT) (dark blue for G1 and light blue for G2), white for 200°C, green for 350°C and orange for 550°C.

Table 3-2: Experimental parameters, variables and the fixed conditions.

Parameters	Levels	Symbol	Nominal Values
Amplitude of slip	2	A_1, A_2	$\pm 10 \mu\text{m}, \pm 15 \mu\text{m}$
Normal load	2	F_{n1}, F_{n2}	10 N, 30 N
Bulk temperature	3	T_1, T_2, T_3	RT, 350°C, 550°C ¹
Contact pair	4	CP0, CP1, CP2, CP3	See Table 3-3
Cylinder geometry	2	G1, G2	See Figure 3-10
Frequency	1	f	200 Hz ($\pm 10\%$)
Test duration	1	N	2×10^6 Cycles

Table 3-3: Contact pairs used in the experiments.

Contact pair	Cylinder sample	Ring sample
CP0	Cobalt Alloy 1 [85]	Cobalt Alloy 1
CP1	Cobalt Alloy 2 [86]	Cobalt Alloy 1
CP2	Cobalt Alloy 1	Nickel Alloy 1 [87]
CP3	Cobalt Alloy 2	Nickel Alloy 1

¹ An additional test at 200°C was conducted for the Cobalt Alloy 2 cylinder against the Cobalt Alloy 1 ring at $A = \pm 15 \mu\text{m}$ and $F_n = 30 \text{ N}$.

Table 3-4: Full project test matrix.

Test No.	Temp	Contact Pair			Amplitude	Load	Actual Work Rate	Nominal Work Rate
	°C		Cylinder	Ring	± μm	N	mJ/s	mJ/s
1	Room Temp (RT)	CP0-G1	Cobalt Alloy 1	Cobalt Alloy 1	5	14	56	55
2					5	20	80	80
3					4	29	92.8	90
4					9	15	108	110
5					10	20	160	160
6					10	29	232	230
7					15	11	132	130
8					15	29	348	350
9					10	11	88	90
10	Room Temp (RT)	CP1-G2	Cobalt Alloy 2	Cobalt Alloy 1	10	11	88	90
11					10	29	232	230
12					15	11	132	130
13 (R)					15	11	132	130
14					15	29	348	350
15	200°C	CP1-G2	Cobalt Alloy 2	Cobalt Alloy 1	15	29	348	350
16	350 °C	CP1-G2	Cobalt Alloy 2	Cobalt Alloy 1	10	11	88	90
17					10	29	232	230
18 (R)					10	29	232	230
19					15	11	132	130
20					15	29	348	350

Table 3-4 (cont.): Full project test matrix.

Test No.	Temp	Contact Pair			Amplitude	Load	Actual Work Rate	Nominal Work Rate
	°C		Cylinder	Ring	± μm	N	mJ/s	mJ/s
21	350 °C	CP2-G2	Cobalt Alloy 1	Nickel Alloy 1	10	11	88	90
22					10	29	232	230
23					15	11	132	130
24 (R)					15	11	132	130
25		CP3-G2	Cobalt Alloy 2	Nickel Alloy 1	15	29	348	350
26					10	11	88	90
27					10	29	232	230
28					15	11	132	130
29					15	29	348	350
30	550°C	CP1-G2	Cobalt Alloy 2	Cobalt Alloy 1	10	11	88	90
31					10	29	232	230
32					15	11	132	130
33					15	29	348	350
34		CP2-G2	Cobalt Alloy 1	Nickel Alloy 1	10	11	88	90
35					10	29	232	230
36					15	11	132	130
37					15	29	348	350
38		CP3-G2	Cobalt Alloy 2	Nickel Alloy 1	10	11	88	90
39					10	29	232	230
40					15	11	132	130
41					15	29	348	350

Chapter 4 Experimental Results:

Comparison between the Different Contact Pairs

4.1. Introduction

In this chapter, the tribological behaviour of the different contact pairs is assessed. All experimental results are shown in the form of a comparison that includes the evolution of the wear coefficient, the maximum wear depth, the dynamic friction, and the contact pressure with work rate and temperature. In order to summarize the results, material selection maps are developed at the end of each section showing the recommended contact pair(s) at different working conditions.

4.2. Comparison methodology and notes on the reported results

1. The comparison methodology adopted in this study is based on the following logic:
 - a. First, the effect of work rate and temperature on the tribological behavior of each contact pair is investigated.
 - b. Second, the bulk temperature is fixed, and the evolution of the wear damage criterion with work rate for all materials is assessed for comparison purposes.
2. Unless stated, the reported results belong to the cylinder samples shown in Figure 10 (b). For some special cases, the ring results are reported to complete the picture and strengthen understanding.
3. When the comparison takes place between different contact pairs, a red arrow indicates the favorable choice according to the damage criterion of the study.
4. For the sake of discussion, the actual work rate values of 88, 132, 232, and 348 mJ/s are sometimes replaced to by their nominal corresponding values; 90, 130, 230 and 350 mJ/s, respectively.

4.3. Normalization procedure

Due to confidentiality reasons, all results are normalized with respect to a reference case. The selected reference case belongs to the contact pair exhibiting the overall lowest wear damage at the highest bulk temperature (550°C) and the highest work rate value (≈ 350 mJ/s). In the current study, it was CP1 (Cobalt Alloy 2 cylinder/ Cobalt Alloy 1 ring) that

showed the lowest wear coefficient, least maximum wear depth and lowest coefficient of friction at the above mentioned running conditions, and therefore, is considered the reference case.

4.4. Evaluation of the material wear coefficient

Figure 4-1 shows the effect of temperature and work rate on the fretting wear coefficient for CP1. First, at RT and at 350°C, there exist two distinct regimes: the low work rate regime (corresponding to $\dot{W}=90$ and 130 mJ/s), which is characterized by a relatively high wear coefficient, and the high work rate regime (corresponding to $\dot{W}=230$ and 350 mJ/s), which is characterized by a relatively low wear coefficient. The decrease in the wear coefficient which occurred when moving from the low to the high work rate regimes can be interpreted by Uhlig's work [25] who studied the effect of the fretting process parameters on wear losses. In his model, he considered the mechanical and the oxidation (chemical) effect of the wear process, as shown in equation (4-1):

$$V = [k_o \cdot F_n \cdot 2A \cdot N] + \left| (k_1 \sqrt{F_n} - k_2 F_n) \frac{N}{f} \right| \quad (4-1)$$

where, V , F_n , A , N and f are the wear volume, the normal load, the amplitude of oscillation, the number of cycles and the frequency of oscillation, respectively, and k_o , k_1 and k_2 are constants that depend on the temperature and material. In equation (4-1), the first term $[k_o \cdot F_n \cdot 2A \cdot N]$ represents the mechanical component, while the second term $\left| (k_1 \sqrt{F_n} - k_2 F_n) \frac{N}{f} \right|$ is the chemical component. By dividing the total wear volume by the mechanical work ($W = 4 \cdot F_n \cdot A \cdot N$), the wear coefficient becomes:

$$K = [k_o/2] + \left| (k_1/4A \sqrt{F_n} - k_2/4A) \frac{1}{f} \right| \quad (4-2)$$

The negative term in equation (4-1) implies that an increase in the work rate (coming from an increase in the normal load and/or amplitude of slip) leads to a decrease in the wear coefficient. This is also consistent with the findings of Attia [88] who observed the same trend when investigating the impact/sliding fretting wear of Zr-alloy pressure tubes.

At 550°C, a large difference is observed between the low amplitude condition ($A = \pm 10\mu\text{m}$, $F_n = 10\text{ N}$ and $\dot{W} = 90\text{ mJ/s}$) and the high amplitude condition ($A = \pm 15\mu\text{m}$, $F_n = 10\text{ N}$ and $\dot{W} = 130\text{ mJ/s}$) in the low work rate regime only. The explanation of this behaviour lies in the key role played by the contact pressure in the formation of protective oxides at high temperatures. The two mating alloys, Cobalt Alloy 2 and Cobalt Alloy 1, are both rich in cobalt and chromium. When these alloys are heated to a temperature of around 400°C, and under the effect of the contact pressure, they produce an oxide layer (glaze) [8]. This layer reduces the metal-metal contact, and consequently, adhesion and wear. At this low work rate regime, the normal load is small ($F_n = 10\text{ N}$) and the variation in the damaged area becomes sensitive to the variation in the slip amplitude. Compared to the work rate of $\dot{W} = 130$, the condition of $\dot{W} = 90\text{ mJ/s}$ corresponds to lower amplitude of slip, which leads to a lower damaged area, and therefore, a higher average contact pressure.

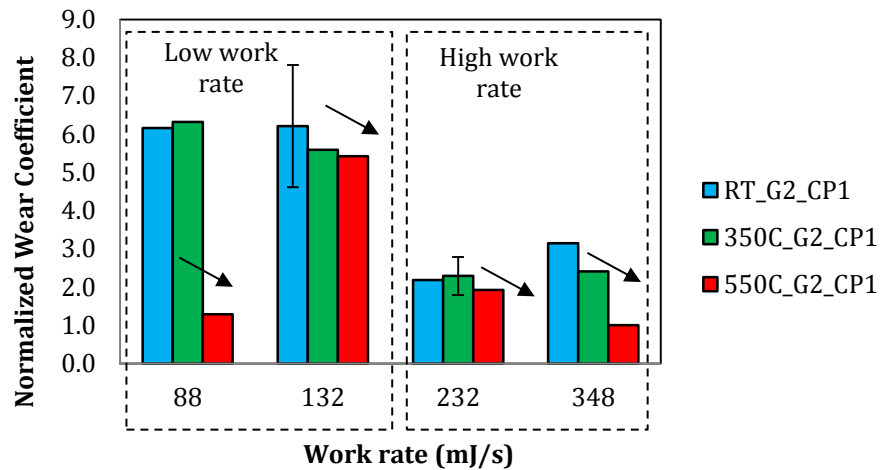


Figure 4-1: Effect of temperature on the wear coefficient when plotted against the work rate for CP1 (Cobalt Alloy 2 cylinder / Cobalt Alloy 1 ring).

Figure 4-2 and Figure 4-3 show that for CP2 and CP3, an increase in the temperature from 350°C to 550°C is associated with an increase in the wear coefficient (except for CP2 at the work rate value of $\sim 130\text{ mJ/s}$). This can be explained by the fact that the ring sample in CP2 and CP3 is made of Nickel Alloy 1, which tends to form protective oxide layers at around 300°C [14]. Above this level of temperature, this layer starts to experience disruption. Similar behaviour was observed by Korashy and Attia [89] when they

investigated the fretting wear behaviour of nickel superalloys at 350°C and 550°C. Iwabuchi [90], who investigated the fretting wear of Inconel 625 at high temperature and different pressures, has also reported a similar trend. Mioyoshi [15] who investigated the fretting wear of gamma titanium aluminide in contact with a typical nickel-base superalloy, reported higher wear losses when the temperature increased from 220°C to 550°C. He also showed that at 450°C and 550°C, oxide disruption occurred and generated cracks, loose wear debris, and pits on the titanium aluminide wear surface. Figure 4-4 shows the effect of temperature and work rate on the wear coefficient for the case of G1-CP0. At low work rate regimes (<130 mJ/s), the wear coefficient showed a peak at 88 mJ/s. This notable rise in damage was attributed to the fact that the cylinder sample belonging to this condition, when received, had the lowest surface roughness when compared to the other similar conditions. The RMS value of the 88 mJ/s cylinder was almost 30% below the average RMS values of the adjacent conditions (80 mJ/s, 93 mJ/s and 108 mJ/s). When the surface roughness increased, the contact asperities behaved like elastic cantilever beams, reducing the fretting wear damage [91].

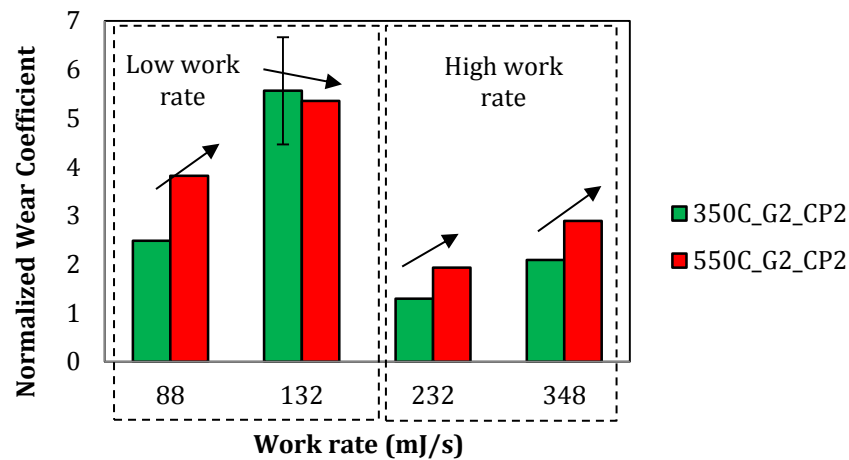


Figure 4-2: Effect of temperature on the wear coefficient when plotted against the work rate for CP2 (Cobalt Alloy 1 cylinder / Nickel Alloy 1 ring).

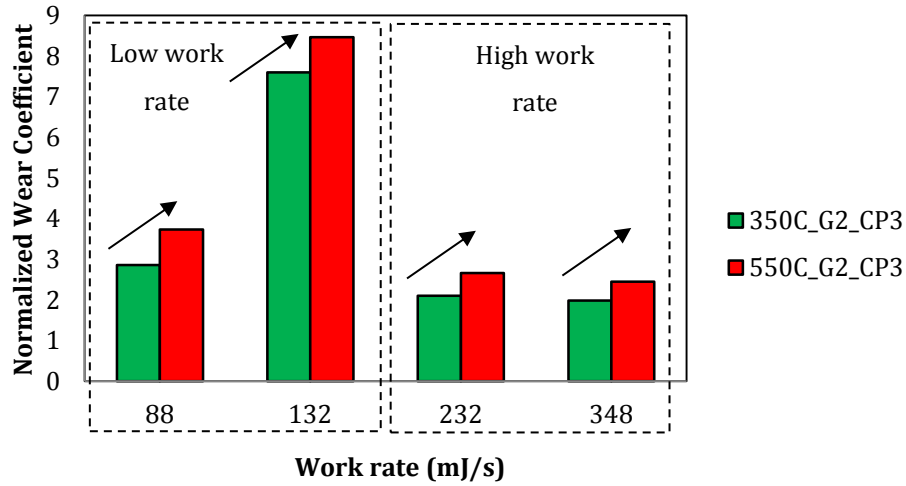


Figure 4-3: Effect of temperature on the wear coefficient when plotted against the work rate for CP3 (Cobalt Alloy 2 cylinder / Nickel Alloy 1 ring).

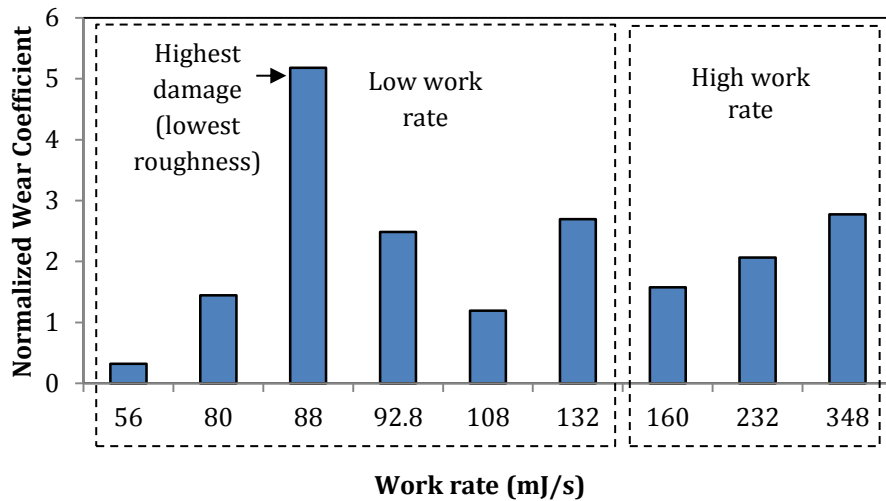


Figure 4-4: Effect of work rate on the wear coefficient for G1_CP0 at RT (Cobalt Alloy 1 cylinder / Cobalt Alloy 1 ring).

By investigating the wear coefficient at 350°C (Figure 4-5) for the three contact pairs; CP1, CP2 and CP3, CP2 generally exhibits the least wear coefficient, except at the highest work rates (~350 mJ/s) where CP3 shows a slightly lower wear coefficient. This difference is, nevertheless, insignificant, considering the variability encountered in wear tests. The superiority of CP2 and CP3 at 350°C originates from the fact that the ring sample is a nickel-base alloy (Nickel Alloy 1) which forms a protective oxide layers at temperature level around 300°C, whereas the cobalt-base alloy ring in CP1 (Cobalt Alloy 1) is not able to

have this layer fully developed at this temperature level. When the temperature was raised to 550°C (Figure 4-6), CP1 showed the least wear coefficient, since CP1 could develop a glaze layer whereas CP2 and CP3 suffered from oxide disruption.

Except CP1 at 350°C, all contact pairs at 350 °C and 550°C show an increase in the wear coefficient at a work rate of ~130 mJ/s. This can be attributed to the fact that this condition represents the lowest contact pressure (refer to Figure 4-31 and Figure 4-32). As reported by Hamdy and Waterhouse [14], the contact pressure enhances the formation of a protective glaze at high temperatures due to the increase in frictional heat.

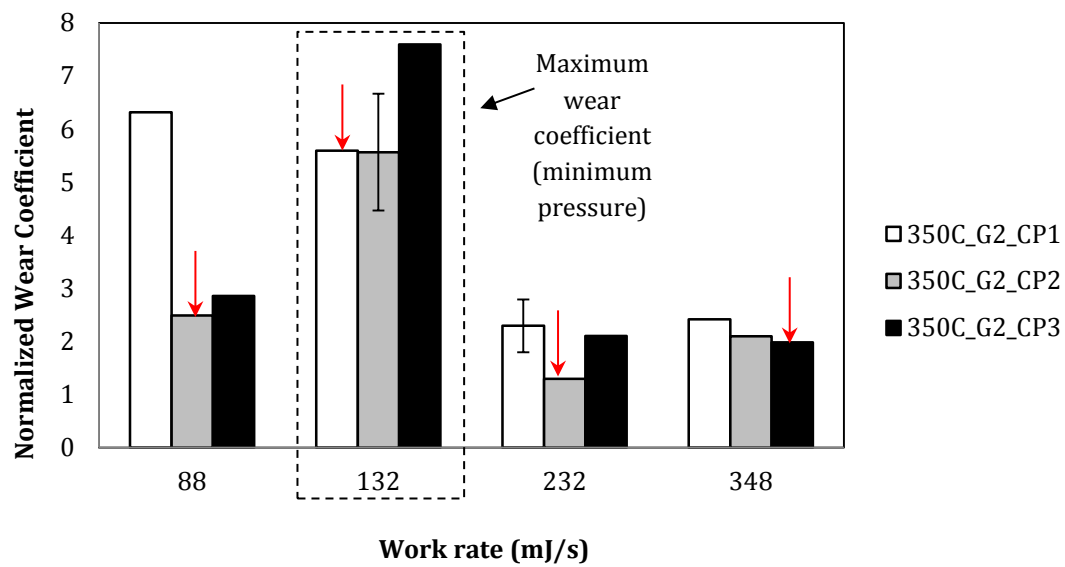


Figure 4-5: Wear coefficient vs. work rate for different contact pairs at 350°C.

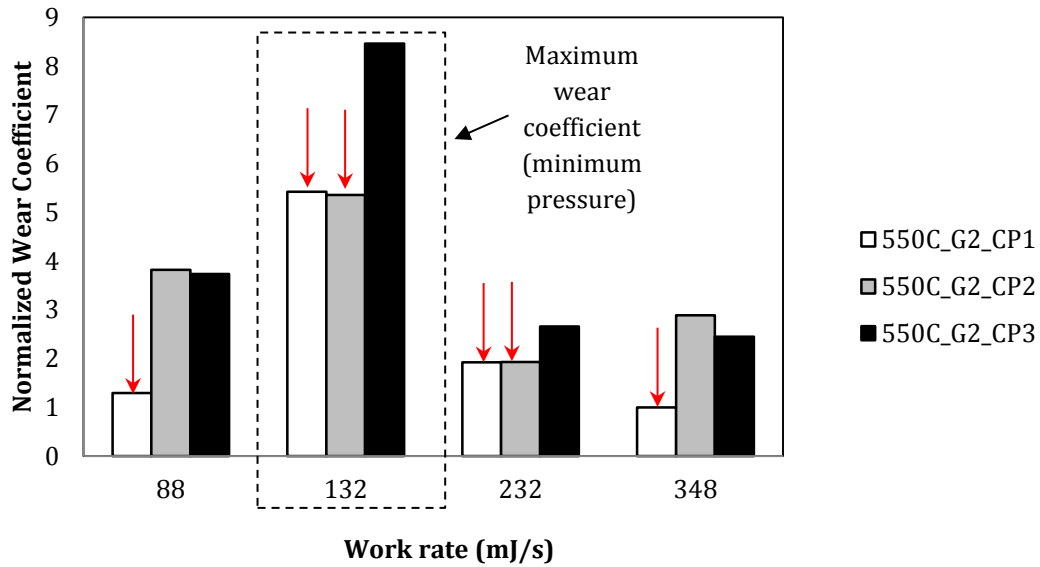


Figure 4-6: Wear coefficient vs. work rate for different contact pairs at 550°C.

In order to summarize the results shown in Figure 4-5 and Figure 4-6, a wear resistance material selection map (based on the wear coefficient) for a given temperature and work rate has been developed as shown in Figure 4-7.

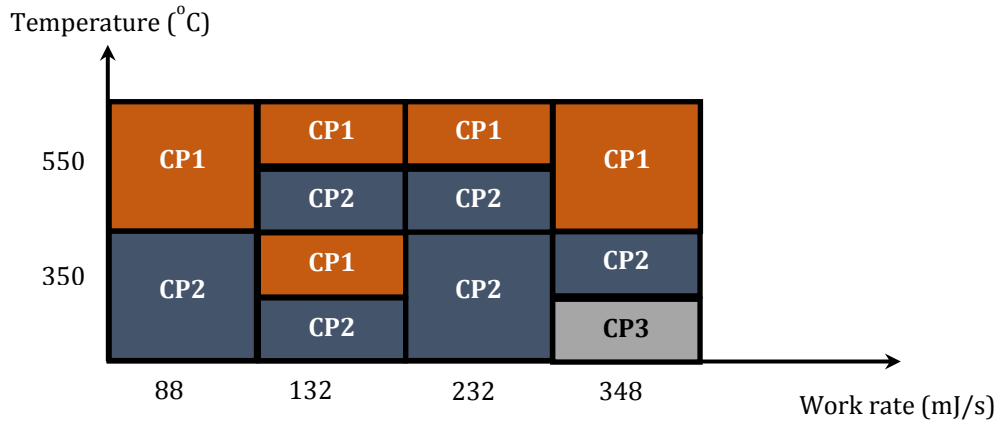


Figure 4-7: Wear resistance material selection map (based on the wear coefficient).

4.5. Evaluation of the maximum wear depth

Figure 4-8 shows the effect of temperature and work rate on the maximum wear depth for CP1. At room temperature, no significant change in the maximum wear depth is seen when

the work rate changes. At 350°C, there is a monotonic increase in the maximum wear depth with an increase of the work rate. At 550°C, however, the opposite behaviour is observed; a monotonic decrease in the maximum wear depth is associated with an increase of the work rate. This can be explained by the fact that Cobalt Alloy 2 surface experiences plastic deformation under combined compression and shear. At 350°C, an increase in work rate (or load) leads to an increase in this plastic deformation, and the protective oxide layer, which is not yet well developed, is easily disrupted. This is why a monotonic increase in the maximum wear depth is observed when the work rate is increased. On the other hand, at 550°C, the transition temperature at which the glaze layer is formed (around 400°C for cobalt-base superalloys [8]) has already been achieved. This layer forms some load bearing areas. Consequently, an increase in work rate (or load) leads to the formation of a harder, more resistant and more stable protective oxide layer, and hence, a monotonic decrease in the maximum wear depth with an increase in work rate.

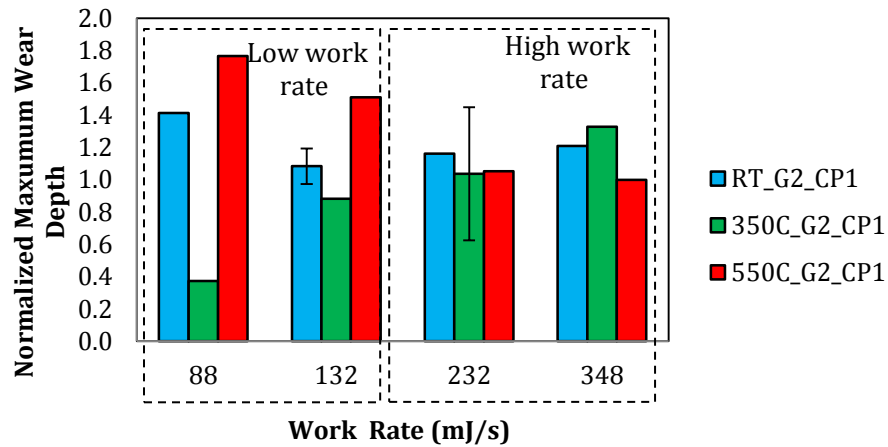


Figure 4-8: Effect of temperature on the maximum wear depth when plotted against the work rate for CP1 (Cobalt Alloy 2 cylinder / Cobalt Alloy 1 ring).

For CP2 and CP3, the existence of the nickel-base ring results in an opposite trend. Figure 4-9 and Figure 4-10 show that an increase in temperature is always associated with an increase the maximum wear depth for CP2 and CP3, respectively (except for CP2 at a work rate of ~130 mJ/s). This can be attributed to the disruption of the oxide layer when the

temperature rises from 350°C to 550°C. It is worth mentioning that the wear depth increase (or decrease) with temperature for CP1 and CP2 (Figure 4-9 and Figure 4-10) are very close to the wear coefficient trends (Figure 4-2 and Figure 4-3).

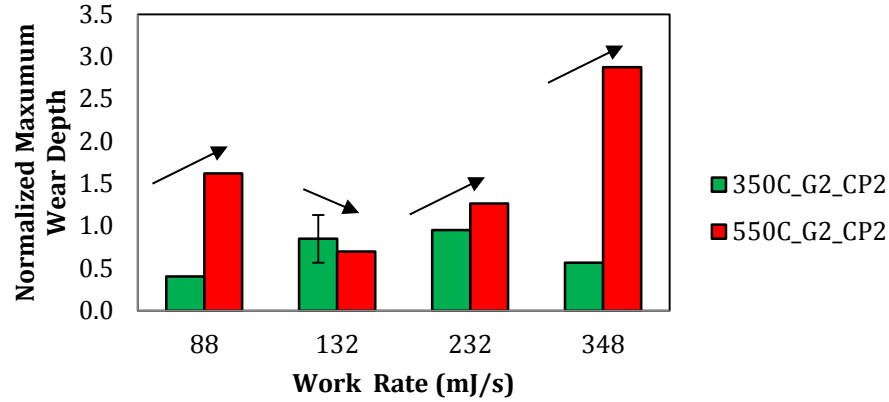


Figure 4-9: Effect of temperature on the maximum wear depth when plotted against the work rate for CP2 (Cobalt Alloy 1 cylinder / Nickel Alloy 1 ring).

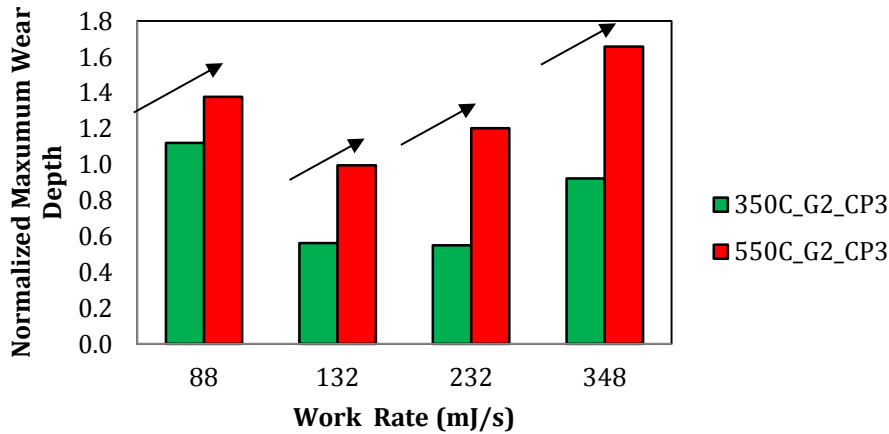


Figure 4-10: Effect of temperature on the maximum wear depth when plotted against the work rate for CP3 (Cobalt Alloy 2 cylinder / Nickel Alloy 1 ring).

Figure 4-11 shows the effect of the work rate on the maximum wear depth for G1_CP0 at RT. In the low work rate regime (< 132 mJ/s), the maximum wear depth experienced a peak at 88 mJ/s (similar the wear coefficient; Figure 11) because of the low roughness of the cylinder sample used in this test. In the high work rate regime (> 132 mJ/s), there is a

monotonic increase in the maximum wear depth. This increase comes from the increase in the normal load that directly affects the maximum wear depth.

When comparing the different contact pairs at 350°C (Figure 4-12), it can be seen that at the lowest work rates (~ 90 mJ/s), CP1 exhibits the lowest maximum wear depth. At work rates ~ 130 and ~ 230 mJ/s, CP3 exhibits the lowest maximum wear depth, whereas at the highest work rates (~ 350 mJ/s) CP2 has the lowest maximum wear depth. At 550°C, CP1 shows better performance at the higher work rate levels (~ 230 and ~ 350 mJ/s), whereas CP3 and CP2 shows a lower maximum wear depth at ~ 90 mJ/s and ~ 130 mJ/s, respectively (Figure 12). This observation is similar to the previous observation on the wear coefficients trends, that at 350°C, the nickel-based alloys are more resistant to damage, whereas at 550°C, the cobalt-based alloys become more resistant to damage, especially at high work rates.

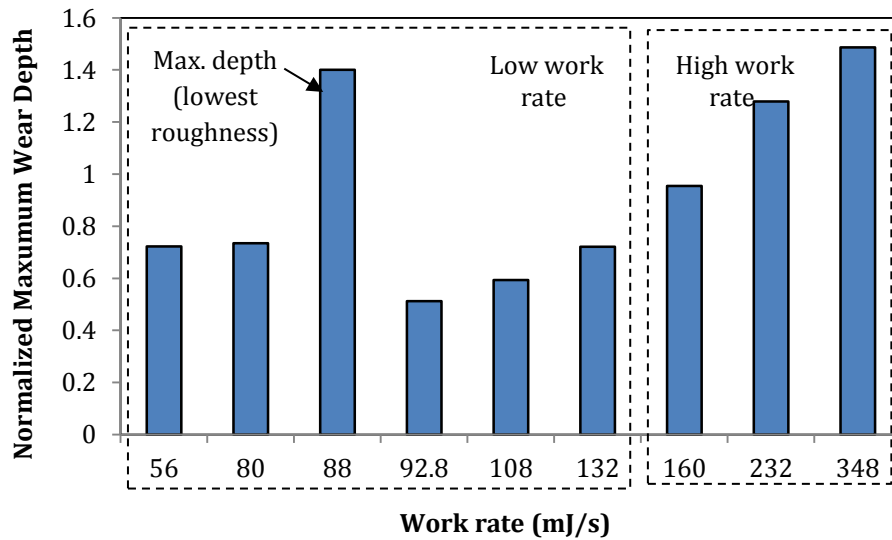


Figure 4-11: Effect of the work rate on the maximum wear depth for G1_CP0 at RT (Cobalt Alloy 1 cylinder / Cobalt Alloy 1 ring).

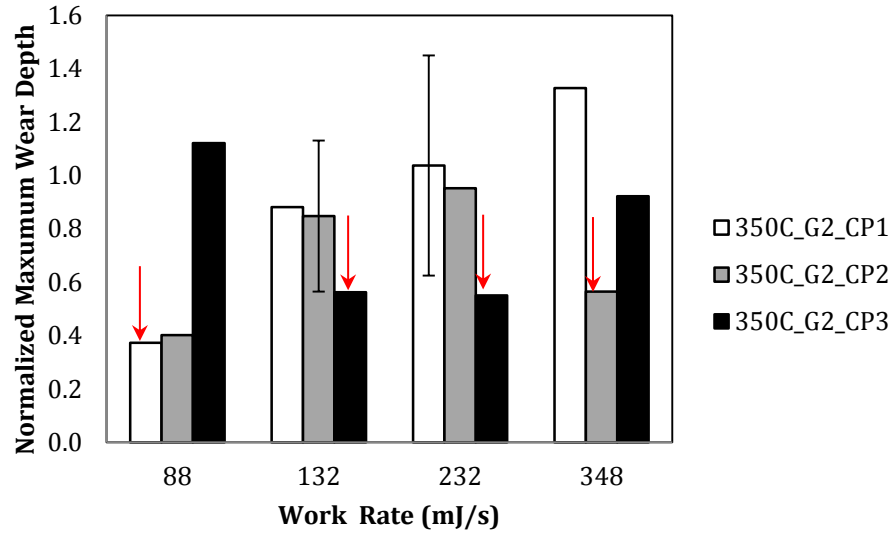


Figure 4-12: Maximum wear depth vs. work rate for different contact pairs at 350°C.

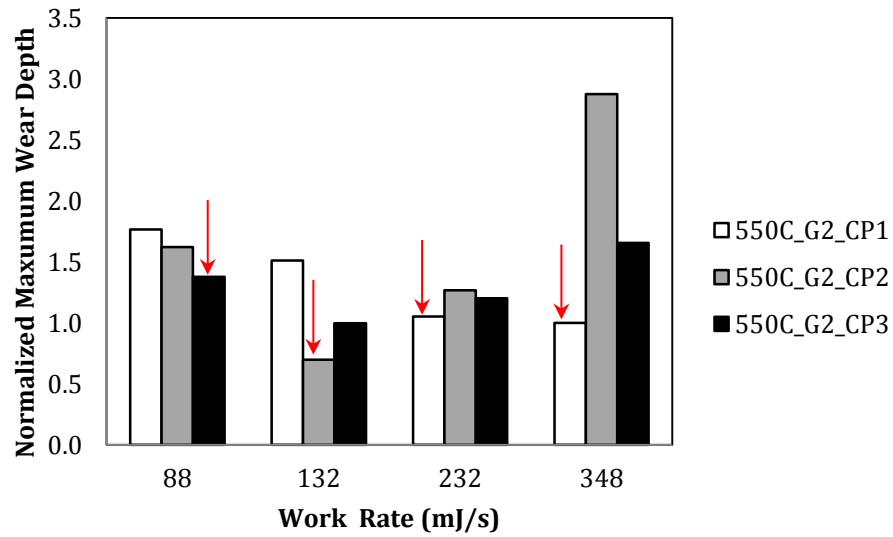


Figure 4-13: Maximum wear depth vs. work rate for different contact pairs at 550°C.

In order to summarize the results shown in Figure 4-12 and Figure 4-13, a wear resistance material selection map (based on the maximum wear depth), for a given temperature and work rate, has been developed, as shown in Figure 4-14.

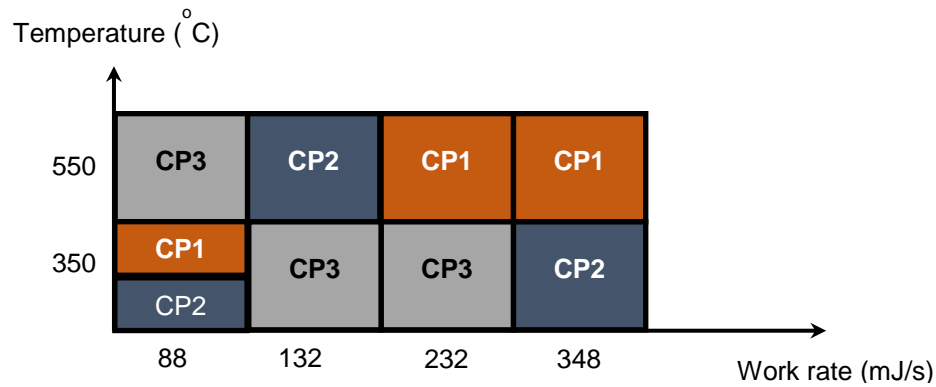


Figure 4-14: Wear resistance material selection map (based on the maximum wear depth).

4.6. Evaluation of friction properties

Figure 4-15, shows the steady state coefficient of friction plotted against the work rate for CP1. It can be seen that there is a monotonic decrease in the coefficient of friction with an increase of temperature due to the development of a protective oxide layer for this contact pair. With the increase in temperature, this layer becomes more stable contributing to lower interfacial shear strength at the contact interface and resulting in a lower coefficient of friction [92]. A detailed study on the effect of temperature on the oxide layer formation for CP1 is presented in Chapter 5.

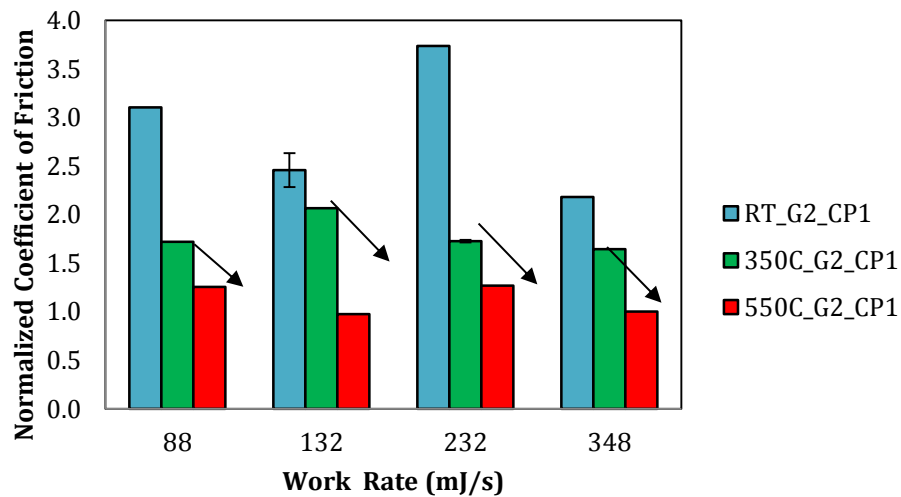


Figure 4-15: Effect of temperature on the coefficient of friction when plotted against the work rate for CP1 (Cobalt Alloy 2 cylinder / Cobalt Alloy 1 ring).

Typical plots of the normalized friction force - displacement loop for CP1 are shown in Figure 4-16 for the extreme cases of low load ($F_n = 10$ N) and high amplitude ($A = \pm 15$ μm) and high load ($F_n = 30$ N) and low amplitude ($A = \pm 10$ μm) at 550°C. The corresponding energy ratios ER are 0.53, and 0.30, respectively. When the energy ratio was calculated for the CP1 tests, it was found that the ER values were between 0.30 and 0.85. For CP2, the ER values were between 0.38 and 0.78, while for CP3, the ER ranged between 0.24 and 0.72. Appendix B shows the energy ratios for all the tests conducted in this research, and since all of them lie within the gross slip regime, the use of Eq. 3.2 in the calculation of the coefficient of friction is justified.

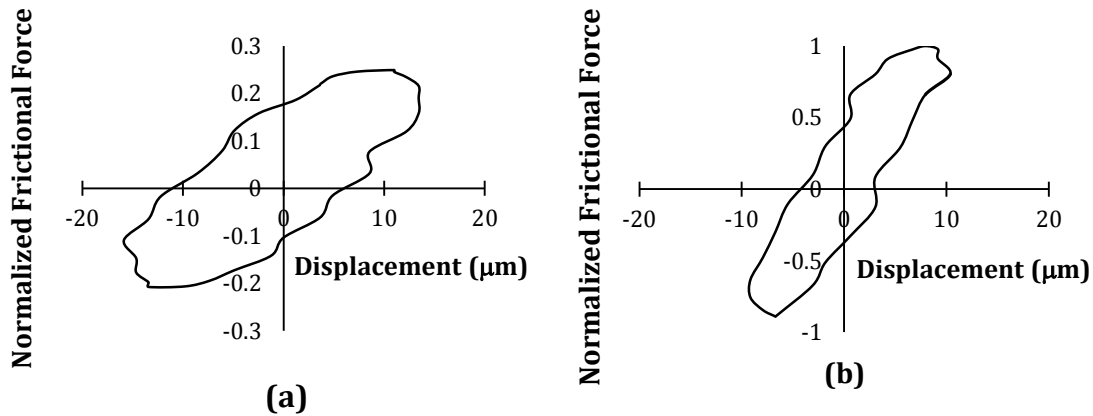


Figure 4-16: Typical fretting loop for CP1 (a) low load ($F_n = 10$ N) - high amplitude ($A = \pm 15$ μm) case at 550°C, with $ER = 0.53$ and (b) high load ($F_n = 30$ N) - low amplitude ($A = \pm 10$ μm) case at 550°C, with $ER = 0.3$.

Figure 4-17 and Figure 4-18 show that an increase of temperature was associated with a decrease in the coefficient of friction for CP2 and CP3, respectively. Although a decrease in friction was associated with a decrease in the wear coefficient for CP1 (Figure 4-1), it was surprisingly associated with an increase in the wear coefficient for CP2 and CP3 (Figure 4-2 and Figure 4-3). Similar behaviour was reported by Klaffke et al. [93] when they studied the effect of grain refinement on the high temperature fretting wear of Inconel 738 LC. A detailed analysis conducted to explain this behaviour is presented in Chapter 5.

Figure 4-19 shows the steady state coefficient of friction plotted against the work rate $G1_CP0$, where the tests showed fluctuation in the coefficient of friction. At 350°C, CP2

shows better friction characteristics in the high work rate region, which can be attributed to the role played by the load (i.e., average contact pressure) in the formation of a glaze on the Nickel Alloy 1 surface (Figure 4-20).

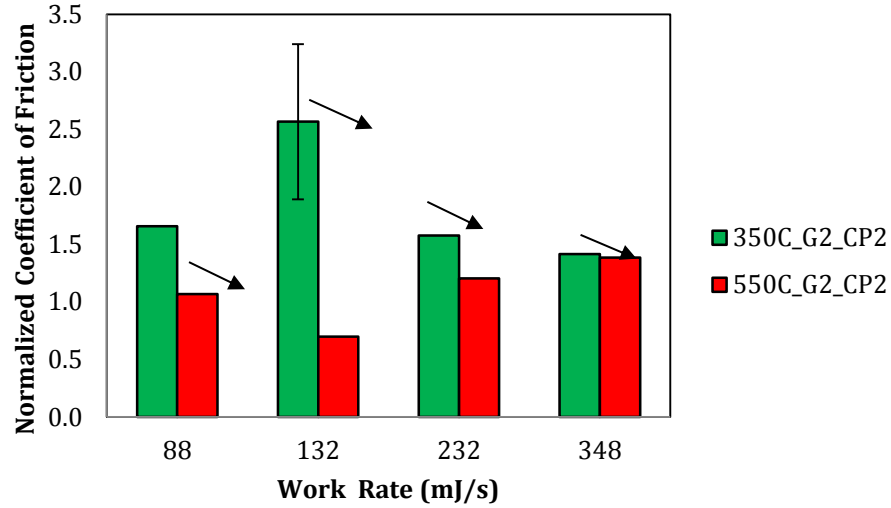


Figure 4-17: Effect of temperature on the coefficient of friction when plotted against the work rate for CP2 (Cobalt Alloy 1 cylinder / Nickel Alloy 1 ring).

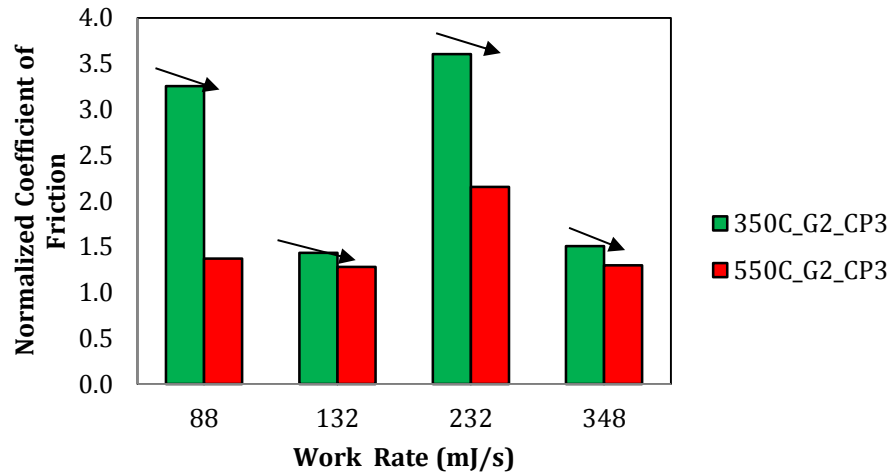


Figure 4-18: Effect of temperature on the coefficient of friction when plotted against the work rate for CP3 (Cobalt Alloy 2 cylinder / Nickel Alloy 1 ring).

At 550°C, the higher content of cobalt in CP1 makes it exhibit less friction at high loads (or pressures), whereas CP2 shows the least friction at the load conditions (Figure 4-21).

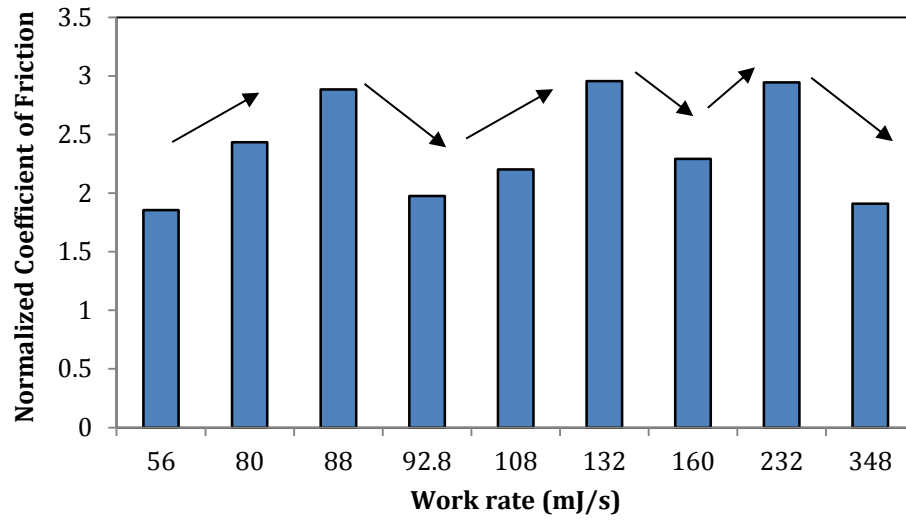


Figure 4-19: Effect of the work rate on coefficient of friction for G1_CP0 at RT (Cobalt Alloy 1 cylinder / Cobalt Alloy 1 ring).

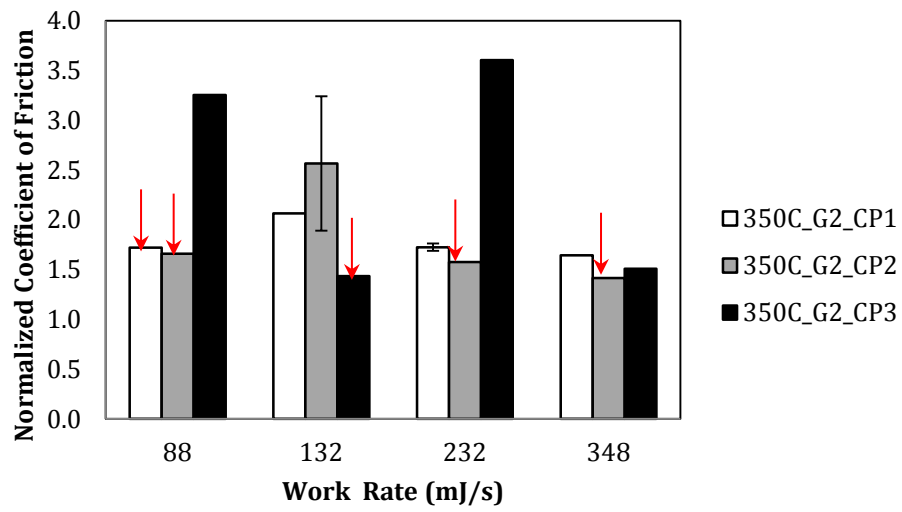


Figure 4-20: Coefficient of friction vs. work rate for different contact pairs at 350°C.

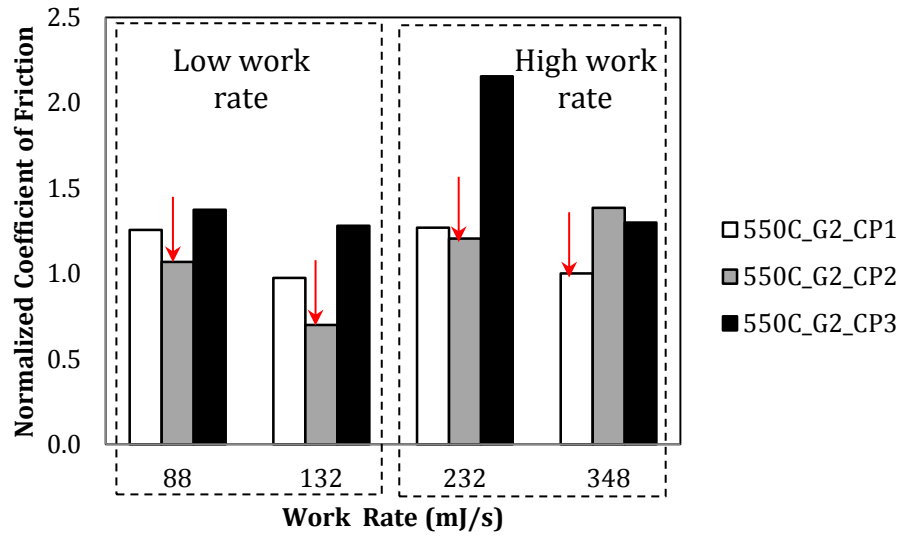


Figure 4-21: Coefficient of friction vs. work rate for different contact pairs at 550°C.

In order to summarize the results shown in Figure 4-20 and Figure 4-21, a wear resistance material selection map (based on the coefficient of friction) for a given temperature and work rate has, been developed as shown in Figure 4-22.

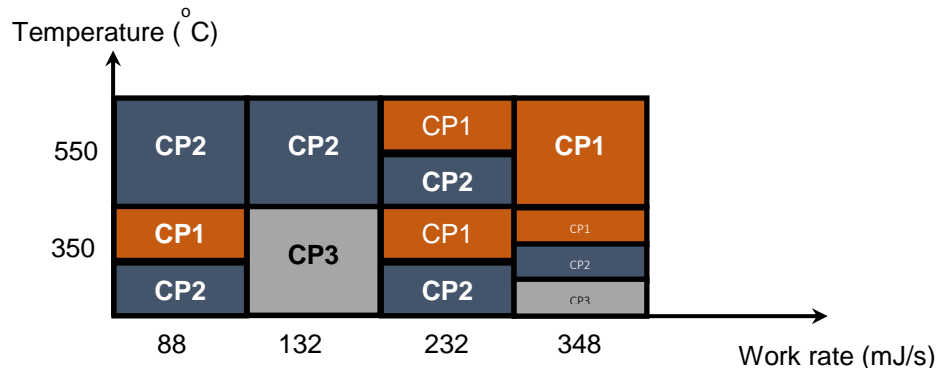


Figure 4-22: Material selection map (based on the coefficient of friction).

The evolution of the coefficient of friction with the number of cycles (or time) for all contact pairs and test conditions, is shown in Figure 4-23 to Figure 4-30.

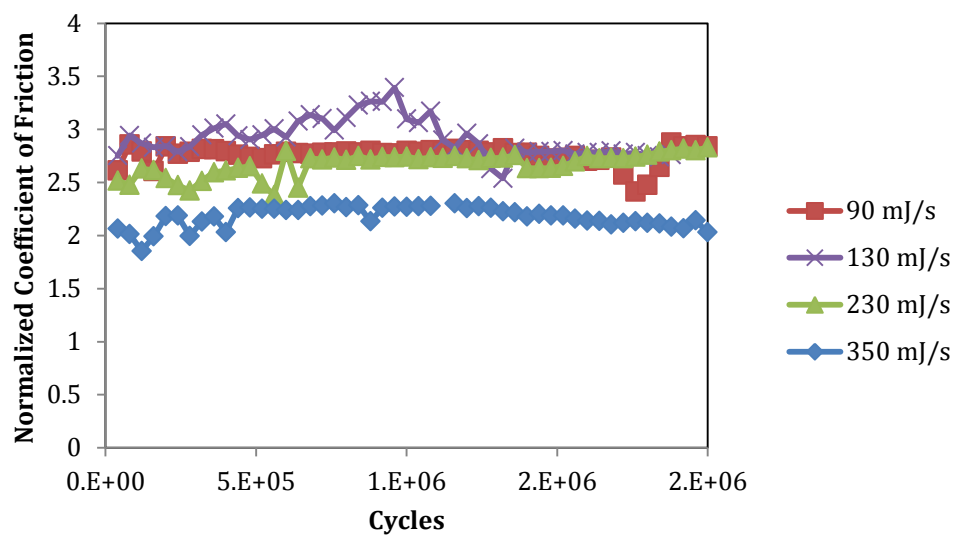


Figure 4-23: COF vs number of fretting cycles for CP0 at RT.

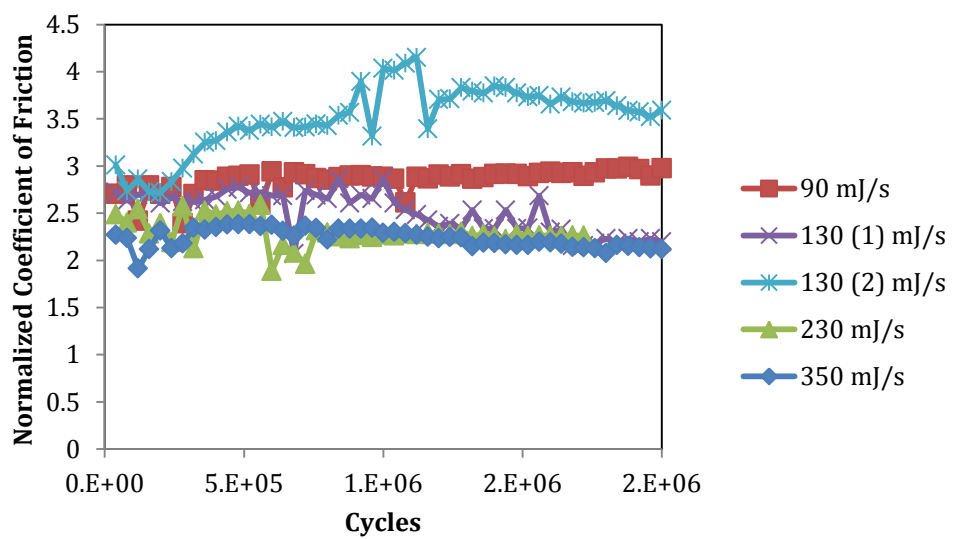


Figure 4-24: COF vs number of fretting cycles for CP1 at RT.

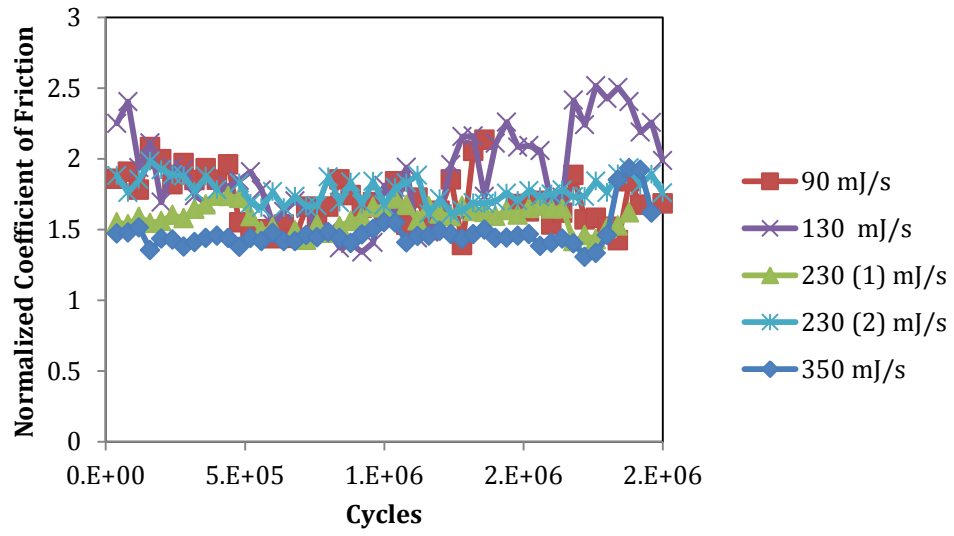


Figure 4-25: COF vs number of fretting cycles for CP1 at 350°C.

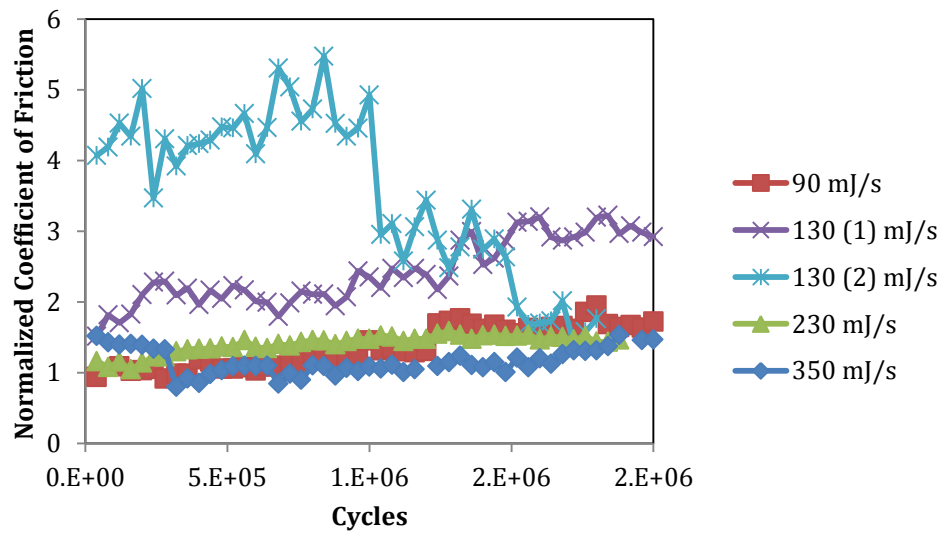


Figure 4-26: COF vs number of fretting cycles for CP2 at 350°C.

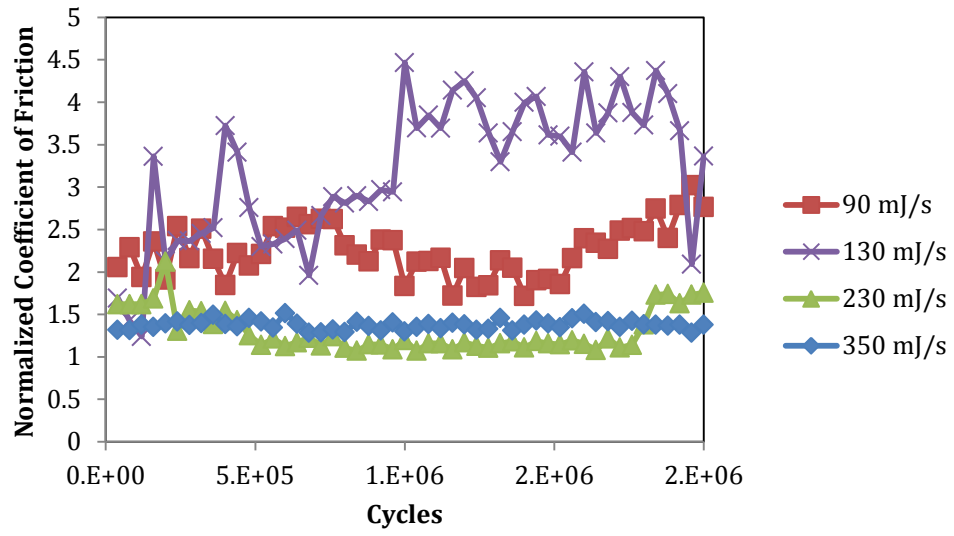


Figure 4-27: COF vs number of fretting cycles for CP3 at 350°C.

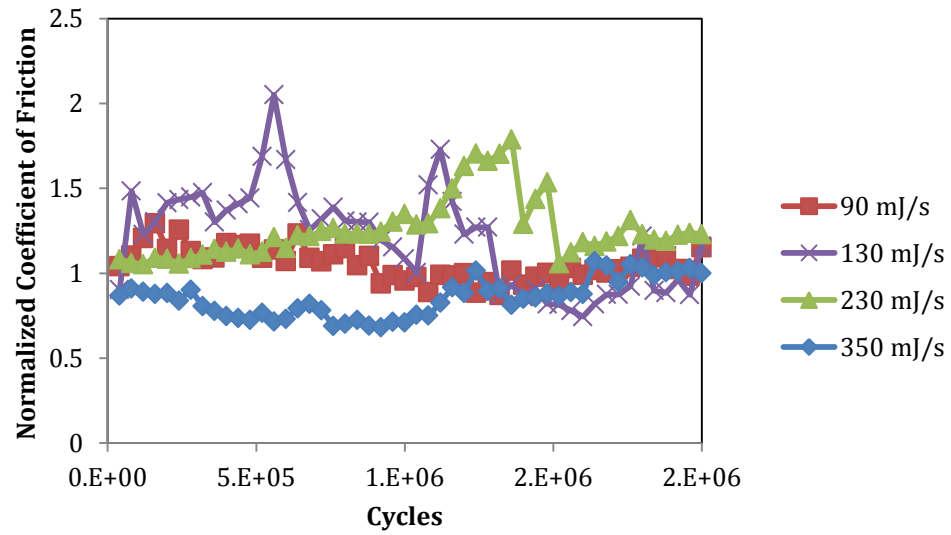


Figure 4-28: COF vs number of fretting cycles for CP1 at 550°C.

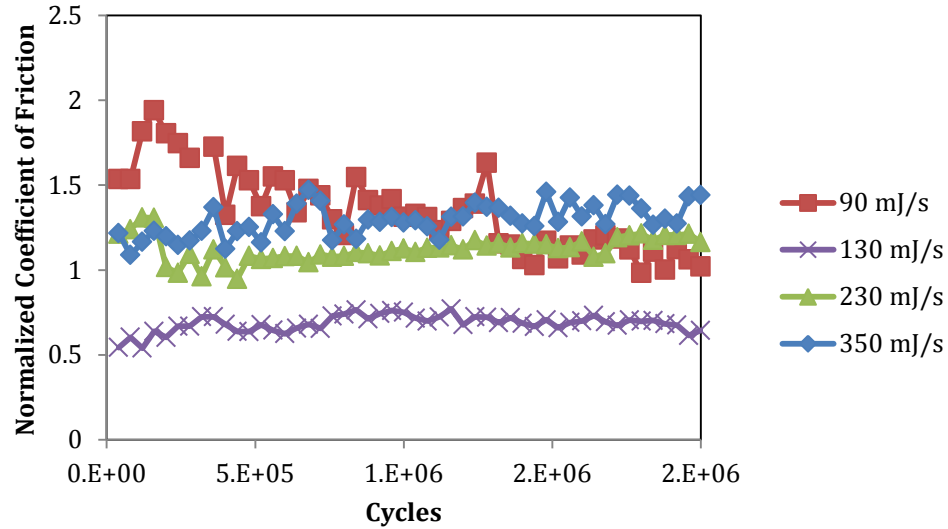


Figure 4-29: COF vs number of fretting cycles for CP2 at 550°C.

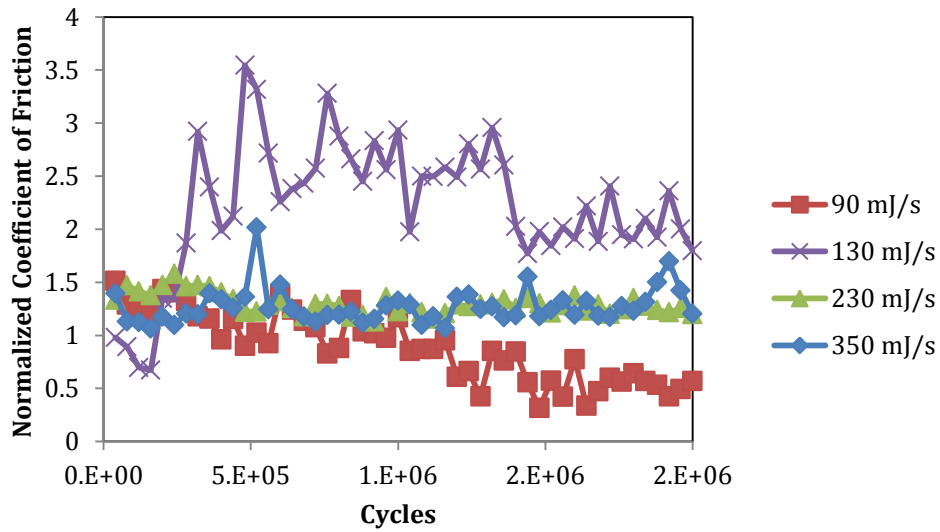


Figure 4-30: COF vs number of fretting cycles for CP3 at 550°C.

4.7. Evaluation of contact pressure

Figure 4-31 and Figure 4-32 show the mean contact pressure when plotted against the work rate for the different contact pairs at 350°C and 550°C, respectively. It can be clearly seen that the condition of the work rate of ~ 130 mJ/s represents the lowest contact pressure. This low pressure originates from the fact that this condition corresponds to the

lowest load and the largest amplitude of slip ($F_n = 11$ N and $A = 10\mu\text{m}$), which means an increased damaged contact area and a decreased mean contact pressure. The low pressure value is the reason for the distinct increase in the coefficient of friction at ~ 130 mJ/s because of the important role played by the pressure in the formation of glaze at high temperatures [14]. Low pressure means a lower number of asperities involved in the contact, and therefore, less frictional heat. The reduction in the frictional heat leads to a lower formation of glaze. This in turn leads to metal-to-metal contact, and therefore, higher coefficient of friction. From the wear point of view, the increase in the coefficient of friction is associated with an increase in adhesion [33]. Usually, it is also associated with an increase in the wear damage, following the delamination theory of wear [31, 32].

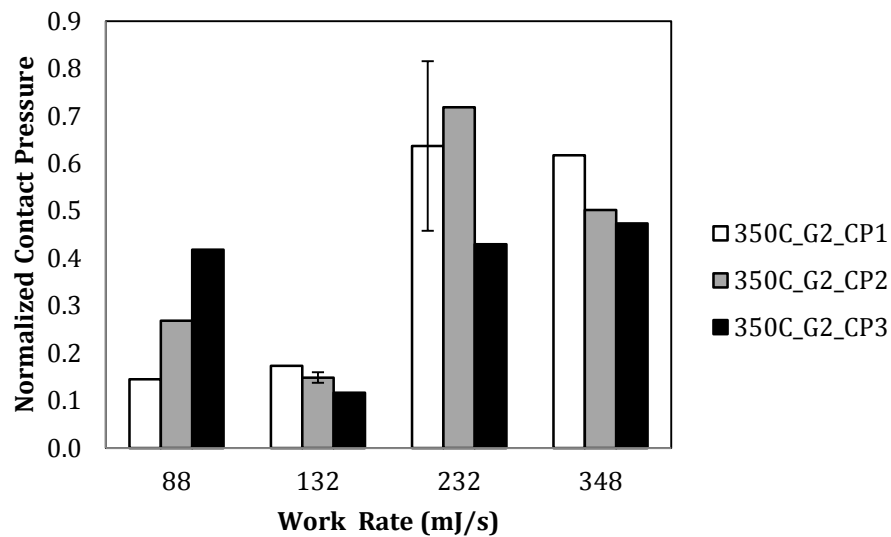


Figure 4-31: Contact pressure vs. work rate for different contact pairs at 350°C.

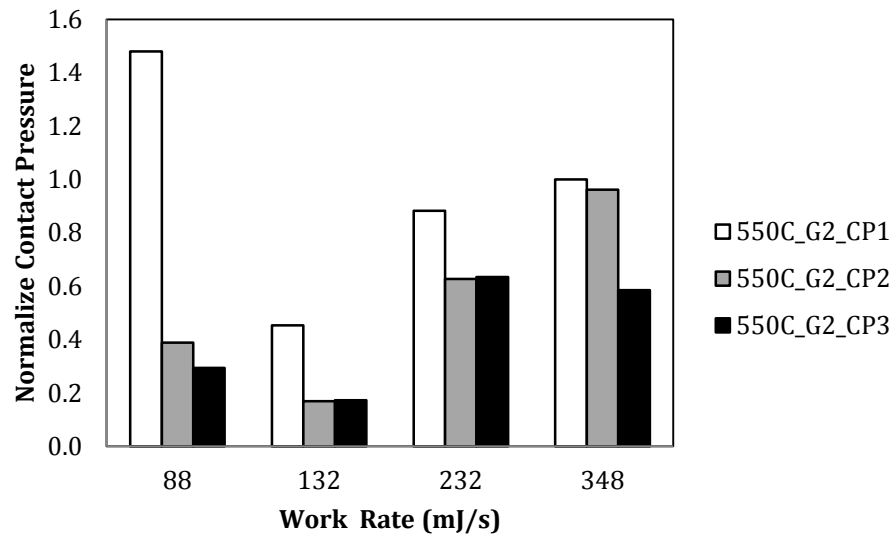


Figure 4-32: Contact pressure vs. work rate for different contact pairs at 550°C.

Chapter 5 Experimental Results:

In-depth Investigation for some Selected Case

5.1. Introduction

Since the contact pair CP1 showed the best overall tribological behaviour at 550°C, more investigation was needed in order to explain the effect of temperature on oxide formation, and consequently, on the friction and wear for this contact pair. In addition, for some selected cases related to CP2 and CP3, detailed investigations were also reported. The detailed study included in-depth investigation of the effect of fretting conditions on the wear resistance, samples cross sectioning, inspection using the scanning electron microscopy (SEM), chemical analysis using energy dispersive X-ray analysis (EDX) and Raman spectroscopy for oxide analysis.

5.2. Effect of loading conditions on friction and wear resistance

As was seen in Chapter 4, for CP1, there was an increase in the wear coefficient at 130 mJ/s (Figure 4.1). This was accompanied by an increase in the adhesion coming from the counterpart Cobalt Alloy 1 ring to the Cobalt Alloy 2 cylinder stationary specimen, as shown in Figure 5-1. In this figure, the material removed by abrasion (the negative wear) is shown in blue and the material transferred from the mating counterpart by adhesion (positive wear) is shown in red. Surprisingly, the steady state coefficient of friction does not show a notable rise at 130 mJ/s, as shown in Figure 4.15. Therefore, it was necessary to investigate the change of the coefficient of friction with time for CP1 at 550°C, and not to rely only on the steady state value that could mask some details happening during the process.

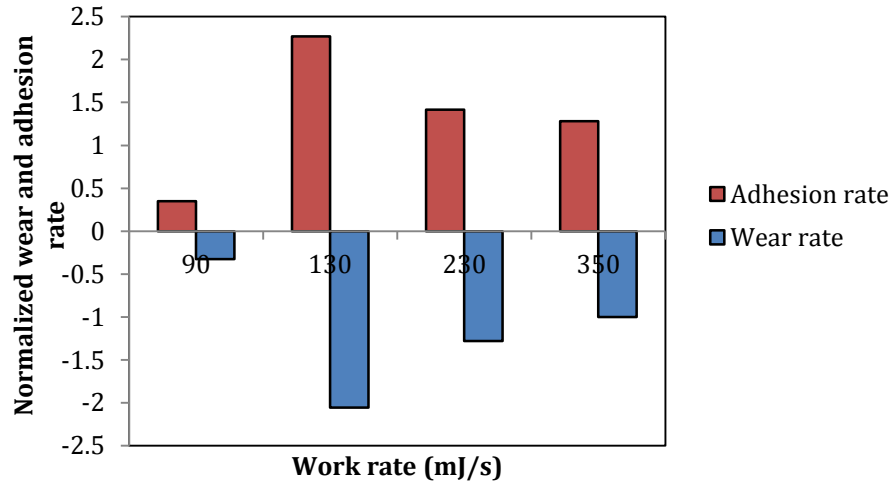


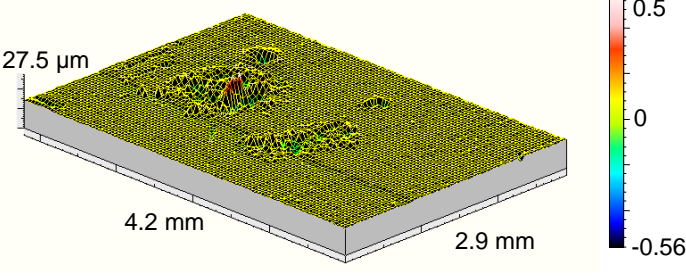
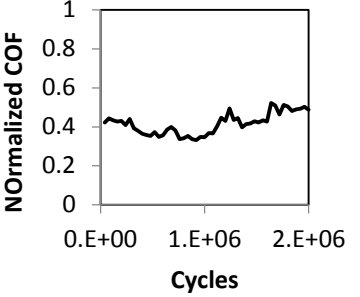
Figure 5-1: Wear rates and adhesion rates vs. the work rate for the Cobalt Alloy 2 specimen fretted at 550°C.

Table 5-1 shows the 3D topography and the evolution of the coefficient of friction with the number of fretting cycles for the different work rates at 550°C. At $\dot{W} = 130$ mJ/s, there is a clear increase in the coefficient of friction associated with high adhesion compared to other work rate conditions. It is suggested that the decrease in the contact pressure at $\dot{W} = 130$ mJ/s (Figure 4.31) affected the formation of protective oxides causing an increase in adhesion, especially at the early fretting stages, where breakdown of the oxide layer took place, leading to metal-to-metal contact, and consequently an increase the coefficient of friction. The role of the contact pressure in the formation of protective oxides was also reported by Hamdy and Waterhouse [14] who indicated that the increase in normal pressure in the contact area has a greater role in promoting formation of the glaze than the bulk temperature due to the frictional heat. The increase in wear associated with the increase in the coefficient of friction is in agreement with the delamination wear theory [31, 32], since an increase in friction increases the depth at which subsurface cracks initiate forming thicker wear debris. Waterhouse [33] reported similar observations when examining the role of adhesion and delamination in the fretting wear of different types of steels.

Table 5-1: 3Dtopography and evolution of the COF with the number of cycles at different work rates when the temperature was fixed to 550°C.

Conditions	3D Topography	Evolution of the coefficient of friction with time
$F_n = 10 \text{ N}$ $A = \pm 10 \text{ }\mu\text{m}$ $\dot{W} = 90 \text{ mJ/s}$		
$F_n = 10 \text{ N}$ $A = \pm 15 \text{ }\mu\text{m}$ $\dot{W} = 130 \text{ mJ/s}$		
$F_n = 30 \text{ N}$ $A = \pm 10 \text{ }\mu\text{m}$ $\dot{W} = 230 \text{ mJ/s}$		

Table 5-1 (cont): 3D topography and evolution of the COF with the number of cycles at 550°C.

Conditions	3D Topography	Evolution of the coefficient of friction with time
$F_n = 30 \text{ N}$ $A = \pm 15 \text{ }\mu\text{m}$ $\dot{W} = 350 \text{ mJ/s}$		

5.3. Effect of temperature on friction and wear resistance

In order to further investigate the wear reducing effect associated with the increase in temperature, the bulk temperature was varied between 25°C and 550°C at a fixed work rate of 350 mJ/s. Figure 5-2 shows that, within the investigated range, the wear coefficient for the Cobalt Alloy 2 cylinder stationary specimen (negative wear in blue) decreases with the increase of temperature, showing no transition temperature at which the wear resistance suddenly changes. When the volume of deposition on the counterpart Cobalt Alloy 1 ring oscillating specimen is plotted on the same graph, it can be observed that there is a peak at the temperature of 200°C after which the adhesion decreases. Figure 5-3 (a) shows the evolution of the coefficient of friction with the number of fretting cycles at different temperatures. It is notable that, at 200°C, the coefficient of friction drops first with time (or the number of cycles), then experiences some fluctuations before stabilizing. The high friction value observed at 200°C explains the rise in adhesion shown in Figure 5-2 at the same temperature. It is suggested that the development of the wear debris and the type of oxide formed at the interface are the reasons for this behaviour, as will be discussed in detail in the coming sections.

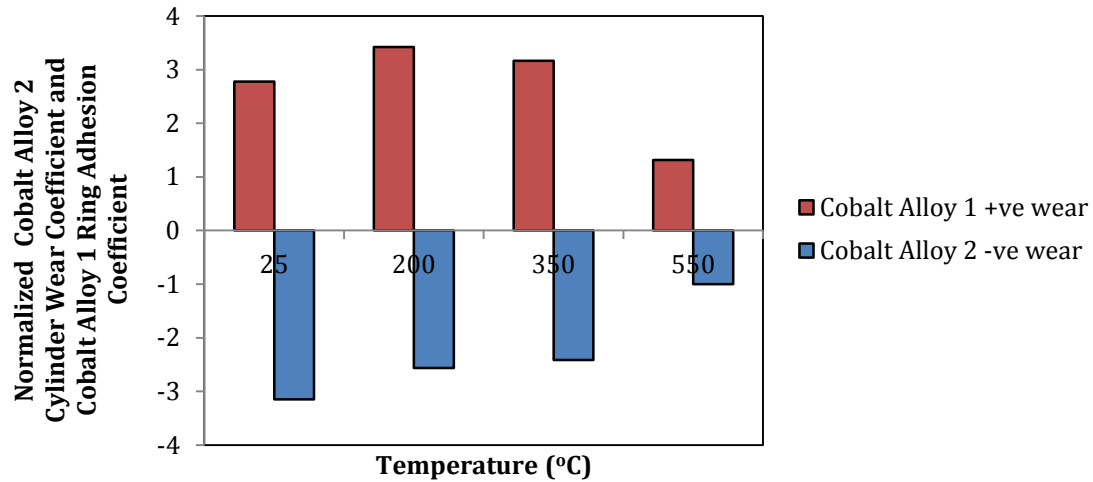


Figure 5-2: Effect of temperature on the wear coefficient for the Cobalt Alloy 2 stationary specimen and the adhesion coefficient of the Cobalt Alloy 1 oscillating specimen at $\dot{W} = 350 \text{ mJ/s}$ ($A = \pm 15 \text{ } \mu\text{m}$, $F_n = 30 \text{ N}$).

A plausible explanation is that with time (or cycles), the thin oxide film gets interrupted and transforms into loose wear debris. At this low bulk temperature level, the wear debris cannot form a protective layer; however, it experiences plastic deformation and hardening and performs a ploughing action, giving rise to the friction value. The newly created surface forms a thin oxide layer and the cycle repeats itself until a steady state situation is reached with entrapped debris causing an increase to the steady state friction value. Patel et al. [94] reported the rise in friction due to the entrapment of wear debris during the sliding wear of cobalt-based orthopaedic alloys at room temperature. Figure 5-3 (b) shows that the steady state coefficient of friction increases with temperature up to 200°C, then decreases steadily up to 550°C. This observation is consistent with previous investigations in unidirectional sliding for the Haynes 25 when rubbed against Hastelloy X within the same temperature range [8].

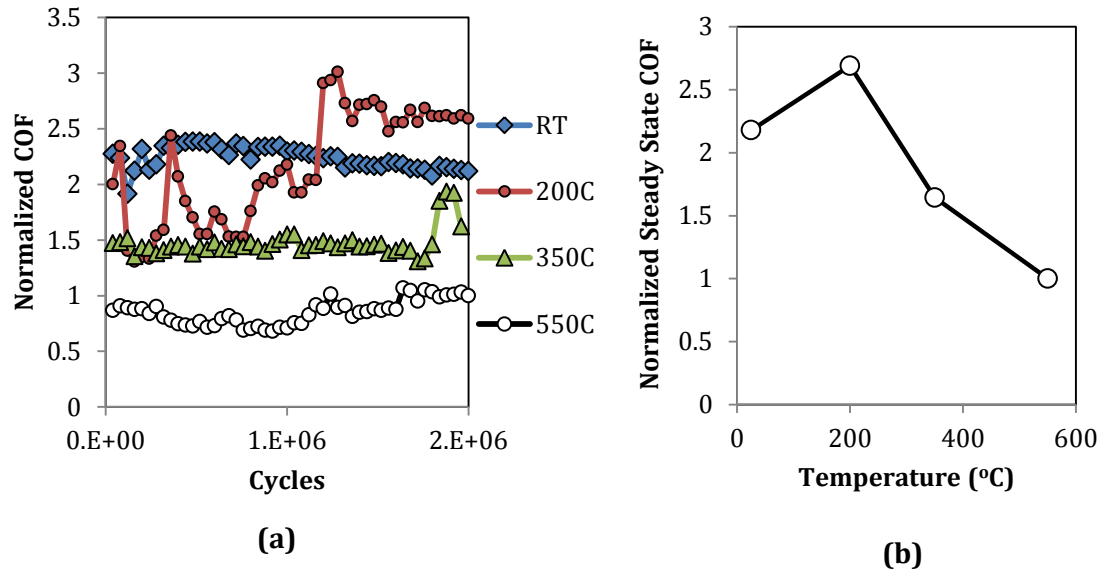


Figure 5-3: (a) Evolution of the coefficient of friction with time during the test and (b) steady state coefficient of friction at different temperatures.

5.4. Effect of temperature on oxide film composition and thickness

The surfaces of the Cobalt Alloy 2 cylinder specimens were examined by scanning electron microscope (SEM) and chemically analysed using Energy-dispersive X-ray spectroscopy (EDX) in order to understand the wear mechanism. Figure 5-4 shows the evolution of the oxide layer, formed on the fretted area, with temperature at a work rate of 350 mJ/s. At room temperature and at 200°C (Figure 5-4 (a) and (b), respectively), considerable abrasive wear is observed together with scratches and striations parallel to the fretting direction. Figure 5-4 (c) shows that at 350°C, a layer of glaze starts to form; however, this layer experiences surface cracking due to the lack of ductility at this temperature level. At 550°C (Figure 5-4 (d)), the oxide layer becomes more developed, and forms some load bearing areas, which are elevated above the nominal surface and within which damage takes place.

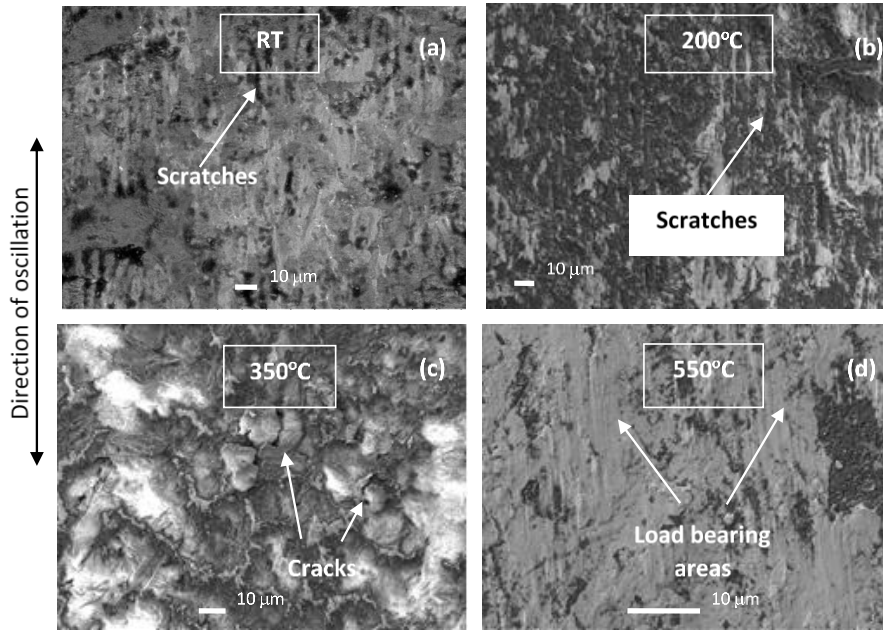


Figure 5-4: Evolution of the oxide layer on the surface of the Cobalt Alloy 2 cylinder with temperature at a work rate of 350 mJ/s (a) RT, (b) 200°C, (c) 350°C, and (d) 550°C.

Figure 5-5 (a) shows the 3D topography of the cross section for the specimen fretted at 200°C. The load bearing areas are not seen on the specimen, but instead, striations and scratches are visible. On the other hand, the specimen fretted at 550°C (Figure 5-5 (b)) has some of the load bearing areas appearing to be higher than the nominal surface of the specimen and within which the damage takes place.

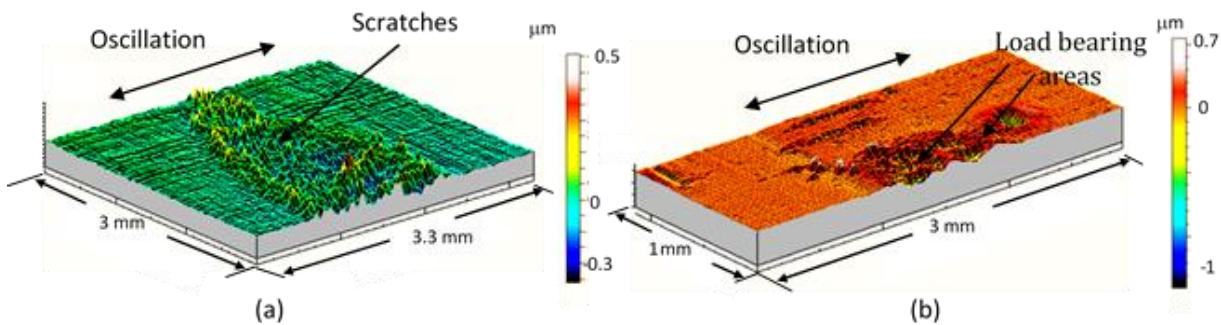


Figure 5-5: 3-Dimensional topography of the extent of the fretted area at 2×10^6 cycles for the Cobalt Alloy 2 cylinder at a work rate of 350 mJ/s, (a) specimen fretted at 200°C and (b) specimen fretted at 550°C.

Figure 5-6(a) and (b) show the cross section of the specimen fretted at 200°C, illustrating that the debris found within the fretted region is characterized by its small size and is likely to be the reason for the striations appeared on the surface in Figure 5-4 (a) and (b). In addition, extremely thin scattered oxide zones (around 1 - 2 μm) were identified above the fretted area, and appeared in the cross section as darker zones. The EDX chemical analysis of points in the substrate and in the oxide film (points A and B, respectively) is shown in Figure 5-6 (c), revealing high oxygen content in the oxide layer when compared to the substrate chemical composition.

Figure 5-6(d) and (e) show the cross section of the specimen fretted at 550°C. A thicker continuous oxide layer (2-10 μm) is constituted over the substrate. This layer, experiencing plastic deformation and delamination of its upper portion, adheres to the underlying substrate while bearing the load during the contact. Therefore, the wear takes place in the oxide itself and not in the substrate. The presence of this oxide film explains the substantial reduction in the coefficient of friction shown in Figure 5-3 resulting from the precluded metal to metal contact. In this layer, delamination takes place and the plate-like wear debris is formed as a result of subsurface crack initiation and propagation, as shown in Figure 5-6(e).

The oxidation behaviour for this alloy, at that temperature level, is similar to behaviour proposed by Bill [12] who suggested that for the Ni-Cr-Al alloy, between 650°C and 800°C, metal-to-metal contact is inhibited through the development of a protective continuous oxide film. This film remains intact, adhering to the substrate and thick enough to support the contact load. When the oxide film reaches a thickness value of 5 - 6 μm , it experiences delamination, and the delaminated flake-like wear debris is broken down or crushed into smaller particles in the form of wear debris as shown in Figure 5-6(f). This is consistent with the oxidational wear mechanism proposed by Quinn [95], who suggested that when the oxide film thickness reaches a critical value, the film becomes unstable and breaks up to form flakes, and eventually, wear debris.

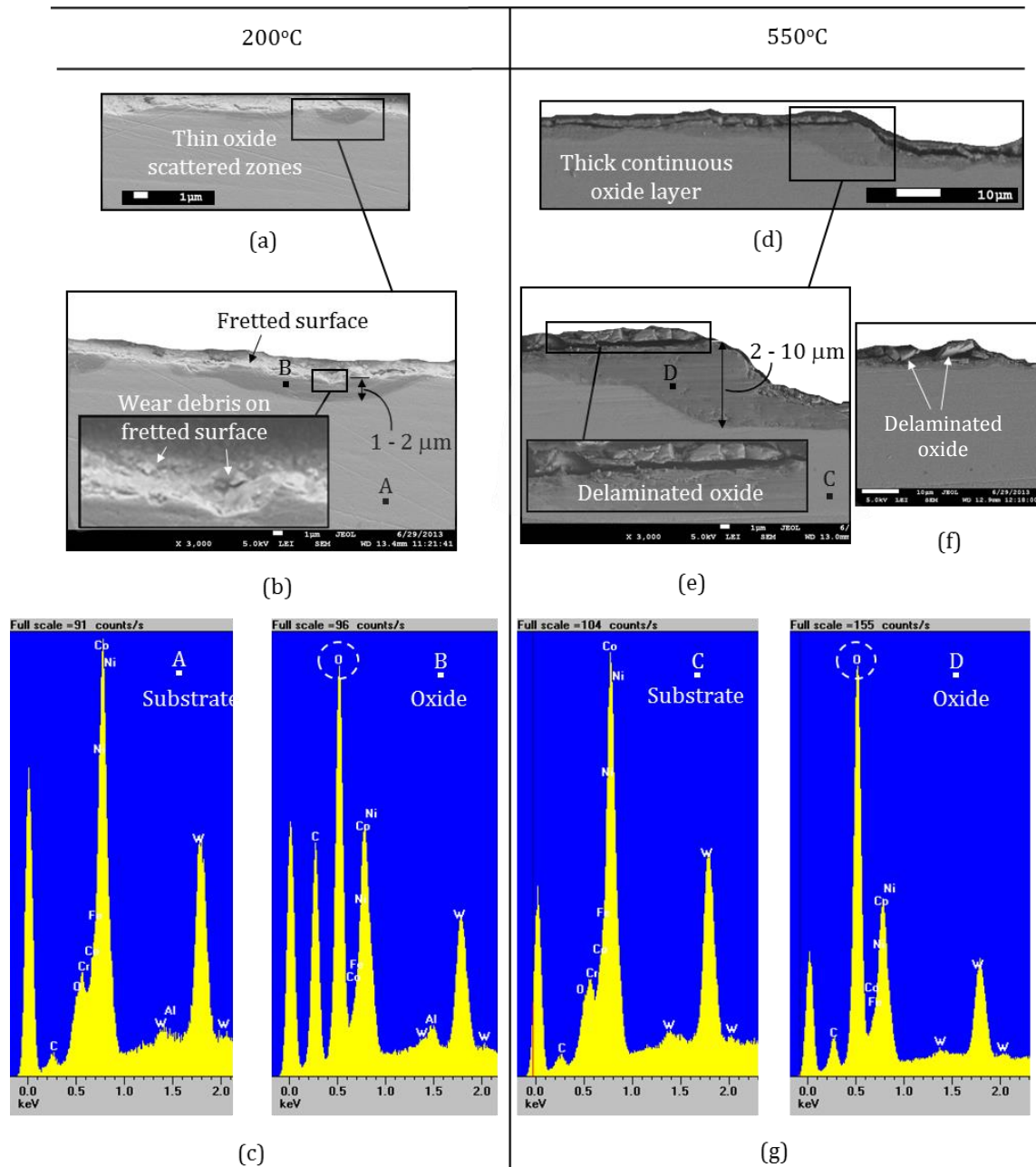


Figure 5-6: SEM photomicrographs and EDX chemical analysis of the Cobalt Alloy 2 cylindrical specimens cross sections (a) cross section of the specimen fretted at 200°C, (b) scattered thin oxide zones at 200°C, (c) EDX chemical analysis of the specimen fretted at 200°C, (d) cross section of the specimen fretted at 550°C, (e) thicker oxide layer at 550°C, (f) delaminated oxide broken into smaller debris and (g) EDX chemical analysis of the specimen fretted at 550°C.

In addition, this is similar to the mechanism proposed by Stott [3] who suggested that for nickel-based alloys, between 600°C and 800°C, the glaze once formed, remains stable and oxidation of the alloy can continue below the glaze as a result of severe deformation. Figure

5-6 (g) shows the chemical analysis of the specimen fretted at 550°C where high oxygen content identifies the oxide layer (point D) when compared to the substrate chemical analysis (point C).

5.5. Oxide film composition and contact temperature

The surfaces of the Cobalt Alloy 2 cylinder specimens fretted at 200°C and 550°C were analyzed using Raman Spectroscopy in order to identify the composition of oxides formed on the surface at bulk temperatures of 200°C and 550°C. Figure 5-7 shows the Raman spectroscopy at the points corresponding to the shown optical images for the specimens fretted at 200°C and 550°C.

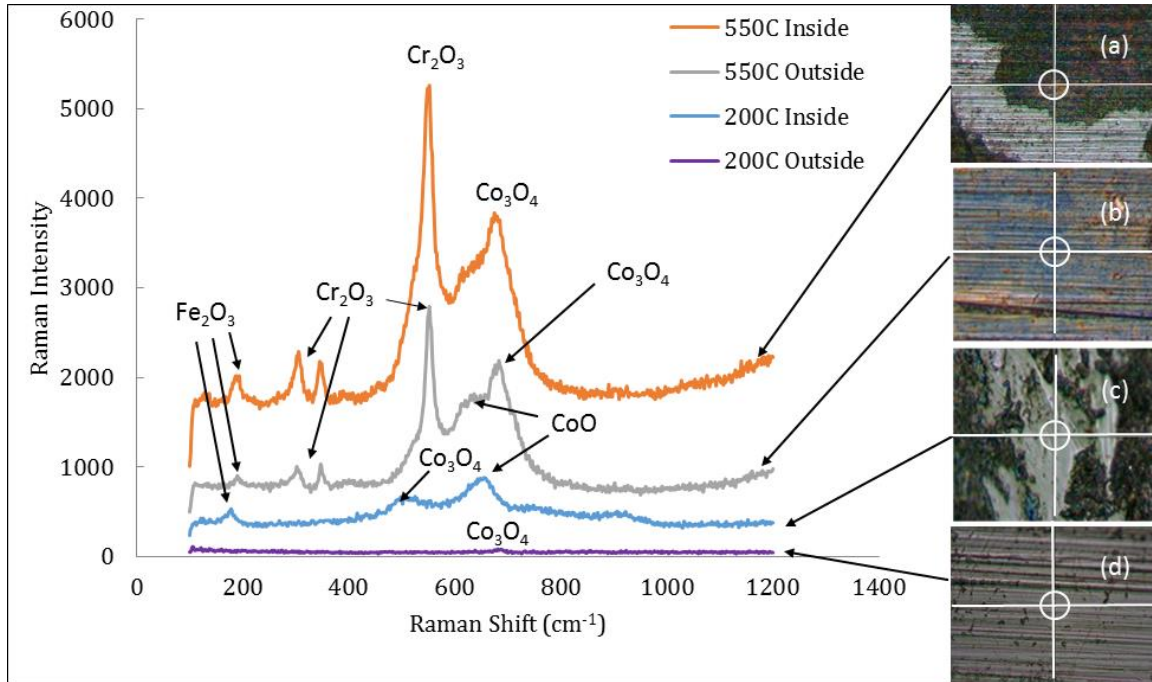


Figure 5-7: Raman spectroscopy for the Cobalt Alloy 2 cylinder specimen fretted at 200°C and 550°C and the corresponding optical images (a) within the fretted area at 550°C, (b) outside the fretted area at 550°C, (c) within the fretted area at 200°C, and (d) outside the fretted area at 200°C

Table 5-2 summarizes the series of identified oxides and their corresponding wave numbers (Raman shift). These wave numbers are compared to the analysis of similar oxides in [96-99] in order to identify the existence of these oxides.

Table 5-2: Series of oxides existing on the surfaces of the specimens fretted at 200°C and 550°C.

Oxide	Wave number (cm ⁻¹)			
	200°C outside	200°C inside	550°C inside	550°C outside
Cr ₂ O ₃	-	-	305.9 - 345.7 - 552.6	302.4 - 347.5 - 552.6
Co ₃ O ₄	681.8	525.5	680.1	683.4
CoO	-	653.4	-	656.8
Fe ₂ O ₃	-	178.1	185.1	185.1

As Figure 5-7 shows, the Raman analysis reveals the highest peaks representing the major oxides existing on the surface. Chromium III oxide (Cr₂O₃) peaks were observed to be the dominant oxide within and outside the fretted area of the specimen fretted at 550°C at a frequency (or Raman shift) of 304 cm⁻¹, 345.7 cm⁻¹ and 552.6 cm⁻¹. However, the same oxide was not observed on the specimen fretted at 200°C. Since the Cr₂O₃ is known for its good tribological characteristics of low coefficient of friction, high hardness and resistance to microcracks and particles fracture [100], its existence on the specimen fretted at 550°C explains the lower friction values exhibited at that temperature level when compared to the specimen fretted at 200°C.

In addition, cobalt monoxide (CoO) was found on the specimen fretted at 200°C at a frequency of 653.4 cm⁻¹, and only outside the damaged area of the specimen fretted at 550°C at a wave numbers of 656.8 cm⁻¹. It is suggested that this oxide is one of the main reasons why there is an increase in the coefficient of friction at 200°C, as shown in Figure 5-3. This is strengthened by the work of Foley et al. [101] who investigated the frictional characteristics of pure cobalt sliding against pure cobalt in air. They discovered that, at room temperature, the presence of CoO led to a two fold increase in the coefficient of friction at the latter stages of the wear process when compared to the early stages. The absence of this oxide from the damaged area of the specimen fretted at 550°C is an indication that the contact temperature within this area is between 600°C and 700°C since

CoO transforms into Co_3O_4 at that temperature range [102]. The intensive blue-green colour seen on the specimen fretted at 550°C shown in the optical image of Figure 5-7 (b) is proof of the existence of the Co-oxide responsible for the blue colour and the Cr-oxide responsible for the green colour.

By considering the thicknesses of the oxide to be proportional to the peak of the Raman spectrum [99], the Arrhenius equation can be used to correlate the oxide thickness to the contact temperature. Figure 5-9, which is adopted from Stachowiak [103], shows the schematic of a typical cross section of a metallic surface during high temperature oxidative wear with the oxide layer formed on the surface. Considering the film thickness within the fretted area to be δ_{o1} and the film thickness outside the fretted area to be δ_{o2} , where $\delta_{o1} > \delta_{o2}$. The Arrhenius equation can be written as [91];

$$k_{\text{oxidation}} = A_{\text{Arrhenius}} e^{\frac{-E_a}{RT}} \quad (5-1)$$

where $k_{\text{oxidation}}$ is the oxidation rate constant, $A_{\text{Arrhenius}}$ is the pre-exponential factor, E_a is the activation energy for the oxidation process, R is the universal gas constant, and T is the absolute temperature. The previous equation is applied to the dominant oxide, which is the Cr_2O_3 , having an average activation energy of approximately 150 kJ/mol[104]. Assuming the oxide growth to follow a parabolic equation, the ratio of the rate constants is equivalent to the square of the film thicknesses ratio. The relationship between the film thickness within the fretted area δ_{o1} and the film thickness outside the fretted area δ_{o2} can be expressed as:

$$\left(\frac{\delta_{o1}}{\delta_{o2}}\right)^2 = e^{-E_a(\frac{1}{T_1} - \frac{1}{T_2})/R} \quad (5-2)$$

The ratio δ_{o1}/δ_{o2} can be considered proportional to the ratio of the Cr_2O_3 intensity peaks within and outside the fretting region in Figure 5-7, which is around 2. If the temperature outside the fretted area T_2 is 550°C, then one can estimate the contact temperature within the fretted area T_1 to be around 600°C. The previous analysis underlines the effect of the frictional heat and the importance of calculating precisely the contact temperature in order to properly understand and predict the oxide composition, the kinetics of oxidation, and

consequently, the tribological aspects associated with the formed oxides during fretting and wear, especially at high temperature.

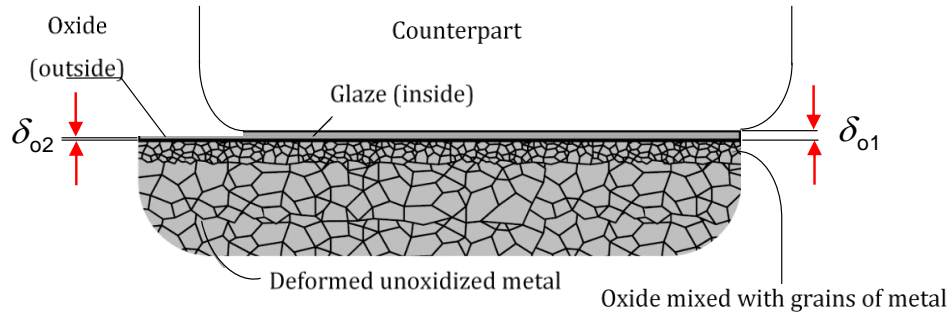


Figure 5-9: Typical cross section of a metallic surface during high temperature oxidative wear, showing the oxide thickness within and outside the fretted area. Image adopted from Stachowiak and Batchelor [103].

5.6. Further investigation of some selected ring samples

When looking at the wear coefficients values shown in Figure 4.6, it can be seen that, at 550°C and at the highest work rate value (350 mJ/s), the pairCP1 showed less wear coefficient than CP3, although they share the same cylinder sample material (Cobalt Alloy 2). Moreover, when the temperature rose from 350°C to 550°C, the pairCP3 showed an increase in the wear coefficient (Figure 4.3) associated with a decrease in the coefficient of friction (Figure 4.17). As mentioned previously, this behaviour was recorded in [89] and [90], but no real attempt was made to explain it. Therefore, the following ring samples were further analysed in order to answer the above mentioned questions:

1. The CP1 Cobalt Alloy 1 ring fretted at 550°C (against a Cobalt Alloy 2 Cylinder).
2. The CP3 Nickel Alloy 1 ring fretted at 550°C (against a Cobalt Alloy 2 Cylinder).
3. The CP3 Nickel Alloy 1 ring fretted at 350° (against a Cobalt Alloy 2 Cylinder).

Figure 5-10(a) and (b) show that the Cobalt Alloy 1 ring sample fretted at 550°C formed a thick dense oxide layer having a thickness of 7 - 12 µm. It can be seen also that the wear occurs only in the oxide layer with some deformation taking place in the substrate. Figure 5-10(c) and (d) show that the Nickel Alloy 1 ring sample fretted at 550°C formed a thinner,

less dense oxide layer having a thickness that ranges between 3 and 5 μm , and that the wear started in the oxide until reaching the substrate at some points. Figure 5-10(e) and (f) show that the Nickel Alloy 1 ring sample fretted at 350°C formed a thin and dense oxide layer that had a thickness of 2 - 4 μm and that this layer was interrupted at some points.

The EDX chemical analysis of the oxide film for the samples mentioned above is shown in Figure 5-11. The high oxygen peaks confirms that this layer represents the oxide. Despite the fact the Nickel Alloy 1 sample does not contain tungsten, a relatively high peak of tungsten could be observed in the oxide layer of the Nickel Alloy 1 ring samples fretted at 550°C and 350°C. This confirms that material has been transferred from the counterpart (the Cobalt Alloy 2 cylinder), as a result of high adhesion. In addition, the Nickel Alloy 1 ring samples fretted at 350°C shows higher Molybdenum content than the Nickel Alloy 1 ring sample fretted at 550°C.

Figure 5-12 shows the Raman spectroscopy of the three ring samples, and Table 5-3 summarizes the series of oxides identified and their corresponding wave numbers (Raman shift). The following observations can be made:

1. The Nickel Alloy 1 ring sample fretted at 350°C shows the highest peak of cubic chromium oxide Cr_2O_3 , followed by the Cobalt Alloy 1 ring sample fretted at 550°C, then the Nickel Alloy 1 ring sample fretted at 550°C. Since Cr_2O_3 is known for its good tribological characteristics of high hardness and resistance to microcracks and particles fracture [100], its concentration on the sample explains the better behaviour of the CP3 at 350°C when compared to its behaviour at 550°C.
2. Table 5-4 shows that the maximum wear depth decreases with the increase of Cr_2O_3 content on the surface of the analysed ring samples.
3. The Nickel Alloy 1 ring sample fretted at 350°C showed a high peak of molybdenum trioxide MoO_3 , which works with the Cr_2O_3 to reduce the wear damage [105].
4. The two ring samples fretted at 550°C show peaks of tungsten trioxide WO_3 which is an oxide that offers dry lubrication based on its relative softness [106]. Its absence from the Nickel Alloy 1 ring sample fretted at 350°C explains the dense and hard-looking oxide shown in Figure 5-10 (e) and (f).

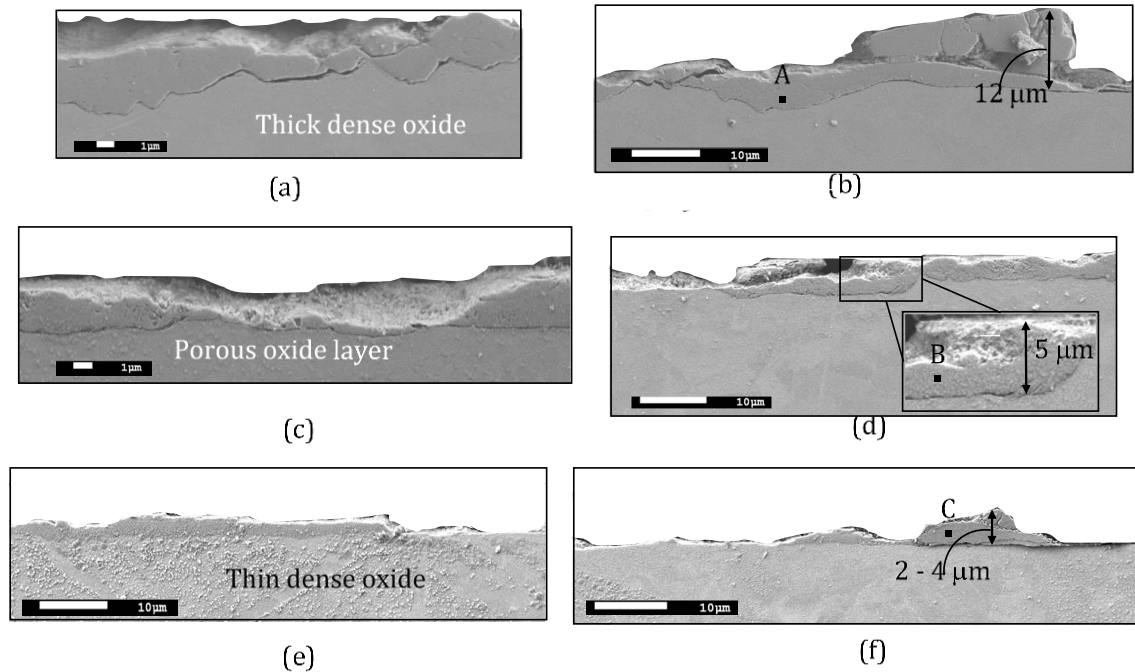


Figure 5-10: SEM photomicrographs of the cross section for the analysed ring samples, (a) and (b) the CP1 Cobalt Alloy 1 ring sample fretted at 550°C, (c) and (d) the CP3 Nickel Alloy 1 ring sample fretted at 550°C, and (e) and (f) the CP3 Nickel Alloy 1 ring sample fretted at 350°C.

5. The tungsten trioxide WO_3 is prone to water adsorption from air based on its hygroscopic properties [107]. Its high concentration on the Nickel Alloy 1 ring sample fretted at 550°C explains the porous structure shown in Figure 5-10 (c) and (d).
6. For the two CP3 Nickel Alloy 1 ring samples, although the increase in temperature from 350°C to 550°C is associated with a decrease in the friction, it is not associated with a decrease in wear damage (wear coefficient and wear depth). This can be attributed to two reasons. First, more Cr_2O_3 exists on the surface of the 350°C sample which hinders the increase in the wear depth. Second, a high content of WO_3 exists on the surface of the 550°C sample, which makes the oxide softer with lower interfacial shear strength (lower friction), and at the same time, causes the damage to occur in the oxide, giving high wear rate and maximum wear depth values.

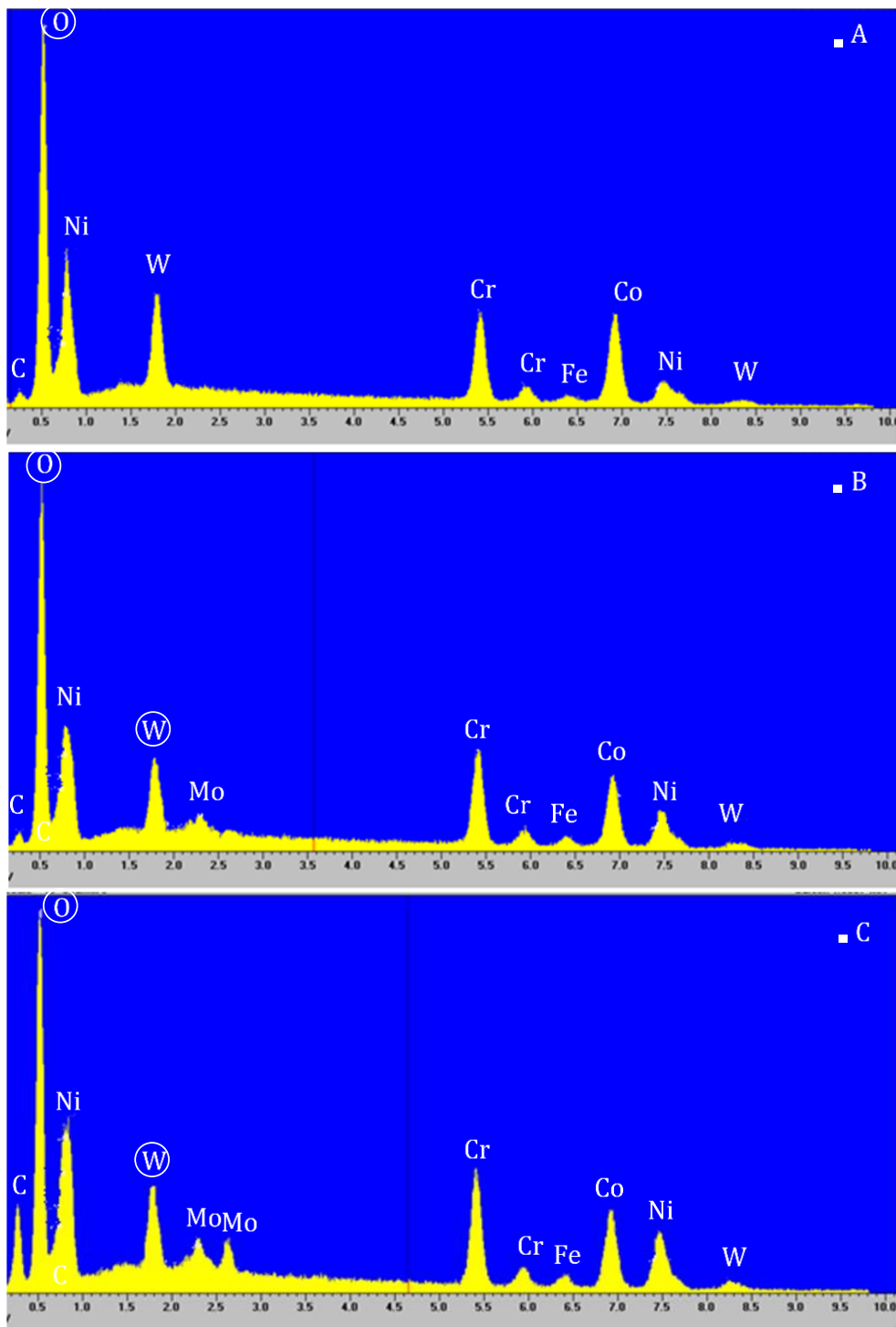


Figure 5-11: EDX chemical analysis of the analysed ring samples, (a) CP1 Cobalt Alloy 1 ring sample fretted at 550°C, (b) CP3 Nickel Alloy 1 ring sample fretted at 550°C, and (c) CP3 Nickel Alloy 1 ring sample fretted at 350°C. The spectra show high tungsten content in the oxide transferred from the Cobalt Alloy 2 cylinder sample.

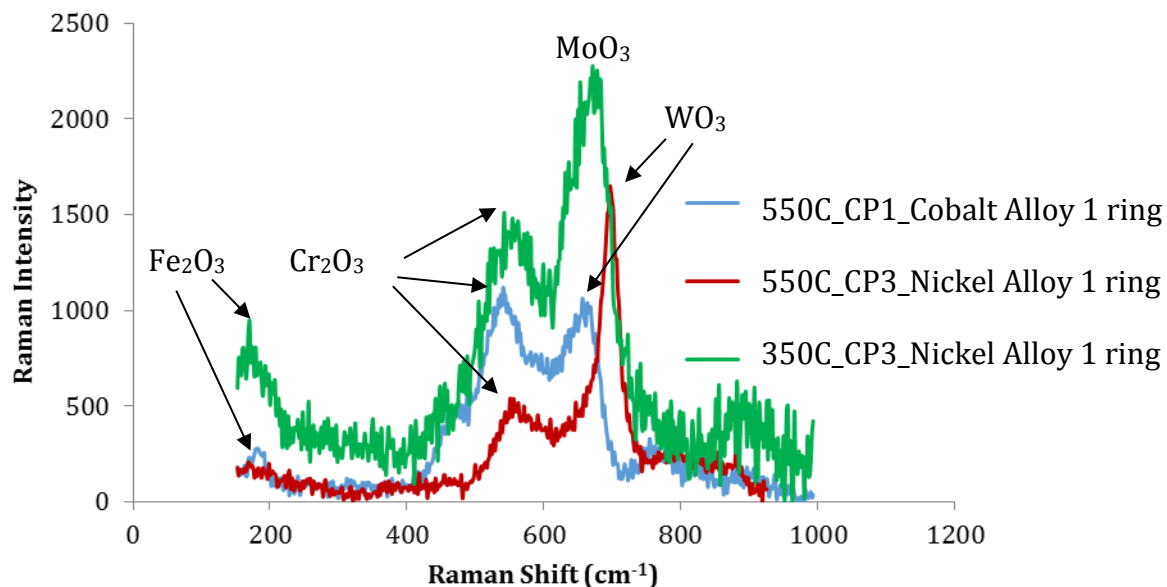


Figure 5-12: Raman spectroscopy for the CP1 Cobalt Alloy 1 ring sample fretted at 550°C, CP3 Nickel Alloy 1 ring sample fretted at 550°C, and CP3Nickel Alloy 1 ring sample fretted at 350°C

Table 5-3: Series of oxides existing on the surfaces of the samples fretted at 200°C and 550°C.

	Wave number (cm ⁻¹)		
	550°C-CP1-Cobalt Alloy 1 Ring	550°C-CP3-Nickel Alloy 1 Ring	350°C-CP3-Nickel Alloy 1 Ring
Co ₃ O ₄ [108]	475	-	-
Cr ₂ O ₃ [97]	540.5	550.6	542.5
WO ₃ [109]	656.4	698	-
MoO ₃ [110]	-	-	673
Fe ₂ O ₃ [99]	187	-	170

Table 5-4: Chromium oxide Cr_2O_3 peaks and the corresponding wear depth.

	550°C-CP1- Cobalt Alloy 1 Ring	550°C-CP3- Nickel Alloy 1 Ring	350°C-CP3- Nickel Alloy 1 Ring
Cr_2O_3 Peaks	1117.2	538	1509
Maximum wear depth (μm)	8.2	13.6	7.5

Chapter 6 Contact Temperature Prediction in Fretting Wear: Significance of the Frictional Heat and Model Description

6.1. Introduction

The frictional heat developed at the contact interface has a decisive effect on the wear behaviour of the tribo-systems during fretting wear. The experimental results in Chapter 4 and Chapter 5 showed that the contact temperature at the interface is higher than the bulk temperature due to frictional heating. With the difficulties of measuring contact temperature and the oversimplification existing in available models, the need for more reliable models becomes essential. The fretting wear damage is a complicated process that involves interaction between several components. Any damage changes the geometry of the mating components and produces frictional heat that has a crucial effect on the oxidation process, mechanical and physical properties, material microstructure and subsurface deformation. It can be concluded that contact temperature affects and is being affected by the wear damage, making the process nonlinear by nature. In addition, there exist a transition temperature(s) for some alloys, at which the wear rate changes significantly. It is therefore essential to identify the contact temperature in order to properly understand the fretting wear process [18]. A proper understanding of the nature of engineering surfaces and the development of frictional heat is also imperative to adequately handle the prediction of contact temperature.

6.2. Nature of engineering surfaces, development of frictional heat and constriction effect

When two engineering surfaces are brought into contact under mechanical loading, the contact takes place at some discrete points named 'micro-contact areas' (MCAs) due to the existence of roughness and waviness in a material, as shown in Figure 6-1. The nature of engineering surfaces makes the real area of contact much smaller than the apparent area

and the waviness in the surface makes these micro-contact areas cluster in a much smaller number of zones called the 'contour areas' [111].

At the state of equilibrium, the applied normal force on the micro-contact areas is balanced with the resistance of the material, which can be mathematically expressed as:

$$F_n = p_a \cdot A_a = p_m \cdot A_r \quad (6-1)$$

where F_n is the normal load, p_a is the average applied contact pressure, A_a is the apparent contact area, p_m is the flow stress of the softer material, and A_r is the real contact area.

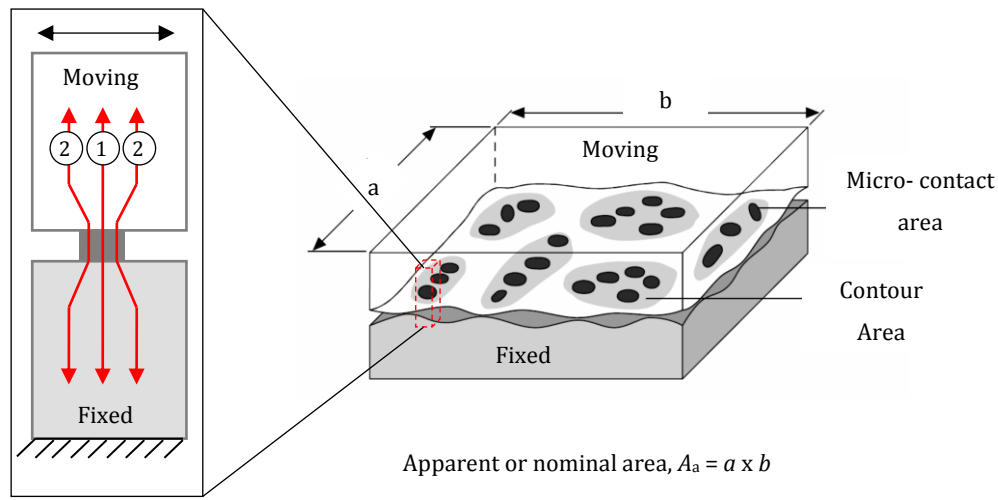


Figure 6-1: Apparent area, contour areas, micro-contact areas and the spreading of heat flow lines to the two bodies.

It should be noted that the flow stress p_m is a function of the coefficient of friction, the slope of the surface asperities and the material strain hardening [60]. However, as an approximation, p_m can be usually taken as the hardness of the softer material at the surface, which is nearly three times the yield strength [112].

Due to sliding, frictional energy is generated at these MCAs, which has undergone plastic deformation. The instantaneous shear flow comes from the multiplication of the frictional force by the sliding velocity,

$$Q = \mu F_n |v(t)| \quad (6-2)$$

where Q is the heat flow, μ is the coefficient of friction, v is the sliding velocity. The instantaneous heat flux supplied to the real contact area at the asperity level or MCA, q_{mic} , is a sinusoidal time-dependent function that can be expressed as:

$$q_{mic} = \frac{Q}{A_r} = \frac{\mu F_n |v(t)|}{A_r} = \mu p_m |v(t)| = \mu p_m (2\pi a f) |\sin(2\pi f t)| \quad (6-3)$$

where A_r is the real area of contact, p_m is the flow stress of the softer material, a is the amplitude of slip, f is the frequency of oscillation and t is the time.

The ratio ε^2 , between the apparent and the real contact area, is called the constriction ratio, and is defined as:

$$\varepsilon^2 = \frac{A_r}{A_a} = \frac{p_a}{p_m} \quad (6-4)$$

When $A_r = A_a$, ε^2 equals unity, the contact is perfect and that the heat flow lines do not spread as they leave the micro-contact areas, like line 1 in Figure 6-1. On the other hand, when ε^2 is not unity, the spreading of heat flow lines takes place instead of following the least resistance straight path, like line 2 in Figure 6-1. This adds more thermal resistance termed the “thermal constriction resistance”.

6.3. Effect of frictional heat on fretting wear by delamination

The experimental results in Chapter 5 showed that the oxide layer formed on the surface experienced delamination and formed plate-like wear debris. This debris was further broken down forming smaller particles. It is believed that during fretting wear at high temperature, delamination occurs at steady state, which was confirmed by Waterhouse [33] when he pointed out that delamination happens after the fall of adhesion due to the formation of protective scales at high temperature. Therefore, an important step towards the understanding of the significance of the frictional heat on the wear process is to study its effect on the fretting wear by delamination.

Figure 6-2 shows a schematic explaining the detachment of plate-like debris by delamination when a slider (representing the contact asperity) oscillates over the upper surface of a substrate. During the debris formation, a subsurface crack is initiated around

an inclusion or a second phase particle at a certain depth, h_{cr} , and then, propagated parallel to the surface until it reaches a critical length, l_{cr} , at which it kinks and changes its direction towards the surface causing a plate of material to be detached [31].

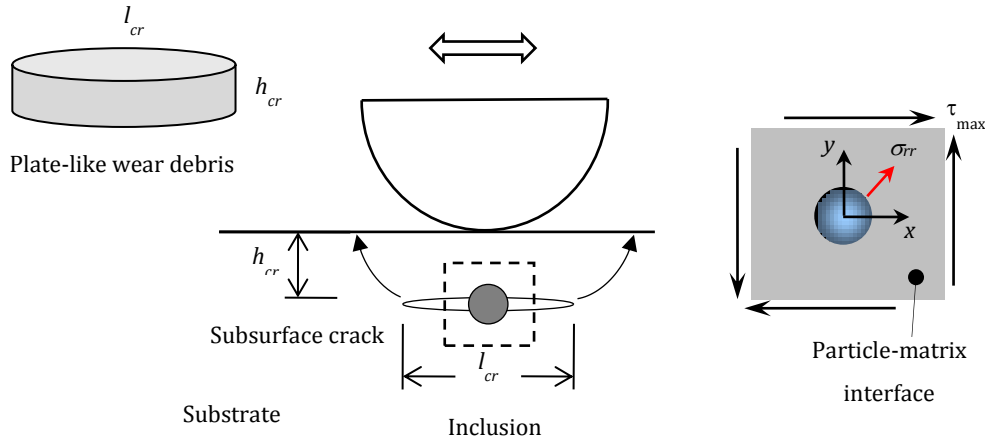


Figure 6-2: Wear debris formation by delamination as a result of subsurface crack initiation and propagation.

According to the delamination theory of wear proposed by Suh [31], the thickness of the debris (h_{cr}) has a wide range between 0.1 and 20 μm , depending on the thickness of the dislocation free layer, which depends on the material.

6.3.1. Selected criteria for crack initiation and crack propagation

As shown in the extensive literature review in Chapter 2, the crack initiation can be predicted using a number of criteria. The local stress criterion seems to be appropriate for this study. In this criterion, a void can nucleate at a point around the particle-matrix interface when the interfacial normal stress at that point exceeds the cohesive strength of the interface. Figure 6-2 shows the schematic of an asperity-substrate contact with a subsurface inclusion. Mathematically this criterion can be expressed as [32]:

$$\sigma_{rr} = \sqrt{3}\tau_r + \sqrt{3}\tau_{max} + \sigma_h \geq 2k_s \quad (6-5)$$

where σ_{rr} is the interfacial normal stress, τ_r is the residual shear stress, τ_{max} is the maximum applied shear stress, σ_h is the hydrostatic stress and k_s is the shear yield strength. If σ_{rr} exceeds $2k_s$, then the crack is initiated. Gesees et al. [34] used a homogenous model without a physical inclusion based on the assumption that at any point in the domain there

is a small control volume encompassing a single inclusion. They found that the interfacial normal stress σ_{rr} developed around the inclusion was two times the same stress developed in the homogeneous model. Consequently, it is reasonable to take the critical value of σ_{rr} to be equal to k_s instead of $2k_s$ as it was proposed by Jahanmir and Suh [32], and that this low value of σ_{rr} takes into consideration the inclusion elasticity. Since the spacing between the inclusions is an order of magnitude larger than the void characteristic dimension, each inclusion can be treated separately without considering the effect of the adjacent inclusions [113].

For crack propagation, due to the large extent of plastic deformation below the asperity contact and the cyclic nature of loading in fretting wear, the adopted criterion is the crack tip sliding displacement CTSD used by Sin and Suh [52], which is the difference between the displacement of the upper and lower crack surfaces. The same criterion was successfully employed by Gessesse et al. [11] in their prediction of crack propagation in elastoplastic materials during impact-sliding fretting wear.

6.3.2. Finite element crack initiation and propagation model

To investigate the effect of the frictional heat on the wear debris formation during fretting, a finite element model was developed. The model studied the plastic deformation at an asperity-substrate contact, and therefore, the process of crack initiation and propagation required to form wear debris by delamination. The contact of the two rough surfaces was replaced by a contact of an equivalent rough surface (represented by the asperities) and a counter smooth surface (represented by the substrate) as shown in Figure 6-3 (a). The equivalent surface had the equivalent standard deviation of the asperity heights $\bar{\sigma}$, and an equivalent mean absolute slope $|\bar{m}|$ [59-62], as shown in Figure 6-3 (b).

The micro-contact asperities were assumed to have equal size and to be uniformly distributed within the contour area, i.e., arranged in a square pattern, as shown in Figure 6-4.

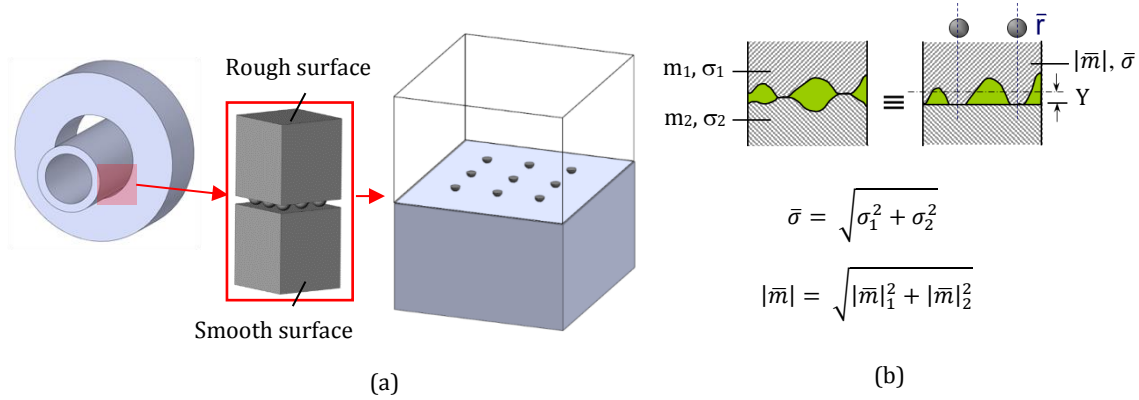


Figure 6-3: Rough surfaces replaced by an equivalent rough surface and a smooth surface (a) schematic of the 3D equivalent surface and (b) the standard deviation of the asperity heights $\bar{\sigma}$, and the absolute mean slope of the equivalent surface $|\bar{m}|$.

The thermal part of this FE model followed the analytical model developed by Attia et al. [71] who proposed that the frictional induced heat developed at any point was the superposition of the heat generated at the asperity contact under consideration (the starting heat source), the contribution from the neighbouring asperity contacts (image heat source in the near region), and the contribution of all other asperity contacts in the contour area, but outside the near region (i.e., the far region), as shown in Figure 6-4 (a) and (b). For the near region, a 3x3 asperity pattern is sufficient to achieve the desired accuracy of prediction. For the far region, the heat generated by the surrounding was considered to be the overall contribution of the asperity contacts depicted as black crosses in the far region, as shown in Figure 6-4 (a). The frictional-induced heat generated by each asperity was modelled using a sinusoidal varying heat flux according equation (6-3).

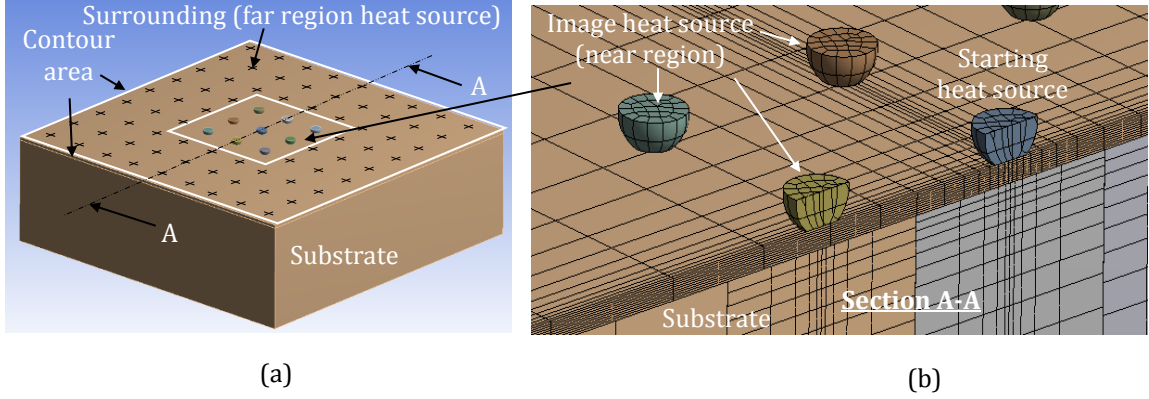


Figure 6-4: FE thermal model used to predict the contact temperature for crack initiation and propagation (a) model overview showing the 3 x 3 array of asperities and the surrounding, (b) a cross section showing the central and the neighbouring asperities.

When assuming that the asperity heights of the surfaces are normally distributed, the micro-contact parameters, e.g., the size of the micro-contact area, the asperities density and the separation (distance between the medians of the two contacting surfaces) are calculated using the following equations [114]:

$$\varepsilon^2 = \left(\frac{A_r}{A_a} \right) = \frac{p_a}{p_m} = \frac{1}{2} \operatorname{erfc}(X) \quad (6-6)$$

$$\gamma = \frac{M}{A_a} = \frac{1}{16} \left(\frac{|\bar{m}|}{\bar{\sigma}} \right)^2 \left(\frac{\exp(-2X^2)}{\operatorname{erfc}(X)} \right) \quad (6-7)$$

$$r = \sqrt{\frac{8}{\pi}} \left(\frac{\bar{\sigma}}{\bar{m}} \right) \exp(X^2) \operatorname{erfc}(X) \quad (6-8)$$

$$\bar{r} = r \left(\frac{|\bar{m}|}{\bar{\sigma}} \right), \bar{\gamma} = \gamma \left(\frac{\bar{\sigma}}{|\bar{m}|} \right)^2, \bar{Y} = \frac{Y}{\bar{\sigma}} \quad (6-9)$$

where ε^2 is the constriction ratio, γ is the density of the MCAs, r is the radius of the MCA, σ is the standard deviation of the asperity heights, m is the mean absolute slope of the asperities, M is the number of micro-contacts over the apparent area A_a and Y is the separation.

The parameter X , in the complimentary error function $\text{erfc}(x)$, is defined as:

$$Y = \sqrt{2} \bar{\sigma} x \quad (6-10)$$

This single parameter x , which can be uniquely defined by the ratio p_a/p_m , interrelates the other parameters ε^2 , γ , and r , as shown in Figure 6-5. Table 6-1 shows the input parameters used to estimate the micro-contact parameters and employed in the FE model geometry, the material properties and the loading.

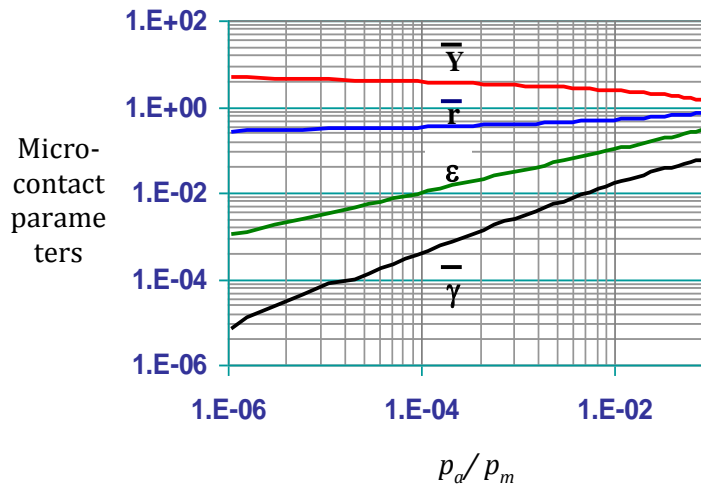


Figure 6-5: Graph used in the estimation of the micro-contact parameters.

With $p_a = 70$ MPa, $\varepsilon^2 = 2.9\%$, $\bar{\sigma} = 1.69 \mu\text{m}$, $|\bar{m}| = 0.14$, the estimated asperity density is 200 asperity/ mm^2 , the separation Y is $1.7 \mu\text{m}$ and a micro-contact radius r is $6 \mu\text{m}$. The 3×3 array representing the near region (Figure 6-4 (a)) has dimensions of $210 \mu\text{m} \times 210 \mu\text{m}$. The far region or the surrounding, depicted as crosses in Figure 6-4 (a), has dimensions of $630 \mu\text{m} \times 630 \mu\text{m}$.

Table 6-1: Parameters used in the FE model.

Parameter	Symbol	Value	Units
Contact pair	CP	Cobalt Alloy 2 – Cobalt Alloy 1	
Amplitude of slip	A	± 20	μm
Normal load	F_n	30	N
Frequency	f	200	Hz
Coefficient of friction	μ	0.3 , 0.8	-
Contact pressure	p_a	70	MPa
Yield strength	σ_y	800[86]	MPa
Flow stress	p_m	2400 [86]	MPa
Constriction ratio	ε^2	2.9	%
Thermal conductivity	k	10 [86]	W/m.K
Density	ρ	9130	Kg/m ³
Specific heat	C_p	450	J/Kg.°K

On the structural (mechanical) side, the fact that the crack initiation and propagation studies at one asperity-substrate contact cannot be handled in isolation from neighbouring asperity contacts drove the need for the construction of two models: a thermoelastic global model and a thermoplastic submodel. The global model is used to study the elastic behaviour of the whole structure containing the 3 x 3 asperities and the surrounding. The submodel encompasses only one asperity (the starting heat source or the central asperity) and one substrate. It uses the outputs of the global model to investigate the plastic deformation, crack initiation and crack propagation at that single asperity contact, as shown in Figure 6-6.

In the global model, the stiffness of the springs was set to produce the radius of the micro-contact area calculated from the micro-contact attributes (Figure 6-5). In addition, when the equivalent plastic strain values developed from the effect of these springs were investigated, it was found the material reached the shake down limit [115]. For the investigated case shown in Table 6-1, a longitudinal stiffness of 630 N/mm for each spring

was adequate. To connect the single asperity-substrate submodel to the global model, the ANSYS submodeling capabilities were employed to convey the thermal and displacement values at each loading step. Figure 6-7 shows how the boundary conditions on the heat flow channel (HFC) boundaries vary with time during the fretting cycle.

For the thermoplastic submodel, a coarsely meshed, rigid hemispherical asperity was used to produce the contact zone, as shown in Figure 6-8 (a). In order to capture the plastic deformation, the zone of the substrate adjacent to the asperity was finely mesh, and the element size was around 1 μm leading to a total number of 9308 SOLID 186 tetrahedral elements.

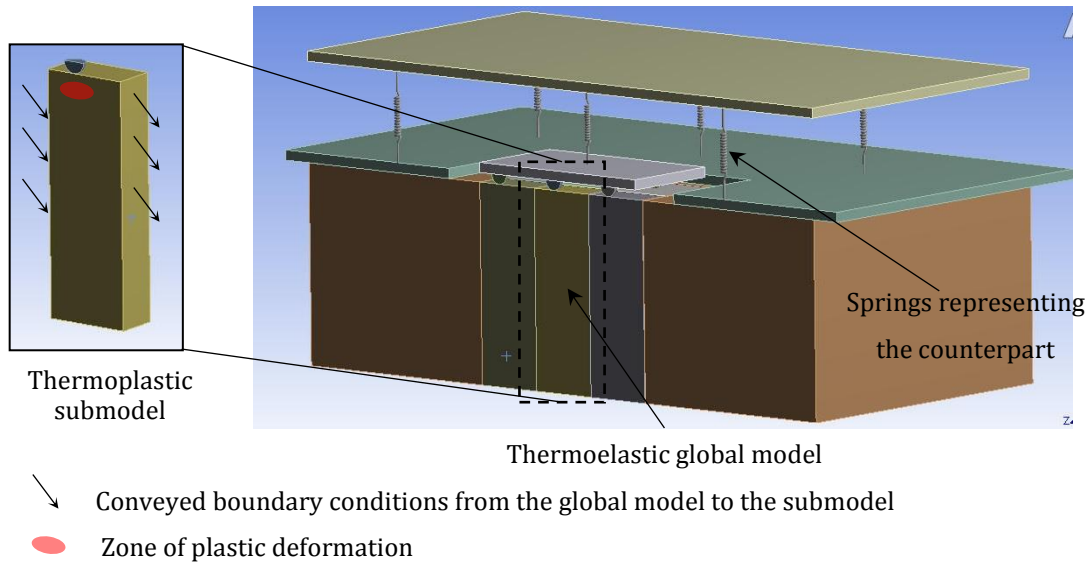


Figure 6-6: Global thermoelastic model and the boundary conditions conveyed to the local thermoplastic submodel.

The contact between the asperity and the substrate was defined to be frictional. For comparison, two values for the coefficient of friction were used: 0.3 and 0.8. The asperity starts sliding from position 1, goes to position 3, and returns to position 1 to complete one loading cycle. For the loading cycle, the solution was divided into 40 steps and during each step, the thermal boundary conditions were conveyed from the global model to every node in the submodel, whereas the displacement boundary conditions were conveyed to the asperity and the outer boundaries of the substrate. The assumed material model is a bilinear stress-strain curve with linear strain hardening, as shown in Figure 6-8 (b). The

modulus of elasticity E and the tangent modulus E_{tan} , were selected to be 225 GPA and 2.3 GP, respectively.

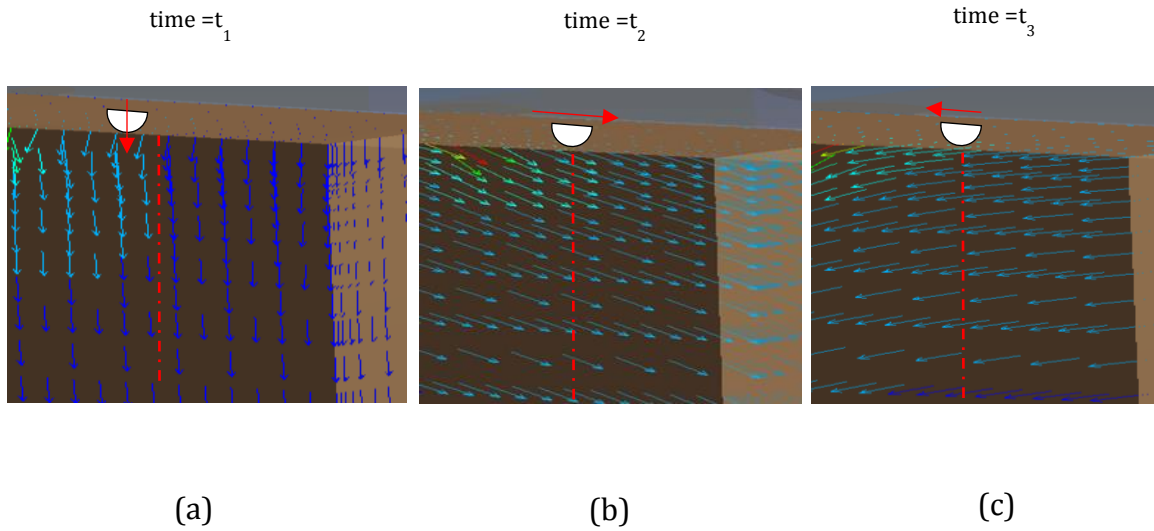


Figure 6-7: Variation of the resultant displacement on the HFC boundaries with time during the loading cycle.

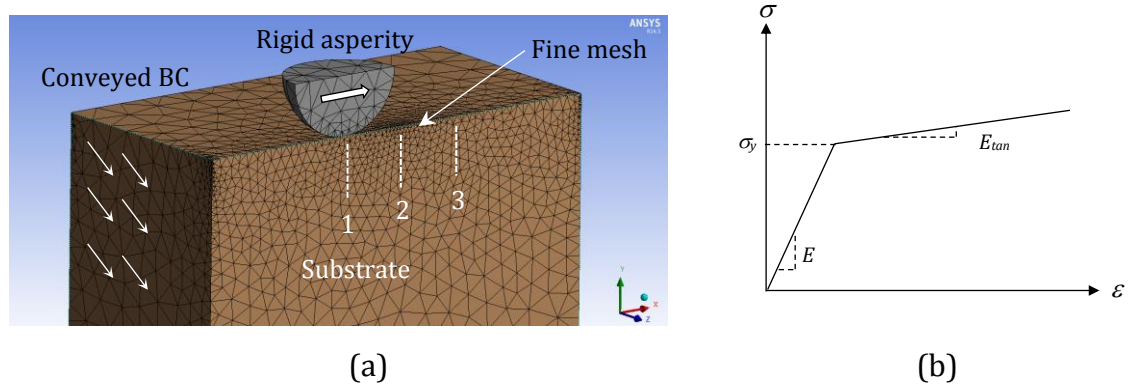


Figure 6-8: (a) Mesh details of the thermoplastic submodel and (b) assumed material model, where E is the modulus of elasticity, E_t is the tangent modulus and ϵ_y is the yield strain.

6.3.3. Effect of frictional heat on crack initiation

In order to investigate the effect of frictional heat on crack initiation process, a comparison was made between two cases: a case where only the effect of the mechanical load is considered, named “Mechanical”, and a case where frictional heat is present, named “Thermo-mechanical”. As can be seen in Figure 6-9, the presence of the frictional heat directly affects the whole deformation of the substrate. After one quarter of a cycle (position 2 in Figure 6-8 (a)), the mechanical loading tends to push the substrate material downwards while dragging it to the sliding direction, and the resultant is in the direction of the red arrow. On the other hand, during thermomechanical loading, the material is raised due to thermal expansion and dragged to the sliding direction. The thermal field causing this thermal expansion is shown in Figure 6-9.

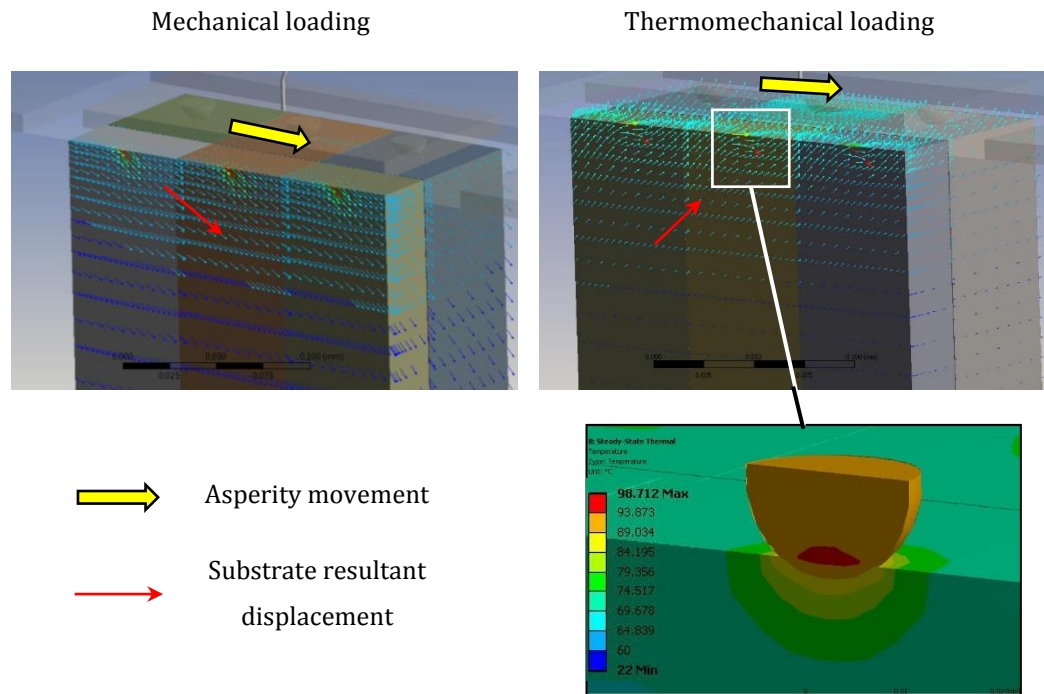


Figure 6-9: Effect of the frictional heat on the elastic behaviour of the global model showing the resultant displacement mechanical loading (left) vs the thermomechanical loading (right) with the temperature field at the asperity contact ($\mu = 0.8$ and the asperity is at position 2 in Figure 6-8 (a)).

A close up look at the deformation in the contact zone shows that during mechanical loading (Figure 6-10 (a)) the asperity tends to plastically deform the material in the direction of the yellow arrow. This direction is the combination of the downward asperity pressure exerted upon the contact and the asperity sliding to the right. On the other hand, during thermomechanical loading, there exists a competition between two opposing deformations (Figure 6-10 (b)); the first is the mechanical load tending to push the material downwards and to the right, while the second is the deformation coming from thermal expansion leading to the rise of the material (as indicated by the yellow arrows). This means that the areas situated at the horizontal dashed line level witness the two opposing streams of deformation; downwards deformation is opposed by the upwards thermal expansion, which is totally different than the mechanical loading.

When looking at the development of plastic deformation (quantified by the equivalent plastic strain) in the contact zone, it can be seen that for the thermo-mechanical loading case (Figure 6-10 (d)) there was less accumulated plastic strain when compared to the mechanical loading case (Figure 6-10 (c)). It can also be observed that for both loading cases, high values of equivalent plastic strain were obtained, especially at the asperity-substrate interface. This can be attributed to the fact that the employed stress strain curve (Figure 6-8 (b)) did not include a failure strain at which the elements fail or get deleted.

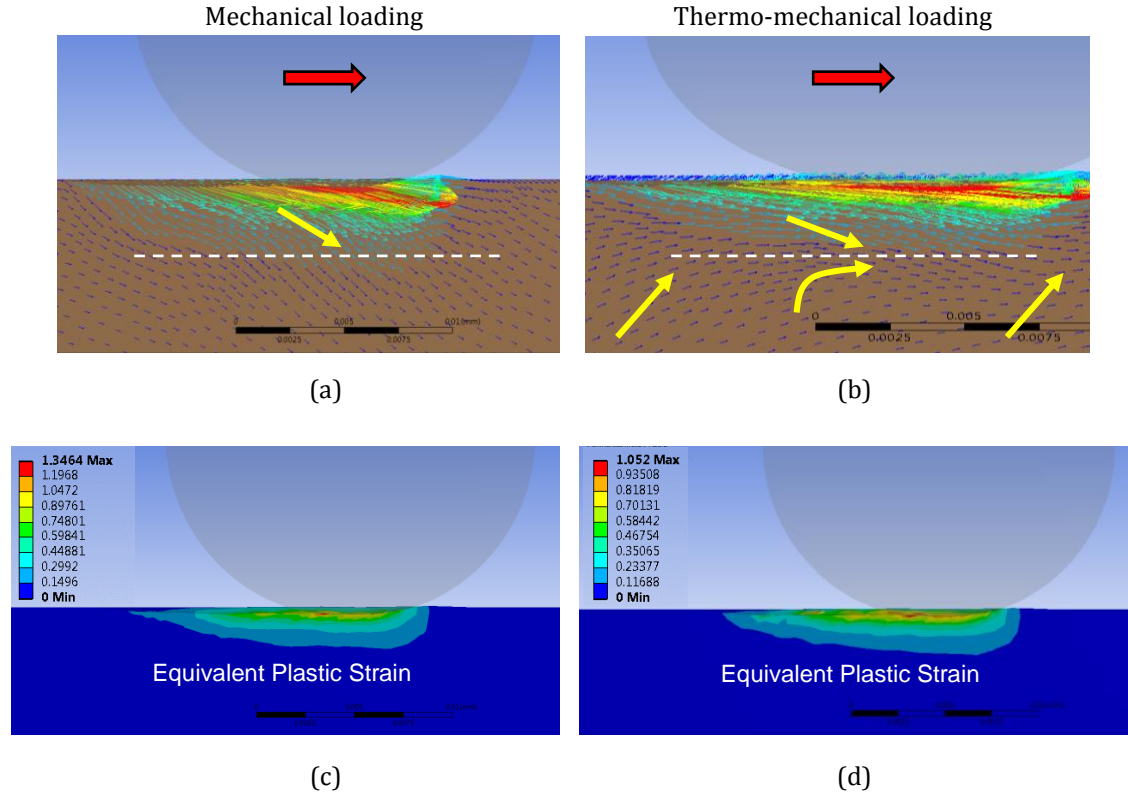


Figure 6-10: Resultant displacement (a) mechanical loading, (b) thermo-mechanical loading, (c) development of plastic deformation (quantified by the equivalent plastic strain) at the contact zone for the mechanical loading and (d) thermo-mechanical loading ($\mu = 0.8$ and the asperity is at position 2 in Figure 6-8 (a)).

Figure 6-11 shows the contour plot of the interfacial normal stress σ_{rr} when divided by the shear yield strength k_s . The probable site of crack initiation are the zones where $\sigma_{rr}/k_s \geq 1$ and the sites at which the crack cannot initiate are the dark blue zones where $\sigma_{rr}/k_s \leq 1$. It can be observed that the introduction of frictional heat at a coefficient of friction value equal to 0.8 caused a shrinkage in the crack initiation site during thermomechanical loading (Figure 6-11 (b)) when compared to mechanical loading (Figure 6-11 (a)).

Figure 6-12 shows, in a more illustrative way, the effect of the frictional heat and the coefficient of friction on the extent of the crack initiation sites. It can be seen that, for both friction values, the crack initiation probable site saw a considerable shrinkage from a depth of 10-12 μm at the mechanical loading to around 5-7 μm at the thermomechanical loading. In addition, when the friction value increased from 0.3 to 0.8, there was an increase in the

size of the crack initiation zone under both loading conditions; mechanical and thermomechanical. The last observation might explain why there is an increase in the wear damage when the friction coefficient increases at the contact interface.

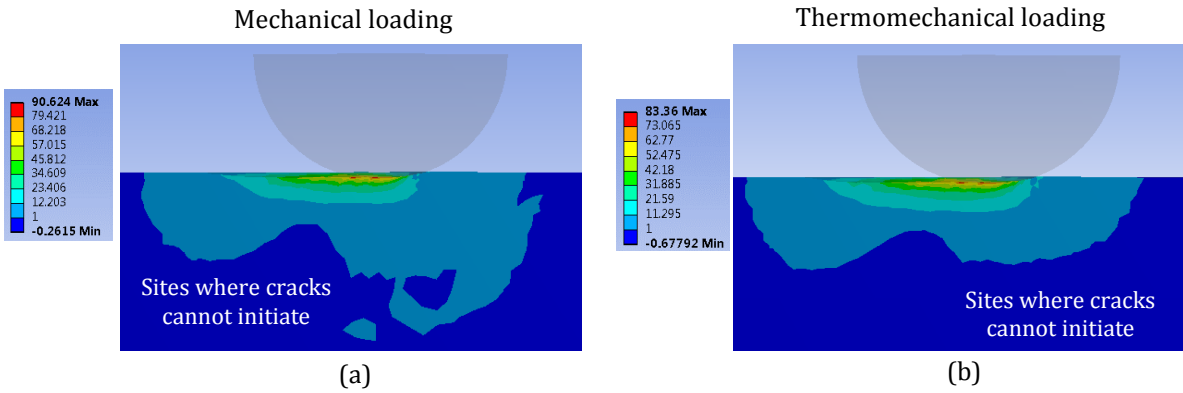


Figure 6-11: Contour plot of the σ_{rr} / k_s , where the probable sites of crack initiation are the regions where $\sigma_{rr} / k_s \geq 1$ (a) mechanical loading and (b) thermomechanical loading ($\mu = 0.8$ and the asperity is at position 2 in Figure 6-8 (a)).

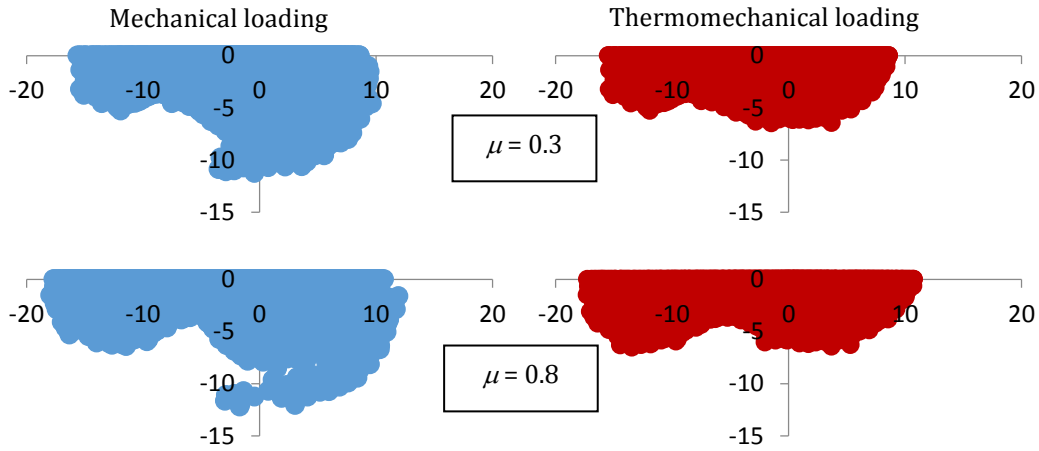


Figure 6-12: Effect of the frictional heat and the coefficient of friction on the probable sites of crack initiation (Dimensions are in μm , asperity is at position 2 in Figure 6-8 (a)).

When looking at the stress criterion for the crack initiation expressed mathematically by equation (6-5), it can be understood that void nucleation is facilitated when the hydrostatic stress is tensile and restrained when the hydrostatic stress is compressive, as suggested by Jahamir and Suh [32]. Figure 6-13 shows the tensile values of the hydrostatic stress, after one quarter of a cycle, for both mechanical and thermo-mechanical loading cases. It is clear that the presence of frictional heat reduces the tensile hydrostatic stresses, and consequently, the void nucleation is less likely to happen.

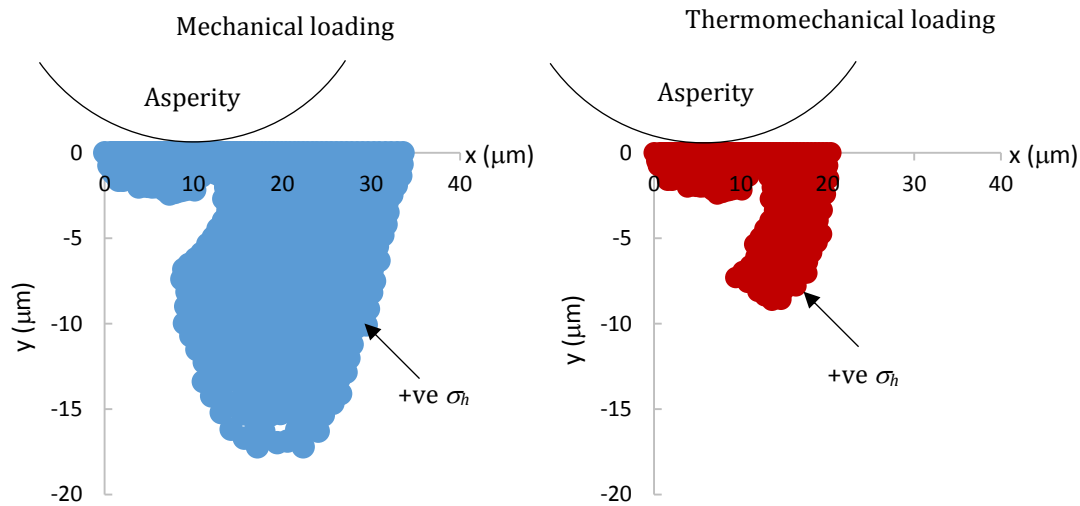


Figure 6-13: Effect of the frictional heat on the tensile hydrostatic stress for the (a) mechanical loading and (b) thermomechanical loading ($\mu = 0.8$ and the asperity is at position 2 in Figure 6-8 (a)).

The previous results are in agreement with the findings of Gong and Komvopoulos [35] who studied the thermomechanical analysis of a semi-infinite solid in sliding contact. They concluded that the increase in the Peclet number led to an increase in the compressive thermal stresses and reduced the likelihood of surface cracking. Another explanation was provided by Sofuoglu and Ozer [36] who showed that, for a fractal surface, the frictional heating increased the contact area and brought more asperities to the contact, which decreased the load carried by each asperity. This reduced the intensity of surface and subsurface stress distributions preventing the propensity of cracks.

6.3.4. Effect of frictional heat on crack propagation

The analysis conducted in the previous section showed the effect of the frictional heat on the location of crack initiation. It is therefore logical to build on that information and study the effect of frictional heat on the process of crack propagation. For this reason, a finite element model encompassing a crack was constructed, as shown in Figure 6-14. The crack had a variable length l and is situated at a probable depth of initiation h . In this model, 186 solid tetrahedral elements were employed for the meshing of the asperity and the substrate. The crack geometry was modeled using a three dimensional penny-shape crack. To account for the stress singularity and the steep gradient at the crack tip, a custom geometry was developed where the meshing mimicked the structure of the singular elements, as shown in Figure 6-14.

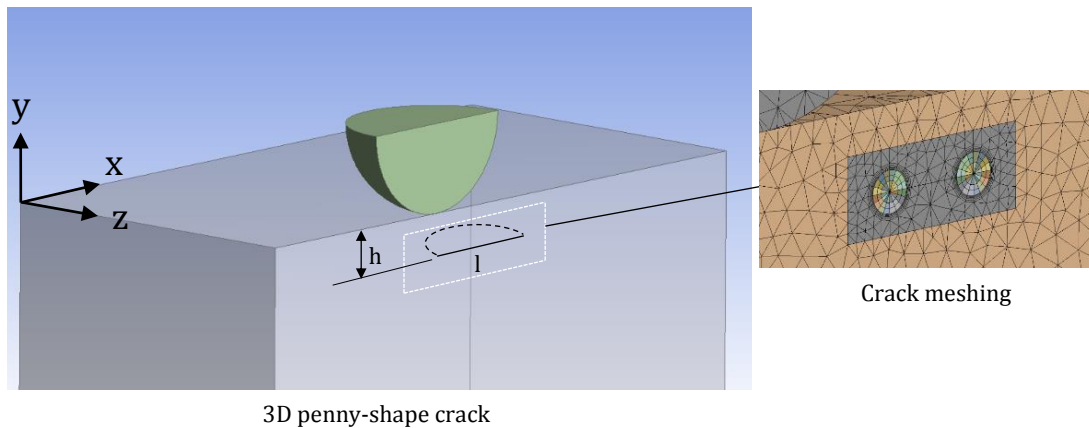


Figure 6-14: Finite element model of crack propagation with a crack inserted at the probable site of initiation showing the mesh and crack details.

From the investigation carried out in the previous section, a depth of $h = 4 \mu\text{m}$ (Figure 6-12) was found to match the crack initiation sites for both mechanical and thermo-mechanical loadings. The crack length was varied to simulate the propagation parallel to the surface and two crack lengths were investigated; $l = 6$ and $l = 12 \mu\text{m}$. The coefficient of friction at the asperity-substrate contact was set to a value of 0.8, while the coefficient of friction at the crack surfaces was set to a value of 0.3, which was found to be a reasonable value from the literature [34, 116]. The re-welding of the crack faces upon load removal and

the linking-up of separate cracks by void coalescence were ignored in this study; therefore, crack growth is solely due to CTSD [34]. Table 6-2 shows the effect of the frictional heat on the CTSD recorded after one loading cycle for the simulated crack lengths.

Table 6-2: Effect of the frictional heat on the CTSD recorded after one loading cycle for the simulated crack lengths.

		Left tip		Right tip	
		CTSD (μm)	CTSD increase due to the frictional heat (%)	CTSD (μm)	CTSD increase due to the frictional heat (%)
$l = 6 \mu\text{m}$	Mechanical	0.029	17.2	0.032	21.9
	Thermo-mechanical	0.034		0.039	
$l = 12 \mu\text{m}$	Mechanical	0.024	33.3	0.023	78.3
	Thermo-mechanical	0.032		0.041	

The following observations could be made:

1. The frictional heat caused an increase in the CTSD for all the tested cases.
2. This increase ranged between 17 to 78 % according to the crack length and the tip at which the CTSD was evaluated.
3. Longer cracks experienced higher CTSD increase than shorter cracks.
4. The right tip experienced higher CTSD increase than the left tip.

A plausible explanation of the results shown in Table 6-2 comes from the understanding of the subsurface deformation. During thermomechanical loading, the existence of opposing streams of deformation shown in Figure 6-10 (d) led to an increase in the shear plastic strain, and consequently, an increase in the shear stress, especially at the right tip. To confirm this explanation, the change in the in-plane (x-y) shear stress at the right tip (Figure 6-15) was calculated when the asperity was at position 2 in Figure 6-8 (a)). It was found that, with the emergence of the frictional heat, the right tip experienced an increase

in the shear stress of 5.6% and 8.3% at $l = 6 \mu\text{m}$ and $l = 12 \mu\text{m}$, respectively. This increase in the shear stress during thermomechanical loading caused an increased in the in-plane crack growth, and consequently, in the CTSD. Similar conclusions were drawn by Cho et al. when they investigated the thermoelastic behaviour of subsurface cracks due to sliding surface traction [39]. They showed that the frictional heat in sliding wear increased the maximum shear stress intensity factor (SIF), and consequently, increased the in-plane crack growth rate.

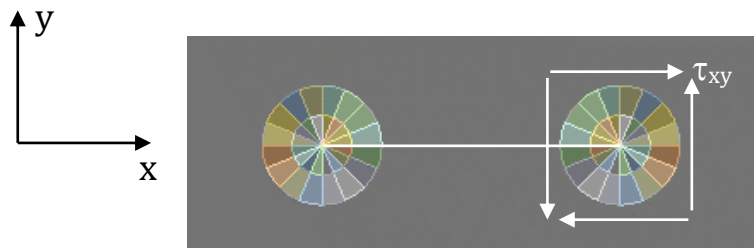


Figure 6-15: In-plane shear stress at the crack tip ($l = 12 \mu\text{m}$).

6.3.5. Conclusions from the crack initiation – crack propagation model

From the previous investigation, it was concluded that the emergence of frictional heat changed the mechanism of subsurface crack initiation and propagation, and therefore, the wear mechanism. Compared to the situation where only a mechanical load was applied, frictional heat caused formation of shallower (thinner) wear debris by reducing the depth at which the crack initiates. Once the crack was initiated, the frictional heat caused quicker propagation. It was therefore indispensable to pay better attention to the models used in the temperature prediction in order to adequately assess the impact of the frictional heat on the fretting wear prediction. The following sections discuss the proposed model developed for contact temperature prediction during fretting wear.

6.4. Thermal model for contact temperature prediction

6.4.1. Overview of the model

Following the extensive literature review conducted in chapter 2, it appears that there is an obvious lack of reliable models that can be used for the prediction of contact temperature during fretting. This study represents an attempt to bring the real surface topography into the prediction of the contact temperature, while being capable of handling the existence of oxides and multi-layers at the interface. The flowchart shown in Figure 6-16 summarizes the approach adopted to predict the contact temperature as well as the steps followed in each section.

The fretted surfaces are scanned, characterized and saved as (x,y,z) points, and then, conveyed to the contact model. The latter detects the MCAs based on the operational applied load, apparent measured contact area, and material properties. This is done through an iterative process in which the real area of contact is detected every time the separation changes. The loop stops when the constriction ratio calculated from the area equalizes the constriction ratio calculated from the pressures, and the recorded contact points represent the real MCAs. The detected MCAs are automatically transformed into elements in the mesh of the finite element thermal model. Using the material properties (flow stress), system properties (coefficient of friction) and the fretting operational conditions (amplitude of slip and frequency of oscillation), the thermal load is applied on the MCAs, simulating the fretting thermal effect and the contact temperature is predicted at the interface. In reality, the generated frictional heat alters the material properties, the oxidation process, and consequently, the surface topography, as indicated by the dashed feedback lines in Figure 6-16. This model stops at the prediction of the contact temperature; however, it is capable of handling the above nonlinear aspects, as is shown in the detailed explanation.

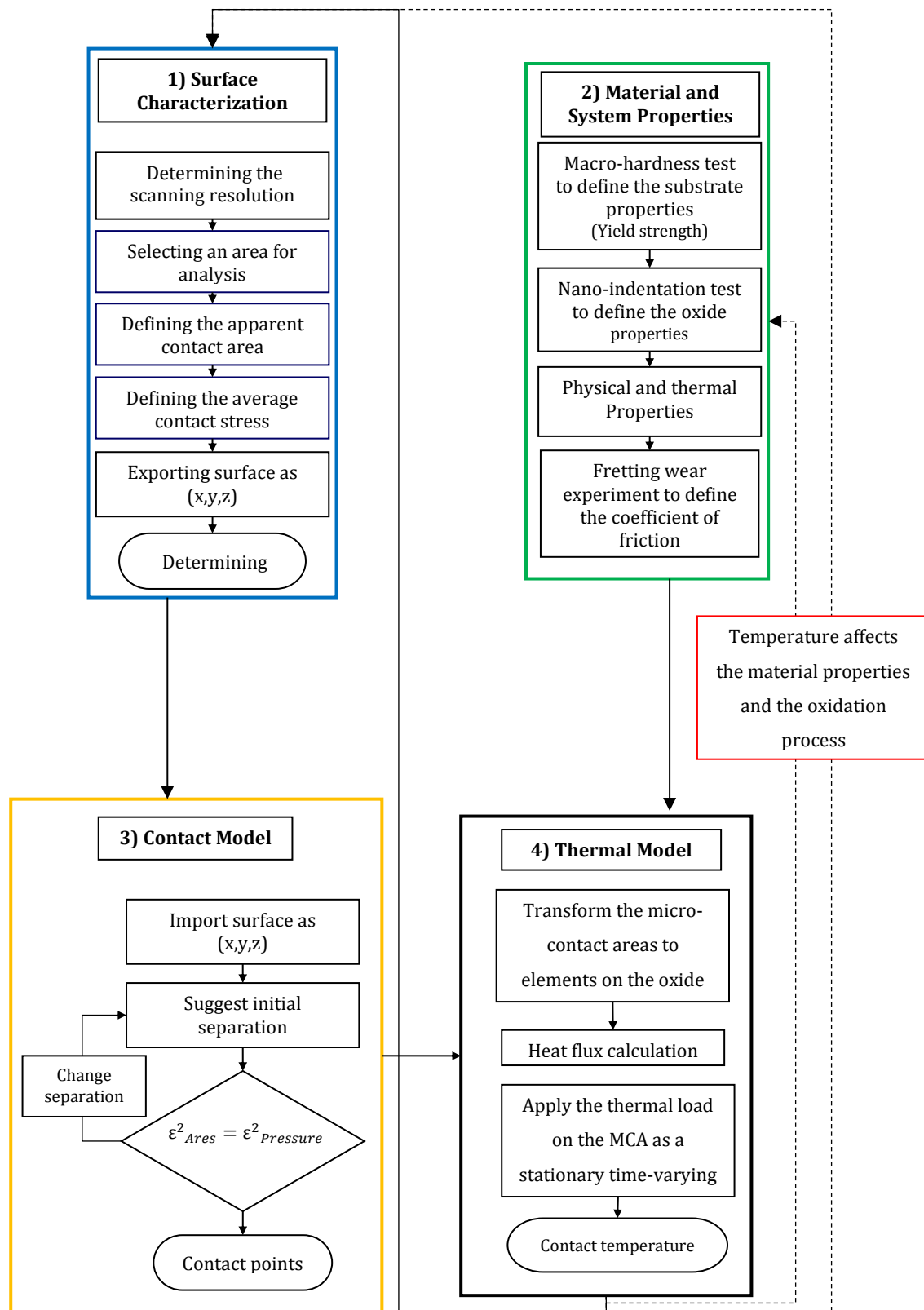


Figure 6-16: Flowchart of the Contact-based Model used to estimate the contact temperature during fretting wear.

6.4.2. Surface characterization

The fretted surfaces are scanned using the surface scanning machine “Taylor Hobson model Form Talysurf 120”. The area where the damage took place is selected and saved as (x, y, z) coordinates, as shown in *Figure 6-17 (a)*. A total of 1000 points were selected in a 4 mm length (i.e. 250points/mm) producing a scanning resolution of 4 μm in the x and y directions. Knowing that the radius of an asperity contact ranges between 5 and 10 μm [61], this scanning resolution is sufficient to capture the contact details in a reasonable scanning time.

The damaged area surrounded by the contour shown in *Figure 6-17 (b)* is considered to be the nominal or apparent contact area, denoted by A_a . The software of the scanning machine calculates this area as the summation of the hole and peak areas mentioned in Section 3.7. For this particular case, the area was:

$$A_a = A_{hole} + A_{peak} = 0.455 + 0.611 = 1.056 \text{ mm}^2 \quad (6-11)$$

The average applied contact pressure definition adopted in this study is calculated from the division of the normal load by the apparent contact area,

$$P_a = F_n / A_a = 30 / 1.056 = 24.3 \text{ MPa} \quad (6-12)$$

It is evident that the values of the apparent contact area and the average contact pressure are different from the ones calculated from the Hertzian elastic contact theory. Table 6-3 shows the comparison between the two contact areas and pressures. It can be observed that the theoretical contact area calculated from the Hertzian equations is around 50% of the actual fretted area. This is attributed to the fact that in reality the applied load, combined with the fretting motion, makes the damage and the contact area increase. The same approach in defining the contact area was adopted by Kalin [117] who argued that the nominal area calculated from the geometric data of the contacting bodies using the Hertzian elastic theory is true for a limited time as long as no wear takes place in the contact.

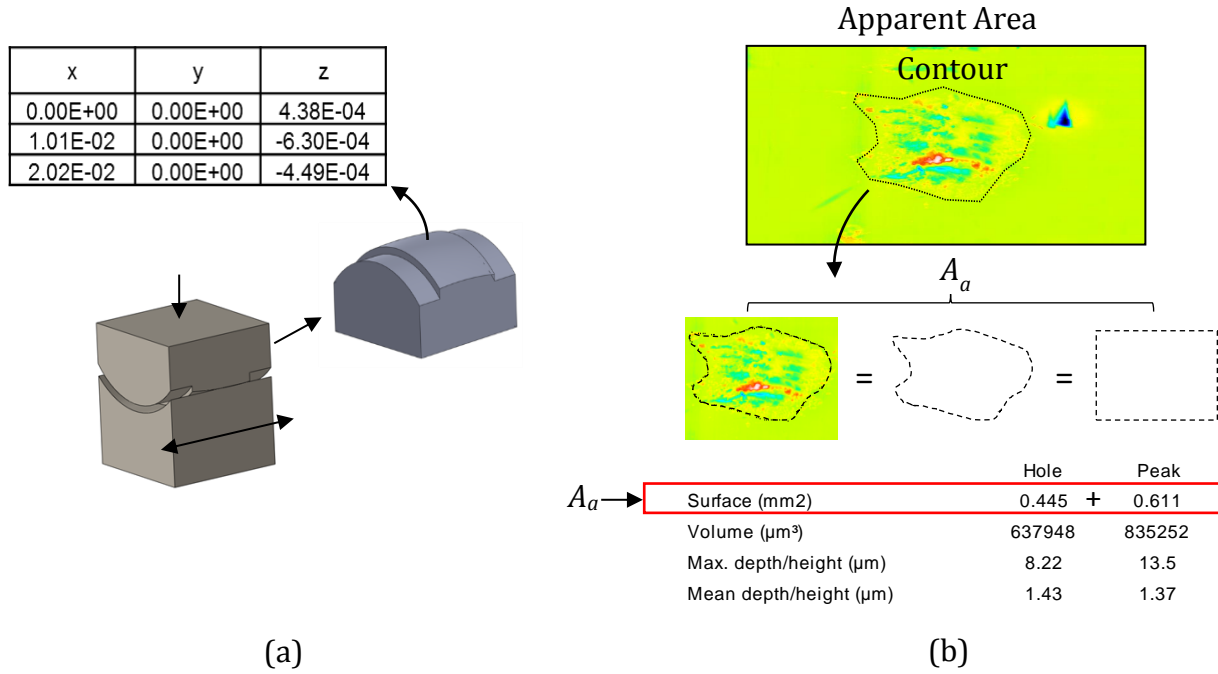
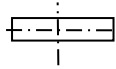



Figure 6-17: Exporting the scanned fretted surface and determination of the apparent contact area (a) contact pair surface when exported as (x, y, z) points (units in mm) and (b) measurement of the apparent area of contact.

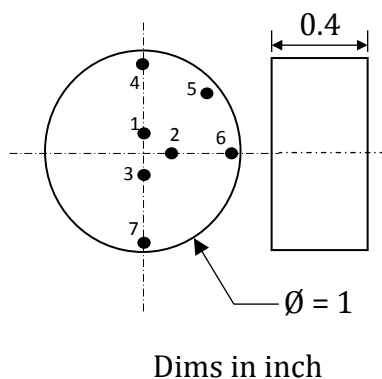
Table 6-3: Hertzian contact calculations of the reference case.

	Symbol (unit)	Hertzian contact	Experimental contact
Contact configuration			
Contact Shape		Rectangular contact	-
Average Contact Area	A_a (mm ²)	0.43	1.056
Maximum contact pressure	p_{max} (MPa)	132.4	-
Average contact pressure	p_{avg} (MPa)	69.3	24.3

6.4.3. Material properties

The proper selection of adequate material properties has a vital role in the validity of this model because the analysis involves the oxide formed on the surface which has different properties than the substrate material. The oxide film has a lower thermal conductivity and higher strength compared to the substrate. Jaeger [67] indicated that for the oxide film to cause an increase in the surface temperature, it must be thick compared to the molecular dimensions. As the experimental results indicated in Chapter 4, the oxide thickness is in the order of few microns, which is orders of magnitude higher than the cobalt, nickel or chromium atomic size.

The mechanical properties of the substrate material are available in the material data sheets [85, 86]. However, to identify the exact alloy supplied by PWC, a macrohardness test was conducted on the raw bar. The geometry of the sample used in the hardness test as well as the recorded hardness values are shown in Figure 6-18. When comparing the hardness values obtained experimentally with the alloys material properties [85, 86], it was found that the stock used in the experiments represented the solution treated condition without cold working.



Point	Hardness (Rc)	Average Hardness (Rc)	
1	20	20.2	22.8
2	21		
3	19.5		
4	27	25.4	
5	25.5		
6	25.5		
7	23.8		

Figure 6-18: Cobalt Alloy 2 cylinder sample used for the macrohardness test and the recorded hardness values in Rc.

For the properties of the oxide layer, a nanoindentation test was conducted in order to correlate the mechanical properties of the oxide to those of the substrate. Figure 6-19 shows the cross section of the tested sample, which was sectioned at the damaged area, mounted in a resin, and gradually polished and etched in order to unveil the oxide layer. The points of indentation are shown in Figure 6-19. From the nanoindentation results given in Table 6-4, it can be seen that the average ratio of the oxide hardness to the substrate hardness is around 2.5. Since there is a correlation between the hardness and the yield strength, this same ratio was used to estimate the oxide yield strength, knowing the substrate yield strength, which is available in the material data sheets (Table 6-5).

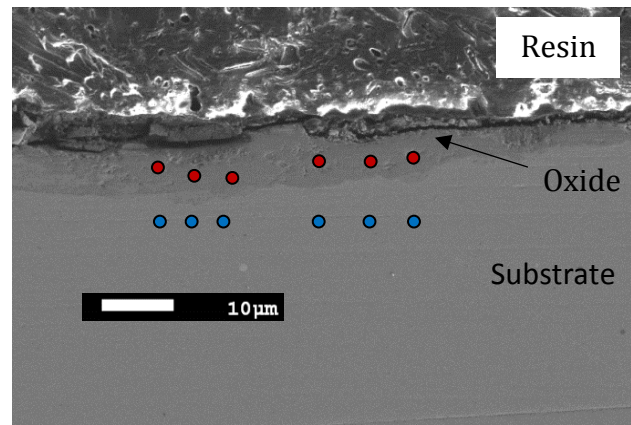


Figure 6-19: Cross section of the Cobalt Alloy 2 cylinder sample used for the nanoindentation test, the indentation point.

Table 6-4: Recorded nanohardness values in GPa.

	Substrate Hardness	Oxide Hardness
Points	(GPa)	(GPa)
1	6.82	22.36
2	8.25	11.73
3	7.68	12.67
4	8.49	18.95
5	9.16	21.54
6	8.09	30.33
Average	7.97	19.60

Table 6-5: Yield values for the solution treated Cobalt Alloy 2 bar and its oxide.

Temperature	Substrate yield strength [86]	Oxide yield strength
°C	MPa	MPa
25	505	1242.02
540	295	725.53
650	295	725.53
760	285	700.94
870	235	577.97
980	130	319.73

The values of the thermal conductivity and the specific heat of the substrate material were taken from the alloy's material data sheets [85, 86]. The thermal conductivity of the oxide layer was assumed to be 1/10 of the substrate conductivity [118, 119]. The values of the coefficient of friction used in this investigation were extracted from the experimentally measured data shown in section 4.6.

6.4.4. Contact model used in the determination of Micro-Contact Areas (MCAs)

To determine the micro-contact area, the two fretted surfaces are imported to the commercial software, MATLAB [120]. The surfaces are initially spaced enough to ensure the absence of any contact, as shown in Figure 6-20 (a). The contact is gradually established by reducing the separation (the distance between the medians of the two surfaces), which brings together the surfaces as shown in Figure 6-20 (b). At every loading step, the contact taking place is detected through an image analysis technique. This technique is based on displaying the upper surface as purely white and the lower surface as purely black, as shown in Figure 6-20 (c). By looking at the contact of the two surfaces from the top view, any overlapping occurring due to contact is seen as a black area inside the white background (Figure 6-20 (d)). The black surfaces are assumed to represent clusters of MCAs, which when added to each other make the real area of contact (A_r). The

summation of the black areas (A_r) and the background represents the apparent area of contact (A_a). This contact detection technique is based on the following assumptions:

1. The profilometric surface measurement conducted at the end of the test is representative for the surfaces topography; therefore, the change in the asperity distribution over time is not considered.
2. The entrapment of wear debris, and consequently, the third body effect, are neglected.

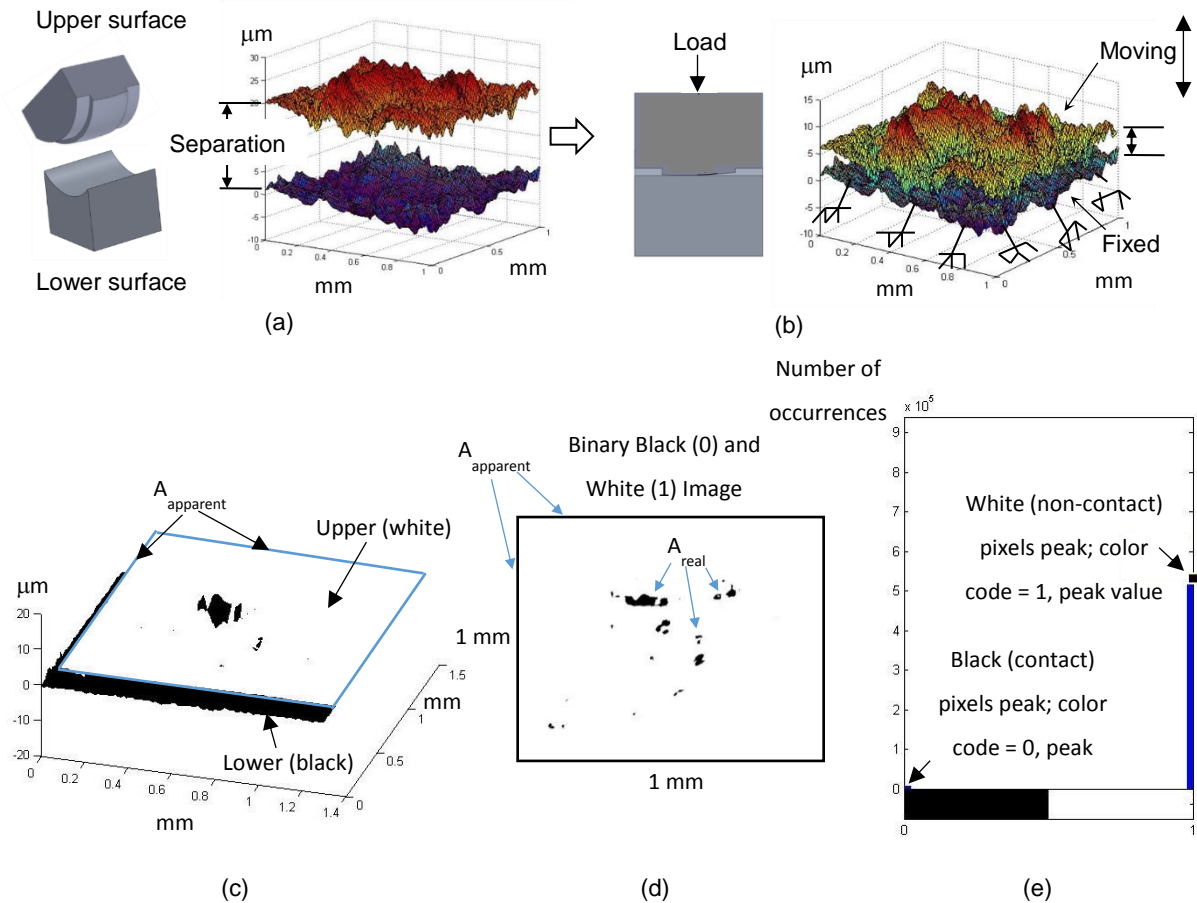


Figure 6-20: Contact establishment, (a) surfaces imported with no load application, (b) load is applied by reducing the separation, (c) the upper surface converted to white and the lower surface is converted to black, (d) contact converted into a binary B&W image (e) colors histogram showing the black (contact) pixels peak and the white (non-contact) pixels.

The top view of the contacted surfaces is converted to a binary Black and White (B & W) image having a resolution identical to the scanning resolution (250 points/mm). This image has only two colors: black, representing the contact and numerically designated by the zeroes, and white, representing the non-contact and numerically designated by the ones. When this binary image is analyzed, as shown in the image histogram (Figure 6-20 (e)), the ratio of the contact pixels (zeroes) to the total number of pixels (zeroes + ones) is the ratio of the real contact area A_r , to the apparent contact area A_a , or the constriction ratio ε^2 . Every time the separation is changed, the constriction ratio calculated from the area ratio (A_r/A_a) is compared to the constriction ratio calculated from the pressure ratio (P_a/P_m). This iterative process stops when the error between the two ratios is $< 1\%$, indicating that the actual contact is reached.

6.4.5. Finite element thermal model

The finite element thermal model used in the prediction of the contact temperature was conducted using the ANSYS software [121]. The model consists of a substrate covered by a thin layer of oxide, as shown in Figure 6-21 (a). The substrate represents the alloy to be studied, having the dimensions of the apparent contact area measured in section 6.4.2. The substrate has a thickness of 200 μm to ensure that the temperature profile along the depth is fully captured, and that the thermal gradient vanishes when reaching the lower substrate surface where the bulk temperature effect dominates. The element type employed in this model is the SOLID70 3-D Thermal Brick Element [122], as shown in Figure 6-21 (b).

Since most of the steep thermal temperature gradient occurs in the oxide layer, a finer mesh was used to capture the temperature variation inside this critical zone. In the x-z directions, the mesh density of the oxide layer is identical to both the surface scanning resolution in section 6.4.2 and the image resolution used in the MCAs determination in section 6.4.4. For the oxide thickness (y direction), a mesh sensitivity analysis showed that a number of 4 elements produced an error less than 0.1% in the temperature value compared to a denser mesh. This means that for a typical oxide thickness of 10 μm , each element covers a thickness of 2.5 μm .

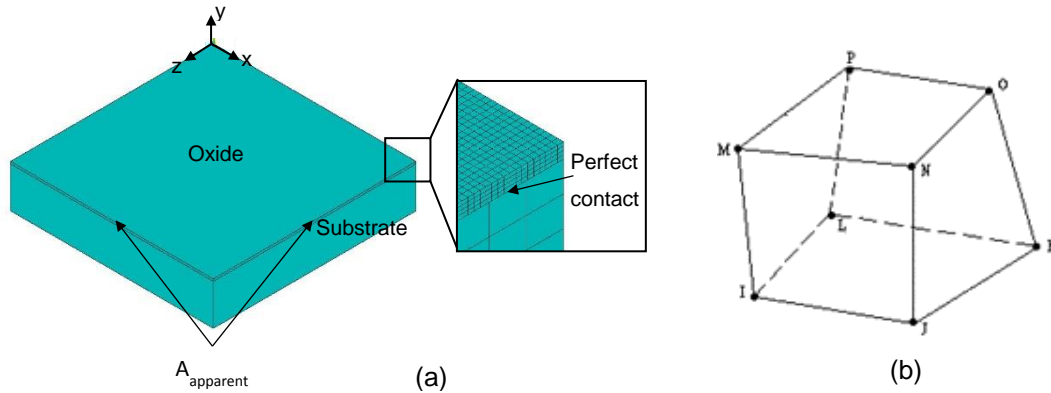


Figure 6-21: Finite element model (a) alloy substrate covered by a thin layer of oxide and (b) the SOLID70-3-DThermal Brick Element used in the analysis.

The substrate has a coarser mesh since it represents the region away from the near-surface temperature gradient. A typical 1 mm x 1 mm substrate area is divided into 40 elements in x and z directions. For the substrate thickness (y direction), a mesh sensitivity analysis showed that a number of 10 elements produced an error less than 0.1% in the temperature value compared to a denser mesh. This means that for a typical substrate thickness of 0.2 mm, each element has a thickness of 20 μm . The contact at the substrate-oxide interface is assumed to be perfect. Therefore, a high value of thermal contact conductance ($1 \times 10^{10} \text{ W/m}^2 \text{ K}$) was chosen to model the perfect adherence of the oxide to the substrate. Figure 6-22 shows an example of a contact pattern belonging to a fretted surface (Figure 6-22 (a)) when automatically conveyed to the FE model (Figure 6-22 (b)).

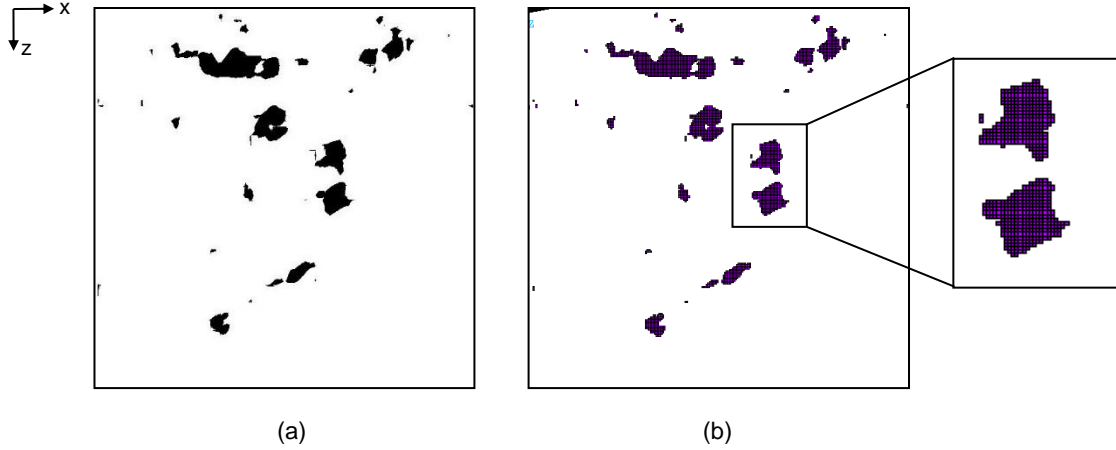


Figure 6-22: Example of a contact pattern automatically conveyed from (a) the contact model to (b) the FE model.

The frictional heat input is calculated using equation (6-3) in the form of a time-dependent heat flux applied as a thermal load function on the MCAs. The bulk temperature of the environment is applied to the lower substrate surface as an initial condition to all the nodes in the transient analysis. Apart from the elements representing the MCAs, the top surface of the oxide is considered to be adiabatic, which means that the heat transfer to the surrounding is ignored. This assumption is valid considering the presence of oxidized debris in the areas surrounding the contact spots. Figure 6-23 shows the heat flux generated in one loading cycle for a typical fretting case.

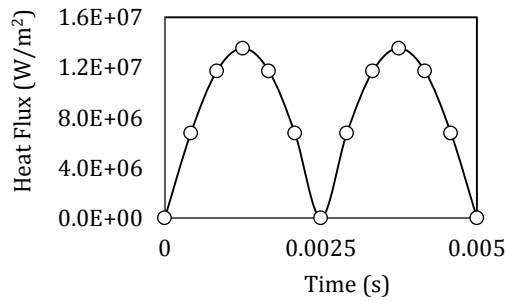


Figure 6-23: The generated heat flux at the contact interface (Material Cobalt Alloy 2, $p_m = 2177$ MPa, $F_n = 30$ N, $A = \pm 15$ μm , $f = 200$ Hz, $\mu = 0.33$).

6.5. Verification of model assumptions

6.5.1. Moving heat flux vs. stationary time-dependent heat flux

To check the validity of replacing the moving heat source by a stationary sinusoidal time-dependent heat flux, a comparative study was carried out. The motion was simulated by physically moving the MCAs for one complete cycle simulating the fretting motion. For the stationary condition, the heat flux was applied on the same MCAs, as a stationary sinusoidal time-varying flux according.

As Figure 6-24 shows, when investigating the time variation of the temperature at the node experiencing the maximum temperature rise during the first half of the fretting cycle, the difference between the moving heat flux and the stationary time-dependent heat flux was 0.4%.

The previous observation is in agreement with Attia and Youvanovich [71] who studied the effect of the different process parameters on the thermal constriction parameter, ψ defined as $\psi = 4.k.L.R_c$, where L is the characteristic length of an asperity MCA and R_c is the thermal constriction resistance at the MCA.

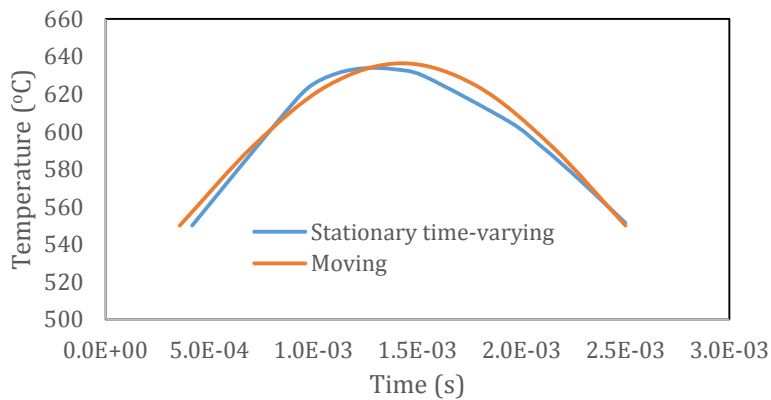


Figure 6-24: Moving heat flux vs. stationary sinusoidal time-varying heat flux at the maximum temperature point (Cobalt Alloy 2/Cobalt Alloy 1, $F_n = 30$ N, $A = \pm 15$ μ m, $f = 200$ Hz, $T_b = 550$ °C, $\delta = 10$ μ m, $\mu = 1$).

They concluded that when the Fourier modulus, Fo ($Fo = \alpha / fL^2$, where α is the thermal diffusivity, f is the frequency and L is the characteristic length) is lower than 250, $\psi_{fretting}$ (or moving) becomes close to ψ_{static} (or stationary). Considering the input parameters

used in this study (Cobalt Alloy 2/Cobalt Alloy 1, $F_n = 30$ N, $A = \pm 15$ μm , $f = 200$ Hz, $T_b = 550^\circ\text{C}$, $\delta = 10\mu\text{m}$, $\mu = 1$), ψ ranges between 10 and 200, depending on the characteristic length value.

When viewing the previous results in the light of the Peclet number introduced by Jaeger [67] and used later by Archard [69] to characterize the temperature rise of a moving heat source. The Peclet number is defined as $Pe = vL/2\alpha$, where v is the sliding velocity. Archard [69] showed that, to a reasonable approximation, when $Pe < 0.1$ (i.e. slow heat sources), the temperature of a moving heat source could be calculated by the same equation used for the stationary heat source. Considering the input parameters used in this study, $v = 0.019$ m/s, and Pe varies between 0.013 and 0.06, depending on the characteristic length.

6.5.2. Number of cycles required to reach steady state

Using the conclusion drawn from the previous study, the thermal load was applied as a stationary time-dependent heat flux over the elements representing the MCA, and the number of loading cycles (or time) required to reach the steady state was estimated. Figure 6-25 shows the temperature at the node experiencing the maximum temperature rise, when plotted against time for the first two cycles. It can be seen that the steady state regime can be reached after the first cycle.

This is in agreement with the work done by Wen and Khonsari [77] who conducted a transient thermal analysis of an oscillatory heat source in fretting. They concluded that the smaller the parameter γ ($\gamma = L\sqrt{\omega/\alpha}$ and ω is the angular frequency) the shorter the time-to-steady state. In their study, when γ was equal to 0.4 the steady state was reached after the first cycle and when γ increased by an order of magnitude to be equal to 4, the steady state is reached after the second cycle. Using the experimental and operational conditions in this study, where $L = 10 - 50$ μm , $\omega = 1257$ rad/s and $\alpha = 3.75 \times 10^{-2}$ cm^2/s , γ ranges between 0.2 and 0.9, which means that reaching steady state at the first cycle is logical.

Greenwood and Alliston-Greinern [74] showed that at low γ values, the maximum temperature rise is similar to the steady temperature resulting from a constant heat supply. Their explanation was that the heat input rate is slow enough to accelerate reaching

the steady state. Hirano and Yoshika [127] who studied the temperature in reciprocating contacts, commented that when $L.A.\omega/\alpha$ is small, the maximum temperature is close to that of a unidirectional source moving steadily at the maximum speed.

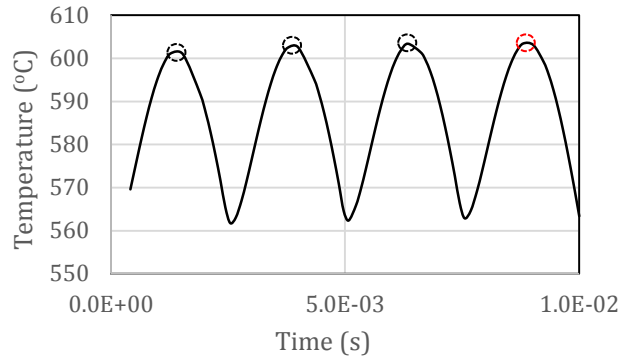


Figure 6-25: Nodal temperature at the point experiencing the maximum temperature rise when plotted against time (Cobalt Alloy 2/Cobalt Alloy 1, $F_n \approx 30$ N, $A = \pm 15$ μ m, $f = 200$ Hz, $T_b = 550^\circ$ C $\delta = 10$ μ m, $\mu = 0.33$).

6.5.3. Analysis of heat partitioning

The amount of frictional heat flowing into each contacting bodies is determined based on its total thermal resistance. This total resistance is the summation of the material bulk resistance, R_b and the thermal constriction (spreading) resistance, R_c . Since the heat flow is time dependent in fretting, the term thermal impedance, Z is used instead of the term thermal resistance, R [18]. Since it has been established that the periodic (transient) term of the temperature is small and that the steady state is quickly reached in the first cycle, the thermal resistance determines the thermal impedance of the contacting materials. To assess the thermal resistance of each body, an analysis was conducted in which it was assumed that 100% of the heat flows to each body separately, as if the other body did not exist. The input parameters were varied to cover a wide range of experimental conditions. The results are tabulated in Table 6-6 and plotted in Figure 6-26.

As shown in Figure 6-26, the maximum temperature rise ΔT_{max} was plotted against the maximum heat flux values q_{max} (the value of the heat flux at the peak of the loading cycle)

for each body. It can be seen that the $\Delta T_{max} - q_{max}$ relationship can fit a straight line whose slope represents the thermal resistance of the body.

Table 6-6: Maximum temperature rise for the different conditions assuming 100% of the heat flows to each body separately.

		COF	Frequency	Amplitude	Maximum Heat Flux	Maximum temperature rise
		μ	f	A	q_{max}	ΔT_{max}
Material	Case	-	Hz	μm	W/m^2	$^{\circ}\text{C}$
Cobalt Alloy 2	1	0.33	100	± 15	$6.8\text{E}+06$	49.3
	2			± 25	$1.1\text{E}+07$	89.2
	3		200	± 15	$1.3\text{E}+07$	106.8
	4			± 25	$2.3\text{E}+07$	157.8
	5	0.71	100	± 15	$1.4\text{E}+07$	104.9
	6			± 25	$2.4\text{E}+07$	174.9
	7		200	± 15	$2.9\text{E}+07$	199.1
	8			± 25	$4.8\text{E}+07$	357.8
Cobalt Alloy 1	9	0.71	200	± 25	$4.8\text{E}+07$	322.4

In order to find the amount of heat flowing to each body, the following conditions must be satisfied at the interface of bodies 1 and 2 [18]:

1. The conservation of energy or the Fourier's conduction equation in this case.
2. The continuity of the maximum contact temperature at the interface, which means that a point at the interface must have the same temperature, whether it is viewed from body 1 or from body 2. Mathematically, $\Delta T_{max,1} = \Delta T_{max,2}$ at the same point at the interface.

The first condition was satisfied through the FE formulation, while to apply the second condition, a horizontal line was drawn at a chosen maximum temperature rise value of $\Delta T_{max} = 300^{\circ}\text{C}$, represented by the horizontal dashed line in Figure 6-26. This straight line

meets the $\Delta T_{max} - q_{max}$ line at two points, whose abscissa define the ratio of the heat portion going to each body. This ratio was found to be $Q_{Cobalt Alloy 1}/Q_{Cobalt Alloy 2} = 0.95$. In other words, 51% of the generated heat flows to Cobalt Alloy 1, while 49% of the generated heat flows to Cobalt Alloy 2.

A look at the tribo-system thermal circuit explains the previous finding. The ratio of the heat flow is $Q_{Cobalt Alloy 1}/Q_{Cobalt Alloy 2} = (R_c + R_b)_{Cobalt Alloy 2} / (R_c + R_b)_{Cobalt Alloy 1}$. Knowing that the ratio of thermal conductivities $k_{Cobalt Alloy 2} / k_{Cobalt Alloy 1} = 0.94$, more heat (51% of the total generated heat) is expected to flow to the slightly less resistive (more conductive) Cobalt Alloy 1, as shown in Figure 6-26. Since the ratio of heat fluxes was found to be close to unity, it can be assumed that the two bodies share the same amount of frictional heat.

To elaborate on the previous concept, the same exercise was repeated with materials having too different properties, e.g. Cobalt Alloy 2 in contact with AISI 1095 steel, with $k_{Cobalt Alloy 2} / k_{steel} = 0.4$. Figure 6-27 shows the $q_{max} - \Delta T_{max}$ relationship for the two materials. As expected, the heat partitioning looks different than the contact of similar material. At the same maximum temperature rise value of 30°C, more heat flows to the less resistive (more conductive) steel part.

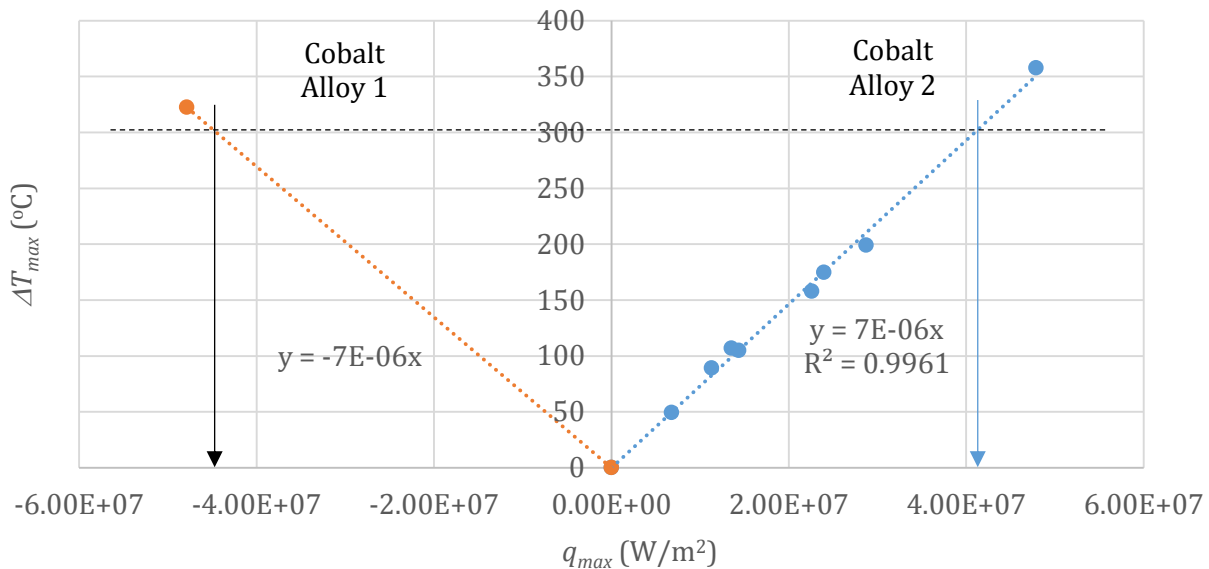


Figure 6-26: Heat partitioning analysis showing the thermal impedance of the Cobalt Alloy 2 / Cobalt Alloy 1 pair as the slopes of the blue and red lines, respectively (Cobalt Alloy 2/Cobalt Alloy 1, $F_n = 30$ N, $A = \pm 10$ and $15 \mu m$, $f = 100$ and 200 Hz, $T_b = 550^\circ C$, $\delta = 10 \mu m$, $\mu = 0.33$ and 0.71).

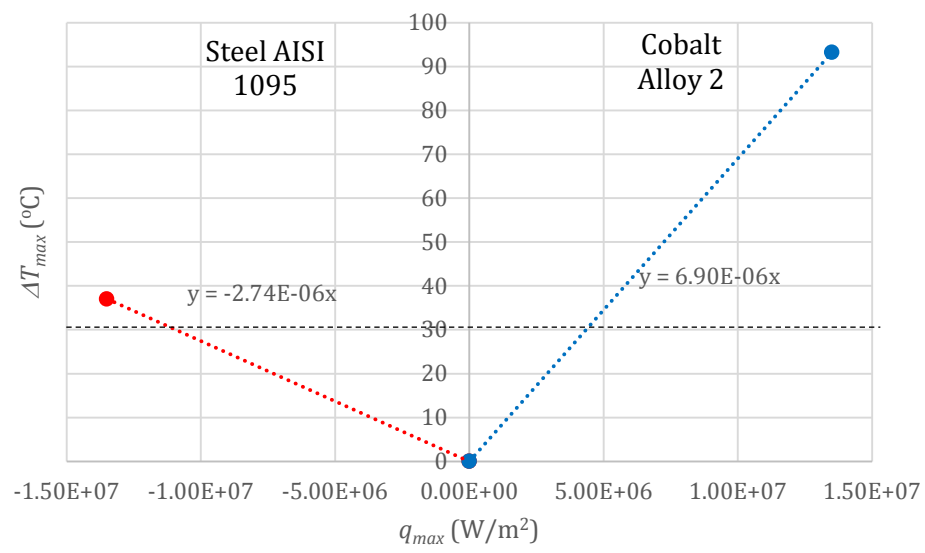


Figure 6-27: Heat partitioning analysis for the Cobalt Alloy 2/ AISI 1095 steel pair.

Chapter 7 Contact Temperature Prediction in Fretting Wear: Model Validation and Sensitivity Analyses

7.1. Introduction

The previous chapter discussed the significance of frictional heat and the idea behind the contact-based thermal model that predicts the contact temperature. In addition, it discussed the assumptions made, their validity and reasonableness, followed by a process of model verification. In this chapter, the model is validated and further employed to carry out some sensitivity analyses used to investigate numerous effects beyond the scope of the available experimental data, which demonstrates the versatility of the model in different applications.

7.2. Model validation

The difficult estimation of the contact temperature during fretting and the uncertainty associated with the assessment of its effect appears to be natural since the localized contact and the small sized thermally disturbed zone hinder the possibility of experimental measurements. As a consequence, relying on indirect measurements along with subsequent surface analysis represents a plausible solution [117]. The aim of this section is to check whether the assumptions which have been made are reasonable with respect to the real system. In order to validate the model, a reference experimental case [123] was simulated for comparison. Table 7-1 shows the condition of this reference case and the predicted temperatures.

To validate the model, the Raman oxide analysis conducted in section 5.5 was used. First, when investigating the analysis shown in Figure 5-7, the absence of CoO in the damaged area of the specimen fretted at 550°C shows that the contact temperature, within this area, is between 600°C and 700°C [102], as explained in section 5.5. This represents a direct and simple approach; however, it remains a rough validation. The second approach is indirect and relies on considering the thicknesses of the oxide to be proportional to the peak of the Raman spectrum [99, 124]. This approach has shown that the contact temperature within

the fretted area is around 600°C, in other words, the temperature rise is around 50°C. This represents 7.5 % higher than the 46.6°C predicted by the FE model, as shown in Table 7-1.

Table 7-1: Reference case conditions and the predicted maximum temperature rise.

Parameters	Symbol	Nominal Values	Units
Contact pair	CP	Cobalt Alloy 2 / Cobalt Alloy 1	
Amplitude of slip	A	± 15	μm
Normal load	F_n	30	N
Frequency	f	200	Hz
Bulk temperature	T_b	550	°C
Max. temperature rise predicted by FE model	$\Delta T_{max, FE}$	46.6	°C
Max. temperature rise estimated by experimental observation	$\Delta T_{max, Exp}$	50	°C

7.3. Real surface vs uniform idealized surface

In order to test the significance of using the real contact of the fretted surfaces, a comparison was conducted between this model and the model based on uniformly distributed equal-sized micro-contact areas. The latter is based on the model developed by Attia et al [71, 73], where equations (6-6) to (6-10) were used to calculate the micro-contact attributes. In this model, an array of 3 x 3 asperities, having dimensions of 165 μm x 165 μm , represents the starting and the near region heat sources, as shown in Figure 7-1 (a) and (b). The heat generated by the surrounding was considered to be the overall contribution of the asperity contacts depicted as black crosses in the far region, as shown in Figure 7-1(a). The far region has dimensions of 495 μm x 495 μm . The thermal conductivity of the bulk material (substrate) is considered to be 10 times the conductivity of the oxide layer.

Figure 7-1 (d) shows the temperature field along the depth for the two model. It can be observed that the uniform model could not capture neither the right temperature value,

nor the thermal gradient when compared to the real contact-based model. The difference in the predicted temperature is around 66 %. This difference comes from the fact that the randomization in the real contact enabled clustering of some MCAs, based on the contact pattern, which could not be occurring in the idealised uniform model.

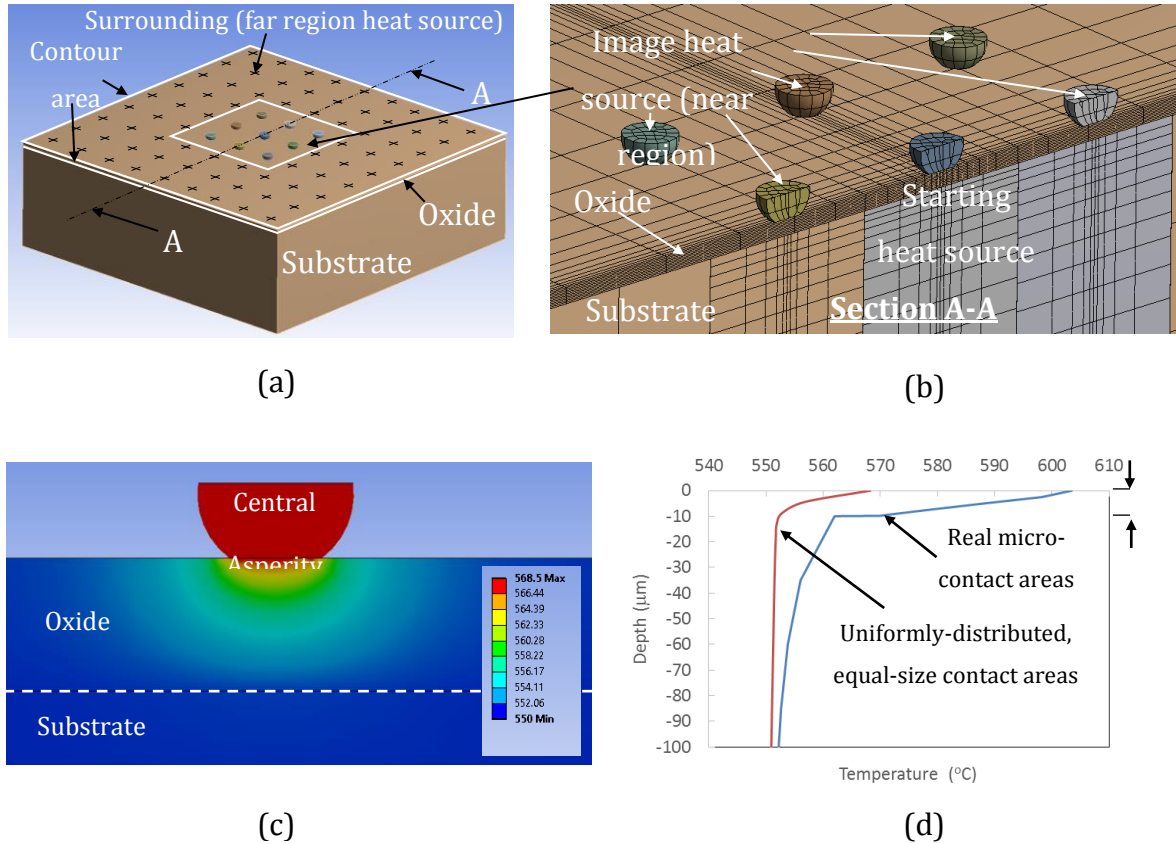


Figure 7-1: Uniformly distributed equal-sized MCAs model (a) model overview showing the 3 x 3 array of asperities, the surrounding and the oxide layer, (b) a cross section showing the central and the neighbouring asperities, and (c) the thermal field along the depth in the contact region (T in $^{\circ}\text{C}$), and (d) comparison of the temperature profile along the depth between the real contact-based model and the uniformly distributed equal-sized MCAs model (Cobalt Alloy 2/Cobalt Alloy 1, $F_n = 30 \text{ N}$, $A = \pm 15 \text{ } \mu\text{m}$, $f = 200 \text{ Hz}$, $T_b = 550^{\circ}\text{C}$, $\delta = 10 \text{ } \mu\text{m}$, $\mu = 0.33$).

7.4. Effect of fretting operation conditions on the maximum contact temperature rise

In the Section 6.5.3, the relationship between the maximum temperature rise and the maximum heat flux value has been established for a given material. When the time dependent sine argument is omitted, equation (6-3) indicates that the maximum heat flux

value depends on the coefficient of friction, the flow stress, the amplitude of slip and the frequency of oscillation, as shown in equation (7-1):

$$q_{max} = \mu p_m (2\pi A f) \quad (7-1)$$

Therefore, for the modeled Cobalt Alloy 2 superalloy, the maximum temperature rise could be expressed in terms of the fretting operation conditions, as shown in Figure 7-2. The 3D plot depicts the change of the temperature with the amplitude of the slip and the frequency of oscillation when the coefficient of friction and the flow stress were fixed. The 3D plot shows also that at high practical values of amplitude and frequency, the maximum temperature rise could reach up to 250°C.

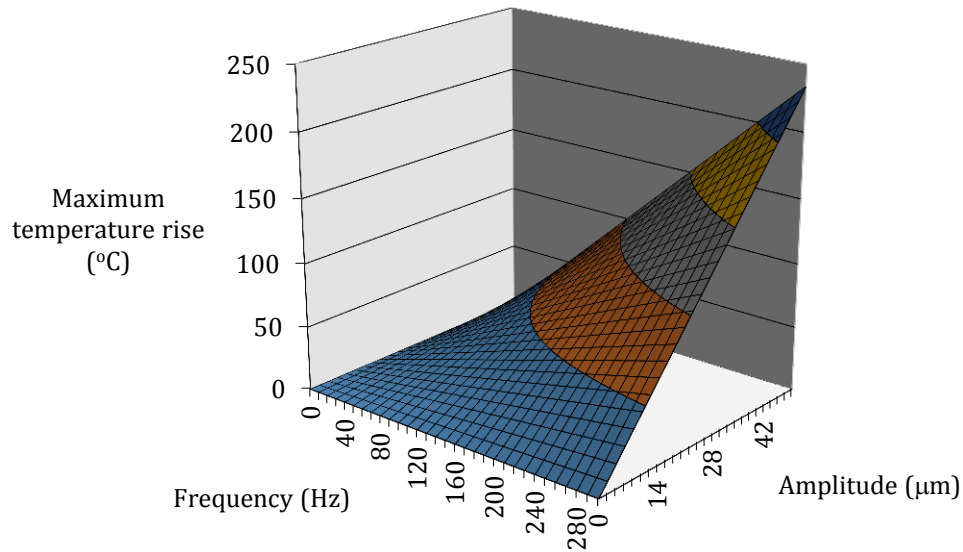


Figure 7-2: Effect of the fretting operation conditions process parameters on the maximum temperature rise
(Cobalt Alloy 2/Cobalt Alloy 1, $F_n = 30$ N, $p_m = 2177$ MPa, $T_b = 550^\circ\text{C}$, $\delta = 10$ μm , $\mu = 0.33$).

7.5. Effect of surface condition

The condition of the surface has an important effect on the contact temperature prediction. At the early stages of the fretting process, the fresh surface is in a machined condition, it bears no oxide and the coefficient of friction has a certain initial value. At the late stages of the fretting process, the surface is highly damaged, having an oxide layer developed at the surface and the coefficient of friction has a value different than the early stages. A comparison between the two surface conditions: the machined and the fretted condition,

was carried out using two different contact pairs: Cobalt Alloy 2 / Cobalt Alloy 1 and Ti-6Al-4V / Ti-6Al-4V. At the machined condition, the contact has the form of regular repeated patterns with no surface oxide as shown in Figure 7-3 (a). On the other hand, in the fretted condition, the contact pattern has the form of random damaged areas covered by a layer of oxide, as shown in Figure 7-3 (b). The fixed conditions are summarized in Table 7-2, while Table 7-3 shows the material properties of the two pairs, including their oxide properties.

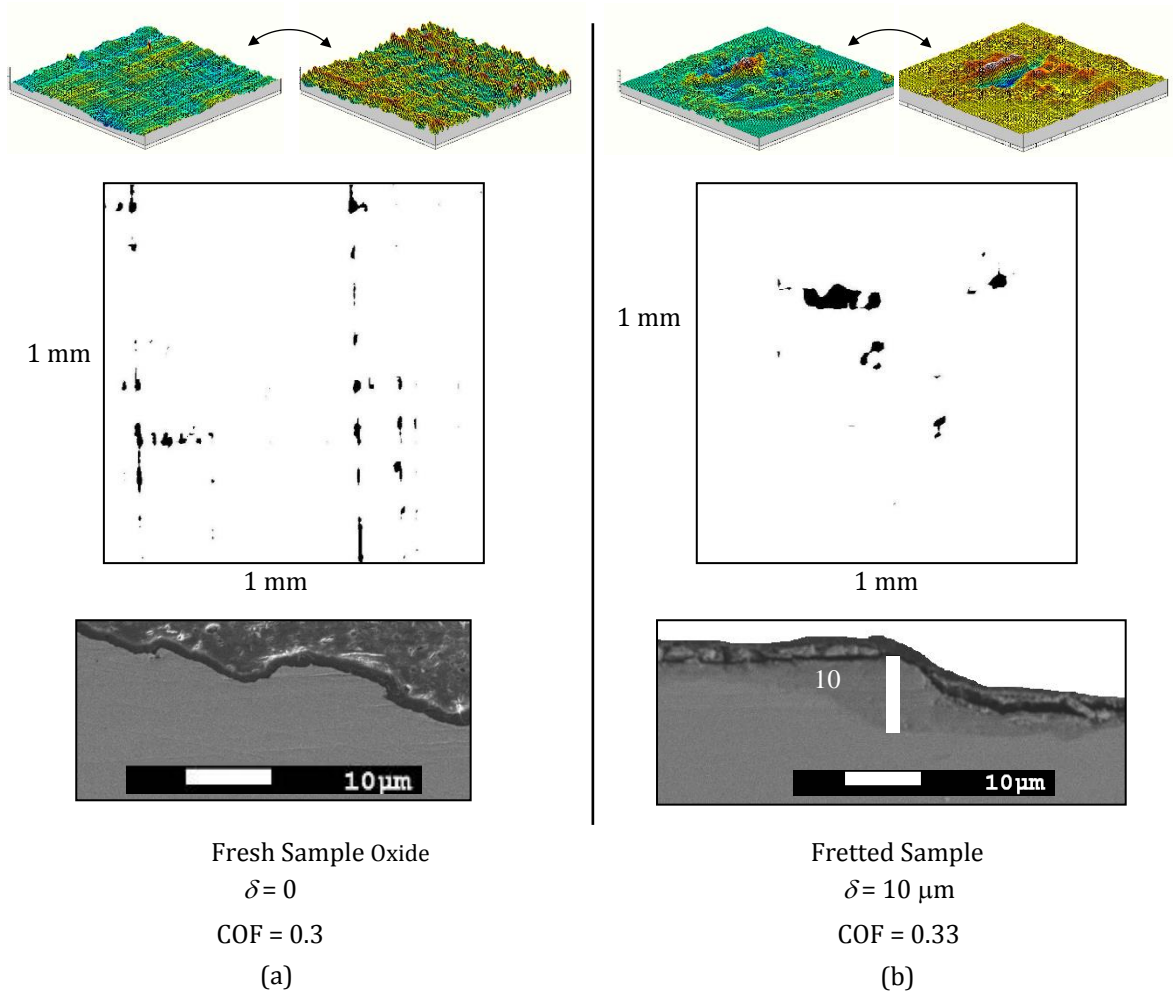


Figure 7-3: Contacting surfaces, contact pattern and cross section of (a) the unfretted sample and (b) the fretted sample ($F_n = 30 \text{ N}$, $\varepsilon^2 = 1.26 \%$, $T_b = 550^\circ\text{C}$, $A = \pm 15 \mu\text{m}$, $f = 200 \text{ Hz}$, $A_a = 1 \text{ mm}^2$).

Table 7-2: Fixed conditions of the simulation conducted to study the effect of the surface condition.

Condition	Symbol	Value	Unit
Normal load	F_n	30	N
Constriction ratio	ε^2	1.26	%
Bulk temperature	T_o	550	°C
Frequency of oscillation	f	200	Hz
Amplitude of slip	A	15	μm
Apparent area of contact	A_a	1	mm ²
Heat partitioning factor	ξ	0.5	-

Table 7-3: Material properties and maximum temperature rise values when the surface condition changed from the unfretted to the fretted state.

	Fresh Surface			Fretted Surface		
	Flow stress	Thermal conductivity	Maximum temperature rise	Flow stress	Thermal conductivity	Maximum temperature rise
	P_m	k	ΔT_{max}	P_m	k	ΔT_{max}
	(MPa)	W/m.K	(°C)	(MPa)	W/m.K	(°C)
Cobalt Alloy 2	885	20.0	2.4	2176.6	2	46.6
Ti-6Al-4V	900	13.5	3.6	2322	1.35	72.7

The results shown in Figure 7-4 indicate the following.

1. The surface contact temperature changes with the change of the surface condition, and consequently, with time.
2. This temperature, which is affecting the oxide kinetics, and the oxide layer formation, is also being affected by the oxide thickness; and hence the process nonlinearity. The thicker the oxide, the higher the temperature rise.

3. The results show that the higher temperature rise in the case of the Ti-6Al-4V / Ti-6Al-4V pair. This can be attributed to the higher flow stress value of its oxide combined with its lower thermal conductivity when compared to the oxide formed on top of the Cobalt Alloy sample.
4. When the damage took place at the fretted sample, the uniform contact pattern of the machined sample disappeared and the micro-contact areas (MCAs) started clustering. This clustering produced a higher surface temperature.

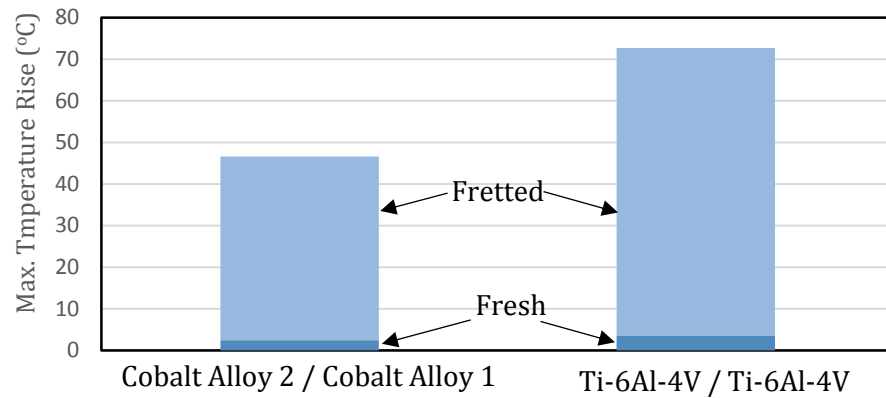


Figure 7-4: Effect of the surface condition on the maximum temperature rise for both pairs; Cobalt Alloy 2 / Cobalt Alloy 1 and Ti-6Al-4V / Ti-6Al-4V.

The presence of low conductivity oxide masked the effect of topography change. This poses the question of whether this temperature rise originated from the topography change or from the presence of the oxide or from the combination of both. In reality, the two effects occur simultaneously; however, for the sake of investigation, they are studied separately. First, a comparison was carried out with two pairs of titanium Ti-5Al-2.5Sn / Ti-5Al-2.5Sn bearing no surface oxide. The machined and fretted surfaces of the reference case (Table 7-1) were used in that simulation with some minor changes in the loading and surface conditions to help investigating the effect of surface topography. First, the normal load was increased to 60 N, which was equivalent to a constriction ratio of 4%. Second, the oxide film was removed to eliminate its effect. Table 7-4 shows the simulation conditions used in this study.

Table 7-4: Simulation conditions used in the study of the effect of surface condition in the absence of an oxide layer.

Condition	Symbol	Value	Unit
Contact pair	CP	Ti-5Al-2.5Sn / Ti-5Al-2.5Sn	-
Normal load	F_n	60	N
Constriction ratio	ε^2	4	%
Bulk temperature	T_o	550	°C
Frequency of oscillation	f	200	Hz
Amplitude of slip	A	15	μm
Apparent area of contact	A_a	1	mm^2
Oxide thickness	δ	0	μm
Heat partitioning factor	ξ	0.5	-

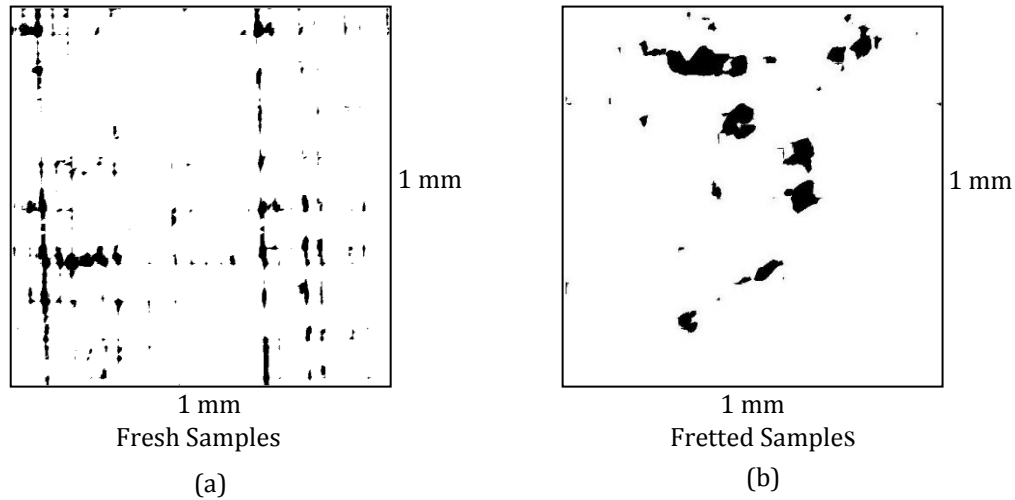


Figure 7-5: Contact pattern of (a) the fresh samples and (b) the fretted samples for the Ti-5Al-2.5Sn / Ti-5Al-2.5Sn simulation ($F_n = 60 \text{ N}$, $\varepsilon^2 = 4 \%$, $T_b = 550^\circ\text{C}$, $A = \pm 15 \mu\text{m}$, $f = 200 \text{ Hz}$, $A_a = 1 \text{ mm}^2$, $\delta = 0 \mu\text{m}$).

Figure 7-6 shows the contour plot of the temperature field at the top surface. It can be seen that, even in the absence of an oxide layer, the change in the topography coming from the surface damage led to a 35% increase in the maximum temperature rise for the same fretting operation conditions.

In addition to the change in the maximum temperature rise, the average contact temperature is also affected. Figure 7-7 shows that the area of $600^{\circ}\text{C} \leq T \leq 650^{\circ}\text{C}$ (the green area) and the area of $650^{\circ}\text{C} \leq T \leq 700^{\circ}\text{C}$ (the red area) have increased in the fretted condition by approximately 50% and 60%, respectively.

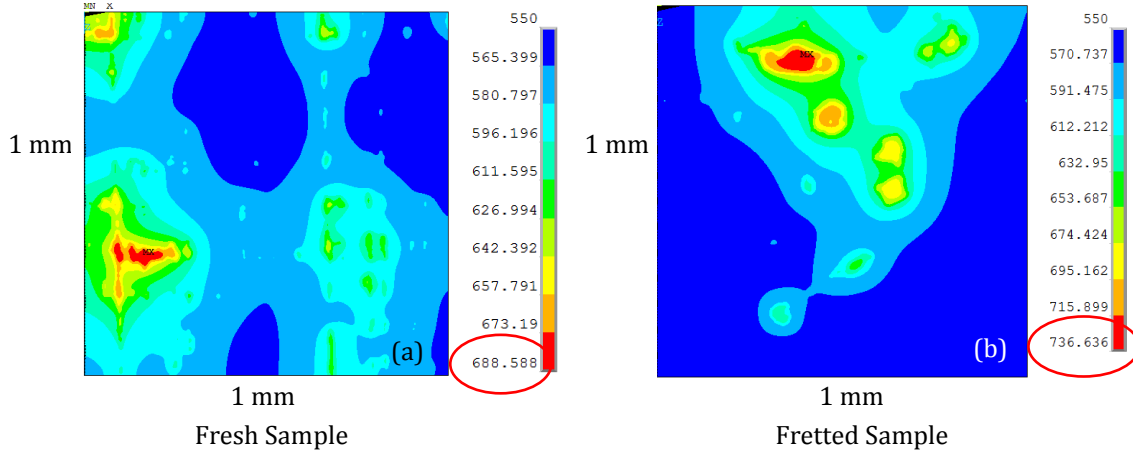


Figure 7-6: Effect of surface topography on the contact temperature rise in the absence of the oxide layer. Temperature field for the (a) fresh sample and (b) fretted sample for the Ti-5Al-2.5Sn / Ti-5Al-2.5Sn simulation ($F_n = 60 \text{ N}$, $\varepsilon^2 = 4 \%$, $T_b = 550^{\circ}\text{C}$, $A = \pm 15 \mu\text{m}$, $f = 200 \text{ Hz}$, $A_a = 1 \text{ mm}^2$, $\delta = 0 \mu\text{m}$).

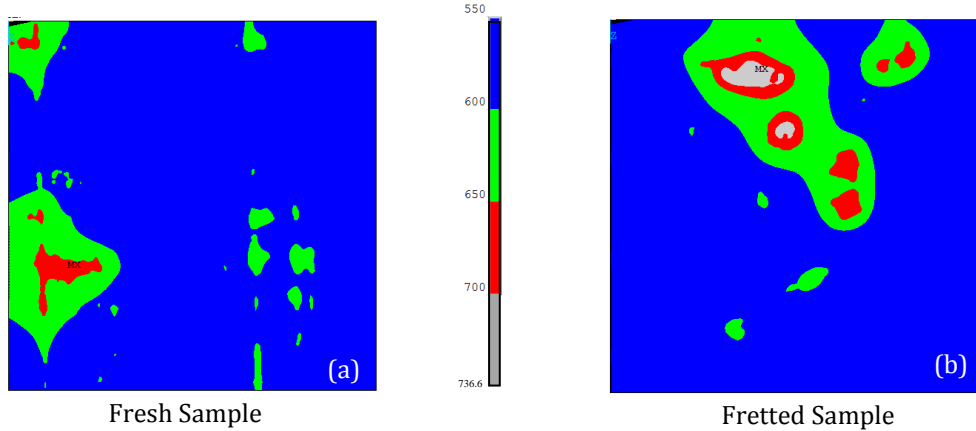


Figure 7-7: Effect of surface topography on the contact temperature rise in the absence of the oxide layer, (a) fresh sample and (b) fretted sample for the Ti-5Al-2.5Sn / Ti-5Al-2.5Sn simulation ($F_n = 60 \text{ N}$, $\varepsilon^2 = 4 \%$, $T_b = 550^{\circ}\text{C}$, $A = \pm 15 \mu\text{m}$, $f = 200 \text{ Hz}$, $A_a = 1 \text{ mm}^2$, $\delta = 0 \mu\text{m}$).

In order to relate the previous results to the surface characterization, Figure 7-8 shows the autocorrelation functions (ACF) of two types of surfaces. The ACF shows the similarity (or repetition) happening in the surface when being translated with respect to itself [125]. It

can be seen that for the machined surfaces (Figure 7-8(a)), the central lobe of the ACF extends primarily along one direction exhibiting a slow decay in such a way that if the surface is translated along this direction, it does not change much. This extension and slow decay along the lay is a result of the constant depth of cut along each valley. In addition, the central lobe extends across the lay exhibiting a faster decay as a result of the periodic peak spacing coming from the constant feed rate during the machining process. When a pair of this kind of surface comes into contact, there is a contact pattern of repetitive MCAs, spreading out their effect and leading to a lower contact temperature.

On the other hand, the ACF of the fretted surface has a wider lobe that extends along one axis up to a certain distance before ceasing (Figure 7-8 (b)). The ACF takes that form because the localized damage covered the effect of the machined surface, and the periodicity of the topography was interrupted by the deep wear scar. This localization of damage agglomerates the MCAs (the heat generators) leading to a higher contact temperature rise.

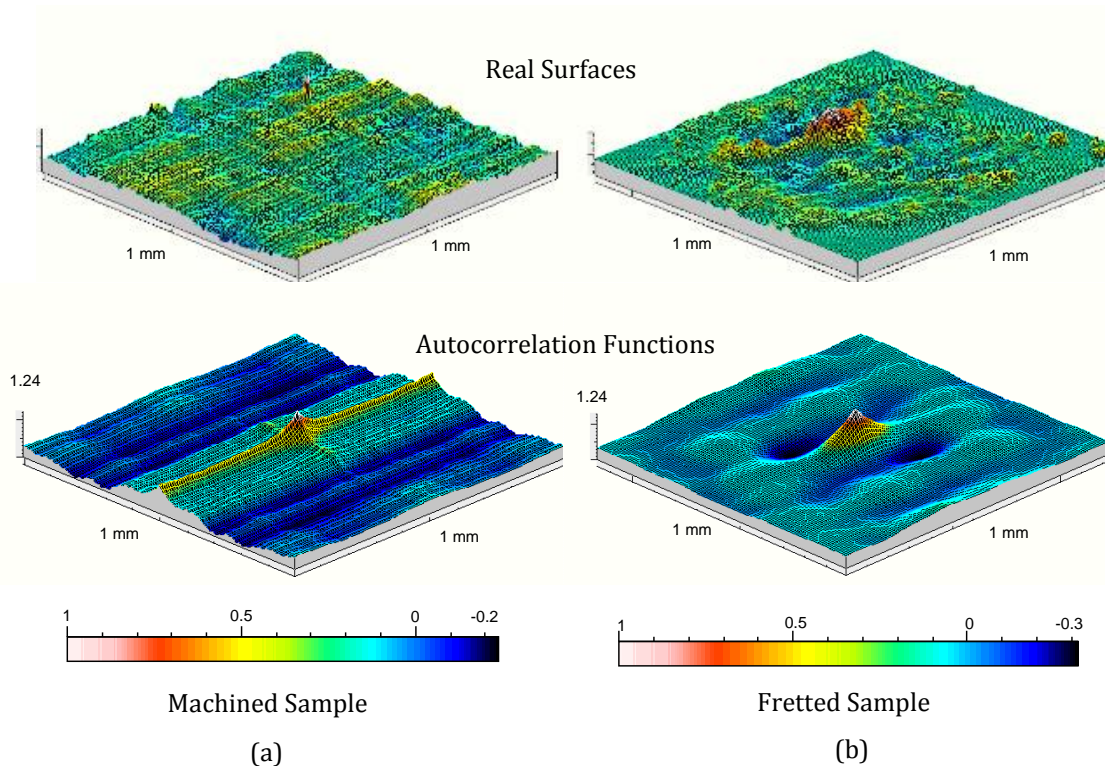


Figure 7-8: Real surfaces (above) and autocorrelation functions (below) of the (a) machined surface and (b) fretted surface.

7.6. Effect of oxide thickness

Previous experimental results [123] have shown that the surfaces fretted at high temperature are covered with an oxide layer that varies in thickness according to the oxidation kinetics, material properties and loading conditions. To investigate the effect of surface oxide separately, a simulation is performed at three different oxide thickness values: zero oxide thickness, simulating the absence of the oxide, 10 μm which is the closest value to the experimental results and at 20 μm . The matrix of the simulation used in the study of the oxide effect, is shown in Table 7-5.

Figure 7-9 shows the $q_{max} - \Delta T_{max}$ relationship, at different oxide thicknesses. Figure 7-10 shows the evolution of the maximum temperature rise with the oxide thickness at a fixed heat flux value of $q = 1.4 \text{ e7 W/m}^2$. The following conclusions can be drawn from the two graphs:

1. In the absence of oxide (the blue line in Figure 7-9), the temperature rise is only around 15°C due to the absence of any higher thermal conductivity oxide resulting from the fretting conditions.
2. When the thickness of oxide was 20 μm , the rise in contact temperature is considerable and can reach up to 130 °C.

Table 7-5: Simulation parameters for the investigation of the oxide thickness effect.

Parameters	Symbol	Nominal Values	Units
Contact pair	CP1	Cobalt Alloy 2/Cobalt Alloy 1	
Amplitude of slip	A	± 15	μm
Normal load	F_n	30	N
Frequency	f	200	Hz
Bulk temperature	T	550	°C
Oxide thickness	δ	0, 10, 20	μm

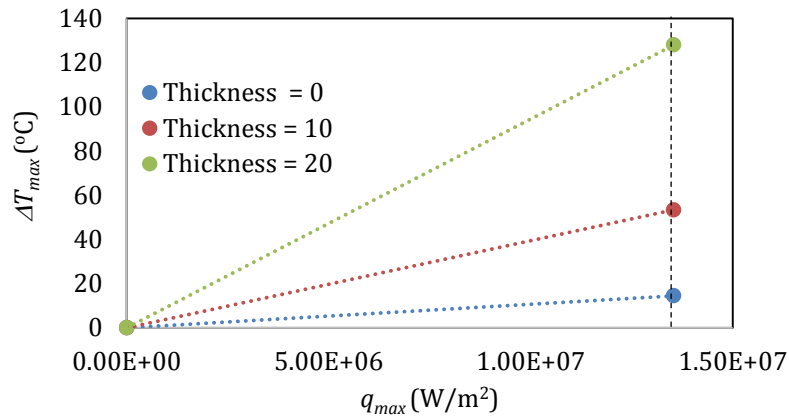


Figure 7-9: Maximum temperature rise at different oxide thickness values (Cobalt Alloy 2 / Cobalt Alloy 1, $q = 1.4 \text{ e}7 \text{ W/m}^2$, $F_n = 30 \text{ N}$, $A = \pm 15 \text{ } \mu\text{m}$, $f = 200\text{Hz}$, $\mu = 0.33$, $T_{bulk} = 550^\circ\text{C}$).

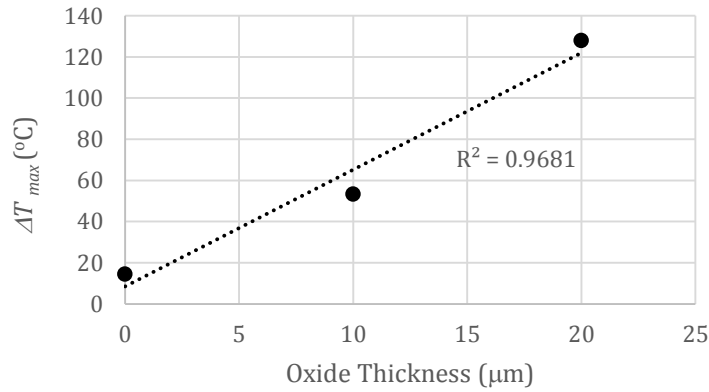


Figure 7-10: Maximum temperature rise vs oxide thickness (Cobalt Alloy 2 / Cobalt Alloy 1, $q = 1.4 \text{ e}7 \text{ W/m}^2$, $F_n = 30 \text{ N}$, $A = \pm 15 \text{ } \mu\text{m}$, $f = 200\text{Hz}$, $\mu = 0.33$, $T_{bulk} = 550^\circ\text{C}$).

7.7. Effect of material properties and normal load

In order to investigate the effect of some process parameters on the friction-induced temperature rise in fretting, different material combinations were used; Aluminum Al 6061 alloy, Cobalt Co-Ni-Cr alloy, Titanium Ti-5Al-2.5Sn alloy and Silicon Nitride Si_3N_4 Ceramic. The normal load was varied to cover a range of contact pressure-to-flow stress ratio, ε^2 between 0 and 4 %. The fixed conditions are summarized in Table 7-6, while the material properties and the corresponding maximum temperature rise are listed in Table 7-7.

Table 7-6: Simulation fixed conditions used to study the effect of material and normal load on the contact temperature prediction.

Condition	Symbol	Value	Unit
Bulk temperature	T_o	25	°C
Frequency of oscillation	f	200	Hz
Amplitude of slip	A	±15	μm
Apparent area of contact	A_a	1	mm ²
Heat partitioning factor	ξ	0.5	-
Oxide thickness	δ	0	μm

In this comparison, the machined contact pattern, shown in Figure 7-5 (a), was considered. The simulation was conducted at room temperature and the dependence of thermal and mechanical properties on the temperature were ignored. Figure 7-11 shows the effect of the applied load on the maximum contact pressure for the different contact pairs.

Table 7-7: Material properties and maximum temperature rise for different materials and constriction ratio values.

Contact pair material	Flow stress	Thermal conductivity
	P_m	k
	(MPa)	W/m.K
Al 6061	828	167.0
Co-Ni-Cr	1515	9.4
Ti-5Al-2.5Sn	2940	7.8
Silicon Nitride Ceramic	19600	30

When looking at the results in Figure 7-11, the following observations could be made.

1. For aluminum alloys, the temperate rise is very small even at high contact loads due to the high thermal conductivity associated with the low flow stress of the material.
2. Although the fretting conditions are not very severe, materials like silicon nitride ceramics experienced high temperature rise values that can go up to 250°C due to its low thermal conductivity associated with its high hardness.
3. Under these selected fretting operation conditions, the maximum temperature rise values for Ti-alloy could go up to 150°C. If the transition temperature for this alloy, at which the fretting mechanism and wear rates change, lies between 400°C and 500°C, the alloy might undergo transition at a bulk temperature as low as 300°C.

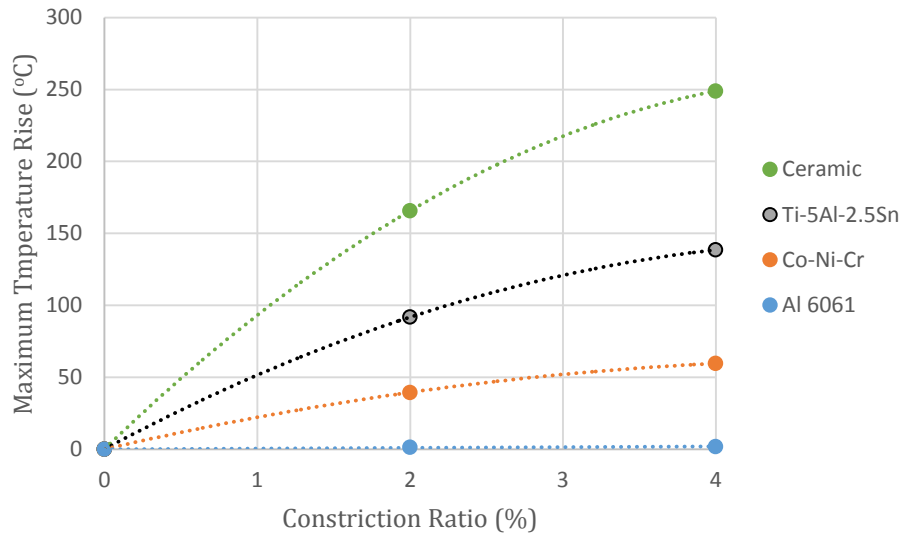


Figure 7-11: Effect of the material properties and applied load (pressure) on the maximum temperature rise ($A = \pm 15 \mu\text{m}$, $f = 200\text{Hz}$, $\mu = 0.33$, $T_{\text{bulk}} = 25^\circ\text{C}$, $\xi = 0.5$, $A_a = 1\text{mm}^2$).

The previous results hold for machined surfaces, however, if the surfaces are fretted, the situation could change. Therefore, a fretted pair similar to the one shown in Figure 7-5 (a) were considered. Two normal loads were used in the simulation; 30 N and 60 N, corresponding to constriction ratio values of 1.26 and 2.61, respectively.

The fretting wear parameters (amplitude of slip, frequency of oscillation and coefficient of friction) were also varied to cover a wider range of heat input. Figure 7-12 shows the maximum temperature rise when plotted against the maximum heat flux for a Cobalt Alloy 2 contact pair when fretted at the conditions mentioned in Table 7-8.

Table 7-8: Simulation conditions used to study the effect of normal load on the contact temperature prediction.

	Oxide thickness	Normal Load	Coefficient of Friction	Frequency	Amplitude	Heat Flux	Maximum temperature rise
	δ	F_n	μ	f	A	q	ΔT_{max}
Case	μm	N	-	Hz	μm	W/m^2	$^{\circ}\text{C}$
1	10	30	0.33	100	± 15	$6.77\text{E}+06$	24.6
2				200	± 25	$2.26\text{E}+07$	78.9
3			0.71	200	± 25	$4.79\text{E}+07$	178.9
4		60	0.33	100	± 15	$6.77\text{E}+06$	24
5				200	± 25	$2.26\text{E}+07$	88
6			0.71	200	± 25	$4.79\text{E}+07$	187.5

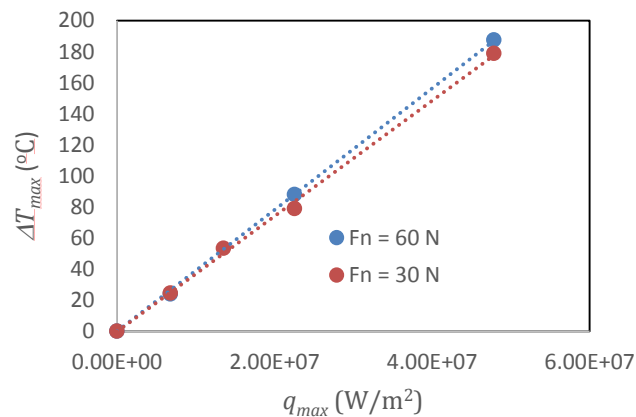


Figure 7-12: Effect of load on the maximum temperature rise – maximum heat flux relationship (Cobalt Alloy 2 / Cobalt Alloy 2, $A = \pm 15$ and $\pm 25 \mu\text{m}$, $f = 100$ and 200 Hz , $\mu = 0.33$ and 0.71 , $T_{bulk} = 550^{\circ}\text{C}$).

It can be seen that at higher load, the maximum contact temperature rise does not change significantly (187.5°C at 60 N vs 178.9°C at 30 N). It has been speculated that when more contact points are engaged, an increase in the contact temperature is expected. However, this study shows that the rise in temperature is not high enough. In an attempt to explain the previous results, the temperature fields corresponding to the two load levels are analyzed (Figure 7-13). It can be observed that the increase in load has led to the following.

1. A slight increase in the maximum contact temperature.
2. A shift in the position of the maximum temperature rise.
3. A larger extent of the high temperature zones, or in other words, there is an increase in the surface average temperature.

The temperature rise associated with the increase of load is expected because when the load increases, the real contact area increases as a result of a growing number of contact points rather than an increase in the size of each micro-contact area separately, as established by Hisakado [61]. Consequently, the total number of heat generators is expected to grow and the amount of heat supplied to the contacting bodies is boosted. However, depending on the contact pattern, the increase in the number of MCAs can have different effects. If the MCAs are distributed in such a way that at higher load they can coalesce and form larger MCAs clusters, there will be a considerable rise in the contact temperature, which is not the case in Figure 7-13.

This case represents a scenario of load increase which does not lead to larger MCAs clusters, but associates more points in the neighbourhood of the old contact points, without considerable coalescence. As a result, a higher load does not lead to a significant increase in the maximum temperature, but leads to an enlargement in the extent of the higher temperature zones. Figure 7-14 shows the change in the areas having a contact temperature value > 700°C (in red) when the load is increases from 30 N to 60 N.

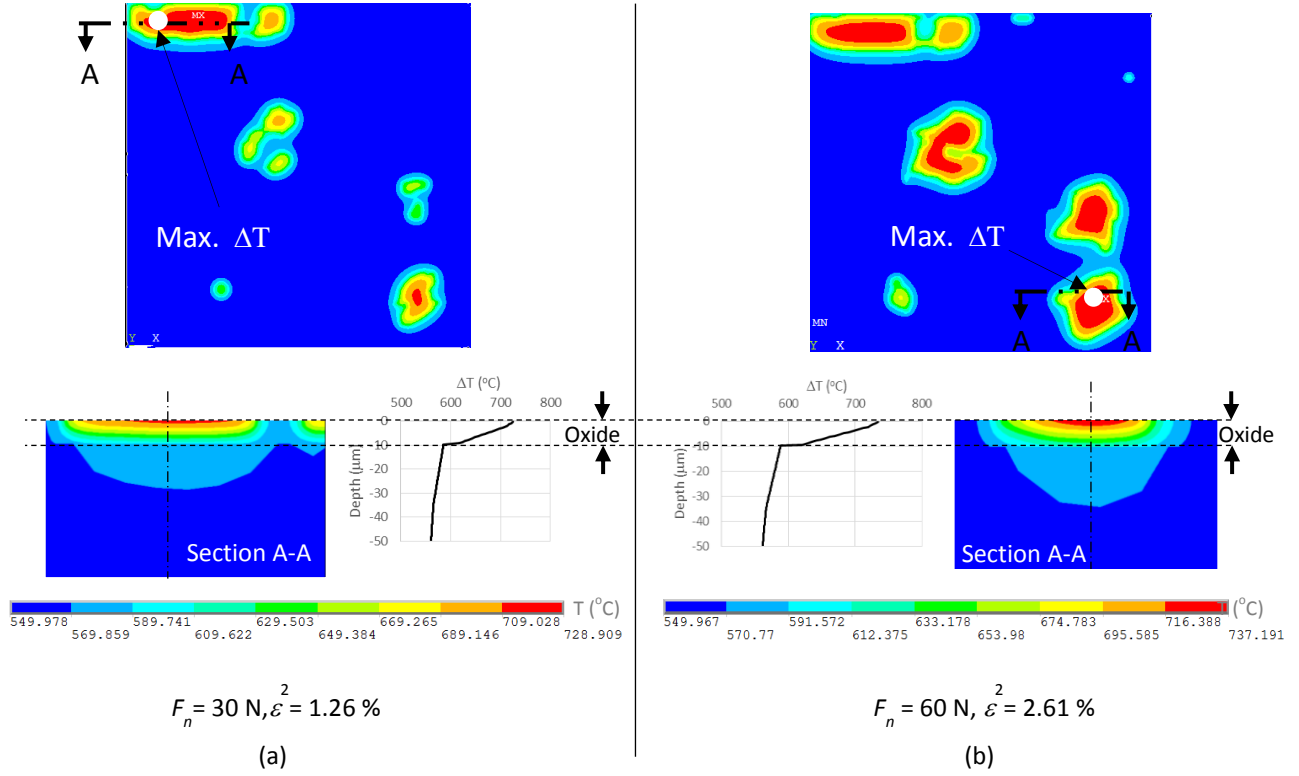


Figure 7-13: Contour plot of the temperature field at the top surface of the central area and the temperature plot along the depth at the point experiencing the maximum temperature rise (a) $F_n = 30 \text{ N}$ ($\varepsilon^2 = 1.26$) and (b) $F_n = 60 \text{ N}$ ($\varepsilon^2 = 2.61$) (Cobalt Alloy 2 / Cobalt Alloy 2, $A = \pm 25 \mu\text{m}$, $f = 200 \text{ Hz}$, $\mu = 0.71$, $T_{\text{bulk}} = 550^\circ\text{C}$).

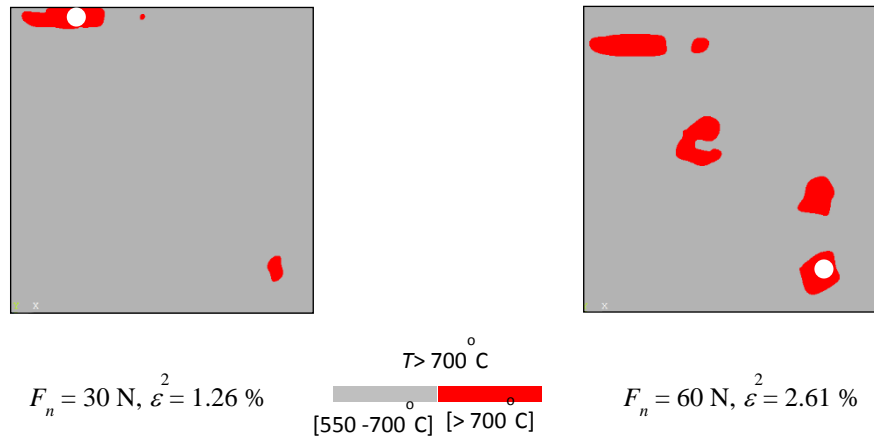


Figure 7-14: Extent of the points having a contact temperature $> 700^\circ\text{C}$, shown as red zones, while the gray areas represent the zones having a temperature value between 550°C and 700°C (Cobalt Alloy 2 / Cobalt Alloy 2, $A = \pm 25 \mu\text{m}$, $f = 200 \text{ Hz}$, $\mu = 0.71$, $T_{\text{bulk}} = 550^\circ\text{C}$).

By investigating the temperature profile along the depth (y) at the point experiencing the maximum temperature rise (Figure 7-13), the following conclusions can be made:

1. There is a sudden change in the temperature gradient when moving from the oxide zone to the substrate. This change can be explained by looking at the Fourier conduction law:

$$Q = -k \cdot A_{os} \cdot \frac{dT}{dy} \quad (7-2)$$

As the heat flow Q crosses the oxide-substrate interface, there is an abrupt change in the thermal conductivities between the oxide and substrate which leads to an abrupt change in the temperature gradient along the depth y . Mathematically this can be expressed as:

$$k_1 \cdot \left(\frac{dT}{dy} \right)_1 = k_2 \cdot \left(\frac{dT}{dy} \right)_2 \quad (7-3)$$

where 1 and 2 denote the oxide and the substrate, respectively. From Figure 7-13, the ratio of the gradients ≈ 0.08 , which is close to the ratio of the thermal conductivities ≈ 0.1 .

2. Inside the oxide film, ($y \leq 10 \mu\text{m}$), a steep temperature gradient is developed. This is known as the thermally disturbed zone (TDZ) inside which the temperature gradient along the depth is high enough to affect the thermal stresses [37, 126].
3. Outside the oxide film, at a depth of $y \geq 10 \mu\text{m}$, the temperature profile takes a linear form until reaching the substrate bulk temperature at the bottom.
4. The temperature profile confirms the findings of Archard [69] who pointed out that the effect of low-conductivity oxide film is to raise the surface temperature and leave the temperature of the substrate unaffected, which means that the substrate temperature cannot be increased by the presence of oxide film.

Chapter 8 Conclusions and Future Work Recommendations

8.1. Conclusions

In order to characterize the fretting wear of aeroengine combustor components, a specially designed room-temperature tribometer was modified for high temperature fretting wear testing (up to 600°C). The tribological behaviours of candidate contact pairs (CP1: Cobalt Alloy 2 / Cobalt Alloy 1, CP2: Cobalt Alloy 1 / Nickel Alloy 1 and CP3: Cobalt Alloy 2 / Nickel Alloy 1) were assessed under different loading conditions and temperature levels. The evolution of the wear damage criteria (wear volume, maximum wear depth and dynamic friction) with work rate and temperature was reported. The following conclusions can be drawn from the experimental investigation:

1. The increase in the temperature from 350°C to 550°C leads to a decrease in the coefficient of friction (COF) for all contact pairs. Although the decrease in friction is associated with a decrease in the wear coefficient for CP1, it was found to be associated with an increase in the wear coefficient for CP2 and CP3.
2. At all tested work rates, CP1 exhibited the lowest wear coefficient at 550°C, whereas CP2 exhibited the lowest wear coefficient at 350°C.
3. From the wear coefficient, maximum wear depth and COF points of view, and at relatively high work rate values (350 mJ/s), CP1 is the best contact pair at 550°C, while CP2 is the best contact pair at 350°C. This can be attributed to the fact that the cobalt-based pair in CP1 tends to form a protective layer of compacted oxides (mainly Cr₂O₃) called glaze. This layer is not fully developed at 350°C and experiences surface cracking, which affects its load bearing capability. At 550°C, this layer becomes continuous, especially at high normal loads, which improves its load bearing capacity and precludes metal-metal contact. This explains the reduced wear damage. For CP2, this layer could develop at 350°C, but at 550°C, its wear reducing effect diminishes due to the formation of tungsten trioxide WO₃, which is an oxide prone to water adsorption.

4. For the investigated CP1, the following observations are made:
- a. At $RT < T < 550^{\circ}\text{C}$, the wear coefficient and the COF generally decrease with the increase of temperature at different work rates.
 - b. At 200°C , hard wear debris promoted abrasive wear and caused an increase in the COF. In addition, the formed oxide was thin, non-continuous and contained mainly CoO, which contributed to the increase in the COF.
 - c. At 350°C , the wear coefficient decreases due to the formation of a protective oxide layer, however this layer experienced surface cracking.
 - d. At 550°C , the wear coefficient decreases due to the formation of a continuous thicker ($2 - 10\text{ }\mu\text{m}$) glaze containing mainly Cr_2O_3 , known for its good tribological characteristics.
 - e. Delamination wear occurs within the oxide layer, and not within the substrate.
 - f. At 550°C , when the oxide inside and outside the fretted area were compared, it was found that contact temperature was around 600°C due to the frictional heat.

In order to predict the contact temperature resulting from the frictional-induced heat in fretting wear, a model was developed based on importing the topographies of the real surfaces to the finite element model. The effect of the fretting wear operation conditions, the material properties, the surface condition and the surface oxide layer on the contact temperature prediction were investigated. The model is validated using the oxide surface analysis. The following conclusions could be made from this theoretical development:

1. Compared to the models based on the uniformly-distributed equal-sized micro contact areas (MCAs), the proposed model improved the prediction of the contact temperature and the temperature gradient inside the thermally disturbed zone.
2. The surface condition, which evolves with time, has a significant effect on the contact temperature prediction. At the early fretting stages, machined surfaces tend to form repeated patterns of MCAs, while fretted surfaces form randomly agglomerated MCAs, which clusters the heat generation and raises the surface temperature.

3. The presence of surface oxides, having a higher hardness and a lower thermal conductivity compared to the substrate, raises the contact temperature, which in turn, affects the oxide kinetics and the material properties.
4. The frictional-induced thermal effect is more pronounced for materials having high hardness and low thermal conductivity (e.g. titanium alloys), and has a negligible effect on materials having low hardness and high thermal conductivity (e.g. aluminum alloys).
5. In the presence of surface oxides, the developed temperature gradient is steep and experiences an abrupt change at the substrate-oxide interface. This change could have an important impact on the stresses developed at this zone, and consequently, on subsurface crack initiation and propagation during the wear process.

Using a finite element thermomechanical model, the effect of the frictional heat on the wear debris formation by delamination was investigated. It is shown that the emergence of frictional heat changes the subsurface deformation mechanism, and the following conclusions can be drawn.

1. Compared to the situation where only a mechanical load is applied, frictional heat creates a competition between two opposing deformation streams which puts the subsurface deformation zone under a state of higher hydrostatic compressive stress. Consequently, there is a formation of shallower (thinner) wear debris through the reduction of the depth at which cracks initiate.
2. Once a crack is initiated, the opposing streams of deformation lead to an increase in the shear plastic strain, and consequently, an increase in shear stress. This shear mechanism causes an increase in the in-plane crack growth, and consequently, in the crack tip sliding displacement (CTSD). Thus, frictional heat causes quicker crack propagation.

8.2. Future Work Recommendations

The present research represents an important milestone in the understanding of fretting wear behaviour of superalloys. It unveils the role of the frictional heat in fretting and

provides a practical tool for the contact temperature estimation in fretting. From the solid foundation that this study has established, the following considerations are proposed for future research work.

1. It is recommended to employ the systematic approach of this research work to investigate other superalloys, especially the ones providing protective oxides with good tribological properties at desired high temperatures (e.g. Cr_2O_3).
2. It is recommended to integrate the model developed for estimating the contact temperature with the oxidation kinetics, to simulate this important nonlinear effect in fretting wear.
3. It is recommended to develop a contact-based thermomechanical model which brings the surface topography detailed information into the study of wear debris formation by delamination. In addition, this study should look inside the oxide layer and not at the substrate, as suggested in this research.
4. It is recommended to study the effect of the fretting conditions on the surface characteristics (e.g., the autocorrelation function) and use that information in the estimation of the contact temperature and the nature of oxides that might develop on the surface. This can reduce the number of required experiments, which will have direct economic and environmental impacts.
5. The methodology developed in this investigation, when combined with its findings, could be transformed into a practical design tool (e.g., software package), that can be conveniently used by designers who are concerned with the safety and reliability of aeroengine components.

References

1. Campbell, F.C., *Chapter 1 - Introduction*, in *Manufacturing Technology for Aerospace Structural Materials*, F.C. Campbell, Editor. 2006, Elsevier Science: Oxford. p. 1-13.
2. Chester T. Sims, N.S.S., William C. Hagel, *Superalloys II*. 1987: Wiley.
3. Stott, F.H., D.S. Lin, and G.C. Wood, *The structure and mechanism of formation of the 'glaze' oxide layers produced on nickel-based alloys during wear at high temperatures*. Corrosion Science, 1973. 13(6): p. 449-469.
4. Bruce, R.W., *Handbook of Lubrication and Tribology, Volume II: Theory and Design, Second Edition*. 2012: CRC Press.
5. Stott, F.H., *The role of oxidation in the wear of alloys*. Tribology International, 1998. 31(1-3): p. 61-71.
6. Laskowski, J.A., *Friction and Wear Characteristics of Candidate Foil Bearing Materials from 25 C to 800 C*. NASA Technical Reports Server (NTRS), 1996.
7. C. DellaCorte, V.L., D.E. Morris, B.M. Steinetz, *Static and Dynamic Friction Behavior of Candidate High Temperature Airframe Seal Materials*. NASA Technical Memorandum, 1994.
8. Coskun, M.B., S. Aksoy, and M. Aksit, *Friction and Wear Characteristics of Haynes 25, 188, and 214 Superalloys Against Hastelloy X up to 540 °C*. Tribology Letters, 2012. 45(3): p. 497-503.
9. Wood, P.D., H.E. Evans, and C.B. Ponton, *Investigation into the wear behaviour of Stellite 6 during rotation as an unlubricated bearing at 600 °C*. Tribology International, 2011. 44(12): p. 1589-1597.
10. Inman, I.A., et al., *Studies of high temperature sliding wear of metallic dissimilar interfaces*. Tribology International, 2005. 38(9): p. 812-823.
11. Inman, I.A. and P.S. Datta, *Development of a simple 'temperature versus sliding speed' wear map for the sliding wear behaviour of dissimilar metallic interfaces II*. Wear, 2008. 265(11-12): p. 1592-1605.
12. Bill, R.C., *Role of oxidation in the fretting wear process*. Wear of Materials: International Conference on Wear of Materials, 1981: p. 238-350.
13. Bill, R.C., *STUDY OF FRETTING WEAR IN TITANIUM, MONEL-400, AND COBALT - 25 PERCENT MOLYBDENUM USING SCANNING ELECTRON MICROSCOPY*. ASLE Trans, 1973. 16(4): p. 286-290.
14. Hamdy, M.M. and R.B. Waterhouse, *The fretting wear of Ti-6Al-4v and aged Inconel 718 at elevated temperatures*. Wear, 1981. 71(2): p. 237-248.
15. Miyoshi, K., B.A. Lerch, and S.L. Draper, *Fretting wear of Ti-48Al-2Cr-2Nb*. Tribology International, 2003. 36(2): p. 145-153.
16. Lavella, M. and D. Botto, *Fretting wear characterization by point contact of nickel superalloy interfaces*. Wear, 2011. 271(9-10): p. 1543-1551.
17. Balić, E.E. and T.A. Blanchet, *Thrust-washer tribological evaluation of PS304 coatings against Rene 41*. Wear, 2005. 259(7-12): p. 876-881.
18. Attia, H., *Thermal constriction phenomenon in fretting: Theory and implications*. Tribology International, 2011. 44(11): p. 1352-1363.

19. Sproles Jr, E.S. and D.J. Duquette, *Interface temperature measurements in the fretting of a medium carbon steel*. Wear, 1978. 47(2): p. 387-396.
20. Weick, B.L., M.J. Furey, and B. Vick, *Surface Temperatures Generated With Ceramic Materials in Oscillating/Fretting Contact*. Journal of Tribology, 1994. 116(2): p. 260-267.
21. Dobromirski, J. and I.O. Smith, *Metallographic aspects of surface damage, surface temperature and crack initiation in fretting fatigue*. Wear, 1987. 117(3): p. 347-357.
22. Waterhouse, R.B., *Influence of Local Temperature Increases on the Fretting Corrosion of Mild Steel*. Iron and Steel Institute, 1961. 190: p. 301-305.
23. Podgornik, B., et al., *Microstructural changes and contact temperatures during fretting in steel-steel contact*. Journal of Tribology, 2001. 123(4): p. 670-675.
24. Kalin, M., *Influence of flash temperatures on the tribological behaviour in low-speed sliding: a review*. Materials Science and Engineering: A, 2004. 374(1-2): p. 390-397.
25. Revie, R.W.U., Herbert H., *Corrosion and Corrosion Control*. 4 ed. 2008, New York: John Wiley & Sons.
26. Khanna, A.S., *Introduction to High Temperature Oxidation and Corrosion*. 2002: ASM International
27. Bill, R.C., *Selected fretting-wear-resistant coatings for Ti-6%Al-4%V alloy*. Wear, 1985. 106(1-3): p. 283-301.
28. C. H. Lund, H.J.W., *Oxidation of nickel and cobalt-base superalloys*. 1965, DEFENSE METALS INFORMATION CENTER: Battelle Memorial Institute, Columbus, Ohio 43201.
29. Hagel, W.C., *The Oxidation of Iron, Nickel and Cobalt-Base Alloys Containing Aluminum*. Corrosion, 1965. 21(10): p. 316-326.
30. Wlodek, S.T., *Institute of Metals Division - The Oxidation of René 41 and Udimet 700*. Transactions of the Metallurgical Society of AIME 1964.
31. P. Suh, N., *The delamination theory of wear*. Wear, 1973. 25(1): p. 111-124.
32. Jahanmir, S. and N.P. Suh, *Mechanics of subsurface void nucleation in delamination wear*. Wear, 1977. 44(1): p. 17-38.
33. Waterhouse, R.B., *The role of adhesion and delamination in the fretting wear of metallic materials*. Wear, 1977. 45(3): p. 355-364.
34. Gessesse, Y.B., M.H. Attia, and M.O.M. Osman, *On the mechanics of crack initiation and propagation in elasto-plastic materials in impact fretting wear*. Journal of Tribology, 2004. 126(2): p. 395-403.
35. Gong, Z.Q. and K. Komvopoulos, *Mechanical and Thermomechanical Elastic-Plastic Contact Analysis of Layered Media With Patterned Surfaces*. Journal of Tribology, 2004. 126(1): p. 9-17.
36. Sofuoglu, H. and A. Ozer, *Thermomechanical analysis of elastoplastic medium in sliding contact with fractal surface*. Tribology International, 2008. 41(8): p. 783-796.
37. Attia, M.H., *Friction-Induced Thermo-Elastic Effects in the Contact Zone Due to Fretting Action in Fretting Fatigue*, in *ESIS 18*. 1994, Mechanical Engineering Publications: Sheffield, England. p. 307-319.

38. Kulkarni, S.M., C.A. Rubin, and G.T. Hahn, *Elasto-Plastic Coupled Temperature-Displacement Finite Element Analysis of Two-Dimensional Rolling-Sliding Contact With a Translating Heat Source*. Journal of Tribology, 1991. 113(1): p. 93-101.
39. Cho, S.S. and K. Komvopoulos, *Thermoelastic finite element analysis of subsurface cracking due to sliding surface traction*. Journal of Engineering Materials and Technology, Transactions of the ASME, 1997. 119(1): p. 71-78.
40. Wang, W.J., et al., *Study on relationship between oblique fatigue crack and rail wear in curve track and prevention*. Wear, 2009. 267(1-4): p. 540-544.
41. Gurland, J., Plateau, J., *The mechanism of ductile rupture of metals containing inclusions*. ASM Transactions, 1963. 56: p. 54-65.
42. Ashby, M.F., *Work hardening of dispersion-hardened crystals*. Philosophical Magazine, 1966. 14(132): p. 1157-1178.
43. Tanaka, K., T. Mori, and T. Nakamura, *Cavity formation at the interface of a spherical inclusion in a plastically deformed matrix*. Philosophical Magazine, 1970. 21(170): p. 267-279.
44. Argon, A.S., J. Im, and R. Safoglu, *Cavity formation from inclusions in ductile fracture*. Metallurgical Transactions A, 1975. 6(4): p. 825-837.
45. Salehizadeh, H. and N. Saka, *The Mechanics of Crack Initiation at Hard Particles in Rolling Line Contacts*. Journal of Tribology, 1992. 114(2): p. 341-347.
46. Prasannavenkatesan, R., et al., *3D modeling of subsurface fatigue crack nucleation potency of primary inclusions in heat treated and shot peened martensitic gear steels*. International Journal of Fatigue, 2009. 31(7): p. 1176-1189.
47. Rice, J.R. and D.M. Tracey, *On the ductile enlargement of voids in triaxial stress fields**. Journal of the Mechanics and Physics of Solids, 1969. 17(3): p. 201-217.
48. E. Stein, R.d.B., T. Hughes, *Computational Fracture Mechanics. , Encyclopedia of Computational Mechanics*. 2007: John Wiley and Sons.
49. Komvopoulos, K. and S.S. Cho, *Finite element analysis of subsurface crack propagation in a half-space due to a moving asperity contact*. Wear, 1997. 209(1-2): p. 57-68.
50. Ye, N. and K. Komvopoulos, *Indentation Analysis of Elastic-Plastic Homogeneous and Layered Media: Criteria for Determining the Real Material Hardness*. Journal of Tribology, 2003. 125(4): p. 685-691.
51. Ragab A. R., S.A. Bayoumi., *Engineering Solid Mechanics: Fundamentals and Applications*. 1999: CRC Press.
52. Sin, H.C. and N.P. Suh, *Subsurface Crack Propagation Due to Surface Traction in Sliding Wear*. Journal of Applied Mechanics, 1984. 51(2): p. 317-323.
53. Anderson, T.L., *Fracture Mechanics; Fundamentals and Application*. 1991: CRC Press.
54. Jackson, R.L., et al., *A Closed-Form Multiscale Thermal Contact Resistance Model*. Components, Packaging and Manufacturing Technology, IEEE Transactions on, 2012. 2(7): p. 1158-1171.
55. Greenwood, J.A. and J.B.P. Williamson, *Contact of Nominally Flat Surfaces*. Proceedings of the Royal Society of London. Series A, Mathematical and Physical Sciences, 1966. 295(1442): p. 300-319.

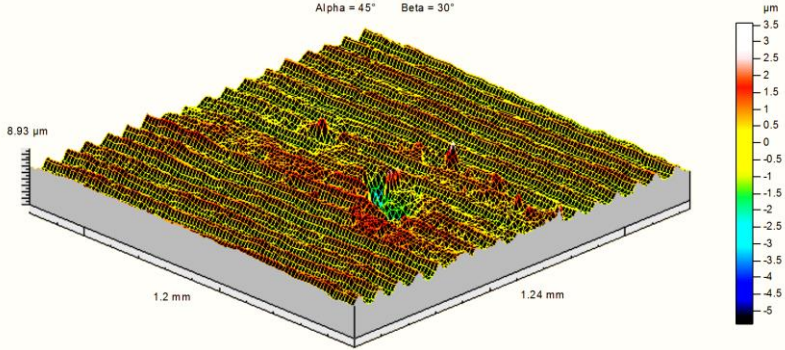
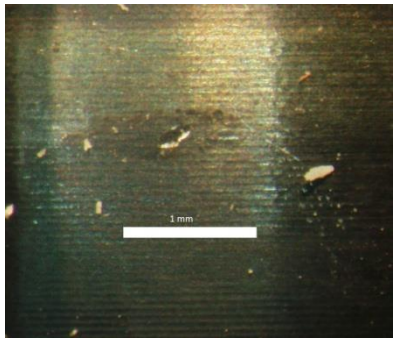
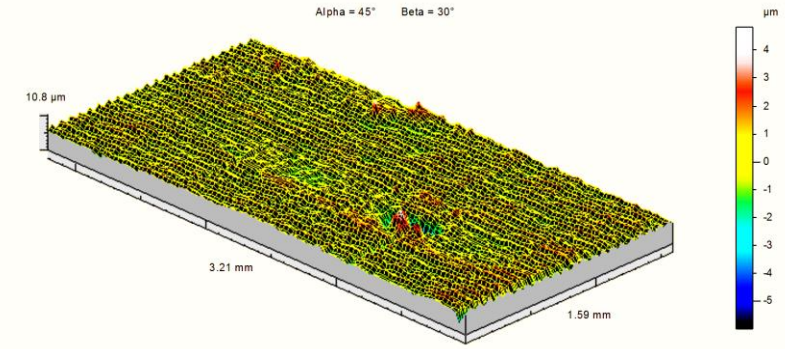
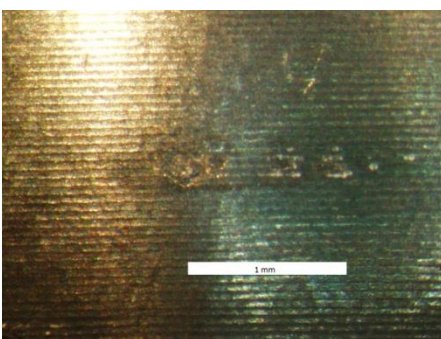
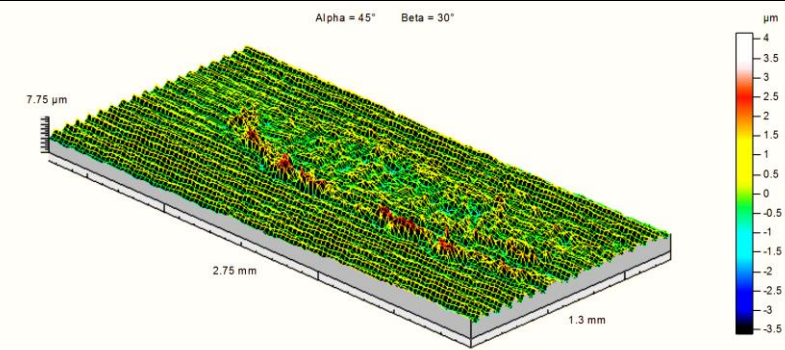
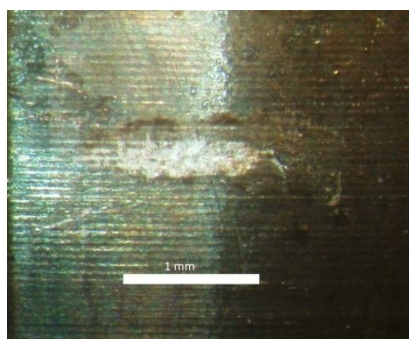
56. Majumdar, A. and B. Bhushan, *Fractal Model of Elastic-Plastic Contact Between Rough Surfaces*. Journal of Tribology, 1991. 113(1): p. 1-11.
57. Thompson, M.K., *Finite element modeling of multi-scale thermal contact resistance* Proc. ASME 1st Int. Conf. Micro/Nanoscale Heat Transfer,, 2008: p. 509-517.
58. Ciavarella, M., et al., *Linear elastic contact of the Weierstrass profile*. Proceedings of the Royal Society of London. Series A: Mathematical, Physical and Engineering Sciences, 2000. 456(1994): p. 387-405.
59. Hisakado, T., *On the Mechanism of Contact Between Solid Surfaces-1*. Bull JSME, 1969. 12(54): p. 1519-1527.
60. Hisakado, T., *On the Mechanism of Contact Between Solid Surfaces-2*. Bull JSME, 1969. 12(54): p. 1528-1536.
61. Hisakado, T., *On the Mechanism of Contact Between Solid Surfaces-3*. Bull JSME, 1969. 12(54): p. 1537-1545.
62. Hisakado, T., *On the Mechanism of Contact Between Solid Surfaces-4*. Bull JSME, 1970. 13(55): p. 129-139.
63. Tsukada, T.A., Yoshiro, *An Analysis of the Deformation of Contacting Rough Surfaces : 3rd Report, Introduction of a New Contact Theory of Rough Surfaces*. Bulletin of JSME, 1972. 15(86): p. 996-1003.
64. Tsukada, T. and Y. Anno, *An Analysis of the Elastic and Plastic Deformations of Machined Surfaces in Contact (1st Report, Deformations of Contacting Rough Surfaces when the Directions of Surface Asperities Cross Each Other)*. BULL. JSME, 1974. 17(105).
65. Fridrici, V., Attia, M. H. , Kapsa, P., Vincent, L., *A Finite Element Approach to Temperature Rise in Fretting with Consideration to the Effect of Random Distribution of The Micro-Contact Areas*. Proceedings of JAST Tribology Conference, 2000. 1: p. 397-402.
66. Blok, H., *Surface temperatures under extreme pressure lubricating conditions*, in *Proceedings of the Second World Petroleum Conference*. 1937: Paris. p. 471-486.
67. Jaeger, J., *Moving sources of heat and the temperature at sliding contacts*. Proc Roy Soc, 1942. 76: p. 203-224.
68. Holm, R., *Electric Contacts - Theory and Application*. 3rd ed. 1997: Springer.
69. Archard, J.F., *Contact and rubbing of flat surfaces*. Japanese Journal Of Applied Physics, 1953. 24(8): p. 981-988.
70. Ashby, M.F., J. Abulawi, and H.S. Kong, *Temperature Maps for Frictional Heating in Dry Sliding*. Tribology Transactions, 1991. 34(4): p. 577-587.
71. Attia, M.H. and M.M. Yovanovich. *Model for predicting the thermal constriction resistance in fretting*. 1993. New Orleans, LA, USA: Publ by ASME.
72. Beck, J.V., *Effects of Multiple Sources in the Contact Conductance Theory*. J Heat Transfer Trans ASME, 1979. 101(1): p. 132-136.
73. Attia, M.H. and N.S. D'Silva, *Effect of mode of motion and process parameters on the prediction of temperature rise in fretting wear*. Wear, 1985. 106(1-3): p. 203-224.
74. Greenwood, J.A. and A.F. Alliston-Greiner, *Surface temperatures in a fretting contact*. Wear, 1992. 155(2): p. 269-275.

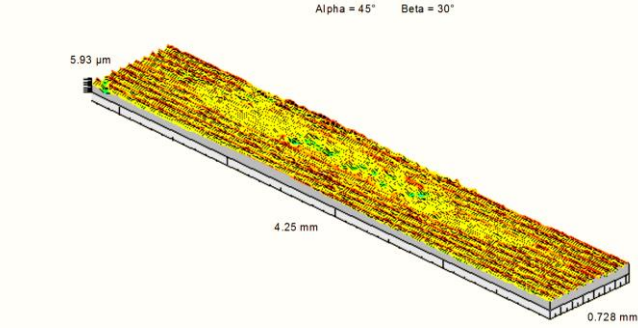
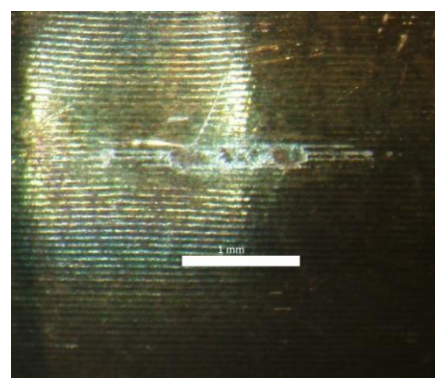
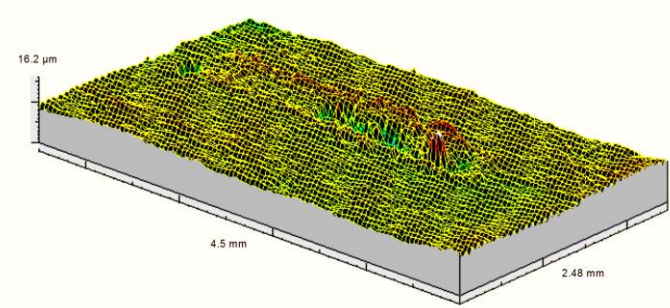
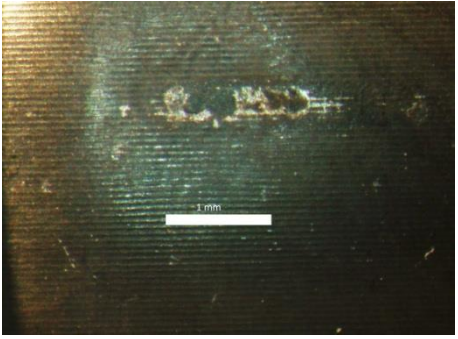
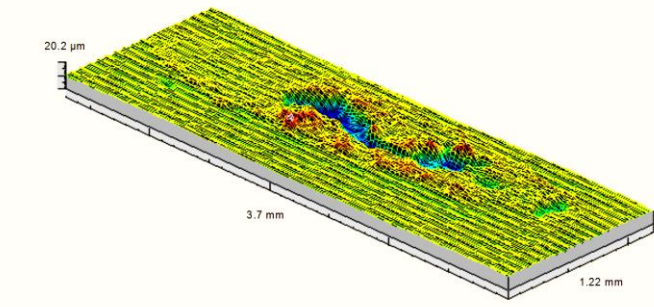
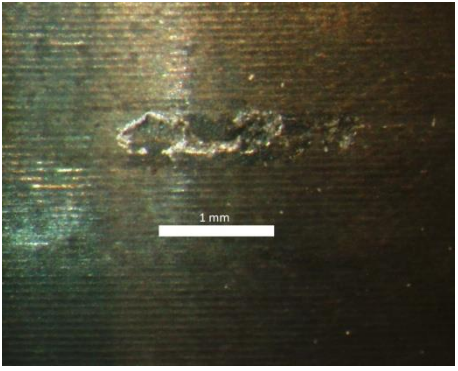
75. Tian, X. and J.F.E. Kennedy, *Maximum and Average Flash Temperatures in Sliding Contacts*. Journal of Tribology, 1994. 116(1): p. 167-174.
76. Pezdernik, J., J. Vižintin, and B. Podgornik, *Temperatures at the interface and inside an oscillatory sliding microcontact — theoretical part*. Tribology International, 1999. 32(9): p. 481-489.
77. Wen, J. and M.M. Khonsari, *Transient Temperature Involving Oscillatory Heat Source With Application in Fretting Contact*. Journal of Tribology, 2007. 129(3): p. 517-527.
78. Thompson, M.K., *A multi-scale iterative approach for finite element modeling of thermal contact resistance*, in *Mechanical Engineering*. 2007, Massachusetts Institute of Technology.
79. Liu, H., et al. *Finite Element Based Surface Roughness Study for Ohmic Contact of Microswitches*. in *Electrical Contacts (Holm), 2012 IEEE 58th Holm Conference on*. 2012.
80. Liu, H., et al. *Finite element multi-physics modeling for ohmic contact of microswitches*. in *Thermal, mechanical and multi-physics simulation and experiments in microelectronics and microsystems (eurosime), 2014 15th international conference on*. 2014.
81. Attia H., Meshreki M., Korashy A., Thomson V., Chung V., *Fretting Wear Characteristics of Cold Gas-Dynamic Sprayed Aluminum Alloys*, in *The 6th International Symposium on Fretting Fatigue*. 2010: Chengdu, China.
82. Fouvry, S., P. Kapsa, and L. Vincent, *Analysis of sliding behaviour for fretting loadings: determination of transition criteria*. Wear, 1995. 185(1-2): p. 35-46.
83. Heredia, S. and S. Fouvry, *Introduction of a new sliding regime criterion to quantify partial, mixed and gross slip fretting regimes: Correlation with wear and cracking processes*. Wear, 2010. 269(7-8): p. 515-524.
84. Kim, K. and A.M. Korsunsky, *Effects of imposed displacement and initial coating thickness on fretting behaviour of a thermally sprayed coating*. Wear, 2011. 271(7-8): p. 1080-1085.
85. Personal communication with Pratt and Whitney Canada.
86. Personal communication with Pratt and Whitney Canada.
87. Personal communication with Pratt and Whitney Canada.
88. Attia, M.H. and E. Magel, *Experimental investigation of long-term fretting wear of multi-span steam generator tubes with U-bend sections*. Wear, 1999. 225-229, Part 1(0): p. 563-574.
89. Korashy A. and H. Attia., *High Temperature Fretting Wear Characterization of MIM Materials*. Report Submitted to PWC, 2013.
90. Iwabuchi, A., *Fretting wear of Inconel 625 at high temperature and in high vacuum*. Wear, 1985. 106(1-3): p. 163-175.
91. Waterhouse, R.B., *Fretting Corrosion*. 1972: Pergamon Press.
92. Kato, K., *Wear in relation to friction — a review*. Wear, 2000. 241(2): p. 151-157.
93. Klaffke, D., T. Carstens, and A. Banerji, *Influence of grain refinement on the high temperature fretting behaviour of IN 738 LC*. Wear, 1993. 160(2): p. 361-366.

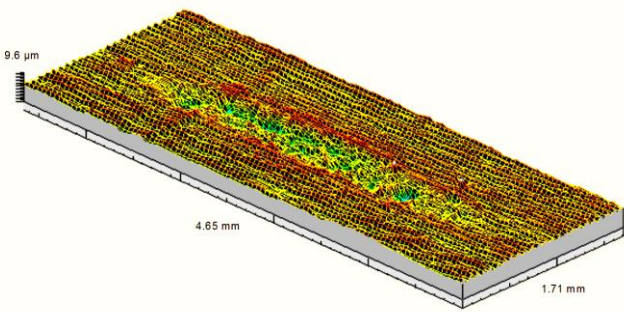
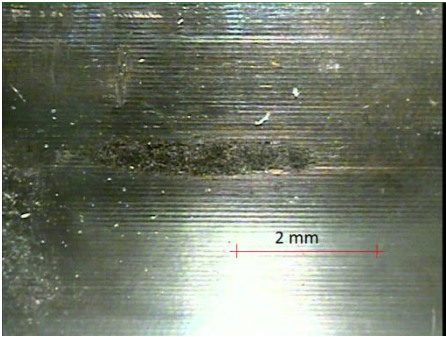
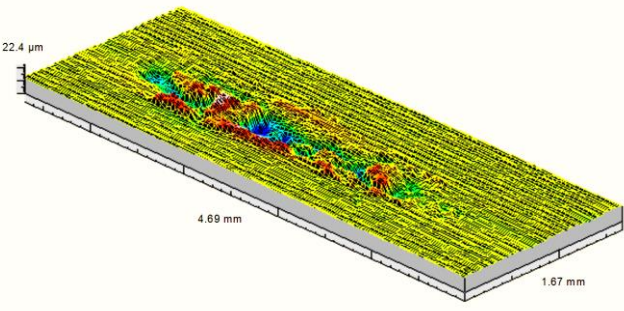
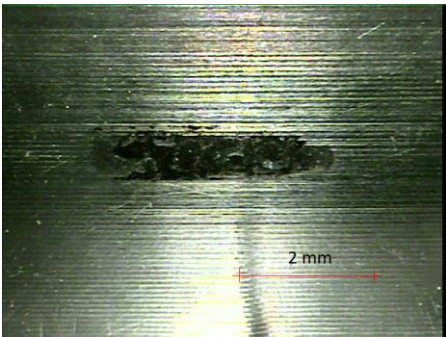
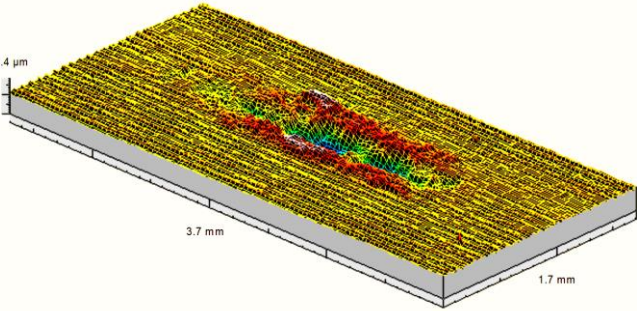
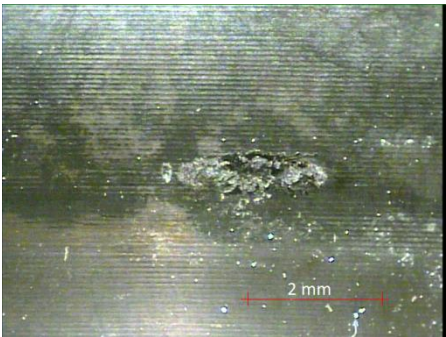
94. Patel, B., et al., *Cobalt-based orthopaedic alloys: Relationship between forming route, microstructure and tribological performance*. Materials Science and Engineering C, 2012. 32(5): p. 1222-1229.
95. Quinn, T.F.J., *Physical Analysis for Tribology*. 1991: Cambridge University Press
96. Tang, C.-W., C.-B. Wang, and S.-H. Chien, *Characterization of Cobalt oxides studied by FT-IR, Raman, TPR and TG-MS*. Thermochemica Acta, 2008. 473(1-2): p. 68-73.
97. Mougin, J., et al., *In situ Raman monitoring of chromium oxide scale growth for stress determination*. Journal of Raman Spectroscopy, 2001. 32(9): p. 739-744.
98. Lee, S.-H., et al., *Raman spectroscopic studies of Ni-W oxide thin films*. Solid State Ionics, 2001. 140(1-2): p. 135-139.
99. Farrow, R.L. and A.S. Nagelberg, *Raman spectroscopy of surface oxides at elevated temperatures*. Applied Physics Letters, 1980. 36(12): p. 945-947.
100. Li, J., et al., *Mechanical and Tribological Properties of Plasma-Sprayed Cr₃C₂-NiCr, WC-Co, and Cr₂O₃ Coatings*. Journal of Thermal Spray Technology, 1998. 7(2): p. 242-246.
101. Foley, R.T., M.B. Peterson, and C. Zapf, *Frictional Characteristics of Cobalt, Nickel, and Iron as Influenced by Their Surface Oxide Films*. A S L E Transactions, 1963. 6(1): p. 29-39.
102. Brauer, G., *Handbook of Preparative Inorganic Chemistry*. Vol. 1. 1963: Academic Press.
103. Stachowiak, G. and A. Batchelor, *Engineering Tribology*. 2006, Elsevier.
104. Taneichi, K., et al., *Oxidation or nitridation behavior of pure chromium and chromium alloys containing 10 mass % Ni or Fe in atmospheric heating*. Materials Transactions, 2006. 47(10): p. 2540-2546.
105. Lyo, I.-W., H.-S. Ahn, and D.-S. Lim, *Microstructure and tribological properties of plasma-sprayed chromium oxide-molybdenum oxide composite coatings*. Surface and Coatings Technology, 2003. 163-164(0): p. 413-421.
106. Industrial Coatings World LLC, *Low Friction Coatings*, Retrieved from: <http://industrialcoatingsworld.com/low-friction-coatings>, 2013.
107. Cui, H.-N., *Preparation and characterization of optical multilayered coatings for smart windows applications*. University of Minho, Braga, Portugal.
108. Bahlawane, N., *Raman Spectroscopy on Metal Oxide Thin Films*, in *LOT-Oriel Group Europe*, U.o. Bielefeld, Editor. 2010.
109. Díaz-Reyes, J.D.-G., V.; Pérez-Benítez, A.; Balderas-López, J. A., *Obtaining of films of tungsten trioxide (WO₃) by resistive heating of a tungsten filament*. Superficies y vacío, Junio-Sin mes., 2008: p. 12-17.
110. Dieterle, M. and G. Mestl, *Raman spectroscopy of molybdenum oxides: Part II. Resonance Raman spectroscopic characterization of the molybdenum oxides Mo₄O₁₁ and MoO₂*. Physical Chemistry Chemical Physics, 2002. 4(5): p. 822-826.
111. Grote, K.-H., Antonsson, Erik K. (Eds.), *Springer Handbook of Mechanical Engineering*. 2009.
112. Johnson, K.L., *The correlation of indentation experiments*. Journal of the Mechanics and Physics of Solids, 1970. 18(2): p. 115-126.
113. Shaw, M. C., *Metal Cutting Principles*, Oxford University Press, U.K., 2005.

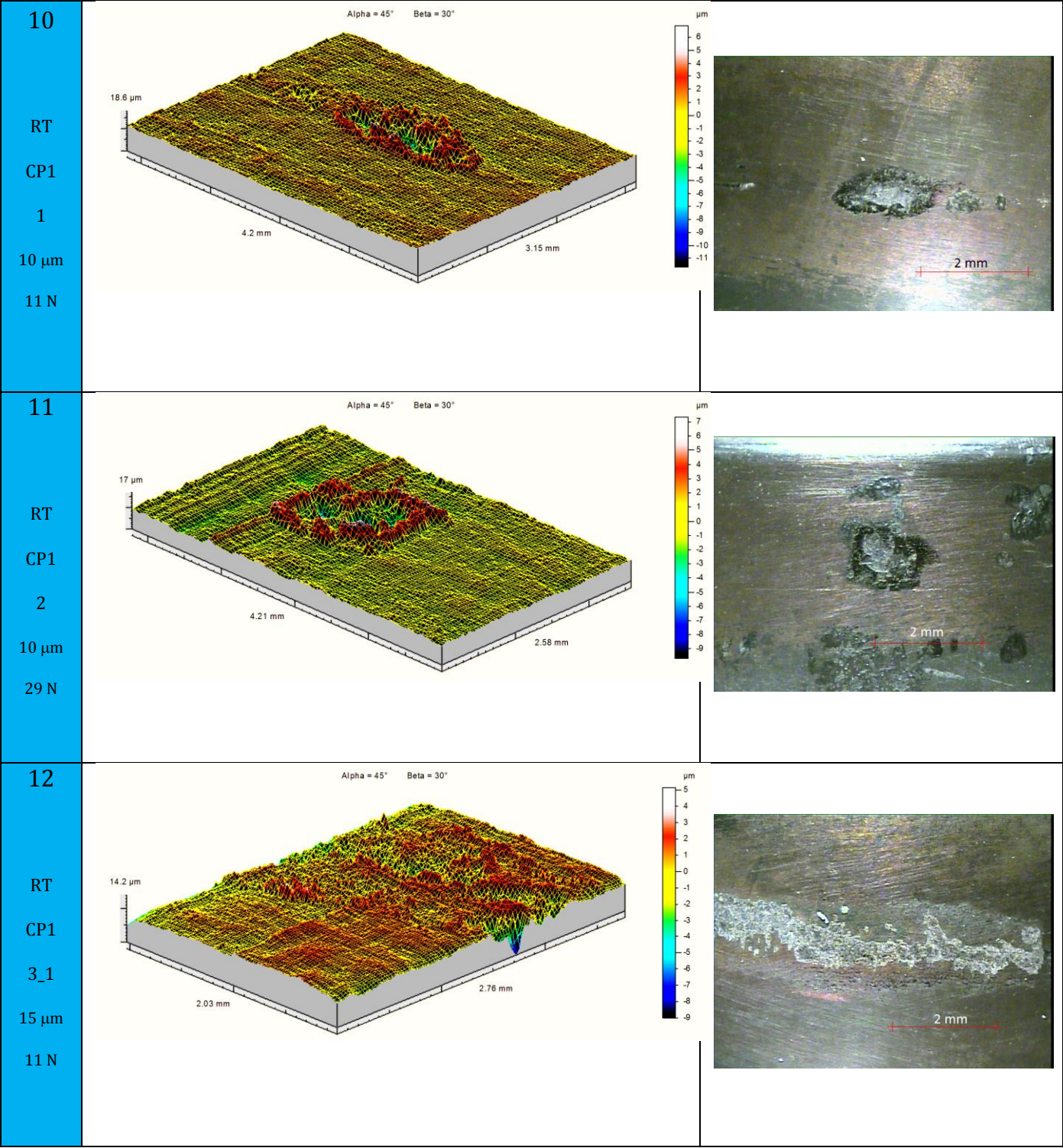
114. Helmi Attia, L.Kops, *Thermal Consideration of the Design of Multilayer Coated Tools for High Speed Machining*. ASME 2004 International Mechanical Engineering Congress and Exposition, 2004.
115. Hills, D.A. and D.W. Ashelby, *A note on shakedown*. Wear, 1980. 65(1): p. 125-129.
116. Ballarini, R. and M. Plesha, *The effects of crack surface friction and roughness on crack tip stress fields*. International Journal of Fracture, 1987. 34(3): p. 195-207.
117. Kalin, M. and J. Vižintin, *Comparison of different theoretical models for flash temperature calculation under fretting conditions*. Tribology International, 2001. 34(12): p. 831-839.
118. Krivoruchko, P.P., et al., *Low density and low thermal conductivity chrome oxide refractories for glass-melting furnaces for fiber production*. Refractories, 1981. 22(3-4): p. 228-233.
119. Keem, J.E.H., J. M. , *Selected electrical and thermal properties of undoped nickel oxide*. 1978.
120. *MATLAB and Statistics Toolbox Release 2012b*, The MathWorks, Inc., Natick, Massachusetts, United States.
121. ANSYS® Academic Research, R. , Help System, Thermal Analysis Guide, ANSYS, Inc. .
122. NSYS® Academic Research, R., Help System, Thermal Analysis Guide, ANSYS, Inc. .
123. Korashy, A.; Attia, H.; Thomson, V.; Oskooei, S., *Characterization of fretting wear of cobalt-based superalloys at high temperature for aero-engine combustor components*. Wear, 2015.
124. Helmi Attia, M., *On the fretting wear mechanism of Zr-alloys*. Tribology International, 2006. 39(10): p. 1320-1326.
125. Thomas, T.R., *Rough Surfaces*. 1982: Longman.
126. Attia MH, Camacho F., *Temperature field in the vicinity of a contact asperity during fretting*. Proceedings of the ASME symposium on contact problems and surface interactions in manufacturing and tribological systems, ASME winter annual meeting, New Orleans, Louisiana, 1993: p. 51 - 61.
127. Hirano, F. and S. Yoshida, *Theoretical study of temperature rise at contact surface for reciprocating motion*, in 3rd Int. Heat Transfer Confl. 1966, American Institute of Chemical Engineers: Chicago,, p. 127-132.

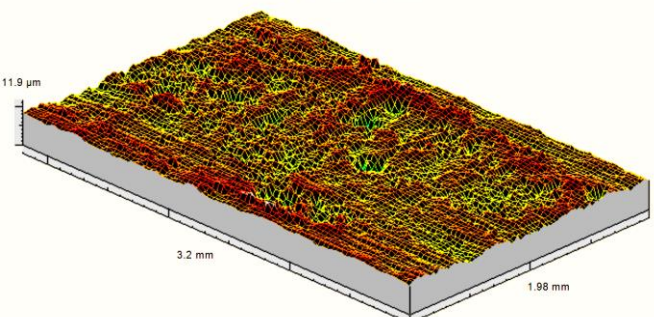
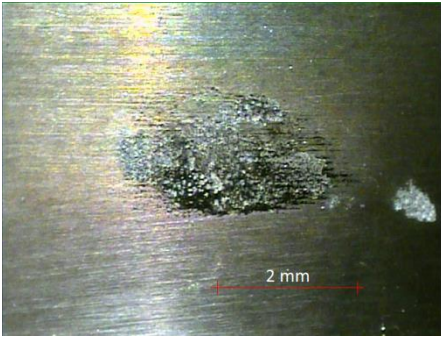
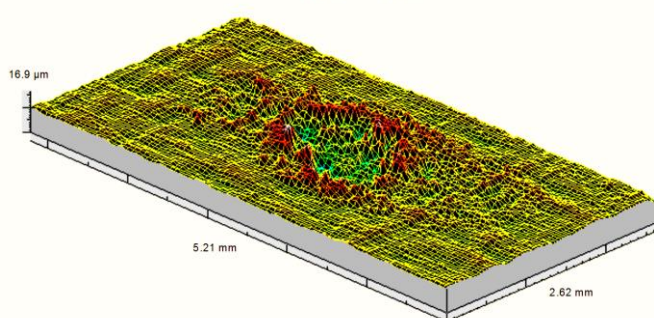

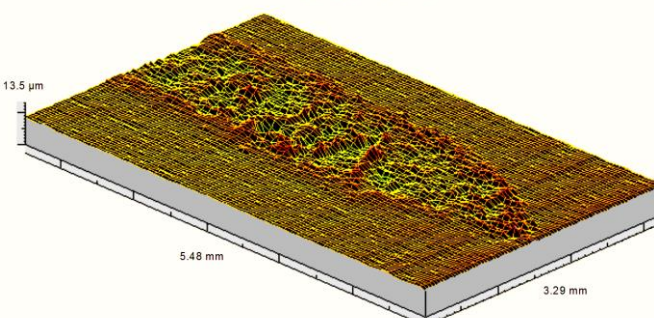
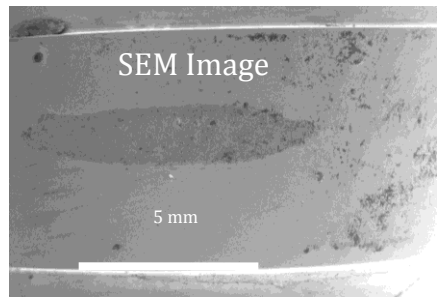
Appendix A: Cylinder sample 3D surface scans and optical images

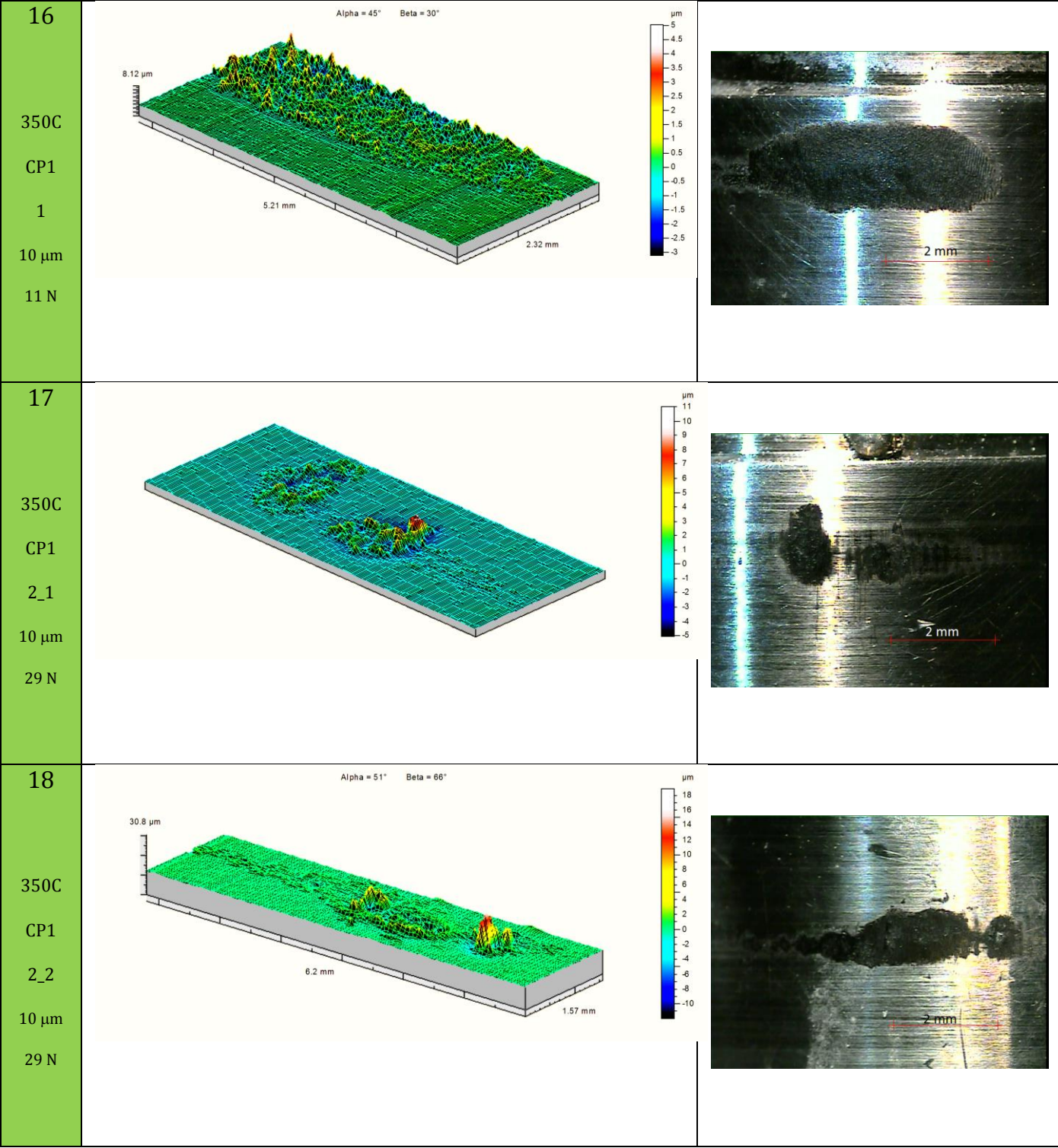
Test No.	3D Surface Topography	Optical Image
1	<p>Alpha = 45° Beta = 30°</p>  <p>8.93 μm</p> <p>1.2 mm 1.24 mm</p>	 <p>1 mm</p>
RT CP0 1 5 μm 14 N		
2	<p>Alpha = 45° Beta = 30°</p>  <p>10.8 μm</p> <p>3.21 mm 1.59 mm</p>	 <p>1 mm</p>
RT CP0 2 5 μm 20 N		
3	<p>Alpha = 45° Beta = 30°</p>  <p>7.75 μm</p> <p>2.75 mm 1.3 mm</p>	 <p>1 mm</p>
RT CP0 3 4 μm 29 N		

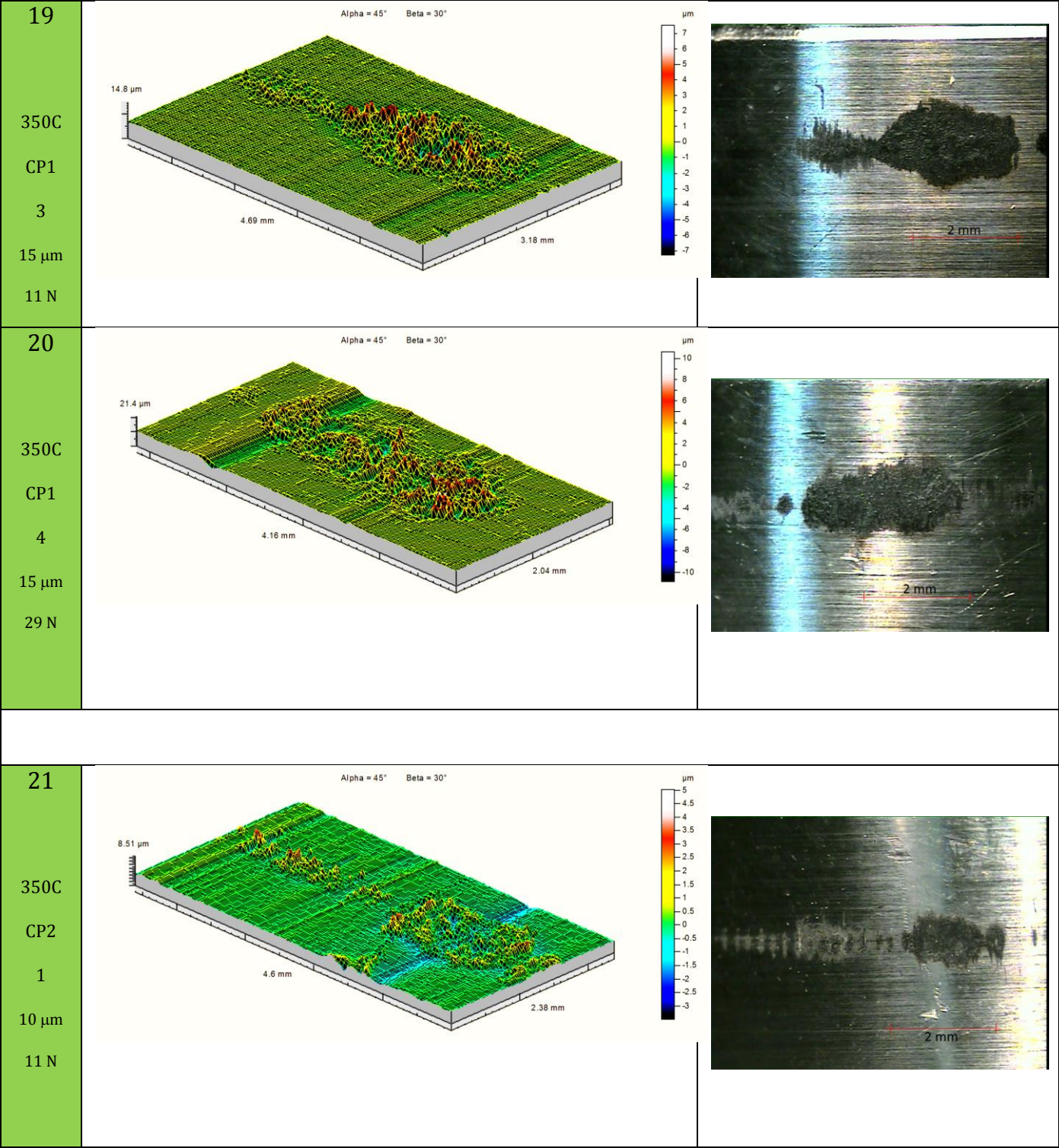
<div>4</div> <div>RT</div> <div>CP0</div> <div>4_1</div> <div>9 μm</div> <div>15 N</div>	<div>Alpha = 45° Beta = 30°</div>  <div>5.93 μm</div> <div>4.25 mm</div> <div>0.728 mm</div> <div>μm</div> <div>2</div> <div>1.5</div> <div>1</div> <div>0.5</div> <div>0</div> <div>-0.5</div> <div>-1</div> <div>-1.5</div> <div>-2</div> <div>-2.5</div> <div>-3</div> <div>-3.5</div>	 <div>1 mm</div>
<div>5</div> <div>RT</div> <div>CP0</div> <div>5</div> <div>10 μm</div> <div>20 N</div>	<div>Alpha = 48° Beta = 47°</div>  <div>16.2 μm</div> <div>4.5 mm</div> <div>2.48 mm</div> <div>μm</div> <div>7</div> <div>6</div> <div>5</div> <div>4</div> <div>3</div> <div>2</div> <div>1</div> <div>0</div> <div>-1</div> <div>-2</div> <div>-3</div> <div>-4</div> <div>-5</div> <div>-6</div> <div>-7</div> <div>-8</div>	 <div>1 mm</div>
<div>6</div> <div>RT</div> <div>CP0</div> <div>6</div> <div>10 μm</div> <div>29 N</div>	<div>Alpha = 45° Beta = 30°</div>  <div>20.2 μm</div> <div>3.7 mm</div> <div>1.22 mm</div> <div>μm</div> <div>8</div> <div>6</div> <div>4</div> <div>2</div> <div>0</div> <div>-2</div> <div>-4</div> <div>-6</div> <div>-8</div> <div>-10</div>	 <div>1 mm</div>

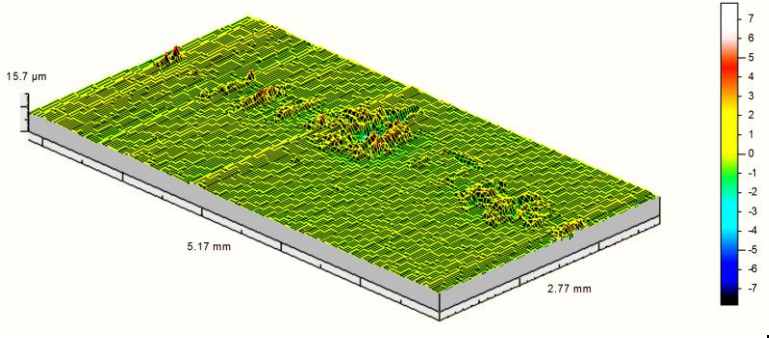
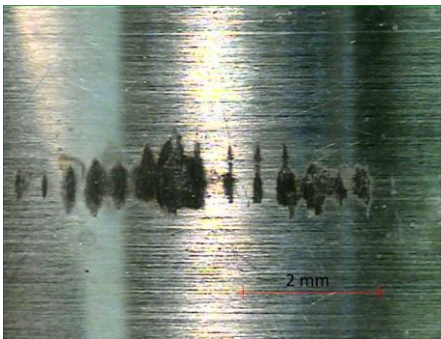
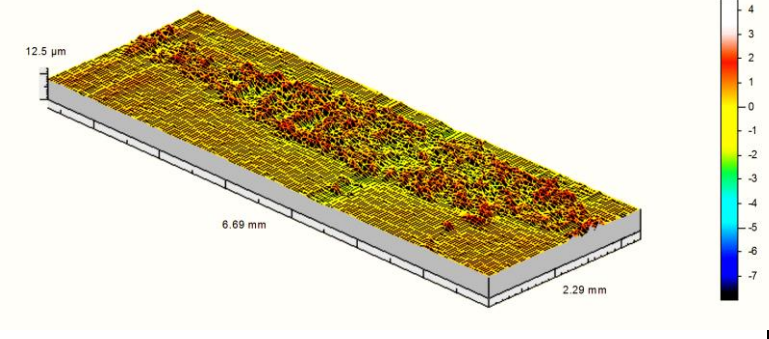
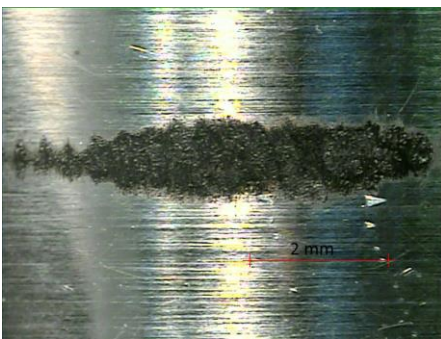
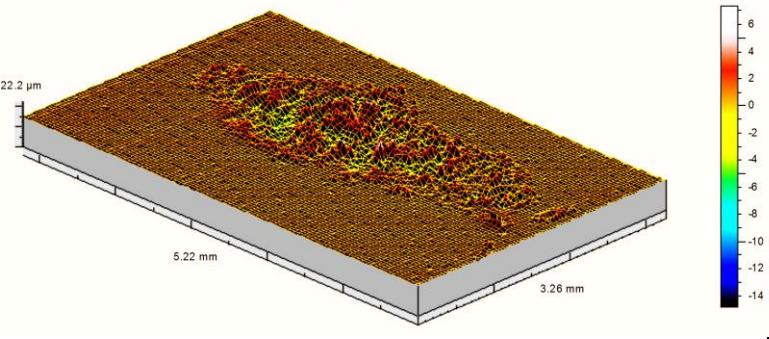
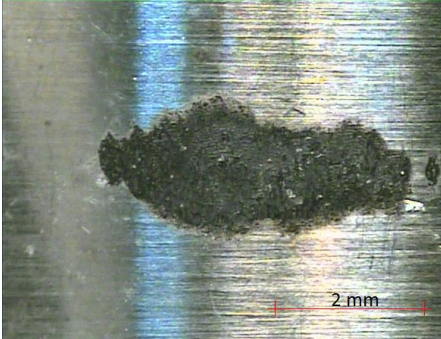
7	RT CP0 7 15 μm 11 N	<p>Alpha = 45° Beta = 30°</p>  
8	RT CP0 8 15 μm 29 N	<p>Alpha = 45° Beta = 30°</p>  
9	RT CP0 4_2 10 μm 11 N	<p>Alpha = 46° Beta = 30°</p>  

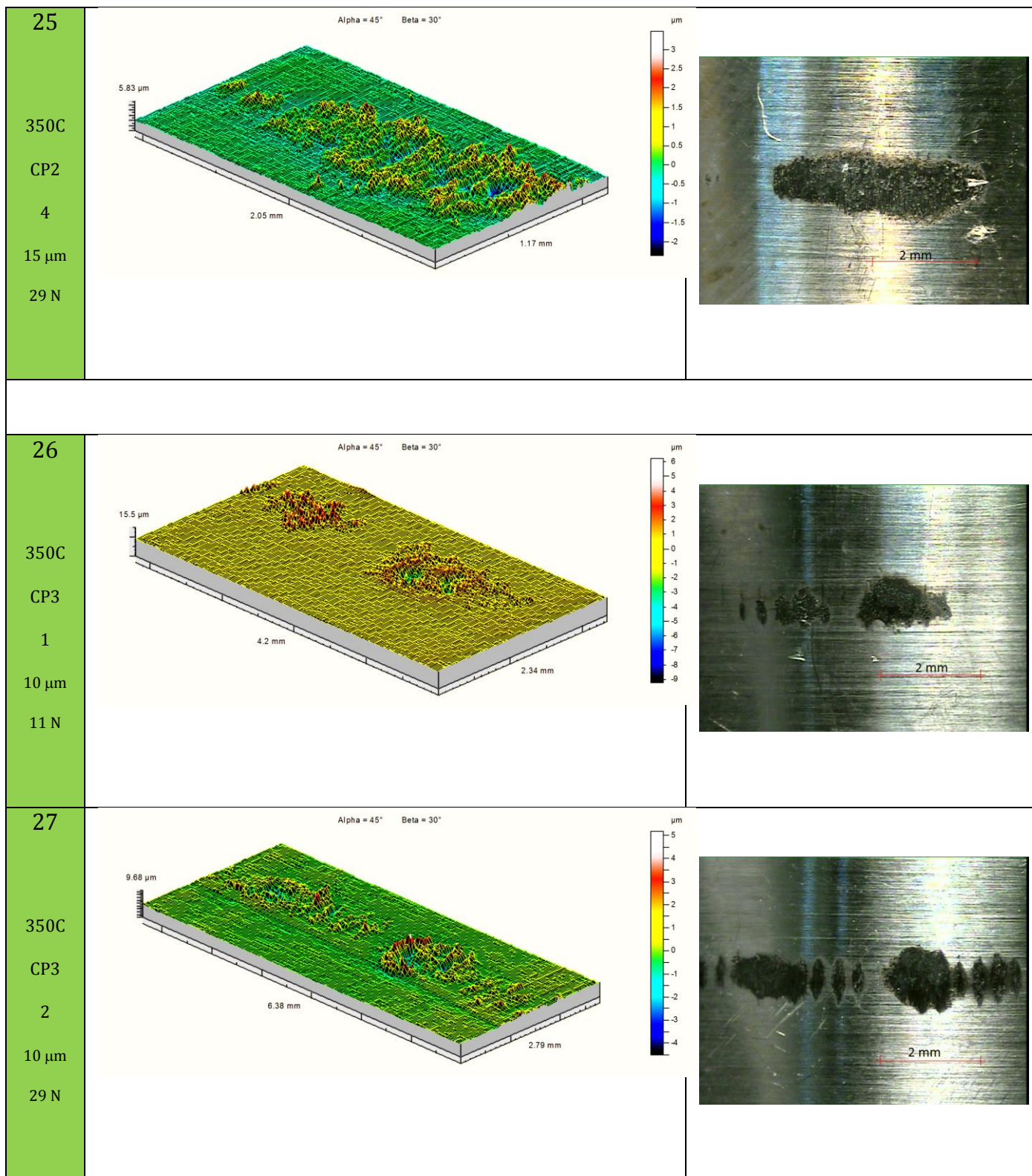


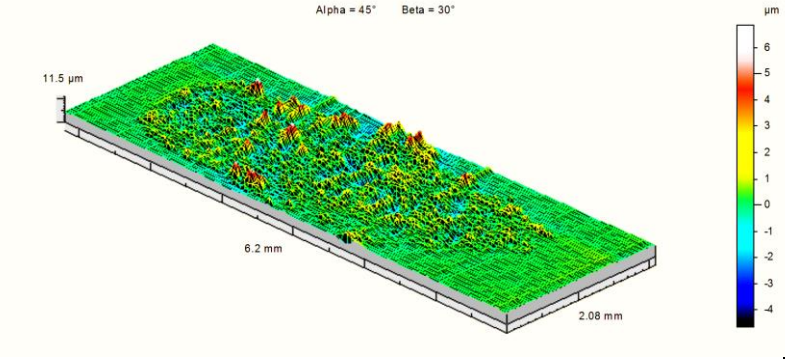
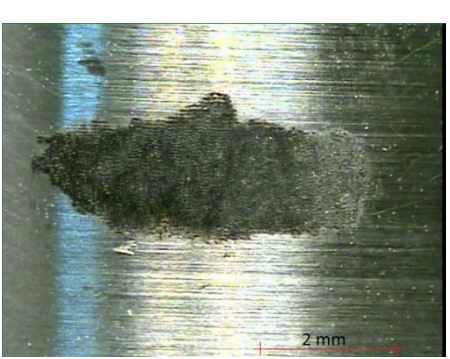
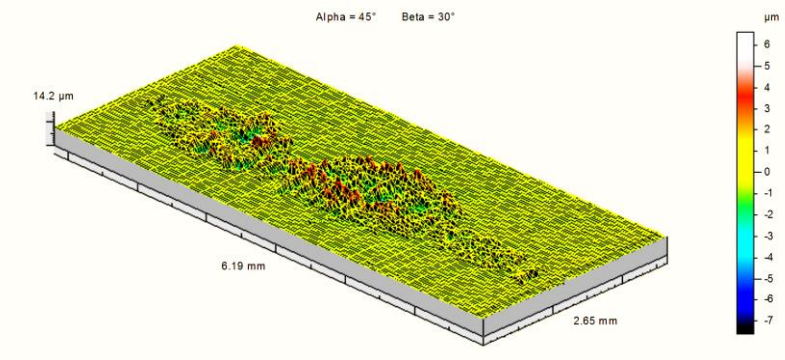

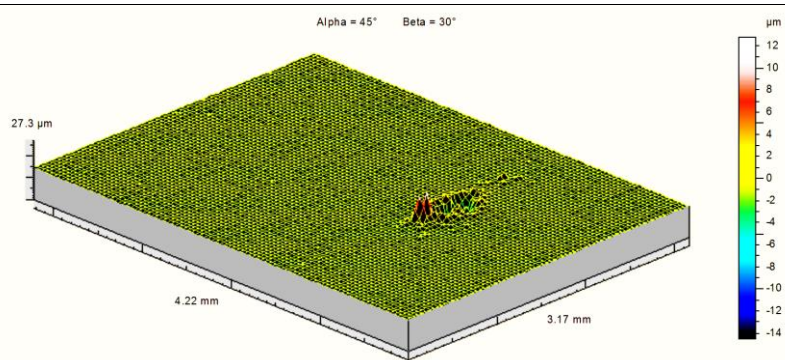
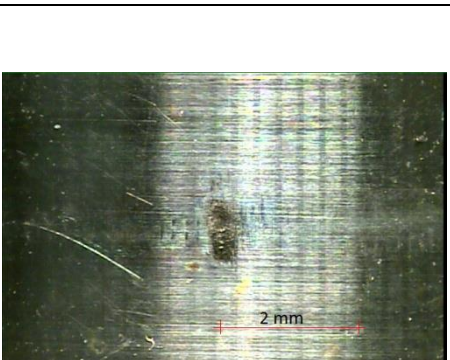
13	<p>Alpha = 45° Beta = 30°</p>  <p>11.9 μm</p> <p>3.2 mm</p> <p>1.98 mm</p>	 <p>2 mm</p>
RT		
CP1		
3_2		
15 μm		
11 N		
14	<p>Alpha = 45° Beta = 30°</p>  <p>16.9 μm</p> <p>5.21 mm</p> <p>2.62 mm</p>	 <p>2 mm</p>
RT		
CP1		
4		
15 μm		
29 N		
15	<p>Alpha = 45° Beta = 30°</p>  <p>13.5 μm</p> <p>5.48 mm</p> <p>3.29 mm</p>	<p>SEM Image</p>  <p>5 mm</p>
200C		
CP1		
4		
15 μm		
29 N		

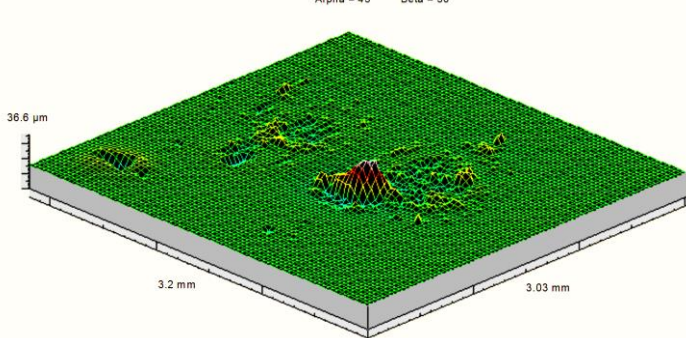
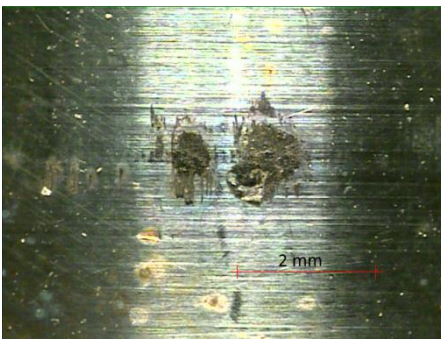
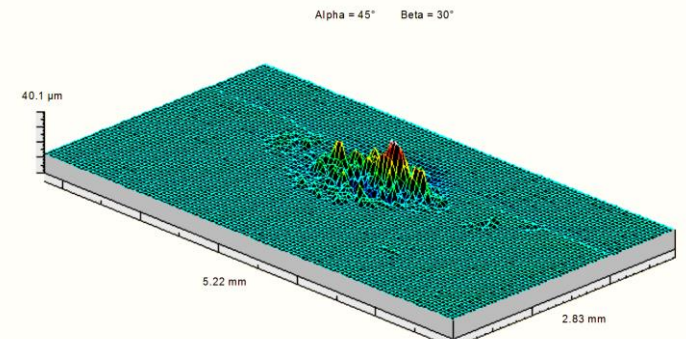
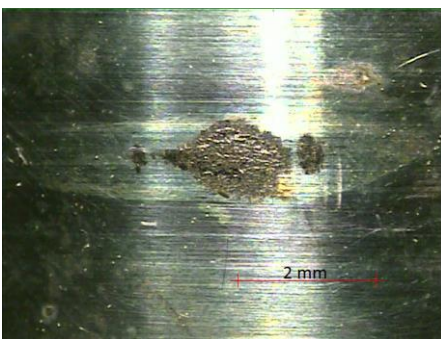
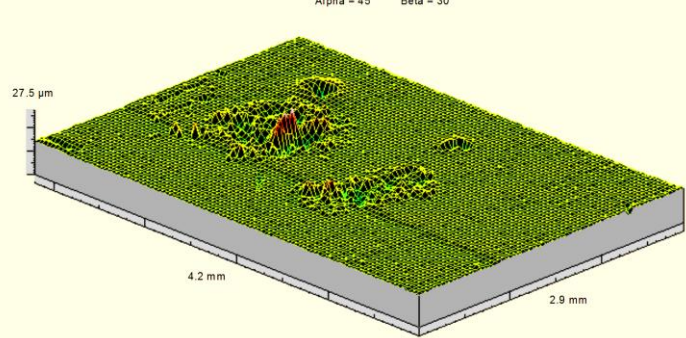
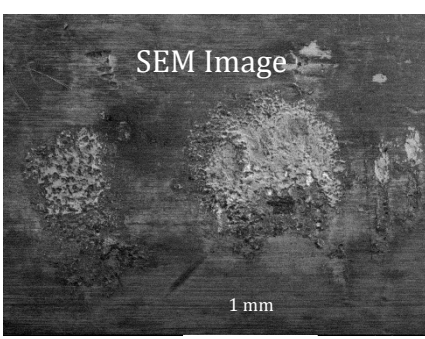


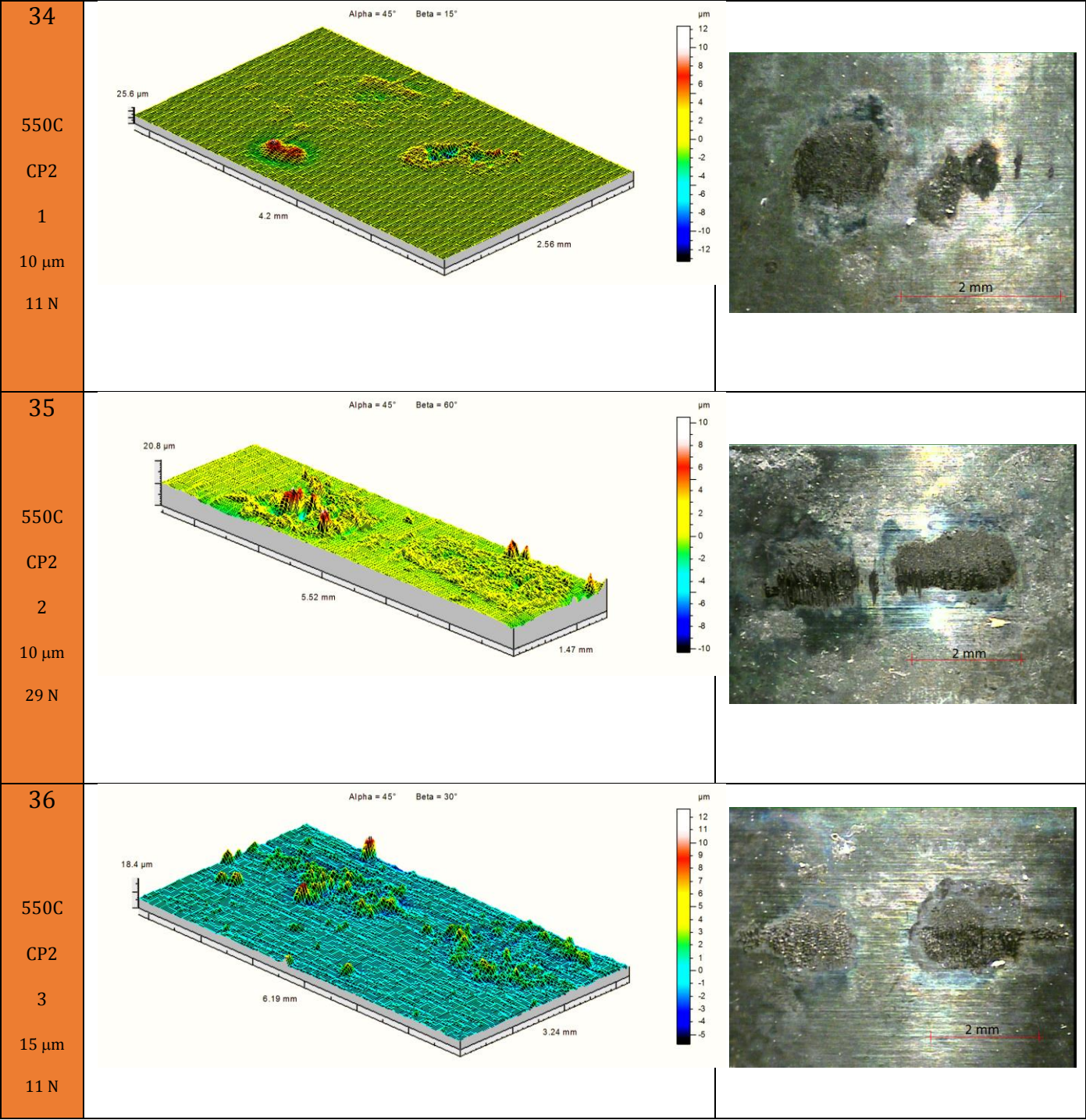


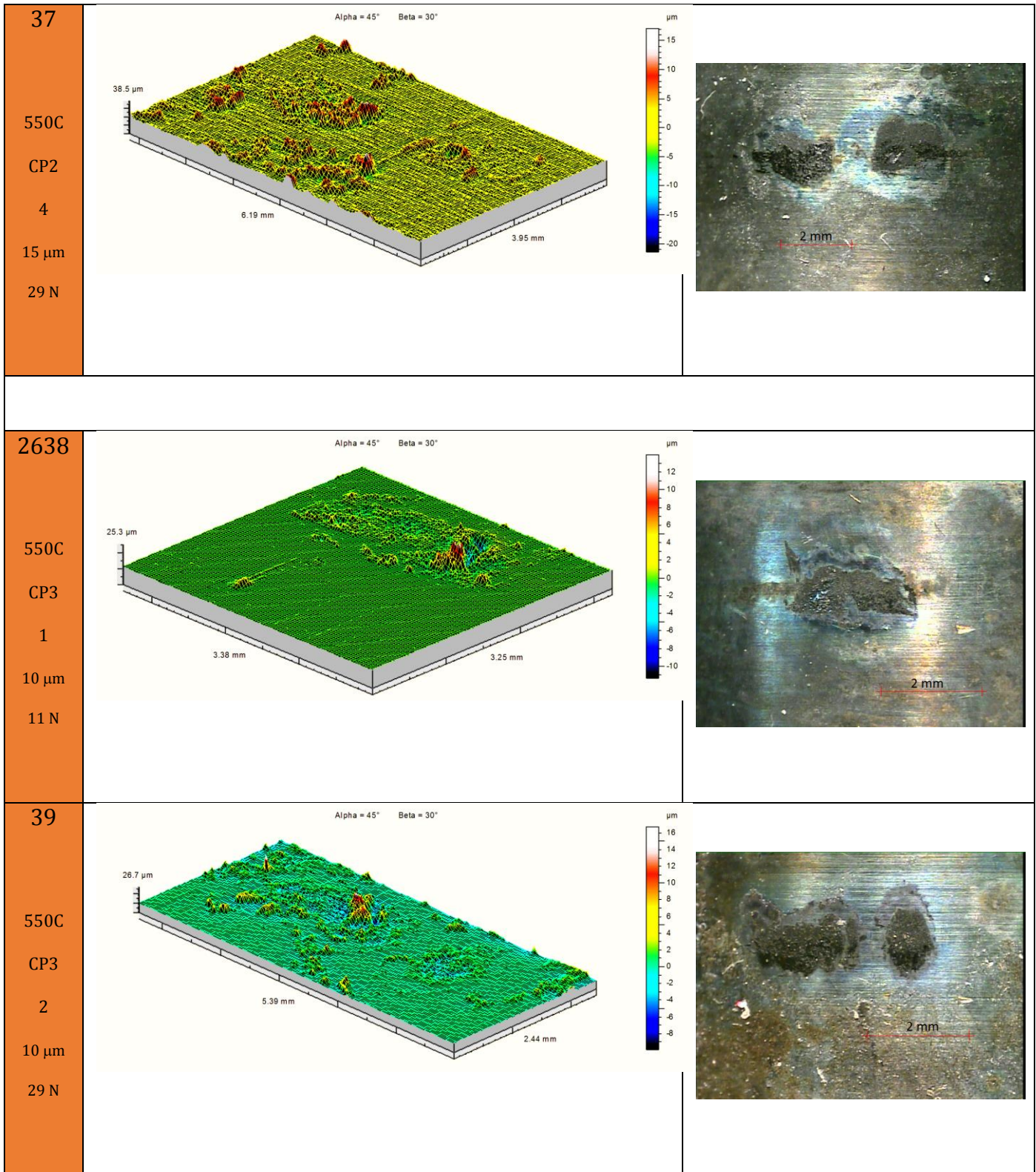
22	Alpha = 45° Beta = 30°		
350C			
CP2			
2			
10 μm			
29 N			
23	Alpha = 45° Beta = 30°		
350C			
CP2			
3_1			
15 μm			
11 N			
24	Alpha = 45° Beta = 30°		
350C			
CP2			
3_2			
15 μm			
11 N			

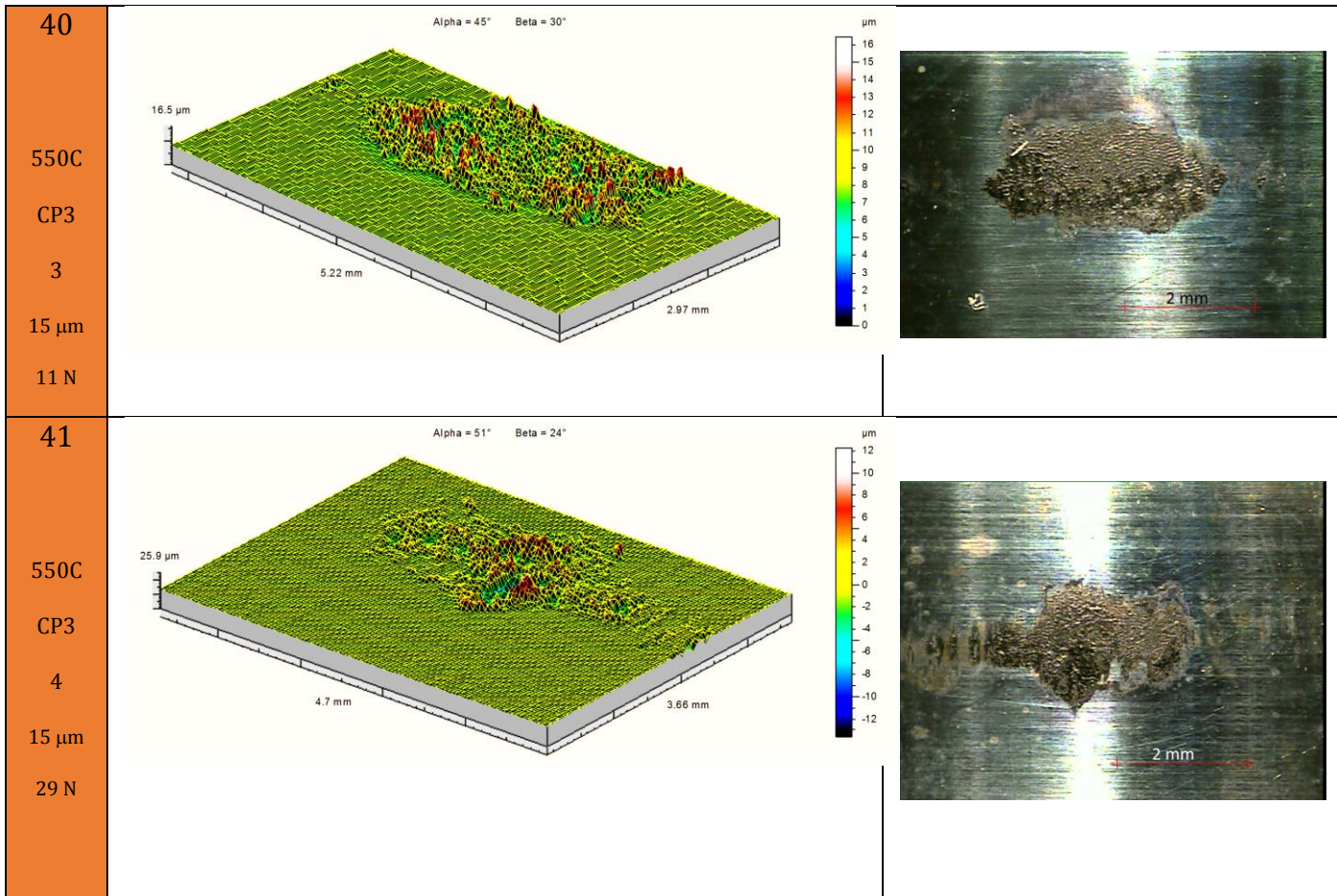


28	Alpha = 45° Beta = 30°		
350C			
CP3			
3			
15 μm			
11 N			
29	Alpha = 45° Beta = 30°		
350C			
CP3			
4			
15 μm			
29 N			
30	Alpha = 45° Beta = 30°		
550C			
CP1			
1			
10 μm			
11 N			

<p>31</p> <p>550C</p> <p>CP1</p> <p>2</p> <p>10 μm</p> <p>29 N</p>	<p>Alpha = 45° Beta = 30°</p>  <p>36.6 μm</p> <p>3.2 mm</p> <p>3.03 mm</p> <p>μm</p> <p>20</p> <p>18</p> <p>16</p> <p>14</p> <p>12</p> <p>10</p> <p>8</p> <p>6</p> <p>4</p> <p>2</p> <p>0</p> <p>-2</p> <p>-4</p> <p>-6</p> <p>-8</p> <p>-10</p> <p>-12</p> <p>-14</p>	 <p>2 mm</p>
<p>32</p> <p>550C</p> <p>CP1</p> <p>3</p> <p>15 μm</p> <p>11 N</p>	<p>Alpha = 45° Beta = 30°</p>  <p>40.1 μm</p> <p>5.22 mm</p> <p>2.83 mm</p> <p>μm</p> <p>25</p> <p>20</p> <p>15</p> <p>10</p> <p>5</p> <p>0</p> <p>-5</p> <p>-10</p>	 <p>2 mm</p>
<p>33</p> <p>550C</p> <p>CP1</p> <p>4</p> <p>15 μm</p> <p>29 N</p>	<p>Alpha = 45° Beta = 30°</p>  <p>27.5 μm</p> <p>4.2 mm</p> <p>2.9 mm</p> <p>μm</p> <p>26</p> <p>24</p> <p>22</p> <p>20</p> <p>18</p> <p>16</p> <p>14</p> <p>12</p> <p>10</p> <p>8</p> <p>6</p> <p>4</p> <p>2</p> <p>0</p>	<p>SEM Image</p>  <p>1 mm</p>







Appendix B: Energy ratio for the conducted tests

Test No.	Temp	Contact Pair			Amplitude	Load	Energy Ratio
	°C		Cylinder	Ring	± μm	N	
1	Room Temp (RT)	CP0-G1	Cobalt Alloy 1	Cobalt Alloy 1	5	14	0.76
2					5	20	0.72
3					4	29	0.29
4					9	15	0.55
5					10	20	0.71
6					10	29	0.61
7					15	11	0.69
8					15	29	0.80
9					10	11	0.85
10	Room Temp (RT)	CP1-G2	Cobalt Alloy 2	Cobalt Alloy 1	10	11	0.76
11					10	29	0.61
12					15	11	0.77
13 (R)					15	11	0.71
14					15	29	0.70
15	200°C	CP1-G2	Cobalt Alloy 2	Cobalt Alloy 1	15	29	0.54
16	350 °C	CP1-G2	Cobalt Alloy 2	Cobalt Alloy 1	10	11	0.85
17					10	29	0.53
18 (R)					10	29	0.58
19					15	11	0.59
20					15	29	0.46

21	350 °C	CP2-G2	Cobalt Alloy 1	Nickel Alloy 1	10	11	0.50
22					10	29	0.56
23					15	11	0.38
24 (R)					15	11	0.59
25					15	29	0.65
26		CP3-G2	Cobalt Alloy 2	Nickel Alloy 1	10	11	0.42
27					10	29	0.72
28					15	11	0.24
29					15	29	0.66
30	550°C	CP1-G2	Cobalt Alloy 2	Cobalt Alloy 1	10	11	0.36
31					10	29	0.30
32					15	11	0.30
33					15	29	0.53
34		CP2-G2	Cobalt Alloy 1	Nickel Alloy 1	10	11	0.46
35					10	29	0.58
36					15	11	0.59
37					15	29	0.78
38		CP3-G2	Cobalt Alloy 2	Nickel Alloy 1	10	11	0.28
39					10	29	0.44
40					15	11	0.31
41					15	29	0.57